INSTITUTO DE ASTROFÍSICA DE ANDALUCÍA
CONSEJO SUPERIOR DE INVESTIGACIONES CIENTÍFICAS

DEPARTAMENTO DE FÍSICA TEÓRICA Y DEL COSMOS
UNIVERSIDAD DE GRANADA

# MOLECULAR GAS AND STAR FORMATION IN HICKSON COMPACT GROUPS: ANALYSIS AND TECHNICAL CHALLENGES

Memoria para optar al grado de doctor por la Universidad de Granada

Granada, 2011

VICENT MARTÍNEZ I BADENES

Directores:
Prof. Ute Lisenfeld
Dr. Daniel Espada Fernández
Dra. Lourdes Verdes-Montenegro Atalaya

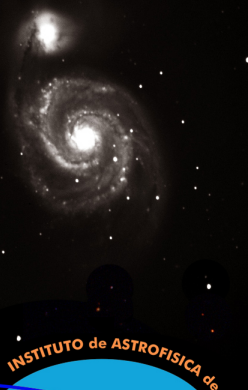

ugr | Universidad de Granada

CSIC
Consejo Superior de Investigaciones Científicas

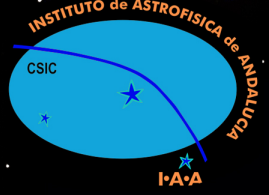

Instituto de Astrofísica deAndalucía- CSIC
Departamento de Física Teórica y del Cosmos
Universidad de Granada

# Molecular gas and star formation in Hickson Compact Groups: Analysis and technical challenges

## Tesis Doctoral

**Vicent Martínez i Badenes**

Directores:
Dra. Ute Lisenfeld
Dr. Daniel Espada Fernández
Dra. Lourdes Verdes-Montenegro Atalaya

Marzo de 2011

Editor: Editorial de la Universidad de Granada
Autor: Vicent Martínez i Badenes
D.L.: GR 2102-2011
ISBN: 978-84-694-2953-2

# Molecular gas and star formation in Hickson Compact Groups: analysis and technical challenges

Vicent Martínez i Badenes

March 4, 2011

.

*A* m'auelo *Vicente,* m'auelo *Vicente i ma tia Pilar.*
*Els que més m'han ensenyat.*
*Els que més xalaran en veure-ho.*

.

*E per tal quels homens coneguessen e sabessen can haurien passada aquesta uida mortal, ço que nos hauriem feyt [...] lexam aquest libre per memoria, a aquels qui uolran hoir de les gracies que nostre Senyor nos ha feytes, e per dar exempli a tots los altres homens del mon, que façen ço que nos*

Jaume I. Llibre dels feyts.

*I quan els vaig veure vaig pensar "estos, estos no són els que jo esperava"*

Vicent Badenes Bertran

# Agradecimientos / Acknowledgements / Agraïments

*I, a vegades, ens en sortim*

Hacemos ciencia, no literatura, me han dicho más de una vez en los últimos 4 años. Para alguien dado a los excesos sintácticos como el que suscribe, tener que plegarse a la concreción, la sobriedad y la supeditación de la forma al fondo ha tornado el aforismo del principio en una losa. Pero siempre queda un resquicio, piensa uno. Siempre le quedan a uno esas páginas basura para explayarse, para soltar todos los rollos, circunloquios e incluso, por poner ejemplos, ejemplos de anadiplosis o sinécdoques. Siempre habrá tiempo, piensa uno. Y en estas que a uno lo que le pasa es que lo deja para el final y se encuentra de madrugada, cuando por la calle sólo hay desgraciados y por los despachos sólo hay genios (o era al revés?), componiendo líneas para ahuyentar el desquicio. Como casi siempre en la vida, no es lo que esperábamos. Y además vinimos a llevarnos la vida por delante, y descubrimos que la vida iba en serio más adelante y todas esas citas que se han acumulado y ahora uno no encuentra dónde meterlas.

Y se encuentra uno nuevamente escondiéndose de las responsabilidades tras la pluma, travistiendo de necesidad (uno se plantea que al fin y al cabo en todo ladrillo hay unos agradecimientos) lo que es puro placer. Y recurre a esa fórmula cuya validez está demostrada al menos empíricamente (no hay argumento de autoridad, pero muchos la usan) por la cual se acepta la tremenda horterada de cambiar de idioma de párrafo a párrafo para saludar a aquellos con los que uno se siente en deuda. Y se imagina uno con pajarita leyendo con voz grave y engolada esas líneas delante del rey de Suecia. O incluso piensa que no serían malos versos para leer en su funeral, y se imagina a algún compañero de despacho con camisa negra declamando las palabras que va escribiendo al lado de la tapa abierta de su propio ataúd. Todo muy british. Y uno sonríe cuando no puede evitar pensar cómo se parece esa sarta lastimosa a las preces que rezaban todas las tardes las tías de su madre al acabar el Rosario, cuando le rezaban sendas avemaría a tantos difuntos que darían para llenar un libro de registros. Y mordiéndose la lengua para no descojonarse delante del rey de Suecia o, lo que sería aún peor, de su propio cadáver, carraspea, se aclara la voz, levanta la barbilla y empieza a enumerar con la vista en un punto indeterminado de la pared del fondo.

Así, sin saber muy bien dónde fechar el principio, se fija aleatoriamente en hace casi 5 años y resulta imperioso dar las gracias a Ute y Lourdes por haberme dado la oportunidad de hacer todo lo que se refleja en estas páginas y hacer realidad un sueño de muchos, muchos años, por más que los sueños y la realidad se lleven mal a veces. Y por supuesto a Dani, que llegó un poco más tarde y se hizo imprescindible, cómplice, confesor y hasta posadero. En el pecado que cometisteis confiando en mí va esta penitencia como tesis.

Ya en la fina línea que separa lo profesional de lo personal correspondería acordarse de Herr Juande, el oráculo, un ejemplo todavía por igualar de excelencia personal y profesional, y la prueba fehaciente de que la justicia universal existe y recompensa a la gente buena, llevándola a lo más alto. De Pique, la sofisticación afrancesada en la sencillez, un hombro más que un compañero al que consultar, y eso habiéndole consultado mucho. De Jack *The Shark*, a twinkle of light in the long night of orthodoxy. De Simon, entussiata cínico e imprescindible en le trabajo que se presenta, de Pepe, con quien se pasó de las correrías memorables (jamon y mus) a la conversación calma. De Gilles, Steph, Chandra y el resto del grupo, gente alegre, que con los tiempos que corren no es poco y que siguen haciendo válido que en AMIGA, como en la interferometría, uno más uno a veces son más de dos. I feel also in debt with Satoki-and Min, who helpfully took me in in Taipei and Amherst, turning out these stays to be, not only profitfull, but also very nice times. Bisognerebbe anche (con dei errori ortografici) mandare un bacio ai italiani di Massachusetts, che per qualche strana raggione mi fanno pensare que, dopo piú di due anni, ho due amici oltre il mare.

Pasando a la familia, la de Granada, cabría empezar una eterna letanía, pero aunque sea temporalmente, los primeros deberían ser Concha y Toni, con quien tanto miedo da quedar para aclarar un problema con un factura, porque sabes cómo y dónde acabará la cosa. Pasando al Zaidín, empezar por los seniors del café, Antxon, Emilio, Pepe, o Fernando, que no era de café, pero casi mejor así. Seguir por los compadres del zulo, la locura más deliciosa de estos años, donde trabajar, no sé si trabajábamos, pero nos lo pasamos en grande. Pasar por la pecera, donde al principio no tenía que repartirme la sonrisa de Yoli con nadie, pero después tuve que compartirla con buena gente. Y, en algún punto después de saludar a los compañeros del fútbol, habría que quedar mal con el resto y particularizar. En Dani, un genio, simplemente. En Charly, que me sacó muchas, muchas veces de problemas con el software o directamente la interpretación de los datos (gracias again, Herr Califa). En Don Paco Navarro, el sentido común. En la Gabi, que a última hora me salvó el pellejo. Y acabar con los más cercanos, a costa de crear agravios: antes Mar y después Belén, o Alba y Rocío. Ale, un remanso de calma y whisky en la tarde del domingo. Antonio, una de las personas que te convencen de que el mundo sigue valiendo la pena porque hay gente como él. Y, como el dolor une, Paco Flópez, intelectual parco de vieja escuela, imprescindible a última hora y me temo que por mucho tiempo

Y por supuesto, Marta, Gorman, el Rabino y Diego, aquí sobra literatura o falta espacio. Me sabréis disculpar, espero.

Como uno tiene tendencia a la melancolía, no podrá evitar el recurso fácil de acordarse de su maestra, la que le enseñó a leer. Pero, más que a ella, me parece más oportuno nombrar a poca gente en nombre de toda la que ha confiado, y en algunos casos sorprendentemente sigue haciéndolo, en el que suscribe. Desde Pepín y Mª Ángeles, incondicionales, hasta Vicente, que tanto se empeñaba en hacernos pensar, Amparo o Marcela, las eternas *mamme*. Y, caiga la vergüenza sobre él, Manolo, Manolo Vectores, que con su sempiterno aire de despreocupación algún día dijo aquello de *Física? Sí, hombre claro! Si en el fondo no es para tanto...* Pensar també en Llorenç, el monstruo, el mestre. Que no sols va arribar a última hora aportant estètica, que és el que fa millor que ningú, sinò que estava ahí des de primera (primeríssima) hora, confiant en mi i recordant-me que sols és impossible el que no s'intenta.

Y aprovechando que se habrá intentado transportar la acción al pueblo, será de ley agradecer mil cosas al Tío Pepe y la Tía Emilia, de quienes, a falta de espacio, se puede resumir mucho agradeciéndoles que me enseñaran a hablar en castellano. A toda la gente de la banda, mi segunda casa. A Miguel, Eva y, simplemente, a la cuadrilla de toda (pero *de toda*) la vida, por hacer tan difícil el explicarle a los extraños cómo es posible que la gente siga estando ahí. A Antonio,

primero profesor en terribles resacas conjuntas y después agitador cultural. A Eva, la que no es del pueblo pero da igual.

Singularmente, y sin solución de continuidad, cabrá hacer una pausa y recordar que prometo estarlo a la Orquesta Piticli: Recu, Floriano y Juanfer. Porque dentro de muchos años no diré que mientras trabajaba en ciencia tocaba con unos amigos. No. Diré que, cuando yo tenía una banda de R&R, mientras tanto, hacía una tesis. Como pillaba por Valencia, será imprescindible agradecer tantos buenos ratos a Marta (perla!), Ame, Emi (López!) Pablo (pum, pum, clank), Caspe (Tigre!) y, por problemas de espacio físico, que no sentimental, a toda la gente del Peset. A Quique, que va ser amfitrió del cap de setmana més gloriós d'aquestos anys i que ha aportat a aquest treball com a ell més li agrada: repartint llenya.

I, per supost, a Pep i Santi. Com als d'uns paràgrafs més amunt, crec que em perdonareu si ho deixe estar i ja s'ho xarrem amb més calma.

I clar: a la família. Als qui realment tenen la culpa de tot el que la gent puga apreciar d'aquest treball o de qui el signa. Als tios i els cosins, a tots, per fer-me sentir estimat. Perquè sempre em toca explicar que no, que a ma casa quan ens juntem uns quants, ens fa comboi. Per fer-me sentir que forme part d'una cosa molt i molt important, perquè sé que m'envolta gent bona, que sols aspira a això mateix, a ser bona gent. I, perquè serà precís particularitzar de nou per tal de quedar malament, a Xavi i Carlos, amb qui compartixc més xerrades que menys, d'unes coses o d'altres. A l'altre Carlos, el menut, perquè el seu padrí s'ho deu. A la tia Amparo, perquè a la meua madrina s'ho dec. A tots els que es miraran pagats aquesta tesi des de molt més enllà d'on jo he arribat. I als nanos: Vicent, Pablo, Ferran i Maria. Per l'esperança que representen.

I ja buscant l'esclat emocional, a Ricardo. Que és el meu germà, i això és més del que podré dir de quasi ningú en aquesta vida. A Matilde, per deixar-me estimar-la , per no deixar-me estimar-la més del que m'estima ella. Per fer-me entendre que allò d'agraïr la paciència no és un tòpic, sinò una necessitat sagnant. I al pare i la mare: tot, senzillament tot.

I tot just a aquest punt, recordar-li al rei de Suècia, o si pertoca demanar a qui declama al costat del taüt que ho esmente, que tota la processó que s'ha fet desfilar és i ha estat veritablement allò que Ortega denominava *la meua circumstància*. I que el que soc, i el que ací a continuació es presenta, no s'entén sense ells i elles, que ho han fet possible i, sobre tot, li han donat significat.

Cavallers, va de bo.

*I a vegades, contra tot pronòstic,*
*una gran bestiesa capgira allò que creiem lògic*
*tot fent evident que,*
*per un moment,*
*ens en sortim.*

*Granada, març de 2011*

# Resumen

## 0.1 Título de la Tesis

**Gas molecular y formación estelar en Grupos Compactos de Hickson: análisis y desafíos técnicos**

## 0.2 Problema planteado

La finalidad de esta tesis es caracterizar el contenido de gas molecular y la tasa de formación estelar de las galaxias pertenecientes a una submuestra de Grupos Compactos de Hickson (Hickson Compact Groups, o *HCGs*), estudiando la influencia del entorno galáctico en estas magnitudes y teniendo en cuenta el contenido de gas atómico de las mismas galaxias y el estado evolutivo del grupo. Se presenta también un estudio sobre una técnica de calibración para interferómetros milimétricos/submilimétricos.

## 0.3 Motivación y estructura del trabajo

El entorno de las galaxias está ampliamente reconocido como actor fundamental en la evolución y propiedades de las galaxias. En el rango de posibles entornos galácticos, desde los pares hasta los grandes cúmulos de más de 1000 galaxias, los HCGs (Hickson 1982), con entre 4 y 8 miembros, constituyen entornos de especial interés debido a su alta densidad galáctica, la baja dispersión de velocidades que presentan sus miembros, y su grado de aislamiento del entorno.

Uno de los efectos más visibles de la interacción en HCGs es la deficiencia de gas atómico que presentan sus miembros. Basándose en la distribución de gas atómico en el grupo, Verdes-Montenegro et al. (2001) propusieron un modelo de secuencia evolutiva en el cual la fase evolutiva de los grupos viene dada por el porcentaje de gas atómico que ha sido arrancado de los discos de las galaxias debido a la interacción con sus vecinas. Sin embargo, los efectos del entorno en el contenido de gas molecular en HCGs no están tan bien determinados como lo están para el gas atómico. Basados en el aumento del contenido de gas molecular observado en sistemas galácticos en interacción fuerte (p.e. Casasola et al. 2004), se podría esperar un comportamiento similar en los HCGs. Sin embargo, los estudios previos (Verdes-Montenegro et al. 1998; Leon et al. 1998) revelan un contenido de gas molecular similar al de las galaxias de campo.

La formación estelar (o Star Formation, *SF*), que viene determinada por la disponibilidad de gas molecular, presenta incertidumbres similares en los HCGs. Se ha hallado que la SF está realzada en sistemas en interacción como los pares de galaxias (ver, p.e. Woods et al.

2006), con lo que un comportamiento similar se podría esperar en los HCGs. Sin embargo, como en el caso del gas molecular, la SF en HCGs, calculada a partir de varios trazadores (Verdes-Montenegro et al. 1998; Leon et al. 1998; Iglesias-Páramo & Vílchez 1999; Bitsakis et al. 2010, entre otros), presenta valores similares a los que se dan en galaxias de campo.

Lo que se busca con este trabajo es determinar el contenido de gas molecular y la tasa de formación estelar (Star Formation Rate, *SFR*) en galaxias pertenecientes a una muestra de HCGs que cubra todas las fases de la secuencia evolutiva de Verdes-Montenegro et al. (2001), intentando obtener datos para todas las galaxias de estos grupos y discernir si hay relación entre el contenido de gas molecular y la SF de las galaxias con el estado evolutivo del grupo. La muestra seleccionada tiene datos de gas atómico disponibles para todos los grupos y para un 75% de las galaxias. La comparación de las propiedades de los HCGs se ha llevado a cabo con la muestra AMIGA de galaxias aisladas (Verdes-Montenegro et al. 2005b), con el fin de determinar si las desviaciones en el contenido de gas atómico con respecto a las galaxias aisladas se traducen en anomalías en la masa de gas molecular y la tasa de formación estelar.

Una vez estudiado el contenido de gas molecular en las galaxias, se ha llevado a cabo el análisis de mapas observados con el interferómetro OVRO para 2 HCGs (HCG 40 y HCG 79) cuyas características los hacen especialmente interesantes, con el objetivo de conseguir una mayor resolución angular en los datos de CO. Esos mapas se han comparado con las imágenes de alta resolución en infrarrojo (emisión trazadora de SF) procedentes del telescopio espacial Spitzer y con los mapas de gas atómico procedentes de VLA.

La inminente puesta en funcionamiento del interferómetro ALMA, que supondrá un enorme salto de calidad en las observaciones en el rango mm/submm es una de las motivaciones que está detrás de este trabajo. Así, paralelamente al estudio del caso científico ya detallado, se incluye también en esta tesis el desarrollo y prueba de una técnica de calibración de posible aplicación en ALMA. La técnica de fast-switching, que busca minimizar los efectos de las turbulencias atmosféricas mediante rápidos y sucesivos apuntados a un calibrador, ha sido probada en el interferómetro SMA con el fin de determinar si su aplicación en ALMA puede implicar una mejora en la calidad de las imágenes observadas.

## 0.4 Aportaciones de la tesis al campo científico

### 0.4.1 Estudio de la masa de gas molecular y la tasa de formación estelar en 20 HCGs

En este trabajo se ha completado por primera vez el estudio del gas molecular y la tasa de formación estelar en una muestra de 86 galaxias pertenecientes a 20 HCGs con datos disponibles de HI y fase evolutiva determinada. Para sólo 2 de las 88 galaxias en dichos grupos no se han obtenido datos de gas molecular. De igual modo, la comparación se ha llevado a cabo también por primera vez con una muestra de galaxias aisladas (la muestra AMIGA), evitando los efectos que los pares, tripletes o pequeños grupos podían tener en las muestras de galaxias de campo utilizadas como referencia anteriormente.

El contenido de gas molecular de las galaxias se ha determinado mediante la observación de la línea de excitación rotacional J(1→0) de la molécula de CO. Hemos observado 47 galaxias con el radiotelescopio de 30 metros de IRAM en el Pico Veleta y recopilado datos de la bibliografía (Verdes-Montenegro et al. 1998; Leon et al. 1998), completando una muestra de 86 galaxias. La tasa de formación estelar se ha calculado a partir de la emisión en infrarrojo lejano (Far Infrared,

*FIR*) en 60 $\mu$m y 100 $\mu$m procedentes del telescopio espacial IRAS. Finalmente, se han utilizado también las masas de HI correspondientes a 66 galaxias observadas con VLA y procedentes de la bibliografía (Verdes-Montenegro et al. 2001, y Verdes-Montenegro, comunicación privada). Para todas estas magnitudes se han calculado las deficiencias respecto a su valor esperado. El valor esperado de la magnitud se ha calculado respecto a la luminosidad de la galaxia en la banda B, utilizando los ajustes procedentes de la muestra AMIGA.

En la comparación de las galaxias en HCGs con la muestra AMIGA no hemos encontrado diferencias significativas en las propiedades del contenido de gas molecular y la emisión FIR entre ambas muestras. Para llevar a cabo la compraración hay que tener en cuenta dos aspectos fundamentales: 1) Los HCGs se hallan a una mayor distancia de nosotros, con lo cual las luminosidades y masas medidas son mayores en promedio, incrementándose la diferencia en el caso del gas molecular 2) El ratio de galaxias elípticas es mucho mayor en la muestra de HCGs, mientras que la muestra AMIGA está dominada por galaxias espirales, por lo que hemos centrado la comparación en las galaxias espirales de los HCGs. Los ajustes lineales entre el gas molecular y la luminosidad óptica en banda B, y entre la luminosidad FIR y la luminosidad óptica arrojan valores similares para las dos muestras, lo cual sugiere que las dos muestras siguen la misma correlación. Como resultado, las galaxias en HCGs prácticamente no son deficientes en emisión FIR. Para el contenido de gas molecular hemos encontrado un ligero exceso, pero no se puede decartar que se deba a una sobreestimación de la masa de $H_2$ debida a la extrapolación que se ha aplicado a la masa de gas molecular observada.

La luminosidad FIR (y por tanto la tasa de formación estelar) y la masa de gas molecular muestran una estrecha correlación, presente también entre la deficiencia de una y otra magnitud. Ello indica la relación que existe entre el gas molecular y la tasa de formación estelar: la falta de gas molecular para alimentar la SFR provoca una caída de ésta. La eficiencia de la formación estelar (*SFE*) de los HCGs, definida como la razón entre la tasa de formación estelar y la masa de gas molecular no presenta diferencia significativas con la de las galaxias AMIGA.

No hemos encontrado ninguna relación entre la deficiencia del gas molecular y la deficiencia de la luminosidad FIR con el contenido de HI del grupo o su estado evolutivo. Sin embargo, sí que presentan una débil relación con el contenido de HI de la galaxia.

El estudio conjunto de la SFE y la tasa específica de formación estelar (sSFR, definida como la razón entre la tasa de formación estelar y la masa estelar de las galaxias), muestra que la sSFR presenta una dependencia con la deficiencia del contenido de gas atómico y la deficiencia del contenido de gas molecular, con una mayor sSFR en las galaxias ricas en gas atómico o molecular. La SFE, sin embargo, no presenta ninguna tendencia, comportándose con independencia de las deficiencias de la galaxia. La bimodalidad en la distribución de la formación estelar específica apuntada entrabajos anteriores (Tzanavaris et al. 2010) no se aprecia con claridad en nuestra muestra.

### 0.4.2 Estudio de alta resolución de HCG 40 y HCG 79

La distribución de gas molecular en el grupo se ha estudiado en HCG 40 y HCG 79 haciendo uso de observaciones de la misma línea de emisión J(1→0) del CO con el interferómetro OVRO, que presenta una resolución angular de entre 3.5 y 5 segundos de arco, frente a los 22 segundos de arco del 30m. Se seleccionaron estos grupos por ser los que muestran una alta densidad de galaxias (la mayor de nuestra muestra) junto a una baja dispersión de velocidades.

El nivel de sensibilidad del interferómetro no alcanzó los valores esperados en la propuesta de observación, detectándose gas molecular en 2 de las 4 galaxias previamente detectadas con

el 30m en HCG 40 y ninguna de las galaxias de HCG 79, de las cuales 2 habían sido detectadas con el 30m. Las masas de gas molecular detectadas con OVRO para HCG 40 coinciden con las obtenidas con el 30m. En el caso de HCG 79, que las 2 galaxias detectadas con el 30m no se hayan podido detectar en OVRO se puede interpretar como el resultado de una distribución extendida del gas molecular a lo largo de la galaxia.

Como complemento a las observaciones de OVRO, se ha realizado un estudio de la tasa y la eficiencia de la formación estelar utilizando los datos procedentes de mapas de alta resolución de 24$\mu$m de Spitzer, hallando valores para la SFE similares a los obtenidos con los datos de IRAS e, igualmente, sin diferencias significativas con los de la muestra AMIGA. La SFE es sorprendentemente constante para todas las galaxias, con independencia de su contenido en gas atómico o molecular.

### 0.4.3 Una técnica de calibración para ALMA: fast-switching

En paralelo al estudio del caso científico de los HCGs, se han llevado a cabo una serie de pruebas de la técnica de calibración del fast-switching, con la vista puesta en su posible aplicación en ALMA. Como estudio previo, se ha hecho una estimación del tiempo necesario para mapear nuestra muestra de HCGs con distintos interferómetros. Hemos hallado que nuestros HCGs no presentan buenas condiciones para su observación en SMA (que requiere de unas 6 horas para alcanzar una sensibilidad de 10 mJy beam$^{-1}$). En PdB (que necesita 8 minutos de integración para llegar a 10 mJy beam$^{-1}$), aunque posible, una observación exitosa requeriría de demasiado tiempo de observación, mientras que su observación con ALMA, aun con un array reducido de 16 antenas (que solo precisa 1 minuto de integración para alcanzar los 10 mJy beam$^{-1}$), requeriría de mucho menos tiempo de observación.

Los datos, procedentes de pruebas llevadas a cabo en el SMA, buscaban simular la respuesta del interferómetro ante distintos periodos de tiempo transcurridos entre sucesivos apuntados al calibrador. Las observaciones fueron llevadas a cabo bajo distintas condiciones atmosféricas. Los resultados que se obtuvieron fueron 1) No existe conexión entre la opacidad y la estabilidad de fase. 2) El calibrador debe estar lo más cercano posible a la fuente observada. 3) La relación señal/ruido de las observaciones mejora a medida que se reduce el tiempo transcurrido entre apuntados al calibrador bajo unas determinadas condiciones atmosféricas, en las que la opacidad no tome valores ni extremadamente bajos ni altos, en cuyas circunstancias el fast-switching sí implicaría una mejoría en la calidad de los datos.

# Contents

# Chapter 1
# Introduction

*El cabaret galàctic ja és obert*
*els paralítics hi aprendran claqué*
*la masovera enganya els innocents*
*cambrers romàntics cremen els diners*

**Jaume Sisa** - Cabaret Galàctic

The environment of the galaxies and the interaction with neighbor systems, as it is widely shown by observations and theoretical models, plays a key role on their evolution. In the very beginning of the extragalactic astronomy, Zwicky (1959), showed that some peculiarities observed in interacting galaxies could be due to tidal forces and that collisions, common in galaxy clusters, should produce changes on the star clusters and the interstellar medium (ISM). The objects in the Arp (1966) catalogue of peculiar galaxies, with 338 catalogued objects, can be taken as the first reference for the study of the effects of the interaction on the galactic kinematics and dynamics, as well as in their morphology, star formation or gas content. The hypothesis of the interaction as inducer of morphology transformations was confirmed by the work of Toomre & Toomre (1972), who showed, using simulations with elementary models, that the peculiar shapes, bridges or tails observed in some galaxies were the result of the interaction and further merging of the galaxies. After that, Dressler (1980) studied 55 rich galaxy clusters, finding a well defined relationship between local density type and the morphological type of the galaxies with an increasing ratio of early-type galaxies in denser environments. The morphology-density relation for higher redshift clusters was studied by Dressler et al. (1997) finding that, even though the fraction of elliptical galaxies is as large, or larger, than in low-redshift clusters, the S0 fraction is 2-3 times smaller, with a proportional increase of the spiral fraction. This trend suggests that a large fraction of spiral galaxies are transformed into lenticulars as the group evolves.

The physical, and not only morphological properties of the galaxies have been found to be strongly affected by their environment. The galaxies in denser and massive environments such as galaxy clusters, have redder colors, older stellar populations and higher luminosities, as shown by the multiwavelength studies and galaxy surveys performed during the last decades. Early simulations like the ones performed by Negroponte & White (1983), Hernquist (1989) or Barnes & Hernquist (1991) have found how the gas is deposited in the center of the remnants of galaxy merging. The gas inflow resulting from the loss of angular momentum by the gas results in an enhancement of the central star formation, like the one shown by the numerical simulations of Di Matteo et al. (2007).

Nevertheless, the role of the interactions is not the same for all the possible enviroments. Galaxies tend to gather in larger structures starting from pairs to large, rich clusters with thousands of members. The role of interactions changes from small to large structures, since the dynamics of the collisions between members strongly depends on the environment. At this point, the study of small groups, but still larger than pairs or triplets can be useful. The gas redistribution, star formation or morphological transformations of the galaxies within those groups can be studied in more detail and, furthermore, the small number of members can help us to determine the dynamics leading to these galactic changes.

## 1.1 The catalogue of Hickson Compact Groups

The compact groups (CG) of galaxies can be defined as a function of their spatial galactic density, which is similar to the one in the center of large clusters. The lower velocity dispersions in CGs lead to smoother interactions, which easily trigger star formation and/or nuclear activity.

Stephan's Quintet (Stephan 1877) was the first of the compact groups reported (as a nebula) in the bibliography, and still attracts a large interest due to its properties (see e.g. Natale et al. 2010, and references therein). Systematic catalogues of compact groups started from the photographical plates of surveys such as the Palomar Observatory Sky Survey (POSS-I), which covered 67% of the sky. The first atlas of compact groups is the one by Shakhbazyan (1973), which covers 377 groups. The selection criteria of Shakhbazyan set the groups to have between 5 and 15 galaxies with relative distances between galaxies ranging from 3 to 5 times their diameter. Their members were mainly red compact galaxies. Further analysis found these groups not to be as isolated as they were originally though to be, as well as showing a morphological distribution biased to early-type galaxies.

Rose (1977), looking for a homogeneous sample suitable for statistical analysis, compiled the first catalogue of compact groups based on specific and quantitative criteria. Rose defined a compact group as an aggregate of galaxies with a blue magnitude equal or brighter than 17.5, with a density contrast of at least $n/0.0035$ the average density of the field, finding 170 triplets, 26 definite (plus seven probable) quartets and 2 quintets. The revision of the Rose catalogue by Sulentic (1983) found only one third of the triplets to really satisfy the selection criteria.

A selection criterion based on the absolute magnitude, as the one adopted by Rose or Shakhbazyan implies the introduction of a bias in the sample. To avoid that, Paul Hickson, in 1982, established a relative magnitude criterion, looking for galaxies within 3 magnitudes of the brightest one, instead of setting an absolute magnitude cut. Studying the red prints of the POSS-I, Hickson catalogued 100 groups in his sample, which has been lately called Hickson Compact Groups (HCGs) catalogue. To set a group of galaxies as a HCG, Hickson applied these three criteria:

- N $\geq$4 (Population criterion). Where N is the number of galaxies within 3 magnitudes of the brightest. This population constraint excludes pairs and triplets of galaxies from the sample. In practice, another criterion set the maximum number of galaxies in a HCG to 8, with a typical number of 4 to 6 members.

- $\theta_N \geq 3\theta_G$ (Isolation criterion). $\theta_G$ is the angular diameter of the smallest circle containing the centers of all the galaxies in the group, while $\theta_N$ is the largest circle that contains no other galaxies within the range of brightness defined above. This way, Hickson avoided centers of clusters to be part of his catalogue.

- $\overline{\mu_G} < 26$ (Compactness criterion). $\overline{\mu_G}$ is the total magnitude of these galaxies averaged over the circle with diameter $\theta_G$.

The redshift of the galaxies, not available in the POSS-I data, were compiled by Hickson et al. (1992). To preserve the compactness of the groups also in the direction of our line of sight, the galaxies must have a velocity within 1000 km/s of the median velocity of the group. This study found only 92 out of the 100 groups to have at least 3 real members, with only 8 of them being chance alignments of galaxies with large velocity differences. Some studies on HCGs still take into account the triplets found in the original Hickson catalogue. Nevertheless, there is some evidence that triplets cannot be considered within the same class of objects that HCGs are. Apart from the fact they do not show significant HI deficiency (Verdes-Montenegro et al. 2001), their galaxies show a larger velocity dispersion (Sulentic 2000), making it more likely that they are unbound systems (Sulentic et al. 2001).

## 1.2 Origin and fate of HCGs

The physics of compact groups of galaxies in general and HCGs in particular have been a matter of debate, with many questions still open. Initially, even the physical existence of such those groups was questioned. Mamon (1986), for example, argued, based on numerical simulations of small groups of galaxies, that approximately half of the groups compiled by Hickson chould be chance alignments of not physically related galaxies. It has also been suggested that compact groups are mainly the result of chance alignments within loose groups or within filaments (Hernquist et al. 1995; Ostriker et al. 1995). Sulentic (1987) determined that only a smaller fraction of the groups could be explained as the chance alignments proposed by Mamon. The main problems with the chance projection hypothesis involve (1) the low surface density of galaxies near compact groups (this gives the best estimate of the potential interloper population) and (2) the compactness of the groups (small projected size on the sky). That makes the probability of such an alignment quite small.

Attempts at modeling both with and without dark matter (Barnes 1985, 1989, 1990; Mamon 1987; Bode et al. 1993) showed the groups to be unstable to coalescence on short timescales, merging into a single elliptical galaxy in a few orbital periods. Compact groups should thus be a major source of field elliptical galaxies. The short lifetimes proposed and the fact that the merger activity should begin after a small number of crossing times pose some problem when compared to the observations (Sulentic 1997): a large number of catalogued groups show evidence for interaction, but component galaxies remain distinct with recognizeable standard morphological types. A stable model of HCGs has also been published by Athanassoula et al. (1997), who showed that compact groups with an appropriate arrangement of luminous and dark matter can persist over several hundred million years, in agreement with the analysis of the dynamics of satellite galaxies by Perea et al. (2000).

Some of the hypothesis suggested to explain the existence of HCGs requires field galaxies falling from time to time onto the group, thus keeping the number of groups approximately constant (Diaferio et al. 1994, 1995; Governato et al. 1996; Ribeiro et al. 1998). However, observational estimates (Zepf et al. 1991; Zepf & Whitmore 1993; Moles et al. 1994; Mendes de Oliveira & Hickson 1994; Coziol et al. 2004) suggest relatively low merger rates. To explain these observations Coziol et al. (2004) put forward two hypotheses: either the evolution of galaxies accelerate in richer systems or HCG's form earlier in massive structures than in lower-mass systems. Solutions to the problem also come (a) from the fact that HCGs are

small subsystems in larger ordinary loose groups (Rose 1977; Sulentic 1987; Rood & Williams 1989; West 1989; Vennik et al. 1993; Rood & Struble 1994; Tovmassian & Chavushyan 2000; Tovmassian 2001) and (b) from a high enough formation rate, so there are still enough groups to be observed at their present numbers despite their short merging times (e.g. Mamon 1990). Ramella et al. (1994) concluded that we see HCGs because they are being continually formed in collapsing loose groups, as was predicted by some N-body simulations of rich groups of galaxies (e.g. Diaferio et al. 1995). On the other hand, well isolated groups with no obvious intruders also exist (e.g. HCG 96 Verdes-Montenegro et al. 1997). Thus, at this point, the origin and fate of HCGs is still controversial.

## 1.3 Gas properties and star formation in HCGs

Focused on the physics of the HCGs, the most visible result of the multiple and strong interactions between the galaxies is that the atomic gas (HI) content in HCG galaxies is usually deficient. A global HI defiency in HCGs has been reported in the literature (Williams & Rood 1987; Huchtmeier 1997). More recently, Verdes-Montenegro et al. (2001) found galaxies in HCGs to have only a 24% of the expected HI mass for their optical luminosities and morphologies. This deficiency is larger than the mean global deficiency they found for the groups (40%). They also found HI deficient groups to have a higher detection rate in X rays. Pietsch et al. (1997) interpreted the large fraction of X-ray emission from the diffuse intergalactic medium of HCG 92 as a result of gas heating by shocks. These evidence suggest that, once the HI is stripped from the galaxies, it is converted more easily into a hot gaseous phase. Based on these evidence, Verdes-Montenegro et al. (2001) proposed an evolutionary sequence model for the HCGs in which HI is continuously stripped from the galaxies. According to this model, HCGs can be classified into 3 phases as follows: in Phase 1 the HI is mainly found in the disks of galaxies. In Phase 2, 30% to 60% of the HI has been removed from disks by tidal interaction. Finally, in Phase 3, almost all the HI is found outside of the galactic disks, either forming tidal tails of stripped gas (Phase 3a) or, in a few cases, a large cloud with a single velocity gradient in which the galaxies are embedded (Phase 3b). A more recent work (Borthakur et al. 2010) has found an excess of the HI content of HCGs coming from Green Bank Telescope (GBT) single dish observations when compared to the HI detected with the Very Large Array (VLA) interferometer, due to the presence of diffuse HI in those groups. The difference between the HI detected with GBT and VLA, and thus the fraction of diffuse gas, increases with the evolutionary phase of the group.

Molecular gas is generally thought to be the main ingredient in forming stars and thus of critical importance in understanding star-forming activity in galaxies. Enhanced molecular gas content among tidally interacting systems (as measured by the $M_{H_2}/L_B$ ratio) has been suggested by past CO surveys, (e.g. Casasola et al. 2004, and references therein), but Perea et al. (1997) suggested that the larger $M_{H_2}/L_B$ ratio reported for the bright interacting galaxies in the literature is entirely caused by the nonlinear dependence of $M_{H_2}$ on $L_B$, independent of their environment, and that the $H_2$ content of these systems is at the same level as that of isolated galaxies. In HCGs galaxies, the CO(1-0) emission, which is a tracer of the bulk of the molecular gas (mainly $H_2$), has been found not to be enhanced with respect to a sample of field galaxies (Verdes-Montenegro et al. 1998) or a sample of field and interacting galaxies (Leon et al. 1998). On the other hand, in a sample of 50 galaxies corresponding to 12 HCGs, Verdes-Montenegro et al. (2001) found the molecular gas mass ($M_{H_2}$) to be lower than expected in HI deficient groups.

The level of Star Formation (SF), has also been subject to considerable debate, with original claims of a FIR excess (Hickson et al. 1989) subsequently challenged (Sulentic & de Mello Rabaca 1993). SF is likely governed by the availability of $H_2$, whose content is affected by the environment on HCGs. It is known that interactions between disk galaxies can modify their Star Formation Rate (SFR) under some circumstances of spin alignment, velocity differences, and impact parameters (Mihos et al. 1991). In particular, if the interaction is strong enough to morphologically disturb the disks, an enhancement in the SFR is expected. This theoretical result has been observationally confirmed for nearby pairs (Kennicutt et al. 1987; Laurikainen & Moles 1989; Woods et al. 2006) and for samples of peculiar galaxies (e.g. Larson & Tinsley 1978; Mazzarella et al. 1991). Thus, an enhancement of SF for galaxies in HCGs would be expected as a consequence of the continuous encounters and tidal interactions which take place within the group. Nevertheless, the SFRs obtained from the far-infrared luminosity ($L_{\rm FIR}$) (Verdes-Montenegro et al. 1998), mid-infrared luminosity (Bitsakis et al. 2010) and H$\alpha$ luminosity (Iglesias-Páramo & Vílchez 1999) in HCGs has been found to be similar to those of field galaxies. Leon et al. (1998) compared the galaxies in HCGs with a control sample including not only field galaxies but also galaxies in interacting systems, finding $L_{\rm FIR}$ to be similar, too. Moles et al. (1994), using broadband photometric data, performed a statistical study on the SFRs of a sample of galaxies in compact groups, finding a slight enhancement compared to the normal galaxies, but with less star formation activity than in paired galaxies. These results suggest that the star formation properties of compact groups of galaxies are not dominated by the effects of strong interactions.

There is evidence that this unexpected behavior is not exclusive of HCGs but it is shared by the broader family of galaxy groups and clusters. The exploitation of large-scale redshift surveys has allowed the study of large samples of galaxies in clusters (Hashimoto et al. 1998) and groups (Wilman et al. 2005), and one of the most appealing results of these works is the realization that the dense galactic environments found in groups and clusters are hostile to SF. Unfortunately, the mechanism that truncates the SF in groups remains virtually unknown. Although there is no shortage of proposed mechanisms to halt SF in dense environments, they are considered ineffective in group conditions. In addition, the merger of galaxies, favored by the conditions in HCGs, has usually also been excluded because it enhances the SF instead of stopping it. Trying to get an explanation for this results, Merluzzi et al. (2000) suggested that the high efficiencies of the ram pressure and evaporative gas stripping in the HCGs environments may inhibit SF, leading to the normal values of SFR shown. Since both the SFR and molecular gas content in HCGs have been found to be similar to those of isolated galaxies, the Star Formation Efficiency (SFE), defined as the SFR per unit of molecular gas, shows no large differences with that of field galaxies either (Verdes-Montenegro et al. 1998).

Verdes-Montenegro et al. (2007), based on former CO, FIR and HI single-dish observations together with VLA maps for 8 groups, found an $H_2$ content and a FIR luminosity lower than expected have been found for HI deficient galaxies, when compared to a sample of isolated galaxies. A possible explanation for this trend is that, as HI is needed to replenish the molecular clouds and molecular gas is necessary to fuel SF, a HI deficiency would finally lead to a decrease in the SFR. However, the sample in Verdes-Montenegro et al. (2007) is not statistically significant to cover the wide range of properties of HCGs. Previous works studying $M_{\rm H_2}$ and SFR of the galaxies in HCGs (Verdes-Montenegro et al. 1998; Leon et al. 1998) have not studied the relation between those magnitudes and the HI content and distribution of the group, or do not cover all the galaxies on the studied groups.

## 1.4 Interferometry as a radioastronomy technique

The observations at millimeter and submillimeter wavelengths are carried out with radiotelescopes, either single-dish (IRAM 30m, JCMT) or interferometers (PdB, SMA), with their specific instrumentation and techniques. Even though single-dish radiotelescopes have discovered the main part of the ISM molecular richness, as well as the properties of the cold dust, their angular resolution is not good enough to study many astrophysical problems, so the higher angular resolution provided by the interferometers is required when trying to resolve small structures.

In this work, interferometer techniques have been used in all the chapters. The HI masses for the galaxies in Chapter 2 have been measured with the Very Large Array (VLA) interferometer. Chapter 3 is based on mm observations of two HCGs performed with the Owens Valley Radio Observatory (OVRO) interferometer, and these data are complemented with VLA maps. Finally, Chapter 4 is dedicated to the development of a calibration technique for mm/submm interferometers tested in SMA, with the aim of a later application in the Atacama Large Millimeter Array (ALMA). Thus, we include here a brief introduction to the interferometry technique, taken from the proceedings of the 2nd IRAM Millimeter Interferometry School, on which we can find the details needed for a better understanding of the problem covered in Chapter 4.

An elemental interferometry consist on two antennas with a separation ranging from some meters to thousands of kilometers. The two antennas are connected via a to a single receiver. Antennas are pointed to the same point of the sky, called phase center or reference position. The response of the interferometer on this direction is determined by the so-called primary beam of the interferometer, which corresponds to the beam of each single antenna (Fig. 1.1).

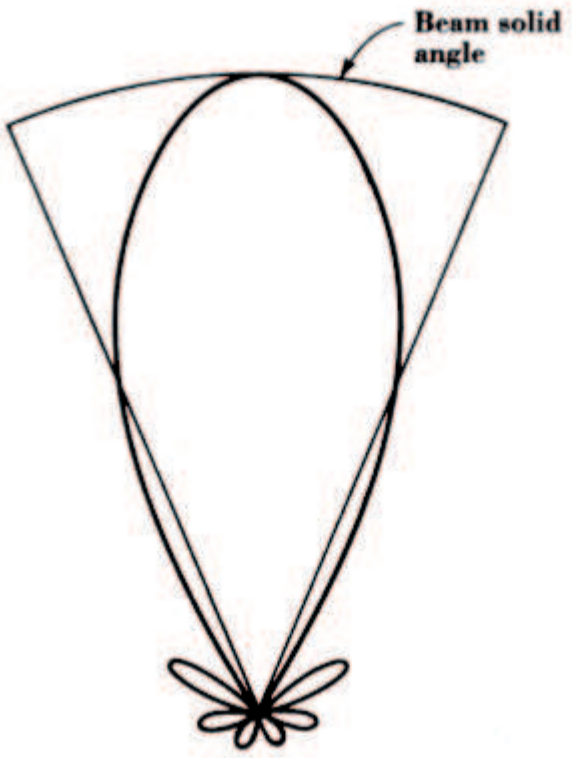


*Figure 1.1: Antenna beam pattern*

The Full Width Half Maximum (FWHM) of the main lobe is a reference of the angular distance to the phase center for which the antenna sensibility is at half its maximum value. The value of the main lobe width is

$$\theta_{HP} = 1.22\frac{\lambda}{D} \tag{1.1}$$

An interferometer can be considered as one antenna with a diameter equal to the baseline, which is the distance between two antennas. Therefore, the angular resolution of an interferometer is

$$\theta_{HP} = 1.22\frac{\lambda}{b} \tag{1.2}$$

where $b$ is the baseline between antennas.

The aperture synthesis technique (Ryle & Hewish 1960) consists on the generalization of this principle to a larger number of antennas, getting N(N-1)/2 baselines for N antennas. We show in Fig. 1.2 a schematic representation of an interferometer composed by two antennas pointing to the direction given by the unitary vector $\overrightarrow{s}$.

The wavefront will have a time delay between antennas, called geometric delay, given by

$$\tau_g = \frac{\overrightarrow{b}\cdot\overrightarrow{s}}{c} \tag{1.3}$$

where $\overrightarrow{b}$ is the baseline of the inteferometer and c is the speed of light.

The signal coming from both antennas is mixed with a local oscillator and amplified. Then, both signals are multiplied in a correlator, which gives an output signal proportional to the time average of the two input signals. The time interval the signals used to average the signals on is called integration time. Since the signals received by each antenna can be expressed as $V_1 = v_1 cos 2\pi\nu(t-\tau_g)$ y $V_2 = v_2 cos 2\pi\nu t$ (where $v_1$ and $v_2$ are the intensity of the received signal), the resultant output signal from the correlator will be

$$r(\tau_g) = v_1 v_2 cos 2\pi\nu\tau_g \tag{1.4}$$

The effective area of the antenna in the $\overrightarrow{s}$ direction is defined as A($\overrightarrow{s}$). The position of the phase center the antenna is pointed at is represented as $\overrightarrow{s_0}$. Thus, for a given direction, $\overrightarrow{s} = \overrightarrow{s_0} + \overrightarrow{\sigma}$, as displayed in Fig. 1.3.

At this point, the complex visibility, with amplitude $|V|$ and phase $\phi$, is defined as the Fourier transform of the source intensity weighted with the antenna response:

$$V = |V|e^{i\phi} = \int_S P(\overrightarrow{\sigma})I(\overrightarrow{\sigma})e^{2\pi i\nu\overrightarrow{b}\overrightarrow{\sigma}/c}d\Omega \tag{1.5}$$

where $P(\overrightarrow{\sigma}) = \mathrm{A}(\overrightarrow{\sigma})/\mathrm{A}_0$ is the beam pattern of the antenna. $\mathrm{A}_0$ is the antenna effective area in the $\overrightarrow{s_0}$ direction, as shown in Fig. 1.3. I($\overrightarrow{\sigma}$) is the source intensity.

In the coordinate system described in Fig. 1.3, the position vector of the observed source (or a point within this source) is given, in radians, by the coordinates $\overrightarrow{\sigma}$ = (x,y). If we consider a

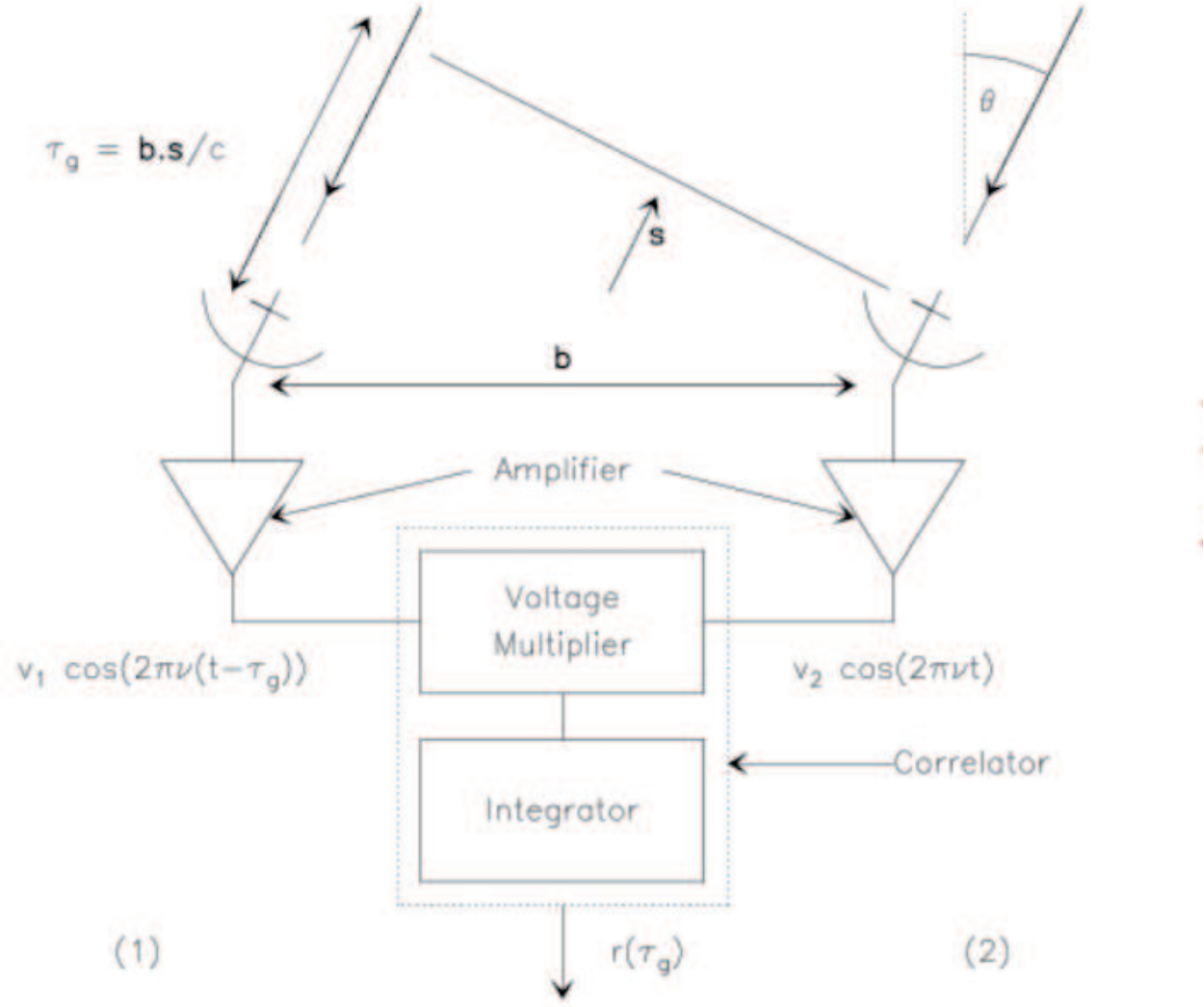


*Figure 1.2: Scheme of a two-antenna interferometer*

basic, two-antenna interferometer, the position of the source in the sky is given by the angles $\theta$ y $\phi$, defined from x=acos$\theta$, y=bcos$\theta$, where (a,b) is the separation between antennas. Thus, (x,y) is the effective baseline. The measurement given by the interferometer is the complex visibility of the brightness distribution on the Fourier plane, using the conjugates $u$ and $v$, (u,v)=(x,y)/$\lambda$. In this coordinate system, the visibility is expressed as

$$V(u,v) = \int_{-\infty}^{+\infty} \int_{-\infty}^{\infty} P(x,y) I(x,y) e^{i2\pi(ux+vy)} dx dy \tag{1.6}$$

For each observation of a pair of antennas, we get a measuremet of the visibility for one point of the (u,v) plane. As the Earth rotates and the source moves on the sky with respect to the interferometer, the (u,v) projection of the baseline changes, and we obtain visibilities at different points of the (u,v) plane in the process called (u,v) plane coverage. The (u,v) plane coverage will depend on the number of antennas, their terrestrial coordinates, geometric distribution and the integration time. If we could ideally sample all the (u.v) plane we would be

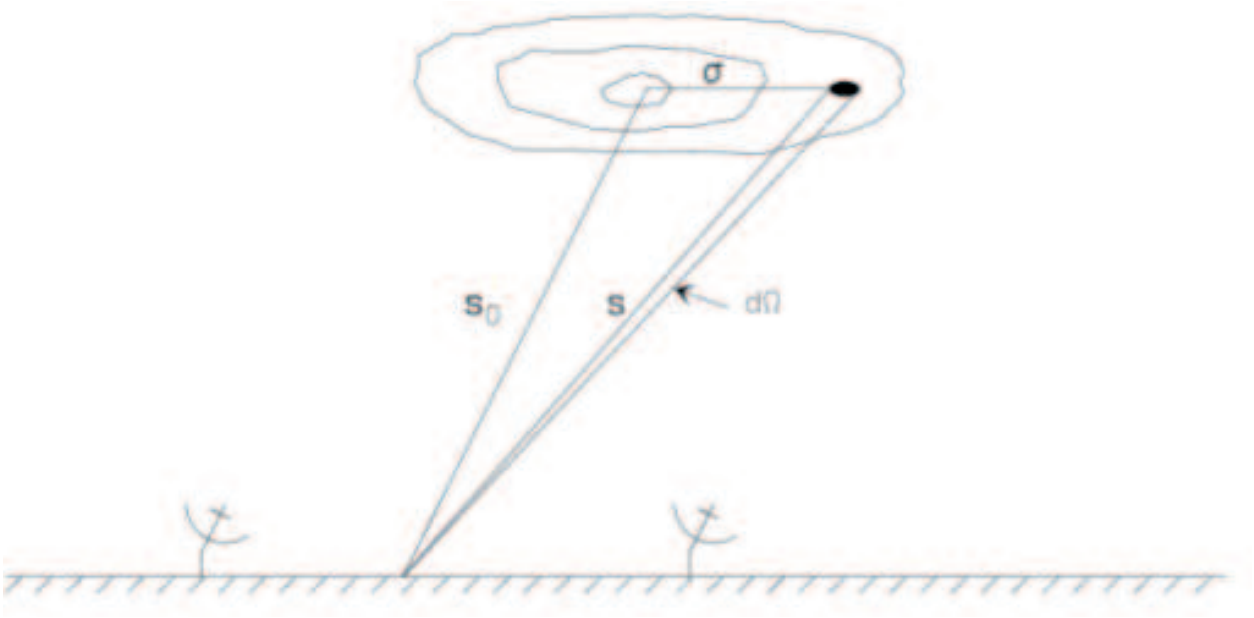


*Figure 1.3: Position vectors of the source with respect to the interferometer*

able to exactly restore the source intensity using an inverse Fourier transform, since P(x,y) is already known

$$P(x,y)I(x,y) = \int_{-\infty}^{\infty}\int_{-\infty}^{\infty} V(u,v)e^{-i2\pi(ux+vy)}du\,dv \tag{1.7}$$

In practice, the (u,v) plane is never totally covered, so the inverse Fourier transform is made using numerical recipes. The better the plane coverage is, the more exactly intensity determination is.

For each pair of antennas (i,j) in a given interval of time, Eq. 1.7 gives a value for the theoretical visibility of

$$V_{ij}(t) = \int_{-\infty}^{\infty}\int_{-\infty}^{\infty} P(x,y)I(x,y)e^{i2\pi(u_{ij}(t)x+v_{ij}(t)y)}dx\,dy \tag{1.8}$$

Nevertheless, the resulting visibilities from an interferometric observation do not match with the real visibility due to the signal variation produced. First, we must take into account the variation on the signal due to the antennas. The resulting visibilities of the observation can be defined as

$$\overline{V}_{ij}(t) = G_{ij}(t)V_{ij}(t) \tag{1.9}$$

where $\overline{V}_{ij}$ is the observed visibility, $G_{ij}$ is the complex gain associated to the (i,j) baseline and $V_{ij}(t)$ is the complex visibility of the source. Thus, to calculate the real source visibility we must first know the gain of the antennas. Data are mainly distorted before the signal is mixed, so we can approximate the complex gain of the baseline as the product of the single antennas gains.

Apart from the effects associated to the antennas, the variations on the signal before and after the reception must be also taken into account. Thus, the formula of the observed visibility is finally set as

$$\overline{V}_{ij} = G_i(t)e^{i\phi_i(t)}G_j(t)e^{-i\phi_j(t)}V_{ij}(t) + \epsilon_{ij} + \delta_{ij} \tag{1.10}$$

where, for each antenna, the amplitude and phase of the complex gain are G and $\phi$. $\epsilon_{ij}$ is the error introduced by the correlator and $\delta_{ij}$ determines the correction needed to avoid the distortions introduced on the signal by the atmosphere. The work we have developed in Chapter 4 is focused on the effect of these atmospherical influences on the observations, looking for a way to minimize its effect on the mm/submm range.

# Chapter 2

# Molecular gas content and star formation in a sample of 20 HCGs

*Tú vienes vendiendo flores*
*las tuyas son amarillas*
*las mías de todos los colores*

**Enrique Morente / Popular granaína**

There have been previous works (Verdes-Montenegro et al. 1998; Leon et al. 1998) studying the properties of $M_{H_2}$ and SFR in HCGs, indicating that the spirals globally show the same $H_2$ content as a comparison sample of isolated galaxies, although 20% appear to be deffi-cient in CO emission. Gas exhaustion through past star formation and removal of the external gas reserve by tidal stripping of the outer HI disk were suggested as possible explanations. The FIR emission in HCG galaxies was also found to be similar to isolated, Virgo Cluster, and weakly interacting galaxies. But in these works, neither the relation with the HI of the galaxies nor with the HI content of the group, nor with the evolutionary phase according to the scheme of Verdes-Montenegro et al. (2001) has been taken into account. A more recent work (Verdes-Montenegro et al. 2007) has studied the relationship between $M_{H_2}$, $M_{HI}$ and FIR emission, but the sample they analyzed was not statistically significant to cover the wide range of properties of HCGs. Thus, to shed light on the relation of $M_{H_2}$ and SFR with the HI content of the HCGs, we present here a systematic study of $M_{H_2}$, SFR and $M_{HI}$ for galaxies in a sample of 20 HCGs for which complete HI information is available. Futhermore, the HI maps enable us to determine the evolutionary stage of the groups. Our goal is to compare the $M_{H_2}$ and SFR of galaxies in HCGs with a well-defined sample of isolated galaxies from the AMIGA project (Verdes-Montenegro et al. 2005b), and their relationship with deviations in the HI content.

## 2.1 The Sample

Our sample was selected from the revision of the original (Hickson 1982) catalogue performed by Hickson et al. (1992). From the groups included in that work, we study 86 galaxies corresponding to 20 different HCGs: 7, 10, 15, 16, 23, 25, 30, 31, 37, 40, 44, 58, 67, 68, 79, 88, 92, 93, 97 and 100. The groups, which cover all the evolutionary stages and a wide range of HI deficiencies, satisfy the following criteria:

- Having at least four members, so triplets are excluded, according to the original Hickson (1982) criterion. We also exclude false groups, where a single knotty irregular galaxy can be confused with separated galaxies (Verdes-Montenegro et al. 2001).
- Containing at least one spiral galaxy, since we are mainly interested in studying the relation between the SF processes and $M_{H_2}$, which are most clearly linked in spiral galaxies.
- Being at a distance $D \leq$100 Mpc (assuming $H_0$=75 km s$^{-1}$ Mpc$^{-1}$), so the groups can be observed with a good sensitivity and avoiding possible source confusion within the telescope beam. At 100 Mpc, the 30m beam would have a spatial resolution of 10.7 kpc and the VLA (considering a 50″×50″ beam) would have a 24.2 kpc resolution.

As said above, the HCGs in our sample cover the full range of HI contents. Their deviation from normalcy is measured with respect to that of isolated galaxies, as given by Haynes & Giovanelli (1984). We note that AMIGA group is currently finishing a revision of the HI content of the full AMIGa sample, but the results are not yet available for this work. The deviation is usually referred as deficiency and is defined as the decimal logarithm of the ratio between the HI mass expected for each galaxy in the group based on their optical luminosity and morphology and the HI mass of the full group as derived from the single dish observations in Borthakur et al. (2010) (see Verdes-Montenegro et al. 2001, and also Sec. 2.3.4). As a function of their total HI deficiency, the HCGs in our sample can be classified as follows:

- HCGs with a normal HI content (at least 2/3 of its expected value): HCG 23, 25, 68 and 79.
- HCGs with a slight HI deficiency (between 2/3 and 1/3 of the expected value): HCG 10, 15, 16, 31, 37, 40, 58, 88, 92, 97 and 100.
- HCGs with a large HI deficiency (under 1/3 of the expected value): HCG 7, 30, 44, 67 and 93.

Verdes-Montenegro et al. (2001) proposed an evolutionary sequence model where the HI is continuously stripped from the galaxies. According to this model, HCGs can be classified into 3 phases as follows: in Phase 1 the HI is mainly found in the disks of galaxies. In Phase 2, 30% to 60% of the HI has been removed from disks by tidal interaction. Finally, in Phase 3, almost all the HI is found out of the galactic disks, either forming tidal tails of stripped gas (Phase 3a) or, in a few cases, in a large HI cloud with a single velocity gradient in which the galaxies are embedded (Phase 3b).

According to the evolutive stages defined in Verdes-Montenegro et al. (2001), the HCGs in our sample were classified by Borthakur et al. (2010) as:

- Phase 1: HCG 7, 23, 67, 79 and 88.
- Phase 2: HCG 10, 16, 25, 31, 40, 58 and 100.
- Phase 3: HCG 15, 30, 37, 44, 68, 92, 93 and 97.

The evolutive stage is an indicator of the ISM evolution of the group but, there is not necessarily a link with the age of the group, as in the case of HCG79, consisting on 3 early-type galaxies and one intruding spiral galaxy (Durbala et al. 2008). In this group, the main part of the HI is located in the disk of this newly entering spiral galaxy and thus, even its stellar halo dates the group as an old one, it is classified in the evolutive Phase 1.

We revised the velocity of the individual galaxies in the HCGs in our sample. Two galaxies not considered in Hickson et al. (1992) have been added: HCG100d, which had no velocity data in that work, and HCG31g, added to the catalogue of HCGs by Rubin et al. (1990).

The individual properties of the galaxies in our sample are detailed in Table 2.1. Next we describe the columns of this table:

- Column 1 Galaxy: galaxy designation, following the notation of Hickson (1982).
- Column 2 V: heliocentric radial velocity in km $s^{-1}$ (weighted average of optical measurements taken from the LEDA[1] database) converted from the optical to the radio definition for comparison with the CO spectra.
- Column 3 $\sigma_V$: velocity dispersion of the galaxies in the group.
- Column 4 D: distance to the corresponding HCG in Mpc, derived from the mean heliocentric velocity of the group as $D = V/H_0$, assuming a value of $H_0 = 75$ km $s^{-1}$ $Mpc^{-1}$. The mean velocity of the group is calculated averaging the velocity of the individual galaxies (column 2).
- Column 5 T: morphological type taken from LEDA, following the RC3 classification (de Vaucouleurs et al. 1991).
- Column 6 $D_{25}$: optical major diameter in arcmin at the 25 mag $arcsec^{-2}$ isophote taken from LEDA.
- Column 7 $B_c^T$: blue corrected apparent magnitude taken from LEDA, corrected for Galactic dust extinction, internal extinction and K-correction.
- Column 8 $L_B$: blue luminosity, derived from $B_c^T$ as:

$$\log\left(\frac{L_B}{L_\odot}\right) = 2\log D - 0.4 B_c^T + 11.95 \tag{2.1}$$

  This definition provides an estimate of the blue luminosity ($\nu L_\nu$) at 4400 Å.

- Column 9 $M_{star}$: stellar mass of the galaxies, in logarithm of solar masses, calculated from the magnitude in the $K_S$ (2.17 $\mu$m) band from the 2MASS Extended Source Catalogue (Jarrett et al. 2000). We calculated the $K_S$ luminosity, $L_K$ , from the total (extrapolated) $K_S$ flux, $f_K$ , as $L_K = \nu f_K(\nu)$ (where $\nu$ is the frequency of the K-band, $1.38\times10^{14}$ Hz) and normalized it to the solar luminosity in the K-band, $L_{K,\odot} = 5.0735 \times 10^{32}$ erg $s^{-1}$ . We then calculated the stellar mass, $M_{star}$, by adopting a mass-to-luminosity ratio of $M_\odot / L_{K,\odot} = 1.32$ (Cole et al. 2001) for the Salpeter Initial Mass Function.
- Column 10: $M_{HI}$, in logarithm of solar masses, for 66 of our galaxies observed with VLA, using different combinations of the C and D configurations with beam sizes ranging from 16″×14″ to 72″×59″ (Verdes-Montenegro et al. 2001, and Verdes-Montenegro, private communication).

[1] http://leda.univ-lyon1.fr/intro.html

*Table 2.1: Basic parameters of the galaxies in the HCG sample*

| Galaxy | V (km $s^{-1}$) | $\sigma_V$ (km $s^{-1}$) | D (Mpc) | T | $D_{25}$ (arcmin) | $B_c^T$ (mag) | $\log L_B$ ($\log L_\odot$) | $\log M_{star}$ ($\log M_\odot$) | $\log M_{HI}$ ($\log M_\odot$) |
|---|---|---|---|---|---|---|---|---|---|
| 7a | 4141 | 117 | 53.4 | 1.0 | 2.06 | 12.96 | 10.22 | 11.21 | 9.12 |
| 7b | 4175 | 117 | 53.4 | -1.9 | 1.27 | 14.29 | 9.69 | 10.90 | <7.83 |
| 7c | 4347 | 117 | 53.4 | 5.0 | 1.71 | 13.36 | 10.06 | 10.92 | 9.56 |
| 7d | 4083 | 117 | 53.4 | -1.4 | 0.94 | 14.04 | 9.79 | 10.23 | 9.00 |
| 10a | 5104 | 269 | 65.6 | 3.1 | 2.92 | 12.53 | 10.57 | 11.39 | ... |
| 10b | 4720 | 269 | 65.6 | -3.2 | 2.22 | 12.85 | 10.44 | 11.44 | ... |
| 10c | 4528 | 269 | 65.6 | 2.7 | 1.77 | 13.87 | 10.03 | 10.88 | ... |
| 10d | 4579 | 269 | 65.6 | 3.9 | 1.02 | 14.45 | 9.80 | 10.48 | ... |
| 15a | 6906 | 465 | 89.8 | -1.8 | 1.29 | 14.50 | 10.06 | 11.26 | <8.36 |
| 15b | 6971 | 465 | 89.8 | -3.0 | 0.96 | 14.76 | 9.95 | 11.03 | <8.36 |
| 15c | 7105 | 465 | 89.8 | -3.0 | 0.85 | 14.37 | 10.11 | 11.00 | ... |
| 15d | 6144 | 465 | 89.8 | -3.0 | 0.91 | 15.00 | 9.86 | 10.81 | <8.36 |
| 15e | 7022 | 465 | 89.8 | -0.5 | 0.70 | 15.57 | 9.63 | 10.72 | <8.36 |
| 15f | 6154 | 465 | 89.8 | 1.3 | 0.67 | 15.59 | 9.62 | 9.98 | 9.06 |
| 16a | 3999 | 102 | 52.2 | 1.9 | 0.87 | 12.91 | 10.22 | 11.31 | 9.07 |
| 16b | 3790 | 102 | 52.2 | 0.8 | 1.63 | 13.27 | 10.08 | 11.10 | 8.90 |
| 16c | 3801 | 102 | 52.2 | 3.8 | 1.34 | 13.17 | 10.12 | 10.99 | 9.48 |
| 16d | 3813 | 102 | 52.2 | -1.1 | 1.49 | 13.80 | 9.86 | 10.96 | 9.65 |
| 23a | 4789 | 376 | 59.0 | -0.7 | 1.58 | 14.47 | 9.70 | 11.07 | 8.92 |
| 23b | 4730 | 376 | 59.0 | 3.2 | 1.67 | 14.27 | 9.78 | 10.99 | 9.70 |
| 23c | 5278 | 376 | 59.0 | -0.9 | 0.90 | 15.32 | 9.36 | 10.78 | 8.36 |
| 23d | 4397 | 376 | 59.0 | 6.1 | 0.68 | 15.65 | 9.23 | 10.34 | 9.15 |
| 25a | 6148 | 69 | 82.1 | 4.2 | 1.36 | 13.57 | 10.35 | 10.71 | ... |
| 25b | 6267 | 69 | 82.1 | 0.9 | 0.94 | 14.43 | 10.01 | 11.13 | ... |
| 25d | 6188 | 69 | 82.1 | -1.5 | 0.40 | 15.80 | 9.46 | 10.34 | ... |
| 25f | 6115 | 69 | 82.1 | -1.9 | 0.43 | 16.21 | 9.29 | 10.37 | ... |
| 30a | 4626 | 122 | 57.3 | -0.8 | 1.46 | 13.34 | 10.13 | 11.11 | <8.08 |
| 30b | 4381 | 122 | 57.3 | -1.2 | 1.21 | 13.91 | 9.90 | 11.00 | <8.08 |
| 30c | 4441 | 122 | 57.3 | 3.6 | 0.61 | 15.24 | 9.37 | 9.89 | <8.08 |
| 30d | 4595 | 122 | 57.3 | -1.5 | 0.56 | 15.93 | 9.09 | 9.95 | <8.08 |
| 31a | 3888 | 65 | 54.1 | 8.9 | 1.21 | 14.76 | 9.51 | 10.19 | 9.46 |
| 31b | 4073 | 65 | 54.1 | 6.8 | 0.93 | 14.44 | 9.64 | 9.54 | 9.28 |
| 31c | 3975 | 65 | 54.1 | 10.0 | 0.65 | 12.29 | 10.50 | 10.19 | 9.20 |
| 31ac[(1)] | | 65 | | | | | 10.54 | 10.49 | 9.65 |
| 31g | 3958 | 65 | 54.1 | 9.7 | 2.51 | 15.11 | 9.37 | 10.04 | ... |
| 37a | 6652 | 452 | 88.3 | -4.8 | 1.98 | 13.32 | 10.52 | 11.62 | <8.43 |
| 37b | 6565 | 452 | 88.3 | 3.3 | 1.45 | 13.89 | 10.29 | 11.12 | <8.43 |
| 37c | 7177 | 452 | 88.3 | -0.9 | 0.44 | 15.56 | 9.62 | ... | <8.43 |
| 37d | 6008 | 452 | 88.3 | 8.0 | 0.38 | 15.89 | 9.49 | 9.90 | <8.43 |
| 37e | 6327 | 452 | 88.3 | -3.3 | 0.36 | 16.07 | 9.41 | 10.23 | <8.43 |
| 40a | 6481 | 177 | 83.4 | -4.8 | 1.33 | 13.38 | 10.44 | 11.51 | <8.22 |
| 40b | 6676 | 177 | 83.4 | -3.0 | 0.90 | 14.62 | 9.94 | 11.09 | <8.22 |
| 40c | 6264 | 177 | 83.4 | 2.4 | 1.55 | 14.60 | 9.95 | 11.25 | 8.96 |
| 40d | 6429 | 177 | 83.4 | 0.0 | 1.02 | 14.53 | 9.98 | 11.03 | 8.52 |

*Table 2.1: Basic parameters of the galaxies in the HCG sample (continued)*

| Galaxy | V (km $s^{-1}$) | $\sigma_V$ (km $s^{-1}$) | D (Mpc) | T | $D_{25}$ (arcmin) | $B_c^T$ (mag) | $\log L_B$ ($\log L_\odot$) | $\log M_{star}$ ($\log M_\odot$) | $\log M_{HI}$ ($\log M_\odot$) |
|---|---|---|---|---|---|---|---|---|---|
| 40e | 6305 | 177 | 83.4 | 1.3 | 0.67 | 16.58 | 9.16 | 10.43 | <8.22 |
| 44a | 1286 | 155 | 18.8 | 0.9 | 3.64 | 11.39 | 9.94 | 11.02 | 8.61 |
| 44b | 1388 | 155 | 18.8 | -4.8 | 2.36 | 11.86 | 9.75 | 10.81 | <7.46 |
| 44c | 1227 | 155 | 18.8 | 2.9 | 2.15 | 12.46 | 9.51 | 10.35 | 8.41 |
| 44d | 1578 | 155 | 18.8 | 5.0 | 2.24 | 12.84 | 9.36 | 9.66 | 8.92 |
| 58a | 6008 | 173 | 82.7 | 0.8 | 1.36 | 13.57 | 10.36 | 11.46 | 9.54 |
| 58b | 6370 | 173 | 82.7 | 1.1 | 1.35 | 13.42 | 10.42 | 11.34 | 8.67 |
| 58c | 5978 | 173 | 82.7 | -0.1 | 1.10 | 13.92 | 10.22 | 11.22 | 8.81 |
| 58d | 6111 | 173 | 82.7 | -4.6 | 0.90 | 14.47 | 10.00 | 11.07 | <8.18 |
| 58e | 5980 | 173 | 82.7 | 3.6 | 0.69 | 14.97 | 9.80 | 10.65 | 8.99 |
| 67a | 7047 | 226 | 94.7 | -2.3 | 1.94 | 12.84 | 10.77 | 11.82 | ... |
| 67b | 7364 | 226 | 94.7 | 3.2 | 1.07 | 14.04 | 10.29 | 11.31 | ... |
| 67c | 7344 | 226 | 94.7 | 5.5 | 1.02 | 14.93 | 9.93 | 10.55 | ... |
| 68a | 2149 | 150 | 26.9 | -2.1 | 2.37 | 11.91 | 10.05 | 11.26 | ... |
| 68b | 2554 | 150 | 26.9 | -2.1 | 3.03 | 12.25 | 9.91 | ... | ... |
| 68c | 2301 | 150 | 26.9 | 3.6 | 2.69 | 11.89 | 10.05 | 10.87 | ... |
| 68d | 2328 | 150 | 26.9 | -2.1 | 1.15 | 13.96 | 9.23 | 10.13 | ... |
| 68e | 2396 | 150 | 26.9 | -0.2 | 1.12 | 14.39 | 9.05 | 9.96 | ... |
| 79a | 4115 | 167 | 57.3 | -1.5 | 1.79 | 14.49 | 9.67 | 10.76 | <7.72 |
| 79b | 4369 | 167 | 57.3 | -1.9 | 2.28 | 14.09 | 9.83 | 10.74 | <7.72 |
| 79c | 4352 | 167 | 57.3 | -1.5 | 1.64 | 14.98 | 9.48 | ... | <7.72 |
| 79d | 4501 | 167 | 57.3 | 5.2 | 1.10 | 15.16 | 9.40 | ... | 9.14 |
| 88a | 5856 | 82 | 80.0 | 2.7 | 1.51 | 13.13 | 10.50 | 11.36 | 9.12 |
| 88b | 6015 | 82 | 80.0 | 1.2 | 1.25 | 13.58 | 10.33 | 11.25 | 9.51 |
| 88c | 5876 | 82 | 80.0 | 4.1 | 1.02 | 14.35 | 10.02 | 10.50 | 10.01 |
| 88d | 5986 | 82 | 80.0 | 4.9 | 1.05 | 14.45 | 9.98 | 10.42 | 9.58 |
| 92b | 5659 | 455 | 85.6 | 4.1 | 2.37 | 13.18 | 10.54 | 11.61 | <8.03 |
| 92c | 6615 | 455 | 85.6 | 3.9 | 1.67 | 13.31 | 10.49 | 11.30 | <8.03 |
| 92d | 6487 | 455 | 85.6 | -0.9 | 1.47 | 13.88 | 10.26 | 11.61 | <8.03 |
| 92e | 6466 | 455 | 85.6 | -4.5 | 0.80 | 14.19 | 10.14 | 11.08 | <8.03 |
| 93a | 4993 | 213 | 62.1 | -3.1 | 1.45 | 12.49 | 10.54 | 11.48 | <8.04 |
| 93b | 4624 | 213 | 62.1 | 5.9 | 1.85 | 12.73 | 10.44 | 10.93 | 9.69 |
| 93c | 5003 | 213 | 62.1 | 0.9 | 1.06 | 13.74 | 10.04 | 11.05 | <8.04 |
| 93d | 5085 | 213 | 62.1 | -4.5 | 0.69 | 14.97 | 9.55 | 10.63 | <8.04 |
| 97a | 6766 | 370 | 83.0 | -3.1 | 1.58 | 13.78 | 10.28 | 11.35 | <8.29 |
| 97b | 6521 | 370 | 83.0 | 5.4 | 1.23 | 14.42 | 10.02 | 10.73 | <8.29 |
| 97c | 5883 | 370 | 83.0 | 0.5 | 0.97 | 14.58 | 9.96 | 10.95 | <8.29 |
| 97d | 6112 | 370 | 83.0 | -3.0 | 1.70 | 14.40 | 10.03 | 11.13 | <8.29 |
| 97e | 6515 | 370 | 83.0 | -1.6 | 0.45 | 16.41 | 9.22 | 10.24 | <8.29 |
| 100a | 5272 | 142 | 70.9 | 1.7 | 0.86 | 13.42 | 10.28 | 11.22 | 8.37 |
| 100b | 5165 | 142 | 70.9 | 9.0 | 0.63 | 14.64 | 9.79 | 10.26 | 9.34 |
| 100c | 5363 | 142 | 70.9 | 4.9 | 0.75 | 14.84 | 9.72 | 10.18 | 8.90 |
| 100d | 5488 | 142 | 70.9 | 5.5 | 0.51 | 15.66 | 9.39 | 9.50 | 9.27 |

(1)The values of $L_B$, $M_{star}$ and $M_{HI}$ for 31ac are the sum of their respective values (see Sec. 2.2.2).

## 2.2 The data

### 2.2.1 CO data

Here we present the CO data coming from our own observations or from the literature, for a sample of the 86 galaxies that belong to the selected 20 HCGs. The aim was to achieve data for all the galaxies in the selected HCGs. CO data are missing for only 2 galaxies in these 20 groups: HCG67d and 92f. The CO(1-0) line was detected for 45 galaxies out of these 86 galaxies.

#### 2.2.1.1 IRAM CO(1-0) and CO(2-1) observations and data reduction

We observed 47 galaxies belonging to 14 different HCGs. The observations of CO rotational transition lines J(1→0) and J(2→1) (at 115.271 and 230.538 GHz, respectively) were carried out with the IRAM 30m radiotelescope at Pico Veleta[2] during June, October and December 2006. We performed single-pointing observations using the wobbler switch mode, with a switch frequency of 0.5 Hz and a throw of 200″. As we observed the center of the galaxies, the CO intensities were corrected assuming an exponential distribution (see Sec. 2.2.1.3). We checked for all the objects that the off-position did not coincide with a neighbor galaxy.

The dual polarization receivers A100 and B100 were used to observe in parallel the CO(1-0) and CO(2-1) lines. The median system temperature was 231 K for the CO(1-0) observations, with ∼80% of the galaxies observed with system temperatures between 150 and 350 K. In the case of CO(2-1), the median system temperature was 400 K, with a temperature range between 230 and 800 K for 85% of the galaxies. For CO(1-0) the 1 MHz filterbank was used, and for CO(2-1) the 4 MHz filterbank. The corresponding velocity resolutions were 2.6 km $s^{-1}$ and 5.3 km $s^{-1}$ for CO(1-0) and CO(2-1), respectively. The total bandwidth was 1 GHz. The Half Power Beam Width (HPBW) is 22″ and 11″ for 115 and 230 GHz, respectively. All CO spectra and intensities are presented on the main beam temperature scale ($T_{mb}$) which is defined as $T_{mb} = (F_{eff}/B_{eff}) \times T_A^*$. The IRAM forward efficiency, $F_{eff}$, was 0.95 and the beam efficiency, $B_{eff}$, 0.75.

The data reduction and analysis was performed using CLASS, while further analysis was performed using GREG, both part of the GILDAS[3] package developed by IRAM. First we inspected and discarded bad spectral scans. The baseline of each spectrum was subtracted and the scans were individually revised to discard those with a bad quality baseline. Any spike on the scans was removed. The scans were then averaged to achieve a single spectrum for each galaxy and transition. These spectra were smoothed to a velocity resolution of 21 to 27 km $s^{-1}$, depending on the rms.

A total of 23 galaxies were detected in CO(1-0), 22 in CO(2-1) and 18 in both transitions. The CO(1-0) spectra of the 47 galaxies, together with the spectra of the 22 detected galaxies are shown in Appendix A.

For each spectrum, we integrated the intensity along the velocity interval where emission was detected. In the case of no-detections we set an upper limit as:

$$I_{CO} < 3 \times rms \times \delta V \sqrt{\frac{\Delta V}{\delta V}} \tag{2.2}$$

[2]IRAM is supported by CNRS/INSU (France), the MPG (Germany) and the IGN (Spain).

[3]http://www.iram.fr/IRAMFR/GILDAS

where $\delta$V is the width of each channel and $\Delta$V is the total line width. We used a value of $\Delta$V = 300 km $s^{-1}$ when there was no detection in CO(1-0) nor in CO(2-1). In those cases were the source was detected in only one transition, this line width was used to calculate the upper limit in the other transition.

The results of our CO(1-0) and CO(2-1) observations are displayed in Table 2.2 as follows:

- Column 1 Galaxy: galaxy designation.
- Column 2 $I_{CO(1-0)}$: integrated intensity of the CO(1-0) emission in K km $s^{-1}$.
- Column 3 rms : rms of the CO(1-0) spectrum (when available) in mK.
- Column 4 Ref.: reference of the CO(1-0) data, detailing whether data come from our observations or from the literature (see 2.2.1.2).
- Column 5 Beam: HPBW of the telescope in arcsec.
- Column 6 $\Delta V_{CO(1-0)}$: line width of the CO(1-0) emission (if detected) in km $s^{-1}$.
- Column 7 $I_{CO(2-1)}$: integrated intensity of the CO(2-1) emission (when observed) in K km $s^{-1}$.
- Column 8 rms: rms of the CO(2-1) spectrum (when observed) in mK.
- Column 9 $\Delta V_{CO(2-1)}$: line width of the CO(2-1) emission (if detected) in km $s^{-1}$.
- Column 10 log($M_{H_2\ observed}$)*:* logarithm of the $H_2$ mass (in solar masses) calculated from the observed $I_{CO}$ (Sec.2.2.1.3).
- Column 11 log($M_{H_2}$)*:* logarithm of the $H_2$ mass (solar masses) extrapolated to the emission from the full disk (see Sec.2.2.1.3).

*Table 2.2: Observed and derived molecular gas properties*

| Galaxy | $I_{CO(1-0)}$ (K km $s^{-1}$) | rms (mK) | Ref. | Beam (arcsec) | $\Delta$V (km $s^{-1}$) | $I_{CO(2-1)}$ K km $s^{-1}$ | rms (mK) | $\Delta$V (km $s^{-1}$) | log$M_{H_2 obs}$ (log$M_\odot$) | log$M_{H_2 extrapol}$ (log$M_\odot$) |
|---|---|---|---|---|---|---|---|---|---|---|
| 7a | 7.20 | | 3 | 43 | 500 | | | | 9.51 | 9.71 |
| 7b | $<0.70$ | | 3 | 55 | ... | | | | <8.71 | <8.80 |
| 7c | 1.40 | | 3 | 55 | 183 | | | | 9.01 | 9.17 |
| 7d | $<0.60$ | | 3 | 43 | ... | | | | <8.43 | <8.52 |
| 10a | 2.72±0.49 | | 2 | 22 | 339 | | | | 8.79 | 9.51 |
| 10b | $<0.90$ | | 3 | 55 | ... | | | | <9.00 | <9.27 |
| 10c | 7.14±0.36 | | 2 | 22 | 359 | | | | 9.21 | 9.54 |
| 10d | $<1.60$ | | 3 | 55 | ... | | | | <9.25 | <9.30 |
| 15a | $<0.42$ | 3.68 | 1 | 22 | ... | $<1.45$ | 6.97 | ... | <8.62 | <8.90 |
| 15b | $<0.75$ | 4.41 | 1 | 22 | ... | $<2.45$ | 11.5 | ... | <8.87 | <9.12 |
| 15c | $<0.52$ | 6.12 | 1 | 22 | ... | $<0.64$ | 3.78 | ... | <8.71 | <8.92 |
| 15d | 0.62±0.16 | 3.94 | 1 | 22 | 160 | <0.35 | 6.99 | ... | 8.31 | 8.56 |
| 15e | $<0.95$ | 5.59 | 1 | 22 | ... | $<2.03$ | 9.79 | ... | <8.97 | <9.14 |
| 15f | $<0.54$ | 4.35 | 1 | 22 | ... | 1.29±0.42 | 7.88 | 180 | <8.73 | <8.84 |
| 16a | 42.86±1.29 | | 2 | 22 | ... | | | | 9.79 | 10.00 |
| 16b | 2.30 | | 3 | 43 | 560 | | | | 8.99 | 9.12 |
| 16c | 9.20 | | 3 | 43 | 270 | | | | 9.59 | 9.73 |
| 16d | 32.96±1.10 | | 2 | 22 | ... | | | | 9.68 | 9.96 |
| 23a | 0.90±0.20* | 3.26 | 1 | 22 | 360 | <1.20 | 5.05 | ... | 8.11 | 8.39 |

*Table 2.2: Observed and derived molecular gas properties (continued)*

| Galaxy | $I_{CO(1-0)}$ (K km $s^{-1}$) | rms (mK) | Ref.(1) | Beam (arcsec) | $\Delta$V (km $s^{-1}$) | $I_{CO(2-1)}$ K km $s^{-1}$ | rms (mK) | $\Delta$V (km $s^{-1}$) | log$M_{H_2\,obs}$ (log$M_\odot$) | log$M_{H_2}$ (log$M_\odot$) |
|---|---|---|---|---|---|---|---|---|---|---|
| 23b | 9.70±0.60 | | 2 | 22 | 318 | | | | 9.26 | 9.68 |
| 23c | < 1.95 | 3.82 | 1 | 22 | ... | < 0.63 | 7.44 | ... | <8.92 | <9.08 |
| 23d | 2.15±0.20 | | 2 | 22 | 83 | | | | 8.60 | 8.76 |
| 25a | 2.56±0.20 | | 2 | 22 | 193 | | | | 8.96 | 9.24 |
| 25b | 2.61±0.25 | 3.37 | 1 | 22 | 510 | 0.84±0.16 | 2.63 | 225 | 8.86 | 9.06 |
| 25d | < 0.40 | 2.38 | 1 | 22 | ... | < 0.59 | 2.85 | ... | <8.52 | <8.58 |
| 25f | < 0.89 | 5.26 | 1 | 22 | ... | < 1.35 | 6.52 | ... | <8.87 | <8.93 |
| 30a | < 0.70 | | 3 | 55 | ... | | | | <8.77 | <8.89 |
| 30b | < 0.70 | | 3 | 55 | ... | | | | <8.77 | <8.85 |
| 30c | < 0.80 | | 3 | 55 | ... | | | | <8.82 | <8.83 |
| 30d | < 0.80 | | 3 | 55 | ... | | | | <8.82 | <8.83 |
| 31a | < 0.40 | | 3 | 55 | ... | | | | <8.47 | <8.55 |
| 31b | < 0.70 | | 3 | 55 | ... | | | | <8.72 | <8.78 |
| 31c | 1.53±0.30 | | 2 | 22 | 148 | | | | 8.38 | 8.48 |
| 31ac(2) | | | | | | | | | <8.73 | <8.82 |
| 31g | < 0.40 | | 3 | 55 | ... | | | | <8.47 | <8.73 |
| 37a | 0.38±0.13* | 2.85 | 1 | 22 | 185 | < 0.79 | 3.81 | ... | 8.08 | 8.41 |
| 37b | 8.65±0.40 | | 2 | 22 | 552 | | | | 9.56 | 9.80 |
| 37c | 0.56±0.10 | 1.94 | 1 | 22 | 240 | <0.60 | 8.08 | ... | 8.25 | 8.31 |
| 37d | 0.50±0.13 | 2.80 | 1 | 22 | 200 | 1.19±0.16 | 3.09 | 170 | 8.20 | 8.27 |
| 37e | < 0.71 | 4.20 | 1 | 22 | ... | < 1.21 | 5.85 | ... | <8.83 | <8.83 |
| 40a | < 1.32 | | 2 | 22 | ... | | | | <8.69 | <8.97 |
| 40b | 1.04±0.13 | 3.80 | 1 | 22 | 110 | 0.96±0.22 | 4.79 | 130 | 8.47 | 8.70 |
| 40c | 9.70±0.65 | | 2 | 22 | 233 | | | | 9.56 | 9.84 |
| 40d | 5.09±0.43 | | 2 | 22 | 295 | | | | 9.28 | 9.44 |
| 40e | 1.62±0.40 | | 2 | 22 | 480 | | | | 8.78 | 8.88 |
| 44a | 10.50±0.60 | | 2 | 22 | 269 | | | | 8.30 | 8.87 |
| 44b | < 0.70 | 4.15 | 1 | 22 | ... | < 0.63 | 3.06 | ... | <7.48 | <8.14 |
| 44c | 7.63±0.50 | | 2 | 22 | 165 | | | | 8.16 | 8.70 |
| 44d | 2.33±0.16 | 4.00 | 1 | 22 | 155 | 2.12±0.12 | 2.65 | 125 | 7.53 | 8.00 |
| 58a | 29.36±0.19 | 2.55 | 1 | 22 | 550 | 39.65±0.26 | 2.75 | 545 | 9.92 | 10.23 |
| 58b | 3.97±0.44 | 5.34 | 1 | 22 | 625 | 7.92±0.61 | 6.21 | 605 | 9.05 | 9.40 |
| 58c | < 0.49 | 2.88 | 1 | 22 | ... | < 1.03 | 4.97 | ... | <8.62 | <8.93 |
| 58d | < 0.48 | 2.83 | 1 | 22 | ... | < 0.88 | 4.25 | ... | <8.61 | <8.79 |
| 58e | 2.98±0.12 | 2.61 | 1 | 22 | 195 | 2.93±0.14 | 2.71 | 180 | 8.92 | 9.08 |
| 67a | < 0.90 | | 3 | 55 | ... | | | | <9.31 | <9.48 |
| 67b | 2.30 | | 3 | 55 | 234 | | | | 9.72 | 9.77 |
| 67c | < 0.80 | | 3 | 55 | ... | | | | <9.26 | <9.32 |
| 68a | < 0.47 | 4.34 | 1 | 22 | ... | 0.95±0.25 | 6.07 | 105 | <7.62 | <8.03 |
| 68b | < 0.70 | | 3 | 55 | ... | | | | <8.10 | <8.35 |
| 68c | 7.02±0.42 | | 2 | 22 | 214 | | | | 8.43 | 9.11 |
| 68d | < 0.30 | | 3 | 55 | ... | | | | <7.75 | <7.83 |
| 68d[3] | < 0.81 | | 1 | 22 | ... | 1.31±0.17 | 2.38 | 328 | | |
| 68e | < 1.11 | 6.59 | 1 | 22 | ... | 1.34±0.33* | 5.52 | 230 | <7.99 | <8.18 |
| 79a | < 1.70 | | 2 | 22 | ... | | | | <8.47 | <9.06 |
| 79b | 0.91±0.13 | 2.24 | 1 | 22 | 320 | 1.42±0.23* | 2.68 | 460 | 8.09 | 8.56 |
| 79c | 0.42±0.12 | 3.68 | 1 | 22 | 105 | < 0.36 | 8.79 | ... | 7.75 | 8.13 |
| 79d | < 0.66 | 3.93 | 1 | 22 | ... | < 1.28 | 6.21 | ... | <8.43 | <8.62 |
| 88a | 6.39±0.23 | 3.06 | 1 | 22 | 550 | 5.41±0.31 | 3.25 | 575 | 9.22 | 9.55 |
| 88b | 3.17±0.13 | 2.16 | 1 | 22 | 355 | 3.11±0.22 | 2.45 | 505 | 8.92 | 9.30 |
| 88c | 2.00 | | 3 | 55 | 251 | | | | 9.52 | 9.60 |
| 88c[3] | 3.83±0.29 | 7.62 | 1 | 22 | 135 | 4.78±0.58 | 11.8 | 150 | | |
| 88d | 1.06±0.17 | 2.96 | 1 | 22 | 330 | 0.79±0.25* | 4.49 | 190 | 8.44 | 8.64 |
| 92b | < 0.50 | | 3 | 55 | ... | | | | <8.97 | <9.17 |

*Table 2.2: Observed and derived molecular gas properties (continued)*

| Galaxy | $I_{CO(1-0)}$ (K km $s^{-1}$) | rms (mK) | Ref.[1] | Beam (arcsec) | $\Delta$V (km $s^{-1}$) | $I_{CO(2-1)}$ K km $s^{-1}$ | rms (mK) | $\Delta$V (km $s^{-1}$) | log$M_{H_2 obs}$ (log$M_\odot$) | log$M_{H_2}$ (log$M_\odot$) |
|---|---|---|---|---|---|---|---|---|---|---|
| 92c | 0.60 | | 3 | 55 | 195 | | | | 9.05 | 9.19 |
| 92d | $<0.50$ | | 3 | 55 | ... | | | | <8.97 | <9.10 |
| 92e | $<0.49$ | 2.91 | 1 | 22 | ... | $<1.06$ | 5.09 | ... | <8.64 | <8.87 |
| 93a | 1.64±0.10 | 1.99 | 1 | 22 | 255 | 3.02±0.17 | 2.46 | 295 | 8.41 | 8.83 |
| 93b | 11.26±0.35 | 5.98 | 1 | 22 | 325 | 13.11±0.48 | 7.27 | 270 | 9.25 | 9.65 |
| 93c | 3.83±0.25 | 3.34 | 1 | 22 | 520 | 3.76±0.23 | 2.67 | 465 | 8.78 | 9.01 |
| 93d | $<0.75$ | 4.45 | 1 | 22 | ... | $<1.27$ | 6.14 | ... | <8.55 | <8.68 |
| 97a | $<1.35$ | 7.94 | 1 | 22 | ... | $<2.82$ | 13.60 | ... | <9.06 | <9.34 |
| 97b | 3.55±0.43 | 6.33 | 1 | 22 | 430 | $<1.04$ | 14.20 | ... | 9.00 | 9.25 |
| 97c | $<0.23$ | 2.90 | 1 | 22 | ... | $<0.36$ | 3.71 | ... | <8.29 | <8.49 |
| 97d | $<0.91$ | 5.39 | 1 | 22 | ... | $<4.06$ | 19.50 | ... | <8.89 | <9.17 |
| 97e | $<0.55$ | 3.27 | 1 | 22 | ... | $<1.34$ | 6.48 | ... | <8.67 | <8.76 |
| 100a | 4.34±0.28 | 4.14 | 1 | 22 | 435 | 3.35±0.29 | 4.44 | 275 | 8.95 | 9.11 |
| 100b | 0.83±0.13 | 2.90 | 1 | 22 | 185 | 1.60±0.23 | 4.28 | 180 | 8.23 | 8.37 |
| 100c | 1.02±0.18 | 3.16 | 1 | 22 | 310 | 1.41±0.28 | 8.75 | 190 | 8.32 | 8.46 |
| 100d | $<0.72$ | 4.27 | 1 | 22 | ... | $<0.79$ | 3.78 | ... | <8.65 | <8.72 |

[1]CO reference: 1: Our observations. 2: Leon'98. 3: Verdes-Montenegro et al. (1998).
[2]The value of the observed and extrapolated $M_{H_2}$ for 31ac are the sum of their respective values (see Sec. 2.2.2).
[3] Galaxies observed by us for which we have selected the data from Verdes-Montenegro et al. (1998).
Galaxies flagged with * present tentative detection.

#### 2.2.1.2 CO(1-0) data from the literature

We have searched for the available CO(1-0) data for the 20 HCGs of our sample, compiling from the literature the data corresponding to the integrated CO(1-0) intensities and line widths of the following galaxies:

- Verdes-Montenegro et al. (1998): 24 galaxies corresponding to 9 different HCGs. 20 of these galaxies were observed with the NRAO 12 m telescope at Kitt Peak with a beam size of 55″. The data from the other 4 galaxies are from Boselli et al. (1996), observed with the SEST 15m telescope, with a 43″ beam.

- Leon et al. (1998): 17 galaxies corresponding to 10 different HCGs. Observed with the IRAM 30m telescope with a similar setting as in our observations (see Sec. 2.2.1.1).

In total, we have CO data for 86 galaxies. There are 16 galaxies in common between the sample we observed and the literature samples. Another 14 out of the 86 galaxies were observed by both Verdes-Montenegro et al. (1998) and Leon et al. (1998). In order to choose between the different existing spectra (either from our observations or from the literature), we applied the following criteria: if available, we chose the spectrum with detected emission. If more than one detected spectrum existed, we chose the one with the lower rms or -in case of comparable rms- the spectrum observed with a larger beam, in order to probe a larger fraction of the disk.

There are 2 galaxies in common between our observations and the sample of Verdes-Montenegro et al. (1998) for which we have chosen the data from the bibliography: HCG68d and 88c. For the other 14 galaxies that we observed, with data available in the literature, we have selected the data coming from our observations.

#### 2.2.1.3 Molecular gas mass

We calculate the molecular gas mass, $M_{\rm H_2}$ using the following equation:

$$M_{H_2} = 75 \times D^2 I_{CO(1-0)} \Omega \tag{2.3}$$

where $\Omega$ is the area covered by the observations in arcsec$^2$ (i.e. $\Omega = 1.13\ \theta^2$ for a single pointing with a gaussian beam where $\theta$ is the HPBW). The former equation assumes a ratio X=$N_{H_2}$/ $I_{CO}$ $= 2 \times 10^{20}$cm$^{-2}$ (K km s$^{-1}$)$^{-1}$ (e.g. Dickman et al. 1986). The $M_{\rm H_2}$ calculated for the 86 galaxies are listed in Table 2.2.

In both the observations we carried out and the data obtained from the literature, a single position at the center of the galaxy was observed. Because of this and the different beams used by us and in the literature we need to correct for possible emission outside the beam. To correct the observed CO intensities we need to know the distribution and extension of the CO emission. Different authors (Nishiyama et al. 2001; Regan et al. 2001; Leroy et al. 2008) have found that the integrated CO intensity in spiral galaxies follows an exponential distribution as a function of radius with a scale lenght $r_e$:

$$I_{CO}(r) = I_0 \propto e^{(r/r_e)} \tag{2.4}$$

We adopt a scale length of $r_e = 0.2 \times r_{25}$, where $r_{25}$ is the isophotal radius at an optical sufrace brightness of 25 mag arcsec$^{-1}$ isophotal radius, following Lisenfeld et al. (in prep.), who derived this scale length from studies of the above mentioned authors and from their own CO data. We have used this distribution to calculate the expected CO emission from the entire disk, taking into account the galaxy inclination. The expected emission has been compared with the observed emission in the central pointing to calculate a correction factor.

The correction factor to the CO(1-0) intensities is shown in Figure 2.1. The ratio between the corrected and uncorrected intensities is below 2 in most of the galaxies (66 out of 86, or 77 %), with an average value of 1.78. To check the consistency of the correction, we have also performed the analysis presented in this paper for a sample restricted to the galaxies with corrections lower than 1.6 (45 galaxies), finding no significant differences with respect to the full sample, so we can conclude that the aperture correction does not introduce a bias in the results.

The values for the extraoplated molecular gas mass are shown in Table 2.2. Here, and in the following, we always use the extrapolated molecular gas mass and denote it $M_{\rm H_2}$ for simplicity. The $M_{\rm H_2}$ distribution is shown in Fig. 2.2. The average value for the full sample and the spiral galaxies is shown in Table 2.3. The distribution and average values of $M_{\rm H_2}$, as well as the statistical distributions and average values throughout this work, have been calculated using the Kaplan-Meier estimator implemented in ASURV[4], to take into account the upper limits in the data.

### 2.2.2 Far-Infrared Data

Far-infrared (FIR) fluxes were obtained from ADDSCAN/SCANPI, a utility provided by the Infrared Processing and Analysis Center (IPAC)[5]. This is a one-dimensional tool that coadds calibrated IRAS survey data. It makes use of all scans that passed over a specific position and

[4]Astronomical Survival Analysis (ASURV) Rev. 1.1 (Lavalley et al. 1992) is a generalised statistical package that implements the methods presented by Feigelson & Nelson (1985)

[5]http://scanpi.ipac.caltech.edu:9000/

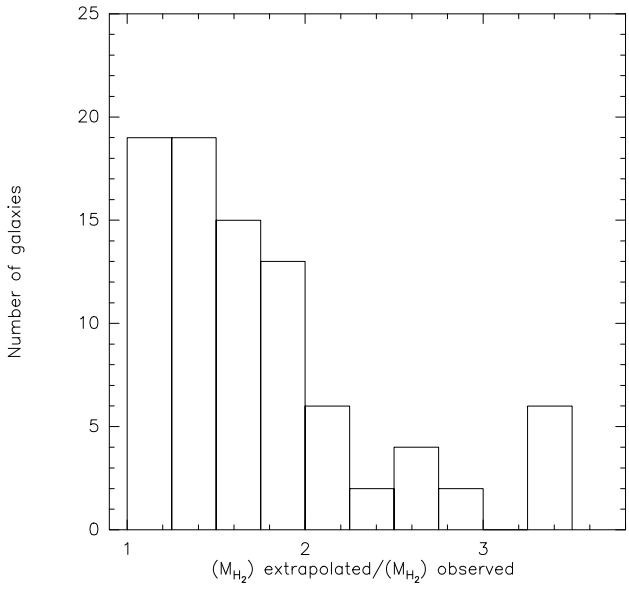


*Figure 2.1: $M_{H_2}$ aperture correction factor distribution.*

*Table 2.3: Average values for $L_B$, $M_{H_2}$, $M_{H_2}$ deficiency, $L_{FIR}$, $L_{FIR}$ deficiency and $M_{HI}$ deficiency for HCGs galaxies and AMIGA isolated galaxies.*

| | **HCGs** | | | | **AMIGA** | | | |
|---|---|---|---|---|---|---|---|---|
| | All | $n_{UL}/n$ | T>0 | $n_{UL}/n$ | All | $n_{UL}/n$ | T>0 | $n_{UL}/n$ |
| $L_B$ | 9.91±0.04 | 0/86 | 9.95±0.06 | 0/46 | 9.72±0.03 | 0/173 | 9.75±0.04 | 0/150 |
| $M_{H_2}$ | 8.71±0.07 | 41/86 | 9.02±0.09 | 11/46 | 8.24±0.09 | 84/173 | 8.32±0.09 | 69/150 |
| Def($M_{H_2}$) | 0.10±0.09 | 41/86 | -0.22±0.09 | 11/46 | 0.05±0.04 | 84/173 | 0.02±0.04 | 69/150 |
| $L_{FIR}$ | 8.96±0.12 | 50/85 | 9.53±0.09 | 15/45 | 9.11±0.05 | 75/172 | 9.16±0.05 | 58/150 |
| Def($L_{FIR}$) | 0.32±0.09 | 50/85 | -0.11±0.08 | 15/45 | -0.05±0.05 | 75/172 | -0.09±0.04 | 58/150 |
| Def(HI) | 1.34±0.10 | 34/68 | 0.93±0.13 | 9/37 | | | | |

In the case of the isolated galaxies, we have calculated the average $L_B$, $M_{H_2}$, $M_{H_2}$ deficiency, $L_{FIR}$ and $L_{FIR}$ deficiency for the subsample of galaxies with $M_{H_2}$ data. For each subsample, $n$ is the number of galaxies and $n_{UL}$ is the number of upper limits. $L_{FIR}$ of the AMIGA galaxies are calculated form the new release (see Sec. 2.3) of the AMIGA sample, while the $M_{H_2}$ values are calculated form the data in Lisenfeld et al. (in prep.)

produces a scan profile along the average scan direction. It is 3-5 times more sensitive than IRAS PSC since it combines all survey data and it is therefore more suitable for detection of the total flux from slightly extended objects.

We have compiled from Verdes-Montenegro et al. (1998) (Table 2.4) the FIR data (also derived using ADDSCAN/SCANPI) for 63 galaxies in our sample. In the case of the remaining 23 galaxies, we derived FIR fluxes directly using ADDSCAN/SCANPI. To choose the best flux estimator we have followed the guidelines given in the IPAC website[6], which are also detailed in Lisenfeld et al. (2007).

This procedure was also followed for 14 galaxies in the list of Verdes-Montenegro et al. (1998) to check for consistency. We found no significant differences, with an average difference of 15% between our reprocessed fluxes and those in Verdes-Montenegro et al. (1998).

[6]http://irsa.ipac.caltech.edu/IRASdocs/scanpi_interp.html

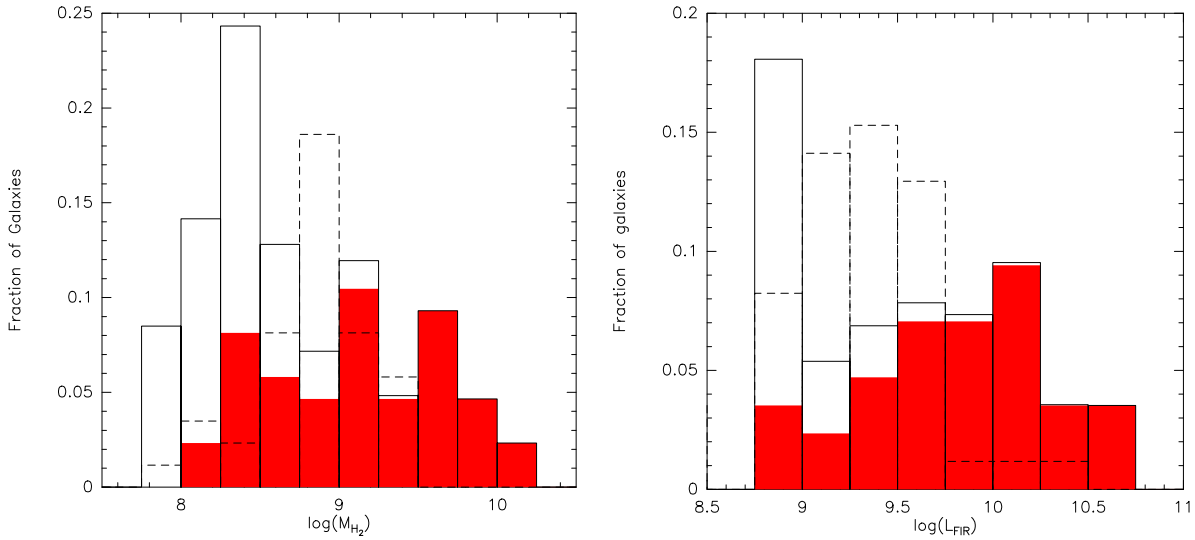


*Figure 2.2: $M_{H_2}$ and $L_{FIR}$ distribution ratios of the HCG galaxies. The (red) filled bins show the distribution of the detected galaxies, t the dashed line gives the distribution of upper limits and the full line shows the combined distribution given by ASURV.*

From the fluxes at 60 and 100 $\mu$m, $L_{FIR}$ is computed as

$$\log(L_{FIR}/L_{\odot}) = \log(FIR) + 2\log D + 19.495 \tag{2.5}$$

where FIR is defined as (Helou et al. 1988):

$$FIR = 1.26 \times 10^{-14}(2.58F_{60} + F_{100})Wm^{-2}. \tag{2.6}$$

The computed $L_{FIR}$, together with the 60 and 100 $\mu$m fluxes compiled from ADDSCAN/SCANPI are detailed in Table 2.4. In this table we also show the values of the Star Formation Rate (SFR), the Star Formation Efficiency (SFE) and the specific Star Formation Rate (sSFR) (see Sec. 2.3.2). The distribution of $L_{FIR}$ is shown in Fig. 2.2. The average value of $L_{FIR}$ for the full sample and the spiral galaxies is shown in Table 2.3.

For galaxies HCG31 *a* and *c* FIR fluxes can not be separated. Therefore, we use the sum of both. When comparing $L_{FIR}$ to other magnitudes ($L_B$, $M_{H_2}$ or $M_{HI}$), we also use the sum of these magnitudes.

*Table 2.4: FIR, SFR, SFE and sSFR*

| Galaxy | Ref[1] | $I_{60}$ (Jy) | $I_{100}$ (Jy) | $\log(L_{FIR})$ ($L_{\odot}$) | SFR ($M_{\odot}$ yr$^{-1}$) | log(SFE)[2] log(yr$^{-1}$) | log(sSFR) ($M_{\odot}$ yr$^{-1}$) |
|---|---|---|---|---|---|---|---|
| 7a | 2 | 3.32 | 6.61 | 10.23 | 5.96 | -8.93 | -10.43 |
| 7b | 2 | $<0.18$ | $<0.32$ | $<8.95$ | $<0.31$ | | $<$ -11.40 |
| 7c | 2 | 0.61 | 2.35 | 9.65 | 1.57 | -8.97 | -10.72 |
| 7d | 2 | $<0.15$ | $<0.39$ | $<8.95$ | $<0.31$ | | $<$ -10.73 |
| 10a | 2 | 0.50 | 1.81 | 9.72 | 1.84 | -9.24 | -11.12 |
| 10b | 2 | $<0.11$ | 0.47 | $<9.10$ | $<0.44$ | | $<$ -11.79 |
| 10c | 2 | 0.78 | 2.06 | 9.84 | 2.43 | -9.15 | -10.49 |
| 10d | 2 | $<0.12$ | $<0.28$ | $<9.00$ | $<0.35$ | | $<$ -10.93 |
| 15a | 1 | $<0.17$ | 0.50 | $<9.48$ | $<1.06$ | | $<$ -11.23 |
| 15b | 1 | $<0.22$ | $<0.70$ | $<9.61$ | $<1.43$ | | $<$ -10.87 |
| 15c | 1 | $<0.24$ | $<0.80$ | $<9.65$ | $<1.57$ | | $<$ -10.80 |

| Galaxy | Ref[1] | $I_{60}$ (Jy) | $I_{100}$ (Jy) | $\log(L_{\rm FIR})$ ($L_\odot$) | SFR ($M_\odot$ yr$^{-1}$) | log(SFE)[2] log(yr$^{-1}$) | log(sSFR) ($M_\odot$ yr$^{-1}$) |
|---|---|---|---|---|---|---|---|
| 15d | 1 | < 0.24 | 0.53 | < 9.56 | < 1.27 | <-8.45 | < -10.70 |
| 15e | 1 | < 0.13 | 0.28 | < 9.29 | < 0.68 | | < -10.88 |
| 15f | 1 | < 0.24 | 0.79 | < 9.65 | < 1.57 | | < -9.78 |
| 16a | 2 | 5.73 | 12.83 | 10.47 | 10.36 | -8.98 | -10.29 |
| 16b | 2 | < 0.12 | < 0.33 | < 8.84 | < 0.24 | <-9.73 | < -11.71 |
| 16c | 2 | 12.20 | 19.99 | 10.74 | 19.29 | -8.44 | -9.70 |
| 16d | 2 | 11.80 | 12.00 | 10.66 | 16.04 | -8.75 | -9.75 |
| 23a | 1 | < 0.30 | < 1.93 | < 9.57 | < 1.30 | <-8.27 | < -10.95 |
| 23b | 1 | < 1.50 | < 4.02 | <10.03 | < 3.76 | <-9.10 | < -10.41 |
| 23c | 1 | < 0.14 | < 0.80 | < 9.21 | < 0.57 | | < -11.02 |
| 23d | 1 | 0.63 | 1.23 | 9.59 | 1.37 | -8.62 | -10.20 |
| 25a | 1 | 0.55 | 1.16 | 9.84 | 2.43 | -8.85 | -10.32 |
| 25b | 1 | < 0.15 | < 0.71 | < 9.46 | < 1.01 | <-9.05 | < -11.12 |
| 25d | 1 | < 0.25 | < 0.63 | < 9.53 | < 1.19 | | < -10.26 |
| 25f | 1 | < 0.13 | < 0.70 | < 9.44 | < 0.97 | | < -10.38 |
| 30a | 2 | < 0.09 | 0.55 | < 9.00 | < 0.35 | | < -11.56 |
| 30b | 2 | 0.10 | < 0.44 | < 8.95 | < 0.31 | | < -11.50 |
| 30c | 2 | 0.17 | 0.75 | 9.19 | 0.54 | >-9.09 | -10.15 |
| 30d | 2 | < 0.10 | < 0.30 | < 8.85 | < 0.25 | | < -10.55 |
| 31ac[3] | 2 | 4.98 | 6.69 | 10.35 | 7.86 | > -7.92 | < -9.29 |
| 31b | 2 | 0.08 | 0.38 | 8.84 | 0.24 | >-9.39 | -10.15 |
| 31g | 2 | 0.50 | 0.40 | 9.29 | 0.68 | >-8.89 | -10.20 |
| 37a | 2 | 0.56 | 2.30 | 10.06 | 4.03 | -7.80 | -11.01 |
| 37b | 2 | 0.66 | 2.13 | 10.07 | 4.12 | -9.18 | -10.50 |
| 37c | 2 | < 0.09 | < 0.26 | < 9.19 | < 0.54 | <-8.57 | |
| 37d | 2 | < 0.08 | < 0.12 | < 9.01 | < 0.36 | <-8.71 | < -10.34 |
| 37e | 2 | < 0.11 | < 0.17 | < 9.13 | < 0.47 | | < -10.55 |
| 40a | 2 | < 0.10 | < 0.30 | < 9.18 | < 0.53 | | < -11.78 |
| 40b | 2 | < 0.08 | < 0.25 | < 9.11 | < 0.45 | <-9.04 | < -11.43 |
| 40c | 2 | 0.85 | 2.00 | 10.06 | 4.03 | -9.23 | -10.64 |
| 40d | 2 | 1.03 | 2.30 | 10.13 | 4.73 | -8.76 | -10.35 |
| 40e | 2 | < 0.10 | < 0.24 | < 9.13 | < 0.47 | <-9.20 | < -10.75 |
| 44a | 2 | 3.40 | 10.72 | 9.43 | 0.94 | -8.89 | -11.04 |
| 44b | 2 | < 0.12 | < 0.39 | < 7.99 | < 0.03 | | < -12.27 |
| 44c | 2 | 1.55 | 3.71 | 9.03 | 0.38 | -9.12 | -10.77 |
| 44d | 2 | 1.30 | 3.12 | 8.96 | 0.32 | -8.49 | -10.15 |
| 58a | 1 | 3.06 | 6.64 | 10.59 | 13.66 | -9.09 | -10.32 |
| 58b | 1 | 0.41 | 1.88 | 9.90 | 2.79 | -8.95 | -10.89 |
| 58c | 1 | < 0.21 | < 0.60 | < 9.49 | < 1.08 | | < -11.18 |
| 58d | 1 | < 0.19 | < 0.94 | < 9.59 | < 1.37 | | < -10.93 |
| 58e | 2 | 0.29 | 0.88 | 9.64 | 1.53 | -8.89 | -10.46 |
| 67a | 2 | < 0.19 | < 0.74 | < 9.64 | < 1.53 | | < -11.63 |
| 67b | 2 | 1.01 | 2.59 | 10.26 | 6.39 | -8.96 | -10.50 |
| 67c | 2 | < 0.21 | 0.90 | < 9.71 | < 1.80 | | < -10.29 |
| 68a | 2 | 0.42 | 1.70 | 8.90 | 0.28 | >-8.58 | -11.81 |

| Galaxy | Ref[1] | $I_{60}$ (Jy) | $I_{100}$ (Jy) | $\log(L_{FIR})$ ($L_\odot$) | SFR ($M_\odot$ yr$^{-1}$) | log(SFE)[2] log(yr$^{-1}$) | log(sSFR) ($M_\odot$ yr$^{-1}$) |
|---|---|---|---|---|---|---|---|
| 68b | 2 | $<0.12$ | $<0.31$ | $<8.25$ | $<0.06$ | | |
| 68c | 2 | 2.34 | 8.45 | 9.62 | 1.46 | -8.94 | -10.70 |
| 68d | 2 | $<0.16$ | $<0.26$ | $<8.28$ | $<0.07$ | | $<$-11.30 |
| 68e | 2 | $<0.18$ | $<0.29$ | $<8.34$ | $<0.08$ | | $<$-11.07 |
| 79a | 2 | 1.28 | 2.82 | 9.90 | 2.79 | >-8.61 | -10.31 |
| 79b | 2 | $<0.13$ | $<0.45$ | $<9.01$ | $<0.36$ | <-9.00 | $<$-11.18 |
| 79c | 2 | $<0.10$ | $<0.40$ | $<8.94$ | $<0.31$ | <-8.64 | |
| 79d | 2 | $<0.09$ | $<0.40$ | $<8.92$ | $<0.29$ | | |
| 88a | 2 | 0.47 | 2.44 | 9.96 | 3.20 | -9.04 | -10.85 |
| 88b | 2 | 0.14 | $<0.50$ | $<9.34$ | $<0.77$ | <-9.41 | $<$-11.36 |
| 88c | 2 | 0.36 | 2.03 | 9.87 | 2.60 | -9.18 | -10.08 |
| 88d | 2 | 0.18 | 0.77 | 9.49 | 1.08 | -8.60 | -10.38 |
| 92b | 2 | 0.85 | 2.78 | 10.16 | 5.07 | >-8.46 | -10.90 |
| 92c | 2 | 0.85 | 2.60 | 10.14 | 4.85 | -8.50 | -10.61 |
| 92d | 2 | $<0.85$ | $<0.75$ | $<9.93$ | $<2.99$ | | $<$-11.13 |
| 92e | 2 | $<0.09$ | $<0.92$ | $<9.52$ | $<1.16$ | | $<$-11.01 |
| 93a | 1 | $<0.40$ | $<1.04$ | $<9.50$ | $<1.11$ | <-8.78 | $<$-11.43 |
| 93b | 1 | 1.82 | 4.90 | 10.16 | 5.07 | -8.94 | -10.22 |
| 93c | 1 | $<0.18$ | $<1.14$ | $<9.39$ | $<0.86$ | <-9.07 | $<$-11.11 |
| 93d | 1 | $<0.20$ | $<1.14$ | $<9.40$ | $<0.88$ | | $<$-10.68 |
| 97a | 2 | $<0.13$ | $<0.38$ | $<9.29$ | $<0.68$ | | $<$-11.51 |
| 97b | 2 | 0.15 | 0.86 | 9.53 | 1.19 | -9.17 | -10.65 |
| 97c | 2 | $<0.12$ | $<0.36$ | $<9.26$ | $<0.64$ | | $<$-11.14 |
| 97d | 2 | $<0.20$ | $<0.36$ | $<9.38$ | $<0.84$ | | $<$-11.20 |
| 97e | 2 | $<0.12$ | $<0.43$ | $<9.31$ | $<0.72$ | | $<$-10.38 |
| 100a | 2 | 2.13 | 4.02 | 10.28 | 6.69 | -8.28 | -10.39 |
| 100b | 2 | $<0.09$ | $<0.44$ | $<9.13$ | $<0.47$ | <-8.69 | $<$-10.58 |
| 100c | 2 | 0.30 | 0.45 | 9.39 | 0.86 | -8.52 | -10.24 |
| 100d | 2 | $<0.12$ | $<0.77$ | $<9.34$ | $<0.77$ | | $<$-9.61 |

[1] Reference code (see 2.2.2): 1: Our data analysis. 2:Verdes-Montenegro et al. (1998).

[2]The value of the SFE is not displayed for the galaxies with upper limits in both $L_{FIR}$ and $M_{H_2}$.

[3]The SFE of 31ac has been calculated using the sum of their respective $M_{H_2}$.

## 2.3 Results

In this section, we perform a comparison of the $M_{H_2}$, $L_{FIR}$, $M_{HI}$ and $L_B$ of the galaxies. The SFR, SFE and sSFR of the galaxies are also studied. We have also calculated the ratio between the CO emission at the two transitions. We have calculated the deficiency of $M_{H_2}$, $L_{FIR}$ and $M_{HI}$ of the galaxies with respect to the AMIGA sample of isolated galaxies to see whether they correlate or not and whether there is a significant difference between isolated and HCGs galaxies.

We have chosen as reference the AMIGA sample of isolated galaxies (Verdes-Montenegro et al. 2005b), which is based on the CIG catalogue (Karachentseva 1973). The FIR properties of an optically complete subsample of this catalogue have been

*Table 2.5: Correlation analysis of $M_{H_2}$ vs $L_B$ and $L_{FIR}$ vs $L_B$.*

| Magnitude | Sample | | Slope (bisector) | Intercept (bisector) | Slope ($L_B$ indep.) | Intercept ($L_B$ indep.) |
|---|---|---|---|---|---|---|
| $M_{H_2}$ vs $L_B$ | HCGs | All | 1.37±0.15 | -4.74±1.48 | 0.81±0.14 | 0.73±1.35 |
| | | T>0 | 1.40±0.16 | -4.94±1.61 | 0.95±0.20 | -0.43±1.97 |
| | AMIGA | | 1.43±0.08 | -5.39±0.78 | 1.08±0.07 | -2.04±0.73 |
| $L_{FIR}$ vs $L_B$ | HCGs | All | 1.51±0.14 | -5.75±1.40 | 0.86±0.14 | 0.70±1.36 |
| | | T>0 | 1.34±0.16 | -3.83±1.63 | 0.95±0.15 | 0.07±1.52 |
| | AMIGA | | 1.39±0.04 | -4.43±0.37 | 1.12±0.04 | -1.73±0.38 |
| $M_{H_2}$ vs $L_{FIR}$ | HCGs | All | 1.02±0.12 | 0.53±0.82 | 0.74±0.09 | 1.95±0.89 |
| | | T>0 | 0.89±0.08 | -0.70±1.16 | 0.84±0.11 | 1.06±1.07 |
| | AMIGA | | 1.15±0.07 | -2.14±0.66 | 0.99±0.05 | -0.60±0.52 |

The slope and intercept are defined as $\log(M_{H_2}) = \log(L_B) \times slope +$ intercept, $\log(L_{FIR}) = \log(L_B) \times slope +$ intercept and $\log(M_{H_2}) = \log(L_{FIR}) \times slope +$ intercept.

The fits on $L_{FIR}$ vs $L_B$ for the AMIGA sample are calculated from the new release of the data shown in Lisenfeld et al. (2007), so there are slight, not significant differences between our fits and the ones in that work. The AMIGA fits involving $M_{H_2}$ are taken from Lisenfeld et al (in prep.).

studied in Lisenfeld et al. (2007). The subsample we have used is slightly different to that of Lisenfeld et al. (2007), since some of the data (blue magnitude, distance, Hubble type and isolation) of the AMIGA galaxies were updated in June 2010. The CO properties have been also studied for a velocity restricted subsample (1500<V<5000 km s$^{-1}$) (Lisenfeld at al, in prep.) and will be used here.

### 2.3.1 Relation between $M_{H_2}$, $L_{FIR}$, $M_{HI}$, $M_{star}$ and $L_B$

We have performed a comparison of $L_B$ with $M_{H_2}$, $L_{FIR}$ and $M_{HI}$ for each HCG galaxy. We have taken $L_B$ as the reference wavelength because the parameters of its correlations with $M_{H_2}$, $L_{FIR}$ and $M_{HI}$ are available for isolated galaxies, it is a reasonable tracer of the stellar population and it should be less affected by interactions than the other three variables.

Early-type galaxies tend to have a significantly lower molecular gas content than late-type ones, and their $L_{FIR}$ emission is not as clearly related to their SFR as it is in late-type galaxies, as a result of the lack of a strong SF. Thus, in this section, as well as throughout this work, the analysis is performed separately for both the full sample and a subsample restricted to spirals.

Fig. 2.3 shows the $M_{H_2}$ (left) and the $L_{FIR}$ (right) of the galaxies versus their $L_B$. Different colors and symbols have been used to differentiate between early and late-type galaxies. A linear fit to the data is also plotted. In both cases, $M_{H_2}$ and $L_{FIR}$ show a good correlation with $L_B$. The coefficients of the fits are shown in Table 2.5.

We note that in contrast to $M_{H_2}$ and $L_{FIR}$, $M_{HI}$ shows no correlation with $L_B$, (Fig. 2.4), reflecting the fact that HI is the most affected variable among the three. This is because our sample contains a large number of very evolved groups, where HI has been removed from galaxies.

The correlation between $M_{H_2}$ and $L_{FIR}$ has been noted by previous surveys such as the ones in Young & Scoville (1991) and Bigiel et al. (2008), who found a linear correlation between both magnitudes, or Gao & Solomon (2004), who found a non-linear one. A linear correlation can be seen in our sample (Fig. 2.5).

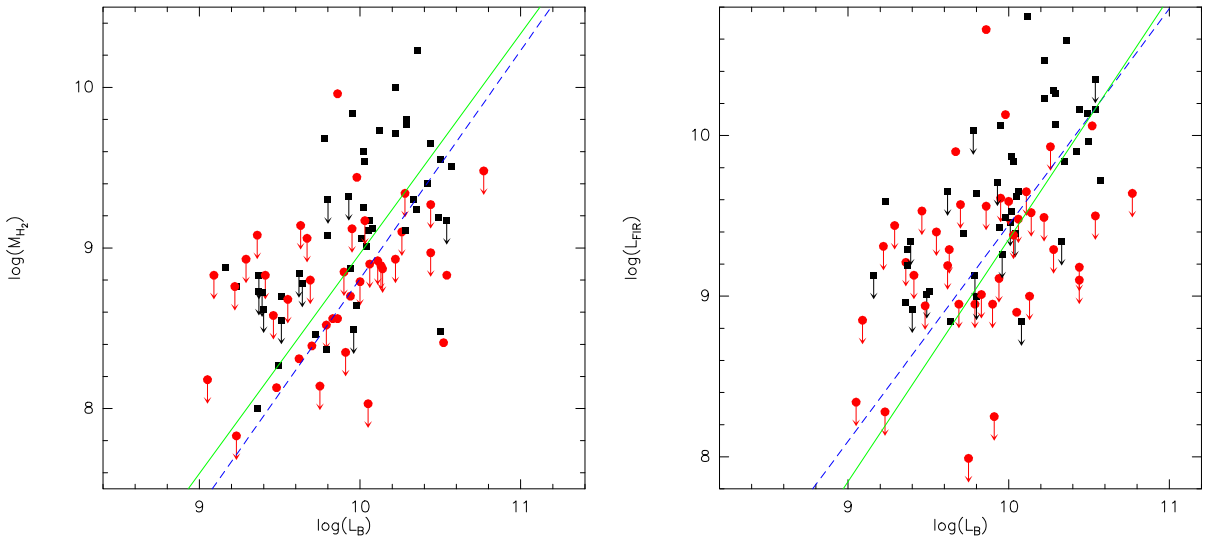


*Figure 2.3: Left: Molecular gas mass vs Blue luminosity. Right: FIR luminosity vs Blue luminosity. Signs: Black squares: late-type (T>0) galaxies; Red circles: early-type galaxies. The green solid line corresponds to the bisector fit found for HCGs galaxies, while the dashed blue line corresponds to the bisector fit found for the AMIGA isolated galaxies. The fit to the isolated galaxies is taken from Lisenfeld et al. (in prep.) in the case of $M_{H_2}$ vs $L_B$ and from Lisenfeld et al. (2007) in the case of $L_{FIR}$ vs $L_B$. All the fits are detailed in Table 2.5.*

### 2.3.2 Star Formation Rate, Star Formation Efficiency and specific Star Formation Rate

Kennicutt (1998) derived the SFR from $L_{IR}$ as

$$SFR(M_\odot/\mathrm{yr}) = 4.5\times10^{-44}\mathrm{L_{IR}(ergs^{-1})} \tag{2.7}$$

where $L_{IR}$ refers to the IR luminosity integrated over the full-, mid- and far-IR spectrum (10-1000 $\mu$m). For $L_{FIR}$, we are are using an approximation to the integrated 42.5-122-5 $\mu$m emission (Eq. 2.6). To extrapolate our $L_{FIR}$ to the range assumed by Kennicutt, we have applied the finding of Bell (2003) of $L_{IR}$ to be on average a factor 2 higher than our $L_{FIR}$. Once this factor is considered, we can express the SFR as a function of our $L_{FIR}$ as

$$SFR(M_\odot/\mathrm{yr}) = 9\times10^{-44}\mathrm{L_{FIR}(ergs^{-1})} \qquad = 3.51\times10^{-10}\mathrm{L_{FIR}(L_\odot)} \tag{2.8}$$

The values of the SFR of the galaxies in our sample are detailed in Table 2.4.

We define the star formation efficiency, SFE, as the fraction SFR/$M_{H_2}$. The SFE gives actually the SFR per molecular gas unit, measuring how efficiently the SF is performed. The SFE of the galaxies in our sample are also displayed in Table 2.4. To calculate the average SFE of our sample we must take into account that ASURV can only handle data showing upper or lower limits, but not both. Thus, we have first calculated the average SFE considering only galaxies detected in CO with an upper limit in FIR, together with the ones detected in both bands. Separately, we considered only those detected in FIR but not detected in CO and the ones detected in both bands. The results coming from the two methods are log(SFE) = -9.00±0.06 yr$^{-1}$ and log(SFE) = -8.78±0.07 yr$^{-1}$.

The specific SFR, sSFR, is defined as the ratio between the SFR and the stellar mass of a galaxy. As detailed in Sec. 2.1, we have calculated the stellar mass from the K band luminosity,

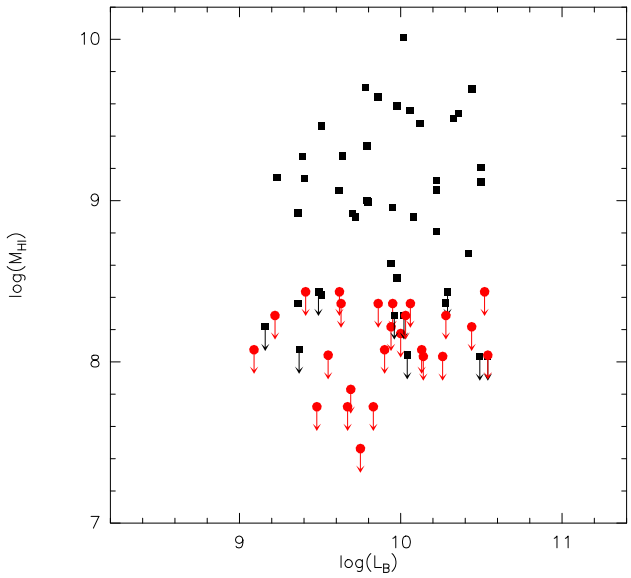


*Figure 2.4: Atomic gas mass vs Blue luminosity. Signs: Black squares: late-type (T>0) galaxies; Red circles: early-type galaxies.*

which is a good tracer because the light in this band is dominated by the emission of low-mass stars, which are responsible for the bulk of stellar mass in galaxies. The values of the sSFR for our galaxies are detailed in Table 2.4. The average sSFR of our sample, in logarithm scale, is -11.27± 0.13 $yr^{-1}$ for the full sample and -10.71± 0.09 $yr^{-1}$ for the spiral galaxies.

### 2.3.3 Line Ratio

Fig. 2.6 shows the CO(1-0) versus the CO(2-1) intensity for the galaxies we observed (Sec. 2.2.1.1). The plotted intensities are not aperture corrected. The ratio between both intensities lies near unity, with a mean value of 1.13±0.11. Taking into account only spiral galaxies, the mean line ratio is the same. To calculate this mean ratio with ASURV, we have taken into account galaxies with detection in both CO transitions as well as those detected in CO(1-0) but not detected in CO(2-1).

From the comparison of CO(2-1) with CO(1-0) maps of nearby galaxies belonging to the SINGS sample, Leroy et al. (2009) found a line ratio of ∼0.8. Braine et al. (1993), for a sample of nearby spiral galaxies, found a line ratio of 0.89±0.06.

In order to interpret the ratio of $I_{CO(2-1)}/I_{CO(1-0)}$ one has to consider two main parameters: the source distribution and the opacity. For optically thick, thermalized emission with a point-like distribution we expect a ratio $I_{CO(2-1)}/I_{CO(1-0)} = (\theta_{CO(1-0)}/\theta_{CO(2-1)})^2 = 4$ (with $I_{CO}$ in $T_{mb}$ and $\theta$ being the FWHM of the beams). On the other hand, for a uniform source brightness distribution we expect ratios larger than 1 for optically thin gas, and a ratios between about 0.6 and 1 for optically thick gas (with excitation temperatures above 5 K).

Due to the different beam sizes of our observations of CO(1-0) and CO(2-1) we cannot distinguish these two cases so that we cannot draw any firm conclusions from our line ratio. However, we can conclude that our values are consistent with optically thick, thermalized gas with an extended distribution. Our mean value is slightly higher than the (beam-corrected) values of Leroy et al. (2009) and Braine et al. (1993) which might indicate that the molecular gas is not completely uniform over the CO(1-0) beam, but slightly concentrated towards the center.

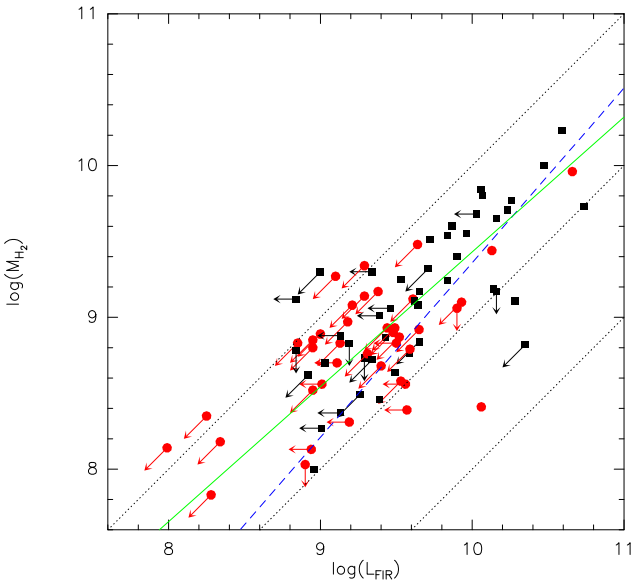


*Figure 2.5: Molecular gas mass vs FIR luminosity. Signs: Black squares: late-type (T>0) galaxies; Red circles: early-type galaxies. The green line corresponds to the bisector fit found for HCGs galaxies, while the blue line corresponds to the bisector fit found for the AMIGA isolated galaxies by Lisenfeld et al. (in prep.). The fits are detailed in Table 2.5. The dotted black lines correspond to the $L_{\rm FIR}/M_{\rm H_2}$ ratios 1, 10 and 100 $L_\odot/M_\odot$.*

### 2.3.4 Deficiencies

We have calculated the $M_{\rm H_2}$, $L_{\rm FIR}$ and $M_{\rm HI}$ deficiencies following the definition of Haynes & Giovanelli (1984) as

$$Def(X) = \log(\mathrm{X_{predicted}}) - \log(\mathrm{X_{observed}}) \tag{2.9}$$

where we calculated the predicted value of the variable X from $L_{\rm B}$. Following this definition, a negative value of the deficiency implies an excess with respect to its predicted value.

The expected $M_{\rm H_2}$ for each galaxy is calculated from its blue luminosity using the fit to the AMIGA sample in Lisenfeld et al. (in prep.). Note that the fit, which is given in Table 2.5, was calculated without distinguishing morphological types. Due to the dominance of spiral galaxies in the AMIGA sample, the fit is correct for spiral galaxies. It has not been possible to derive a separate fit fro only early-type galaxies.

The expected $L_{\rm FIR}$ is calculated from the fit obtained for the AMIGA isolated galaxies (Table 2.5) using the June 2010 release on the sample in Lisenfeld et al. (2007). As the one between $M_{\rm H_2}$ and $L_{\rm B}$, this fit has no dependence on the morphological type.

The HI deficiency of the galaxies is calculated following the morphology-dependent fit between $M_{HI}$ and $L_{\rm B}$ in Haynes & Giovanelli (1984). We have considered h $= H_0/100 = 0.75$. To calculate their fits, Haynes & Giovanelli (1984) used a solar photographic absolute magnitude of +5.37 and calculate $L_{\rm B}$ from $\mathrm{mag}_{zw}$. Assuming the empirical relation between blue magnitudes found by Verdes-Montenegro et al. (2001) ($\mathrm{mag}_{zw} = B_{\rm c}^{\rm T}$+0.136) and the fact that here we express $L_{\rm B}$ as a function of the solar bolometric luminosity (mag = 4.75), we must introduce the following correction:

$$(\log L_{\rm B})_{Haynes} = (\log L_{\rm B})_{ours} + 0.14 \tag{2.10}$$

to express $L_{\rm B}$ in the terms we assume (Sec. 2.1) to calculate the expected content of HI.

The $M_{\rm H_2}$, $L_{\rm FIR}$ and $M_{\rm HI}$ deficiencies are listed in Table 2.6.

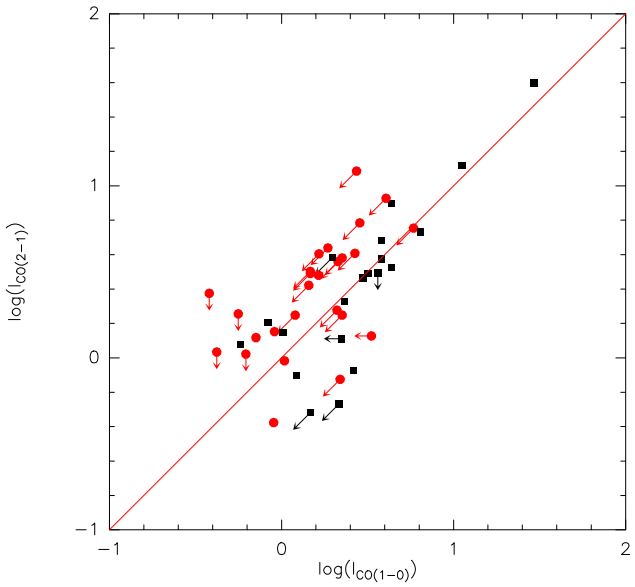


*Figure 2.6: $\log(I_{CO(2-1)})$ versus $\log(I_{CO(1-0)})$ for the galaxies in our sample. Signs: Black squares: late-type (T>0) galaxies; Red circles: early-type galaxies. The y=x line is plotted for orientation and does not represent a fit to the data.*

#### 2.3.4.1 $M_{H_2}$ and $L_{FIR}$ deficiencies

The average $M_{H_2}$ and $L_{FIR}$ deficiencies (Def($M_{H_2}$) and Def($L_{FIR}$)) for the full sample and the spiral galaxies are listed in Table 2.3. For the full sample, Def($L_{FIR}$) is slightly larger than the Def($M_{H_2}$), which is almost zero (0.31±0.09 vs 0.10±0.09, respectively). If only spiral galaxies are considered, Def($L_{FIR}$) have a value closer to Def($M_{H_2}$) (-0.11±0.08 vs -0.22±0.09, respectively). The values for early-type galaxies, not included in the table, are Def($M_{H_2}$) = 0.61±0.14 (30 upper limits out of 40 galaxies) and Def($L_{FIR}$) = 0.84± 0.11 (35 upper limits). The large number of upper limits for early-type galaxies makes these average values somewhat inaccurate. It must be noted that the galaxies showing an excess in $M_{H_2}$ or $L_{FIR}$ show values of $L_B$ that span over its full range, as can be seen looking for the galaxies that are above the fit in the plots in Fig. 2.3. Thus, the excess on $M_{H_2}$ or $L_{FIR}$ is not associated with the brightest objects *per se*.

We have performed a review of the information found in the literature for the 10 detected galaxies with the largest excess of $M_{H_2}$, finding:

- H10c, Def($M_{H_2}$) = -0.687. Amram et al. (2003) found several interaction indicators in this galaxy: (1) A highly disturbed velocity field; (2) disagreement between both sides of the rotation curve; (3) double component in the velocity profiles of the gas; (4) changing position angle along the major axis with rotation of external isophotes; (5) gaseous versus stellar major axis misalignment and (6) the presence of a shell.

- H16a, Def($M_{H_2}$) = -0.878. It was classified as a star forming galaxy by Gallagher et al. (2008), who found a low-ionization nuclear emission region. It shows a huge optical tail. Martínez (2008) (hereafter M08) classified it as AGN.

- H16c, Def($M_{H_2}$) = -0.750, classified as starburst nucleated galaxy by Gallagher et al. (2008). Mendes de Oliveira et al. (1998) found it to host a double gas system, with severe warping of the kinematic major axis. Its velocity field shows kinematic peculiarities. M08 classified it as Transition Object (TO).

*Table 2.6: Deficiencies of $M_{H_2}$ $L_{FIR}$ and $M_{HI}$*

| Galaxy | Def($M_{H_2}$) | Def($L_{FIR}$) | Def($M_{HI}$) | Galaxy | Def($M_{H_2}$) | Def($L_{FIR}$) | Def($M_{HI}$) |
|---|---|---|---|---|---|---|---|
| 7a | -0.59 | -0.49 | 0.67 | 40e | -1.26 | >-0.82 | >0.87 |
| 7b | >-0.43 | >0.07 | > 1.38 | 44a | -0.14 | -0.07 | 1.00 |
| 7c | -0.28 | -0.13 | 0.29 | 44b | > 0.31 | >1.11 | > 1.79 |
| 7d | >-0.01 | > 0.21 | 0.78 | 44c | -0.59 | -0.25 | 1.02 |
| 10a | 0.11 | 0.49 | ... | 44d | -0.10 | -0.38 | 0.47 |
| 10b | > 0.17 | > 0.93 | ... | 58a | -0.91 | -0.66 | 0.35 |
| 10c | -0.69 | -0.36 | ... | 58b | 0.01 | 0.11 | 1.25 |
| 10d | >-0.77 | > 0.17 | ... | 58c | > 0.19 | > 0.25 | 0.74 |
| 15a | >-0.00 | >0.04 | > 1.09 | 58d | > 0.02 | >-0.15 | > 1.23 |
| 15b | >-0.38 | >-0.24 | > 1.02 | 58e | -0.55 | -0.47 | 0.72 |
| 15c | > 0.05 | >-0.06 | ... | 67a | > 0.42 | > 0.84 | ... |
| 15d | 0.05 | >-0.31 | >0.96 | 67b | -0.55 | -0.43 | ... |
| 15e | >-0.86 | >-0.35 | > 1.29 | 67c | >-0.61 | >-0.37 | ... |
| 15f | >-0.57 | >-0.72 | 0.34 | 68a | > 0.85 | 0.61 | ... |
| 16a | -0.88 | -0.73 | 0.72 | 68b | > 0.33 | > 1.07 | ... |
| 16b | -0.20 | > 0.71 | 0.80 | 68c | -0.23 | -0.11 | ... |
| 16c | -0.75 | -1.14 | 0.45 | 68d | >-0.11 | > 0.12 | ... |
| 16d | -1.35 | -1.41 | 0.19 | 68e | >-0.72 | >-0.18 | ... |
| 23a | -0.01 | >-0.54 | 0.79 | 79a | >-0.72 | -0.90 | >1.48 |
| 23b | -1.18 | >-0.89 | -0.08 | 79b | 0.01 | > 0.20 | >1.58 |
| 23c | >-1.18 | >-0.63 | 1.06 | 79c | -0.06 | >-0.20 | >1.36 |
| 23d | -1.04 | -1.19 | 0.16 | 79d | >-0.66 | >-0.29 | 0.27 |
| 25a | 0.07 | 0.07 | ... | 88a | -0.03 | 0.16 | 0.98 |
| 25b | -0.24 | >-0.01 | ... | 88b | -0.02 | > 0.55 | 0.36 |
| 25d | >-0.54 | >-0.82 | ... | 88c | -0.76 | -0.40 | -0.15 |
| 25f | >-1.13 | >-0.96 | ... | 88d | 0.14 | -0.08 | 0.21 |
| 30a | > 0.10 | >0.62 | > 1.99 | 92b | > 0.41 | 0.01 | >2.19 |
| 30b | >-0.18 | >0.35 | > 1.79 | 92c | 0.32 | -0.04 | >2.15 |
| 30c | >-0.92 | -0.60 | >1.33 | 92d | > 0.08 | >-0.14 | > 2.15 |
| 30d | >-1.31 | >-0.64 | > 0.75 | 92e | > 0.14 | >0.11 | > 1.47 |
| 31a | >-0.44 | ... | 0.09 | 93a | 0.75 | > 0.67 | >1.71 |
| 31b | >-0.48 | 0.11 | 0.38 | 93b | -0.22 | -0.13 | 0.64 |
| 31c | 1.04 | ... | 1.18 | 93c | -0.14 | > 0.10 | >1.63 |
| 31ac | >0.75 | -0.18 | 1.27 | 93d | >-0.51 | >-0.57 | > 1.08 |
| 31g | >-0.81 | -0.70 | ... | 97a | >-0.13 | >0.53 | > 1.29 |
| 37a | 1.14 | 0.08 | >1.30 | 97b | -0.41 | -0.06 | >1.53 |
| 37b | -0.58 | -0.24 | >1.52 | 97c | > 0.26 | >0.13 | > 1.33 |
| 37c | -0.04 | >-0.26 | >1.21 | 97d | >-0.32 | >0.10 | > 1.14 |
| 37d | -0.18 | >-0.26 | >1.10 | 97e | >-1.06 | >-0.92 | > 0.63 |
| 37e | >-0.86 | >-0.49 | > 0.61 | 100a | 0.10 | -0.46 | 1.46 |
| 40a | > 0.47 | >0.85 | > 1.47 | 100b | 0.14 | > 0.03 | 0.44 |
| 40b | 0.03 | > 0.25 | >1.15 | 100c | -0.05 | -0.33 | 0.72 |
| 40c | -1.10 | -0.69 | 0.65 | 100d | >-0.78 | >-0.72 | 0.18 |
| 40d | -0.66 | -0.72 | 0.88 | | | | |

- H16d, Def($M_{H_2}$) = -1.349. It shows misalignments between the kinematic and photometric axes of gas and stellar components (Mendes de Oliveira et al. 1998). Its velocity field also shows kinematic peculiarities, and it is linked with H16a and H16c by HI tails (see the HI map in Verdes-Montenegro et al. 2001). It was found to host a star forming nucleus by M08.

- H23b, Def($M_{H_2}$) = -1.182. It is, together with H88c, the galaxy with lower HI deficiency. M08 classified it as TO.

- H23d, Def($M_{H_2}$) = -1.043. It shows only a small HI deficiency, Def($M_{HI}$)= 0.16, with no apparent signs of interaction. It was found to be an AGN by M08.

- H40c, Def($M_{H_2}$) = -1.101. It is part of one of the most compact groups in our sample, for which we have carried out a deeper study presented in Chap. 3, where more details about this galaxy can be found.

- H40e, Def($M_{H_2}$) = -1.263. As in the case of H40c, a deeper study of this galaxy can be found in Chap. 3.

- H58a Def($M_{H_2}$) = -0.909. It is classified as an intermediate Seyfert galaxy (Sy1.9) in the Veron-Cetty catalogue of quasars and active nuclei (Véron-Cetty & Véron 2010). Freeland et al. (2009), studying the HI distribution of the group found the HI morphology of H58a to be severely disturbed, with a HI extension towards H58b.

- 88c Def($M_{H_2}$) = -0.762. It is, together with 23c, the galaxy with lower HI deficiency. It shows a slightly distorted velocity field (see HI map in Verdes-Montenegro et al. 2001), but it was classified as unperturbed galaxy by Plana et al. (2003).

Fig.2.3.4.1 shows Def($M_{H_2}$) vs Def($L_{FIR}$) for each galaxy. Both are strongly correlated, which reflects the relation between the deficiency in the molecular gas and SFR, leading to a lower SFR if the fuel ($H_2$ traced by CO) decreases.

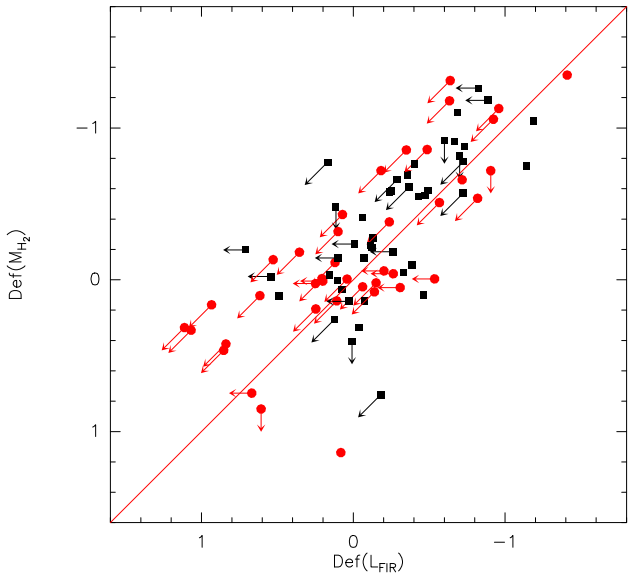


*Figure 2.7: $M_{H_2}$ deficiency vs $L_{FIR}$ deficiency. Signs: Black squares: late-type (T>0) galaxies; Red circles: early-type galaxies. The y=x line is plotted for orientation and does not represent a fit to the data.*

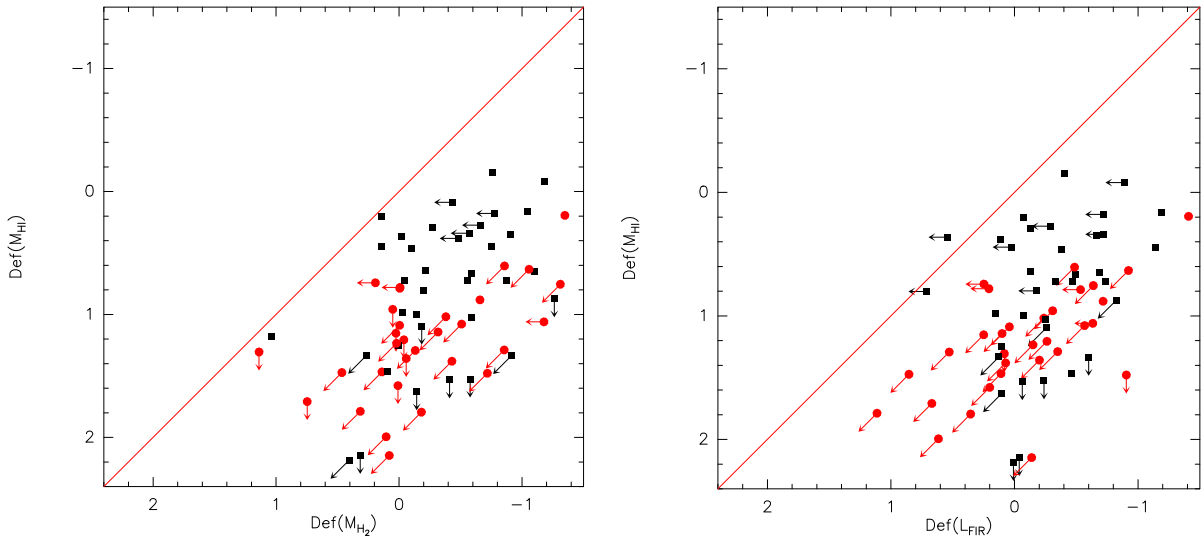


*Figure 2.8: Left: $M_{HI}$ deficiency vs $M_{H_2}$ deficiency. Right: $M_{HI}$ deficiency vs $L_{FIR}$ deficiency. Signs: Black squares: late-type (T>0) galaxies; Red circles: early-type galaxies. The y=x line is plotted for orientation and does not represent a fit to the data.*

As a test, we have also calculated the $M_{H_2}$ expected from the $M_{star}$, using the $M_{H_2}$ vs $M_{star}$ fit derived by Lisenfeld et al. (in prep) for the AMIGA sample, which gives a predicted value of $M_{H_2} = 1.02 \times M_{star}$ - 2.19. As in the case of $L_B$, the fit was derived without discrimination of morphological types. Considering this expected value, the Def($M_{H_2}$) calculated from the $M_{star}$ has an average value of 0.10±0.09 for the full sample and -0.27±0.05 for the spiral galaxies. These values are close to the deficiencies obtained from the blue luminosity of the galaxy, and match within the error bar, showing that there is no significant difference when considering $M_{star}$ or $L_B$ to calculate the expected $M_{H_2}$ of a galaxy.

#### 2.3.4.2 Comparison with $M_{HI}$ deficiency

In Fig. 2.8 we display (Def($M_{HI}$)) vs Def($M_{H_2}$) (left) and Def($L_{FIR}$) (right).

The average Def($M_{HI}$) of the galaxies with available HI data (Table 2.3) is one order of magnitude larger than Def($M_{H_2}$) and Def($L_{FIR}$). There is no clear correlation between Def($M_{HI}$) and Def($M_{H_2}$) or Def($L_{FIR}$), in part due to the large number of upper limits. However, there is a trend in the sense that a larger $M_{HI}$ deficiency leads to larger $M_{H_2}$ and $L_{FIR}$ deficiencies. The average Def($L_{FIR}$) and Def($M_{H_2}$) increase with Def($M_{HI}$) if we classify the galaxies in 2 different groups according to their Def($M_{HI}$) (Table 2.7). This trend is mostly due to elliptical galaxies, which have higher deficiencies in $M_{H_2}$, $L_{FIR}$ and $M_{HI}$, but it is also seen, although weaker, if only spiral galaxies are taken into account.

### 2.3.5 $M_{H_2}$ and $L_{FIR}$ deficiencies as a function of the HI content and evolutionary phase of the group

To study the influence of the global HI content of the group on the $M_{H_2}$ and SFR of the galaxies we have classified the groups as a function of their Def($M_{HI}$) as detailed in Sec. 2.1. The average Def($M_{H_2}$) and Def($L_{FIR}$) of the galaxies belonging to these groups are detailed in Table 2.7. We find no clear relation between the Def($M_{H_2}$) of the galaxies, nor the Def($L_{FIR}$), with the Def($M_{HI}$) of the groups.

*Table 2.7: $M_{H_2}$ and $L_{FIR}$ deficiencies for different samples calculated with ASURV.*

| | | All | | T>0 | |
|---|---|---|---|---|---|
| | | **Def($M_{H_2}$)** | $n_{UL}/n$ | **Def($M_{H_2}$)** | $n_{UL}/n$ |
| | | 0.10±0.09 | 41/86 | -0.22±0.09 | 11/46 |
| **HI content of galaxies** | Def(HI)<0.75 | -0.41±0.10 | 8/25 | -0.41±0.10 | 5/21 |
| | Def(HI)>0.75 | 0.26±0.11 | 21/43 | -0.01±0.12 | 3/16 |
| **HI content of the group** | Normal | 0.01±0.17 | 9/17 | -0.46±0.20 | 1/6 |
| | Slighty deficient | 0.09±0.12 | 22/50 | -0.14±0.12 | 8/30 |
| | Very deficient | 0.13±0.14 | 10/19 | -0.32±0.07 | 2/10 |
| **Evolutionary Phase** | Phase 1 | -0.22±0.11 | 7/19 | -0.43±0.13 | 2/11 |
| | Phase 2 | -0.07±0.14 | 11/30 | -0.24±0.13 | 5/21 |
| | Phase 3 | 0.42±0.14 | 23/37 | -0.12±0.09 | 4/14 |
| | | All | | T>0 | |
| | | **Def($L_{FIR}$)** | $n_{UL}/n$ | **Def($L_{FIR}$)** | $n_{UL}/n$ |
| | | 0.32±0.09 | 50/85 | -0.11±0.08 | 15/45 |
| **HI content of galaxies** | Def(HI)<0.75 | -0.29±0.12 | 9/24 | -0.32±0.11 | 6/20 |
| | Def(HI)>0.75 | 0.54±0.12 | 30/43 | 0.02±0.11 | 6/16 |
| **HI content of the group** | Normal | 0.37±0.21 | 12/17 | -0.19±0.19 | 3/6 |
| | Slighty deficient | 0.20±0.11 | 26/47 | -0.07±0.11 | 9/27 |
| | Very deficient | 0.40±0.17 | 12/21 | -0.23±0.06 | 3/12 |
| **Evolutionary Phase** | Phase 1 | -0.01±0.14 | 10/18 | -0.17±0.15 | 4/11 |
| | Phase 2 | 0.05±0.15 | 14/29 | -0.13±0.13 | 7/20 |
| | Phase 3 | 0.54±0.12 | 26/38 | -0.13±0.05 | 4/14 |

For each subsample, $n$ is the number of galaxies and $n_{UL}$ is the number of upper limits.

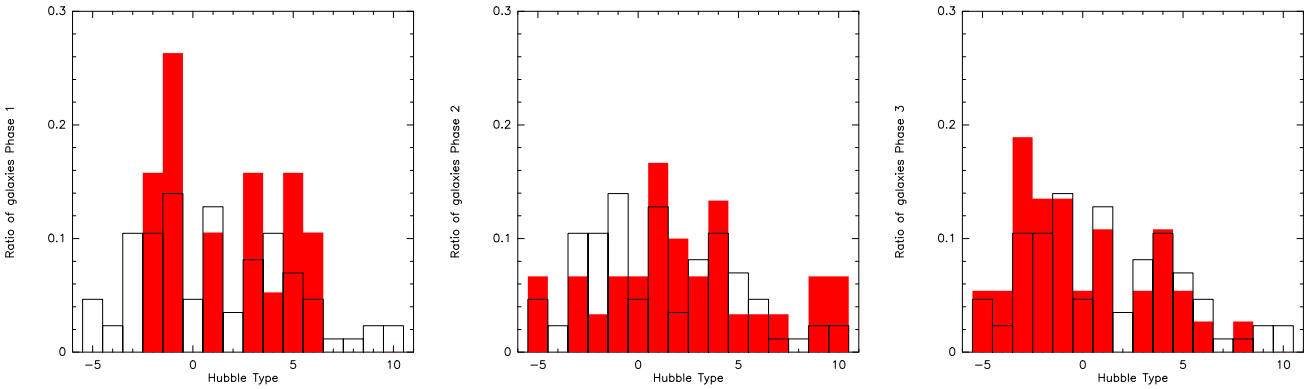


*Figure 2.9: Hubble Type distribution for different evolutionary stages. From left to right, the Hubble type distribution of galaxies in HCGs in evolutionary stage 1, 2 and 3 are plotted. The filled red bins correspond to the distribution for the groups in each evolutionary stage, while the black line bins correspond to the full sample distribution*

In a similar way, we calculated the average Def($M_{H_2}$) and Def($L_{FIR}$) of the galaxies belonging to HCGs in different evolutionary stages, as defined by Borthakur et al. (2010) (Sec. 2.1), which are also detailed in Table 2.7. The Def($M_{H_2}$) of the galaxies increases as the group evolves along the evolutionary sequence if we consider the full sample. Taking into account only the spiral galaxies this trend is only marginally seen, showing that it is mainly due to a changing fraction of ellipticals in the different evolutive stages. The spiral galaxies show, on average, a slight excess of $M_{H_2}$ in all stages. In the case of Def($L_{FIR}$), there is no clear relation for spiral galaxies with the evolutive stage, we only find a trend when considering the total sample, most likely due to a changing fraction of ellipticals.

The importance of morphological type changes is shown in Fig. 2.9, which shows the distribution of the morphological types of the galaxies depending on the evolutionary state of the group. The ratio of elliptical galaxies is much larger in groups on evolution phase 3, so that the average data for the full sample of galaxies in this phase can be strongly affected by this.

Finally, Fig. 2.10 shows the $M_{H_2}$ vs $M_{HI}$ with a color code indicating the evolutionary stage of the group where the galaxies are. We have calculated the average $M_{H_2}/M_{HI}$ ratios for the galaxies belonging to HCGs in the different evolutionary stages. The galaxies may show upper limits in both $M_{H_2}$ and $M_{HI}$, so we have followed a similar procedure as the one followed to calculate the average SFE in Sec. 2.3.2: we have first calculated the average $M_{H_2}/M_{HI}$ taking into account those galaxies showing a lower limit (detected in CO with an upper limit in HI) and, separately, considering those with an upper limit (detected in HI with an upper limit in CO). In both cases we have considered those galaxies detected in both bands and discarded those with an upper limit in both $M_{H_2}$ and $M_{HI}$. In this way, we have found an average value for the $M_{H_2}/M_{HI}$ ratio for the galaxies in Phase 1 HCGs of 1.9±0.7 when considering lower limits (11 galaxies with 2 lower limits) and 0.9±0.3 when considering the upper limits (12 galaxies with 3 upper limits). For the galaxies in Phase 2 HCGs we have found average ratios of 4.3±0.8, when considering lower limits (14 galaxies with 2 lower limits) and 3.2±0.8 when considering the upper limits (15 galaxies with 3 upper limits), which are higher than the ratios for the galaxies in Phase 1 HCGs. The large fraction of galaxies non detected neither in $M_{H_2}$ nor in $M_{HI}$ in Phase 3 HCGs (17 out of 33, with only 5 galaxies detected in both bands) makes the average ratio of this subsample to be highly inaccurate, so we have not consider it in this analysis. Thus, there is an indication that the molecular-to-atomic gas ratio increases with the evolutionary phase.

In summary, we have not found any clear relation between the Def($L_{FIR}$) deficiency with either the HI content of the group nor the evolutionary stage of the group. In the case of Def($M_{H_2}$)

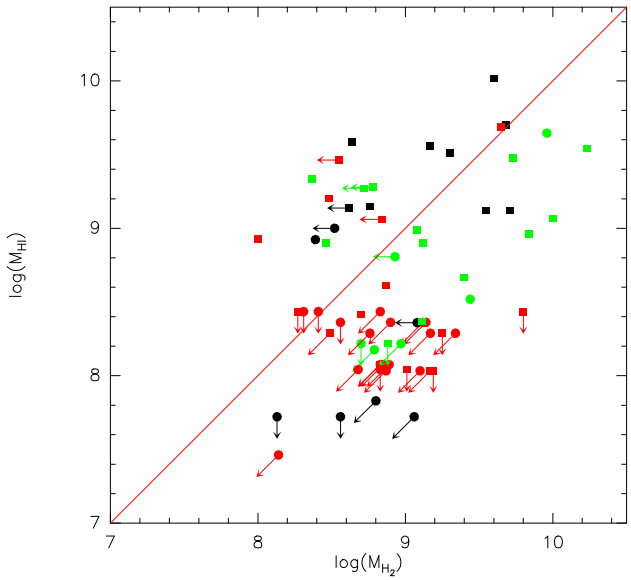


*Figure 2.10: $M_{H_2}$ vs $M_{HI}$ with a color code to indicate the evolutive stage of the HCG where the galaxy is. Signs: Black: galaxies in Phase 1 HCGs; Green: galaxies in Phase 2 HCGs; Red: galaxies in Phase 3 HCGs. The squares represent the late-type (T>0) galaxies and the circles the early-type galaxies. The y=x line is plotted for orientation and does not represent a fit to the data.*

there is no clear relation with the HI content of the group, but there might be a tentative trend of the Def($M_{H_2}$) to increase as the group evolves.

### 2.3.6 SFE and sSFR as a function of the deficiencies of the galaxies

In Fig. 2.11 we display the SFE and the sSFR of the galaxies in our sample as a function of their Def($M_{HI}$) and Def($M_{H_2}$). We see that there is no clear trend of the SFE with the gas deficiency of the galaxies, neither atomic nor molecular. On the other hand, the sSFR is related with the gas deficiency, with a higher sSFR in the galaxies showing a excess of $M_{H_2}$ or $M_{HI}$, as can be seen in Table 2.8. In particular, the trend with $M_{HI}$ is interesting as it suggest that, although the Def($M_{HI}$) of a galaxy has only a weak influence on the absolute SFR, it has a stronger influence on the SFR per stellar mass.

We also note that, in contrast to Tzanavaris et al. (2010), we do not see a gap in the sSFR distribution. They found the sSFR in a sample of 41 galaxies in 12 HCGs, to show a clear bimodality, with a gap in the sSFR distribution between the star-forming galaxies and the quiescent ones. This trend is not seen in our sample (see Fig. 2.11) but it must be taken into account that the sSFRs in Tzanavaris et al. (2010) are calculated, considering Spitzer infrared 24 $\mu$m and Swift UV observations, which gives a more precise measurement, since it takes into account both extincted and unextincted SF tracers. Thus, we would need more sensitive data to set a strong conclusion on the sSFR distribution.

## 2.4 Comparison between HCG and isolated galaxies

There is an intrinsic difference between the AMIGA and the HCG samples that must be taken into account when performing a comparison between both samples: the HCG sample have much more eary-type galaxies (∼45%), whereas 87 % of the AMIGA galaxias are spirals (Fig. 2.12), which can be explained in terms of the morphological type changes due to inter-

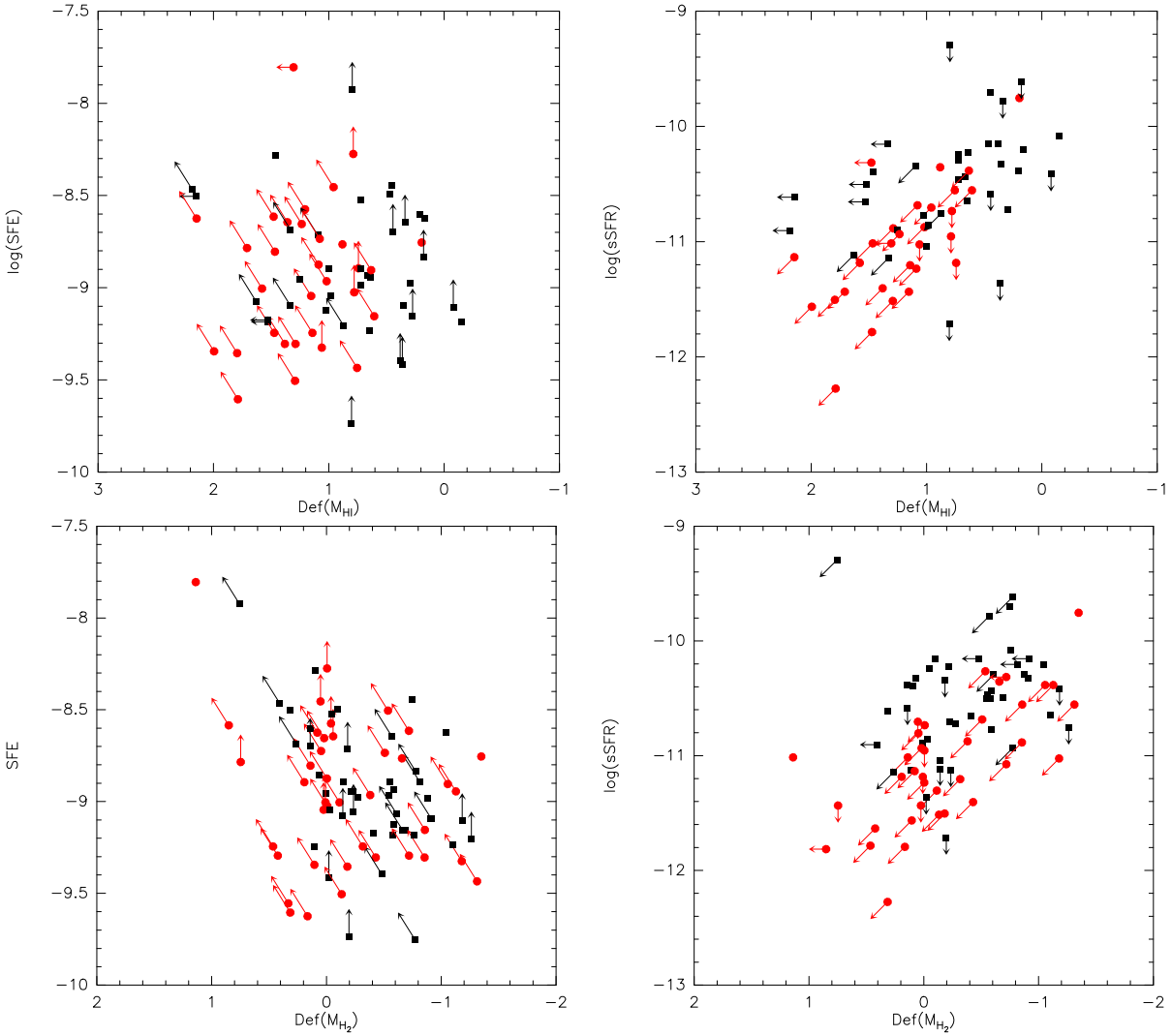


*Figure 2.11: Upper left: Star formation efficiency vs $M_{\rm HI}$ deficiency. Upper right: Specific star formation rate vs $M_{\rm HI}$ deficiency. Lower left: Star formation efficiency vs $M_{\rm H_2}$ deficiency. Lower right: Specific star formation rate vs $M_{\rm H_2}$ deficiency. Signs: Black squares: late-type (T>0) galaxies; Red circles: early-type galaxies.*

*Table 2.8: Average log(sSFR) and log(SFE) depending on Def($M_{\rm HI}$) and Def($M_{\rm H_2}$) for the full sample and the spiral galaxies.*

| | sSFR | | | |
|---|---|---|---|---|
| | Full Sample | $n_{UL}$/n | T>0 | $n_{UL}$/n |
| Def($M_{\rm HI}$) <0.75 | -10.50±0.11 | (8/23) | -10.42±0.10 | (5/19) |
| Def($M_{\rm HI}$) >0.75 | -11.67±0.14 | (28/41) | -10.94±0.13 | (6/16) |
| Def($M_{\rm H_2}$) < -0.25 | -10.73±0.10 | (18/38) | -10.44±0.06 | (6/23) |
| Def($M_{\rm H_2}$) > -0.25 | -11.53±0.15 | (28/43) | -10.93±0.13 | (8/21) |

| | SFE | | | |
|---|---|---|---|---|
| | Full Sample | $n_{UL}$/n | T>0 | $n_{UL}$/n |
| Def($M_{\rm HI}$) <0.75 | -8.87±0.07 | (8/23) | -8.88±0.07 | (5/19) |
| Def($M_{\rm HI}$) >0.75 | -8.86±0.13 | (28/41) | -8.91±0.12 | (6/16) |
| Def($M_{\rm H_2}$) < -0.25 | -8.95±0.06 | (18/38) | -8.99±0.06 | (6/23) |
| Def($M_{\rm H_2}$) > -0.25 | -8.89±0.10 | (24/43) | -8.82±0.11 | (8/21) |

For each subsample, $n$ is the number of galaxies and $n_{UL}$ is the number of upper limits.

actions between galaxies within the groups. In order not to be affected by this difference, we compare only the spiral galaxies.

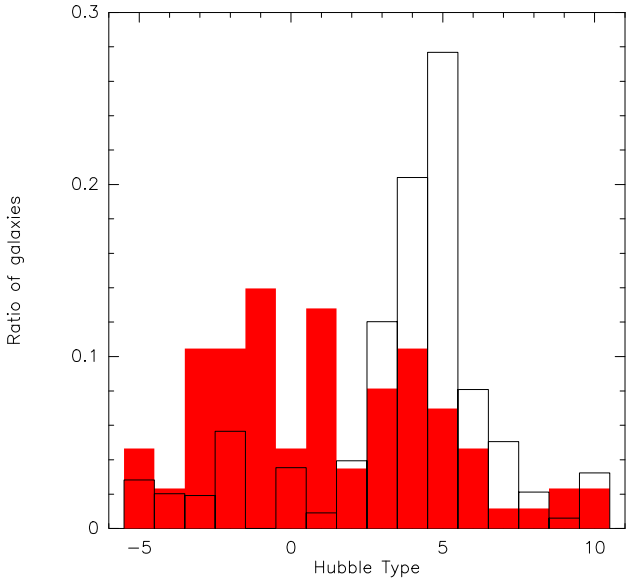


*Figure 2.12: Morphological types for the AMIGA isolated (black line) and HCGs (red filled bars) galaxies*

We have compared the HCG galaxies in our sample with the isolated galaxies in the AMIGA sample. The average values of $M_{H_2}$, $L_{FIR}$ and $L_B$ for the two samples, listed in Table 2.3, show slightly larger values for the HCGs. The difference between the average values of the HCGs and the AMIGA galaxies is larger for $M_{H_2}$ (∼0.7 for spiral galaxies) than for $L_{FIR}$ and $L_B$ (∼0.4 and ∼0.2 respectively, also considering only spiral galaxies). The sample of AMIGA galaxies with available $M_{H_2}$ data is restricted to a velocity range of 1500< $V$ <5000 km s$^{-1}$, while the range of the HCGs extends to larger velocities. Thus, the isolated galaxies are, in average, at a lower distance from us (47 Mpc of average distance versus the 68 Mpc of the HCG sample), which can explain their lower average $M_{H_2}$, since galaxies with a low emission are easier to detect when located at shorter distances. Nevertheless, an intrinsic enhancement of the molecular gas content in HCGs cannot be discarded.

The Def($M_{H_2}$) of the isolated galaxies versus their Def($L_{FIR}$) is displayed in Fig. 2.13. The behavior of the isolated galaxies in this plot do not show a significative difference with the one shown by the HCGs in Fig. 2.3.4.1, with both deficiencies showing a tight correlation. The isolated galaxies show values of the Def($M_{H_2}$) with respect to their Def( $L_{FIR}$) a bit lower than the ones shown by the HCGs, as can be seen when comparing the distribution of the points of both samples around the Def($M_{H_2}$) = Def( $L_{FIR}$) line. This is also reflected in the mean values of Def($M_{H_2}$) and Def( $L_{FIR}$) of AMIGA and the HCGs (Table 2.3): whereas the values of Def( $L_{FIR}$) for spiral galaxies are almost the same for both samples, Def($M_{H_2}$) in spirals is larger by 0.2 for HCG than for AMIGA. This could show a real excess of molecular gas in HCG galaxies. Alternatively, we might have overestimated the molecular gas by our extrapolation (Sec. 2.2.1.3) if the molecular gas extent in HCGs is smaller than in isolated galaxies.

The comparison of the linear regression between $L_{FIR}$ and $L_B$, $M_{H_2}$ and $L_B$ or $M_{H_2}$ to $L_{FIR}$ (Table 2.5) shows no significative differences. In the case of the $L_{FIR}$ versus $L_B$ and $M_{H_2}$ versus $L_B$, the slope and intercept of both samples match within the error bar.

The main difference between HCGs and the AMIGA isolated galaxies is on their $M_{HI}$, where HCGs present $M_{HI}$ deficiencies that are one order of magnitude larger than the ones in $M_{H_2}$ and SFR (Sec. 2.3.4.2).

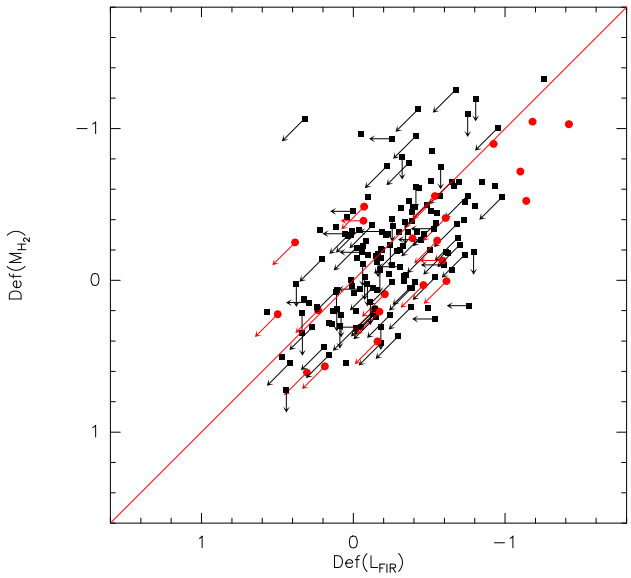


*Figure 2.13: $M_{H_2}$ deficiency vs $L_{FIR}$ deficiency for the isolated galaxies. Signs: Black squares: late-type (T>0) galaxies; Red circles: early-type galaxies. The y=x line is plotted for orientation and does not represent a fit to the data.*

*Table 2.9: Average log(SFE) for different samples and measurements.*

| Sample | log(SFE) (log yr$^{-1}$) | |
|---|---|---|
| | All | T>0 |
| HCGs | -8.78±0.07$^{(1)}$/-9.00±0.06$^{(2)}$ | -8.86±0.05$^{(1)}$/-9.01±0.06$^{(2)}$ |
| CIGs | -8.72±0.03$^{(1)}$/-8.85±0.04$^{(2)}$ | -8.74±0.03$^{(1)}$/-8.87±0.04$^{(2)}$ |
| THINGS* | | -8.68±0.21 |
| HERACLES | | -9.02 |

$^{(1)}$ Values obtained from the galaxies detected in both CO and FIR and galaxies detected in FIR but not detected in CO. $^{(2)}$ Values obtained using galaxies detected in both CO and FIR and galaxies detected in CO but not detected in FIR. (*) Value for 11 galaxies with T=1-5 calculated with the data in Leroy et al. (2008).

We have calculated the average SFE for the AMIGA sample of isolated galaxies, using the $M_{H_2}$ data from Lisenfeld et al. (in prep.) and the $L_{FIR}$ data from Lisenfeld et al. (2007), to compare this value with the one on HCGs. The average SFE of 11 galaxies with T = 1-5 in the THINGS sample (Walter et al. 2008) using IRAS data from Leroy et al. (2008) is also calculated. The SFR we are considering (Eq. 2.7) assumes a Salpeter (1955) Initial Mass Function (IMF), while in Leroy et al. (2008), a Kroupa (2001) IMF is considered. In order to express the SFR as a function of a common IMF, we have converted the THINGS SFE to the Salpeter IMF, applying a correction factor of 1.59, as detailed in the appendix D of Leroy et al. (2008). Finally, we have included also the SFE calculated in Bigiel et al. (2011) for a sample of 30 galaxies in the HERACLES Survey (whose first results can be found in Leroy et al. 2009), calculated from 24$\mu$m data from Spitzer and far ultraviolet maps from the GALEX Nearby Galaxy Survey (Gil de Paz et al. 2007). From the value given in the paper, we have substracted the Helium fraction they included as, as well as for the THINGS SFE, we have converted it from a Kroupa to a Salpeter IMF. All the values are shown in Table 2.9.

A comparison between the average values of the SFE shows no significant difference between the SFE of galaxies in HCGs and the one in isolated or field galaxies, showing there is not a significant dependence of the $M_{H_2}$ to $L_{FIR}$ relation as a result of the environment in HCGs. We must note that, as detailed in Sec. 2.3.2, those galaxies not detected in $M_{H_2}$ nor in $L_{FIR}$ have not

been taken into account to calculate the average SFE. This can explain the fact that, even when the difference on the average $M_{H_2}$ between the HCGs and the AMIGA galaxies is larger than the one in $L_{FIR}$, the samples show similar values of the SFE.

Finally, we have seen it is not common within HCG environments to find interacting galaxies with properties such as LIRGs and ULIRGs, which show much higher SFE (Sanders et al. 1991). Despite the multiple interactions, the properties of the molecular gas does not seem to be very different to normal galaxies.

## 2.5 Is there an evolutionary sequence in the molecular gas content and SFR in HCGs?

In Sec. 2.3.4.2 we have shown that there is a slight relation of the HI deficiency with the deficiency in $M_{H_2}$ and $L_{FIR}$. This partly supports the evolutionary scenario suggested in Verdes-Montenegro et al. (2001), since the HI has been removed more efficiently from the galaxies because of its larger extension, while the molecular gas, which is typically more concentrated in the inner regions, is presumably less affected by the environment. The lower HI mass then might produce a lower $M_{H_2}$ which leads to a lower SFR. However, it is even more noticeable that galaxies with a high HI deficiency can still contain a considerable amount of molecular gas and continue to form stars in a normal way (which is shown by the good correlation between the $M_{H_2}$ and $L_{FIR}$ deficiences). This SF is not expected to last very long because once the molecular gas is used up, no HI is available to provide fuel for future SF.

As can be seen in Fig. 2.8, the galaxies with lower HI deficiencies tend to show a higher $L_{FIR}$ and, especially, a higher $M_{H_2}$. This trend might suggest that two mechanisms are at play. First, the large $M_{HI}$ deficiency can be interpreted within a scenario in which a galaxy entering the groups loses part of its HI as a result of mostly tidal stripping, as suggested by the Verdes-Montenegro et al. (2001) evolutionary model. On the other hand, the HI to $H_2$ conversion could be enhanced as a result of the continuous interactions between galaxies. This enhancement of the $H_2$ formation can not explain the highest values of the HI deficiency, but could explain the lack of HI in the galaxies with lower HI deficiencies, and agrees with the model proposed by Rasmussen et al. (2008), who suggests this process as complementary to the HI ionization in the IGM to explain the larger HI deficiencies that the galaxies in HCGs show with respect to the deficiency of the whole group. The higher $M_{H_2}/M_{HI}$ ratios found for the galaxies in Phase 2 HCGs when compared to those in Phase 1 can be also interpreted as a result of an enhancement of the atomic to molecular gas conversion rate.

Considering these two mechanisms at play, we can suggest an scenario on which the galaxies would originally have $\mathrm{Def}(M_{HI}) = 0$ and $\mathrm{Def}(M_{H_2}) = 0$. Then, the tidal interactions would enhance the conversion from atomic to molecular gas at the same time they strip the HI from the galaxies, which would lead to $\mathrm{Def}(M_{HI}) > 0$ and $\mathrm{Def}(M_{H_2}) < 0$. Finally, the multiple interactions within the group would strip the main part of the HI in the disks of the galaxies, resulting in a $\mathrm{Def}(M_{HI}) >> 0$ and, as a consequence of the lack of HI to form $H_2$, a positive value of the $\mathrm{Def}(M_{H_2})$.

## 2.6 Conclusions

We analyzed data for $M_{H_2}$, $L_{FIR}$ and $M_{HI}$ for 86 galaxies in 20 compact galaxy groups. The results of our study can be summarized as follows:

- We find a slight $M_{H_2}$ enhancement in HCGs relative to AMIGA isolated galaxies with spiral galaxies showing an excess (Def($H_2$) = -0.22±0.09). The mean deficiency of $L_{FIR}$ of galaxies in HCGs (Def($L_{FIR}$) = 0.11±0.08 for spiral galaxies) is similar to the one of the AMIGA galaxies. The $M_{HI}$ deficiency is much larger than deficiencies in $M_{H_2}$ and $L_{FIR}$ with a mean value of 0.93±0.13 for spiral galaxies.

- The correlation between $M_{H_2}$ and $L_{FIR}$ found for galaxies in other environments is also shown by our sample. $M_{H_2}$ and $L_{FIR}$ deficiencies are also tightly correlated.

- There is a trend for $M_{H_2}$ and $L_{FIR}$ deficiencies to increase with the $M_{HI}$ deficiency of the galaxies. This trend is not followed when considering the $M_{HI}$ deficiency of the groups. There is a slight $M_{H_2}$ excess in the least HI deficient. This suggests a larger HI to $H_2$ conversion rate in HCGs as complementary to the HI stripping due to interactions. The $M_{H_2}$ deficiency shows a tentative trend to increase as the group evolves, while the $L_{FIR}$ deficiency shows no clear relation with the evolutionary stage of the group.

- The SFE of the galaxies in the HCGs is not significantly different from the one in isolated or field galaxies, so we have not found the SFE to be affected by the environment in HCGs. We have found no relation of SFE with neither Def($M_{HI}$) nor Def($M_{H_2}$).

- There is a trend of the sSFR to increase with decreasing Def($M_{HI}$) and with decreasing Def($M_{H_2}$).

# Chapter 3
# An individual study of gas content and star formation: HCG40 and HCG79

*tanto ch'i' vidi de le cose belle*
*che porta 'l ciel, per un pertugio tondo.*

*E quindi uscimmo a riveder le stelle.*

**Dante Alighieri** - Inferno · Canto XXXIV

In this chapter, we present a detailed study of two HCGs of our sample, HCG40 and HCG79, focusing on their molecular gas content, the star formation processes and their relation with galactic and group evolution. The data from the 30m telescope and IRAS shown in former sections are complemented with data from the Owens Valley Radio Observatory (OVRO) interferometer and the Spitzer Space Telescope. The Spitzer data give us a better angular resolution and sensitivity than the previously shown data from the IRAS satellite (Chap. 2), which allow us to study the SF taking place within the galaxies. Looking for a better understanding of the SF going on in the groups and its relation to the molecular and atomic gas content of the galaxies, we have studied the star formation rate, its relation to the stellar mass and the star formation efficiency of the galaxies using these data. The study is complemented with HI maps of the groups from VLA, which gives us information about the atomic gas content and distribution of the galaxies and the evolutive stage of the group.

## 3.1 The groups

The groups observed with OVRO were HCG40 and HCG79. These two groups are the ones with highest compactness (as defined by Hickson 1982, who found an average surface brightness of 21.2 and 20.5 mag arcsec$^{-2}$ for HCG40 and HCG79, respectively), and show a low velocity dispersion, below the average of our HCGs sample, leading the galaxies within the group to experience a strong interaction between them. In Fig. 3.1 we display the distribution of the surface brightness averaged over the area of the full group for the 20 HCGs in our sample, to show that HCG79 and HCG40 have the highest compactness. Furthermore, these two groups have been found to show a high degree of isolation from the galaxies in their environment (Durbala et al. 2008, Verdes-Montenegro et al., in prep). Thus, the features that make HCGs interesting targets to study (high density of galaxies, isolation from the environment and low

velocity dispersion) are present in these 2 groups in an extreme way, making them particularly interesting objects out of our full sample of 20 HCGs.

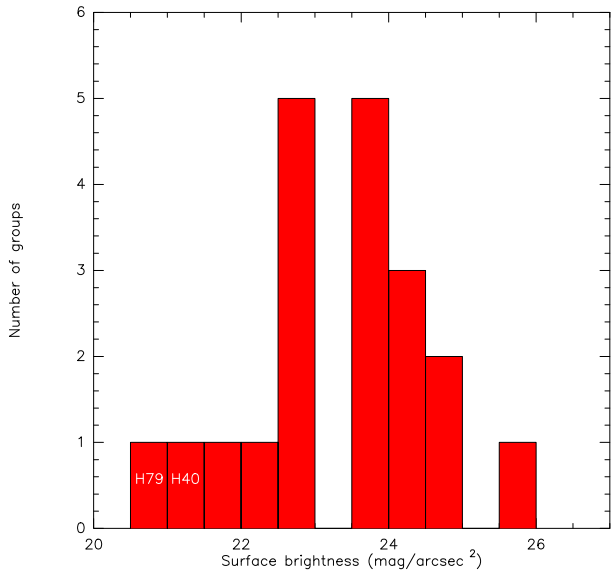


*Figure 3.1: Distribution of the total magnitude of the HCGs averaged over the area of the group (in arcsec) for the HCGs in our full sample. The data are taken from Hickson (1982).*

### 3.1.1 HCG 40

In Fig. 3.2 we display an optical image of HCG40 from the Subaru telescope, which is probably the best optical image available of this group. HCG40 is composed of five galaxies. Three of them are classified as early-type galaxies, as can be seen in Tab. 3.1, where the compilation of the morphologies and nuclear activity of the galaxies in HCG40 is displayed. The median velocity of the group is 6572 km $s^{-1}$, and the velocity dispersion of the galaxies is 177 km $s^{-1}$. Martínez (2008), who studied the nuclear activity in a sample of 65 HCGs using the Kewley et al. (2006) criteria, found 40e to host an AGN and 40c and 40d to be transition objects, with the other galaxies in the group showing no signs of nuclear activity.

Although VM01 found HCG40 to be the most HI deficient group in their sample, new observations of the group (Borthakur et al. 2010) using a larger bandwidth have detected a HI mass almost 5 times larger, so the group is finally classified as slightly HI deficient. In the evolutionary sequence model of Verdes-Montenegro et al. (2001), it was initially classified as very evolved (Phase 3a) due to the low HI content detected in the disks of the galaxies, but new VLA observations performed with a wider velocity range (Verdes-Montenegro et al., in prep.) have detected a larger amount of atomic gas in the galaxies, which set HCG40 in a less evolved stage. Rasmussen et al. (2008) suggested, based on the extended intense X-ray emission they observed in HCG40, that it could be one of the spiral-rich groups with a hot IGM, which are not very common. Nevertheless, the high compactness of the group makes it hard to exclude the individual galaxies as the only sources of the X-ray radiation.

Table 3.1: Basic data, Hubble type and nuclear activity classification of the galaxies in HCG40 and HCG79

| Galaxy | Vel. | $B_c^T$ | B-R | Hubble type | | | | Nuclear activity | |
|---|---|---|---|---|---|---|---|---|---|
| | (km $s^{-1}$) | (mag) | (mag) | NED | LEDA | Sulentic | Durbala | Martinez | Durbala |
| 40a | 6481 | 13.38 | 1.75 | E | E | S0 | | | |
| 40b | 6676 | 14.62 | 1.84 | SA0 | E-S0 | S0 | | | |
| 40c | 6264 | 14.60 | 2.00 | SBb | Sab | Sb | | TO | |
| 40d | 6429 | 14.53 | 1.56 | SB0a | S0a | S0a | | TO | |
| 40e | 6305 | 16.58 | 1.84 | SAB | Sa | Sbc | | AGN | |
| 79a | 4115 | 14.49 | 1.60 | Sa | S0 | E/S0 | E3 | TO | AGN |
| 79b | 4369 | 14.09 | 1.44 | S0 | S0 | S0 | S0 | TO | AGN |
| 79c | 4352 | 14.98 | 1.27 | S0 | S0 | S0 | S0 | | |
| 79d | 4501 | 15.16 | 0.85 | SBc | Sc | Sd | Sd | AGN | |

The morphologies listed are the ones compiled from NED and LEDA, the one set by J. Sulentic (private communication) and the one from Durbala et al. (2008). The nuclear activity classifications are taken from Martínez (2008) and Durbala et al. (2008), where TO stands for *Transition Object*.

### 3.1.2 HCG 79

HCG79 is not only the HCG with the highest compactness, but also one of the most isolated groups of galaxies. An optical image of the group taken by the Hubble Space Telescope is presented in Fig. 3.3 for a better understanding of the description of the group. In spite of being known as Seyfert Sextet, HCG79 has only 4 members. 79f, not included in the original Hickson catalogue (1982), is not considered as a galaxy, but as a tidal tail that lies to the NE of 79b. Even though Hickson (1982) did not classify it as a galaxy, the RC3 catalog (de Vaucouleurs et al. 1991) lists it as a galaxy with designation NGC6027e. Thus, it is usually referred to as 79f, independently of whether the authors consider it to be a real galaxy or not. Following this convention, we design it as 79f, even though we are not considering it to be a real galaxy. 79e, included by Hickson (1982), is an almost face-on spiral located at the southern part of 79b. It was discarded as a member of the group after the redshift measurements of Hickson et al. (1992), who found it to be a background galaxy with v$\sim$20000 km $s^{-1}$, in contrast to a group average velocity of 4398 km $s^{-1}$. The velocity dispersion of the group is 128 km $s^{-1}$. The galaxies in HCG79 are embedded in a massive luminous halo, which contains a significant fraction of the luminosity and stellar mass of the group and implies strong former stripping processes. The 4 real members of HCG79 are classified into three early-type lenticular galaxies and one late-type galaxy (see Tab. 3.1).

Durbala et al. (2008) found 79a and 79c to show evidence for nuclear activity at radio, mid-infrared and optical wavelengths. Martínez (2008), based in the Kewley diagnostic criteria already mentioned, set these two galaxies as transition objects and found 79d to host an AGN.

The properties of HCG79 have been studied in detail by Durbala et al. (2008). Based on the higher luminosity fraction contained in the group halo, they set HCG79 as a highly evolved compact group, with evidences for past accretion events and a low atomic gas fraction. They found 79a, 79b and 79c to have been physically related for a long time and to be the result of a sequential acquisition process. The last galaxy to enter the group is, according to them, 79d, which is at the present entering the group and shows no clear signs of interaction with the other members of the group. As a result, almost all the HI detected in HCG79 is contained in the disk of this new-entering galaxy 79d. The model by VM01 detailed in Chap. 2 establishes the evolutionary stage of a group as a function of the ratio of atomic gas contained in the disks of the

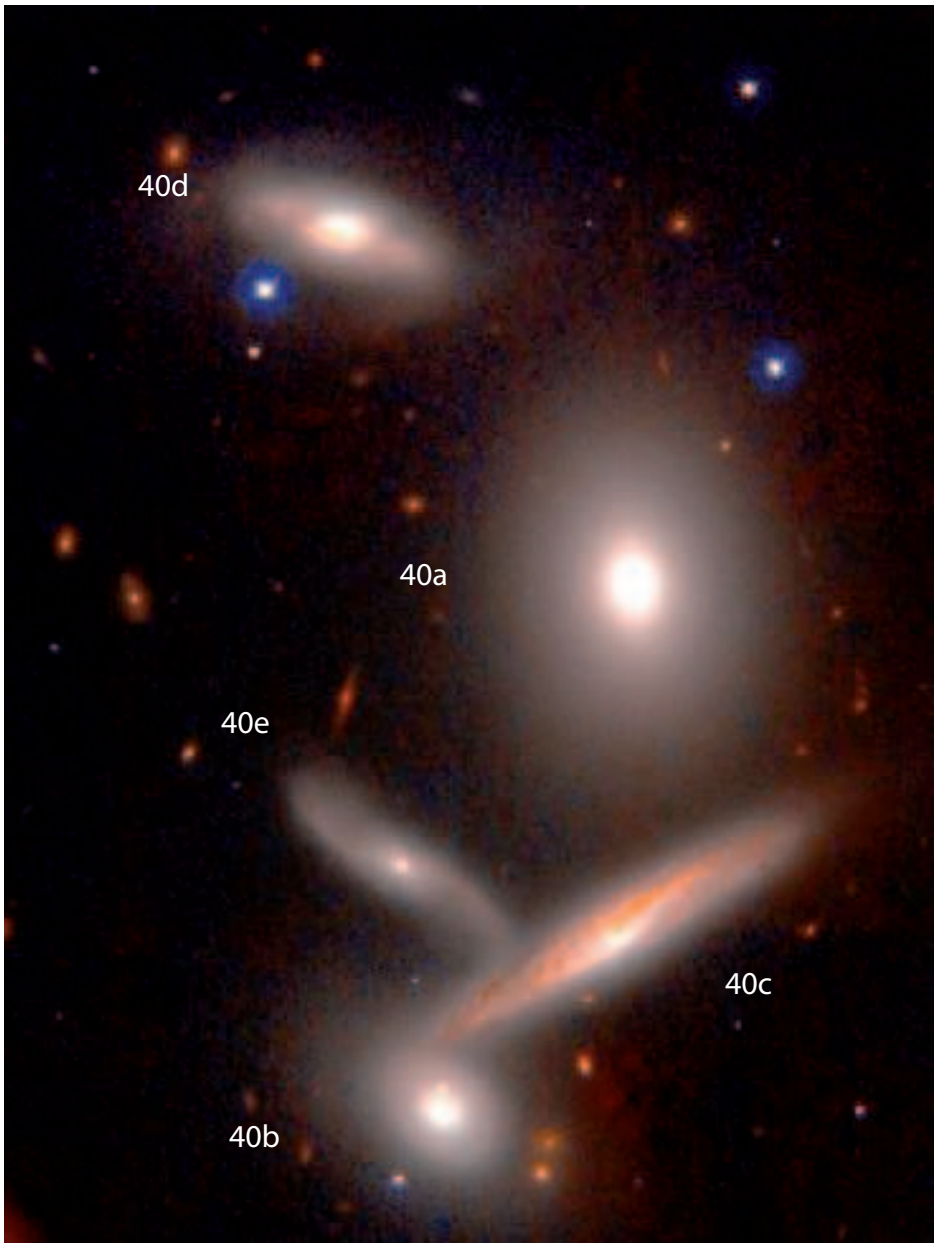


*Figure 3.2: Optical image (combined J and K' bands) of HCG40 taken with the the Subaru telescope. Field of view is 1.9 × 2.9 arcmin. The Subaru telescope is operated by the National Astronomical Observatory of Japan.*

galaxies with respect to the full content of HI of the group. Thus, following this classification, HCG79 is classified in the first evolutionary phase.

## 3.2 Interferometric CO(1-0) observations

To completement the single-dish observations detailed in Chap. 2, we present here the analysis of interferometric observations of HCG40 and HCG79 performed with the Owens Valley Radio Observatory (OVRO) interferometer. The main goal of the observations is to study how the molecular gas distribution is affected by interactions such as tidal disruptions, that are expected in such compact and dense environments. We also aim to study its relation with the SFR, studied from Spitzer IR observations.

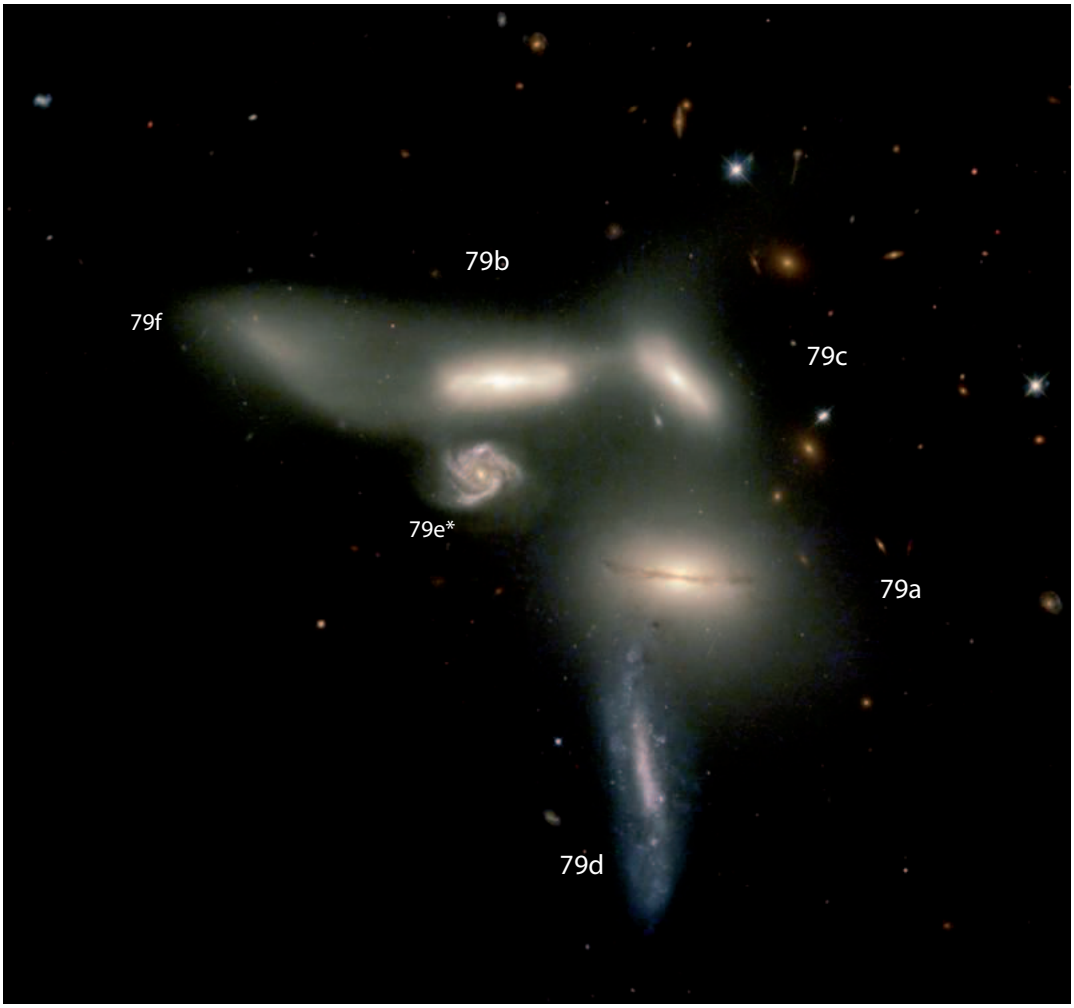


*Figure 3.3: Optical image of HCG79 from the Hubble Space Telescope, observed with the UBVI filters of the Wide Field Planetary Camera 2. The field of view is 2.5 × 2.5 arcmin. (*) 79e is a background galaxy not physically related to the group. 79f is not considered in our work as a galaxy, but as a tidal tail. Image credits: NASA, C. Palma, S. Zonak, S. Hunsberger, J. Charlton, S. Gallagher, P. Durrell (The Pennsylvania State University) and J. English (University of Manitoba).*

### 3.2.1 Observations and data reduction

The OVRO interferometer was an array consisting on six 10.4 meter antennas designed to observe in the millimeter range located near Bishop, California and operated by the California Institute of Technology (Caltech). Before it was relocated to become part of CARMA at a higher altitude site in 2004, OVRO was able to reach baselines up to ∼1 km in its most extended configuration.

The observations of HCG40 and HCG79 were carried out using two different interferometer configurations for each group: the E configuration, with baseline lengths from 35 to 119 meters, and the L configuration, with baseline lengths from 15 to 115 meters. The schemes of the configurations are shown in Fig.3.4. The primary beam FWHM of the telescope at this frequency is 62.5″, which corresponds to the field of view for each pointing. The synthesized beam has a size of 5.03″× 3.95″ for HCG40 and 3.84″× 3.51″ for HCG79.

The spectral window was centered at the 115.271 GHz CO(1-0) emission line. The correlator was configured in 2 sidebands with a bandwidth of approximately 500 MHz each. The sidebands were separated into 4 different sections. Each of these sections were divided into 32

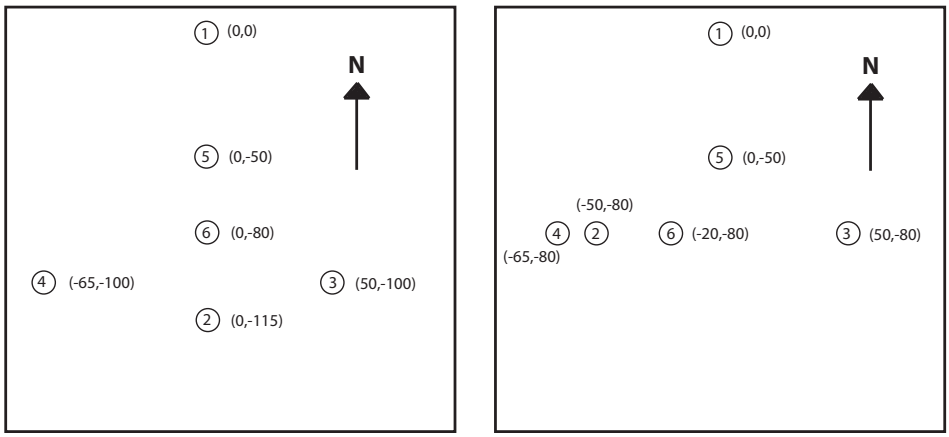


*Figure 3.4: Scheme of the OVRO configurations. Left: E configuration. Right: L configuration. The distances are expressed in meters.*

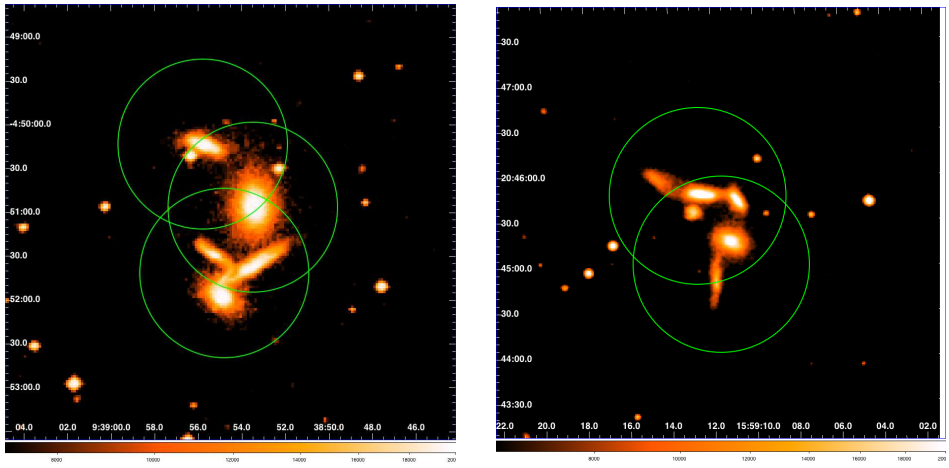


*Figure 3.5: Overlays of the OVRO primary beam over B-band images of HCG40 (Left) and HCG79 (Right).*

channels. The spectral resolution is given by the width of these channels, 4 MHz in our case, which corresponds to 10.8 km s$^{-1}$. There was a 16 MHz overlap between sections and an overlap of approximately 50 MHz between sidebands.

HCG79 was observed in 2 different tracks. Since the group is larger than the field of view of the interferometer in these configurations, the group was covered with a 2-pointing mosaic, one covering 79a+d and other for 79b+c (see Fig. 3.5). The observing strategy was switching from one pointing to the other along both tracks instead of dedicating the full track to a single pointing. All the target scans were 5 minutes long. The details of the tracks are listed in Table 3.2, and the $u$-$v$ coverage of the combined tracks is shown in Fig. 3.6.

HCG40 was observed in 3 different tracks. In this case, a 3-pointing mosaic was required to map the full group, with the pointings covering 40a, 40b+c+e and 40d respectively with the same integration time (5 minutes) as for HCG79 (see Fig. 3.5). The observation strategy was similar to the one used for HCG79, with the three targets observed in all the tracks, switching from one to another. The details of the tracks are also listed in Table 3.2. The quality of the data achieved during the track 3541, with a high median system temperature, was very poor, so we finally discarded them. The $u$-$v$ coverage achieved with the two tracks considerd in the analysis is shown in Fig. 3.7.

*Table 3.2: Details of the OVRO observing tracks*

| Track | Date | Target | Configuration | $T_{sys}$ (K) | Integrations *(Total/On target)* |
|---|---|---|---|---|---|
| 3443 | March 7th, 1997 | HCG79 | E | 513 | 126/76 |
| 3573 | April 30th, 1997 | HCG79 | L | 511 | 129/68 |
| 3541 | April 30th, 1997 | HCG40 | E | 826 | 26/0 |
| 3541(*) | April 20th, 1997 | HCG40 | E | 805 | |
| 3617 | May 21th, 1997 | HCG40 | L | 467 | 132/61 |

(*) The information on the number of integrations in this track is not listed in the observations log

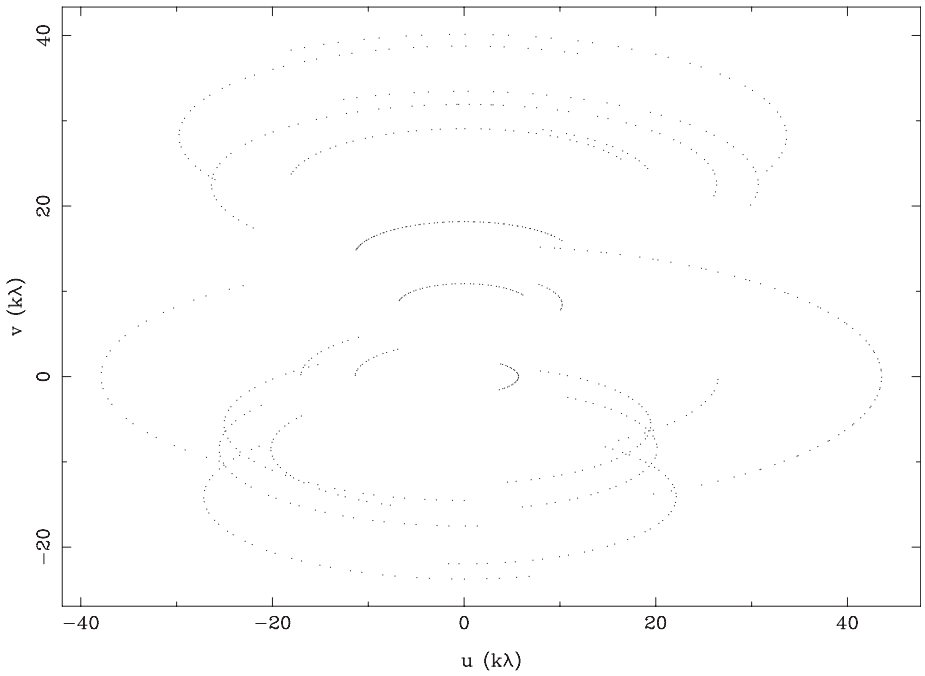


*Figure 3.6: u-v coverage of the OVRO observations corresponding to HCG79*

The coordinates of the different pointings of the mosaic are listed in Tab. 3.3.

The observation scheme was the same for the two groups. The passband calibrator was observed at the very beginning of the track. The main part of the observations consisted of an integration on each of the gain calibrators followed by two (for HCG79) or one (for HCG40) integrations on each target. This cycle was repeated until the end of the track, when the flux calibrators were observed.

Taking into account only the sideband where the emission was expected to be found, the sections were calibrated separately before merging them into a single file for each pointing. The calibration process, performed with the *mma* software (Scoville et al. 1993), followed the next steps:

- Flux density, applying the flux scale set from the calibrators listed in Tab.3.4. This calibration was already applied to the data released to us. The use of 3c273, a variable QSO, as flux calibrator was possible due to a daily tracking of its flux by observing it along with the planets Uranus and Neptune.

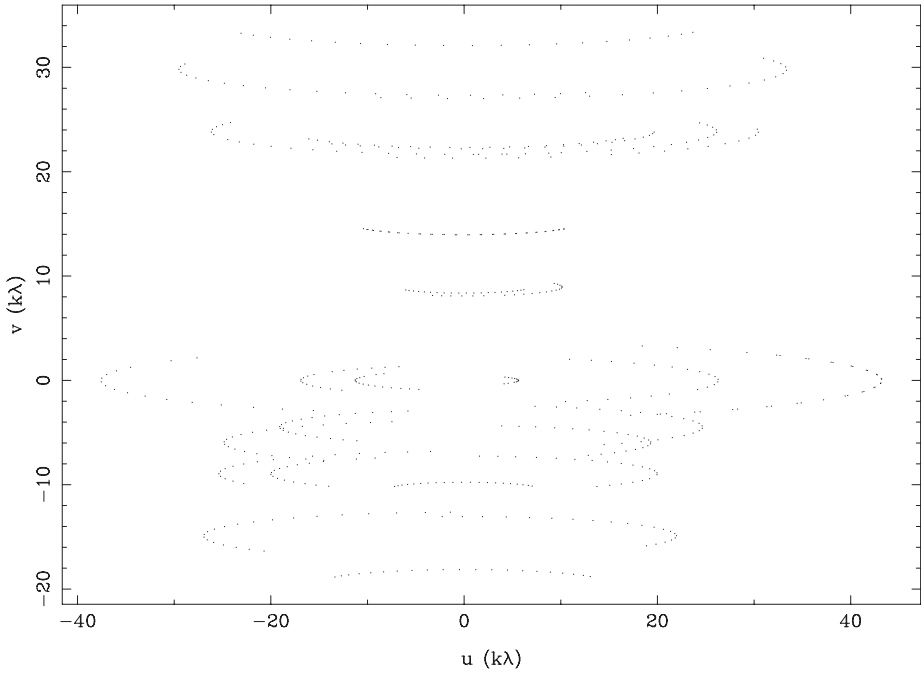


*Figure 3.7: u-v coverage of the OVRO observations corresponding to HCG79*

*Table 3.3: OVRO target pointings coordinates.*

| Sources | RA | DEC |
|---|---|---|
| 40a | 09:38:53.5 | -04:50:56.4 |
| 40bce | 09:38:54.7s | -04:51:41.2 |
| 40d | 9:38:55.7 | -04:50:13.9 |
| 79ad | 15:59:11.5 | +20:45:01.2 |
| 79bc | 15:59:11.9s | +20:45:47.1s |

- Flagging of different integrations. It was performed after visual inspection of the amplitude and phase plots for each baseline, looking for possible coherence loss. The phase noise (related to the de-correlation of the signal as a result of its path through the atmosphere) is, together with the thermal noise (traced by the $T_{sys}$), responsible for the noise in the data. Thus, in this process, we aim to minimize the effect of the phase de-correlation on the quality of the calibrated data.

- Passband calibration, applying the calibration scheme corresponding to low spectral resolution. This calibration is applied to avoid the effects coming from the different responses of the receivers depending on the frequency.

- Time-dependent gain calibration, performed separately for phase and amplitude. In both cases (phase and amplitude), the calibration was antenna-based, which is preferred to the baseline-based in case of low S/N ratio, as in our case. Since we chose a time-dependent calibration, the gain fit is derived as a function of time, not as a function of the elevation of the calibrator, as in the case of the elevation-dependent calibration.

Table 3.4: Calibration sources for the OVRO observations

| | HCG 40 | HCG 79 |
|---|---|---|
| Gain calibrators | 1546+027 1611+343 | 0829+046 1055+018 |
| Passband calibrators | 3c273 | 3c273 3c286 |
| Flux calibrator | Uranus | 3c273 |

To finish the calibration process, the spectra of the gain calibrators and the sources were revised to check the fit applied by the passband and gain calibration. At this point, data from the different tracks were combined into a single file for each pointing. With these files we started the imaging process with the Miriad [1] software, following a standard 3-steps process:

- Mosaicing: generating the dirty image from the UV visibilities with the INVERT task. We applied no gaussian taper. We chose a natural weighting since it provides the best overall sensitivity and a good sensitivity to extended emission. For each section, we create 7 images with a width of 43.5 km $s^{-1}$, joining 4 channels on each of them. The pixel scale chosen was 0.5 arcsec/px. This step was also used to generate a single mosaic image from the several pointings (2 in case of HCG79 and 3 in the case of HCG40), just setting the different pointings as inputs of the task at the same time. Thus, at this point the data for a full group are contained in a single file for each section, getting for each group 4 full-field maps (one per section) with 7 channels each.

- Cleaning: producing the clean components map. There are two tasks on Miriad to do this process: MOSSDI and MOSMEM. We used both, finding no differences between them. The clean maps that we finally used were the ones generated with the MOSSDI task, which deconvolves the mosaiced dirty images using a Steer, Dewdney & Ito (SDI) CLEAN algorithm. A primary beam correction was automatically applied in this process.

- Restoring: generating the clean map and the synthesized beam (with the sizes detailed above) with the RESTOR task.

The reduced data were converted into the FITS format and exported to AIPS[2], where the four 7-channels sections were merged into a single 28-channels datacube for each group, being ready to start their analysis.

The average rms of the channels, calculated averaging the rms of 3 emission-free regions at 6 different channels, is 18.6 mJy/beam for HCG40 and 14.5 mJy/beam for HCG79. When the observations were planned, a sensitivity of 5.6 mJy/beam was expected after 2 8-hours tracks. The total integration time finally reached for each pointing was lower than planned and the weather conditions were not good enough either, so the sensitivity level achieved is around three times worse.

### 3.2.2 Data analysis

To perform the analysis of the data, we produced channel maps, 0-moment maps and position-velocity diagrams. For each group, we examined first the emission of the galaxies in

[1] http://carma.astro.umd.edu/miriad/

[2] AIPS is produced and maintained by the National Radio Astronomy Observatory, a facility of the National Science Foundation operated under cooperative agreement by Associated Universities, Inc.

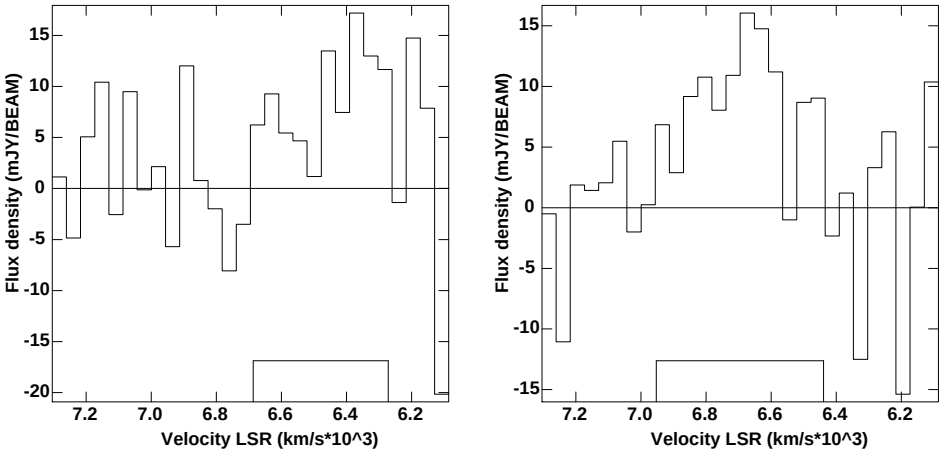


*Figure 3.8: CO(1-0) emission of 40c (left) and 40d (right) from OVRO*

the channel maps. We also looked for emission in a position-velocity diagram along different axis across the galaxy using KARMA[3]. Only the emission that showed continuity across several channels was considered, discarding weak emission present only in one channel, or not connected to other emission features in the position-velocity diagram.

With AIPS, we generated the spectrum of a spatial region of the image, selecting over the datacube the area with emission features in the 0-moment map. This way we compared the emission spectra of the galaxies detected with OVRO with the one achieved with the 30m radiotelescope, either coming from our own observations or from Leon et al. (1998), to be sure that the detection windows coming from both telescopes matched up.

After this analysis, we found none of the galaxies in HCG79 to show clear emission above the noise level. For HCG40, studying the channel maps and the position-velocity diagrams, we found two galaxies with detected emission: 40c and 40d. Their spectra are shown in Fig. 3.8. These spectra were obtained using the ISPEC task in AIPS over a square region containing emission above $3\sigma$ for each galax y. The 0-moment contours for HCG40 are displayed in Fig. 3.9 over an optical image of the group. The contours are set at 3 and $4\sigma$. No emission above $5\sigma$ was found. The feature at 4 $\sigma$ close to the center of 40a, which looks like real emission from the galaxy was discarded after revising the channel maps and the position-velocity diagram since the possible emission features showed a difference of $\sim$ 700 km s$^{-1}$ with the optical velocity of the galaxy. The channel maps for the detected galaxies are shown in Fig. 3.10 and 3.11.

For the detected galaxies, we integrated the emission in velocity (over the spectral detection window) and surface (on the area within the $3\sigma$ contour level). In the case of the non-detected galaxies, the flux upper limit is calculated from the rms using the following formula:

$$\mathrm{Flux(Jy)} < 3 \times \mathrm{rms(Jy\,beam^{-1})}\sqrt{\Delta \mathrm{v}\Delta \mathrm{v_{channel}}}\sqrt{\frac{\mathrm{Area}}{(\mathrm{Area})_{\mathrm{beam}}}} \tag{3.1}$$

where $\Delta$v is the width of the detection window of each galaxy in the 30m telescope observations, and $\Delta\upsilon_{\mathrm{channel}}$ is the width of each OVRO channel. In case there was no detection in the 30m either, we use a default window with $\Delta \mathrm{v} = 300$ km $s^{-1}$. The area used was the SF area of each galaxy, taken as the area within the $5\sigma$ contour of the $8\mu$m emission map (see Sec. 3.3).

[3]http://www.atnf.csiro.au/computing/software/karma/

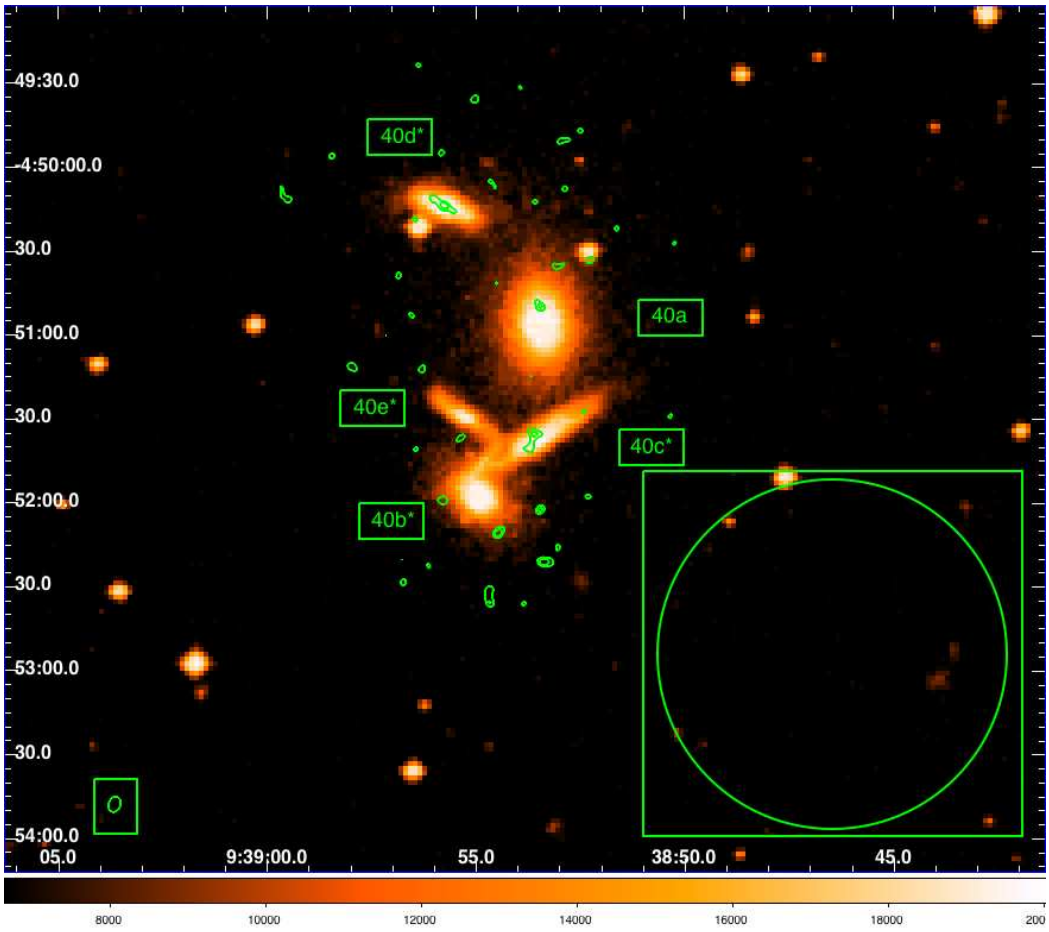


*Figure 3.9: Overlay of OVRO contours on optical (B band) image of HCG40 from the ESO Online Digitized Sky Survey. The field of view is the result of overlapping three circles with a diameter of 62.5 arcsec each, as the one in the bottom right corner. The contour levels are set at 3σ and 4σ. The galaxies whose name is flagged with an * were detected with the 30m telescope.*

$(Area)_{beam}$ is the area of the synthesized beam: 22.5 arcsec$^2$ for HCG40 and 15.2 arcsec$^2$ for HCG79.

### 3.2.3 Results

To calculate $M_{H_2}$ from the integrated flux, we have used the formula by Sanders et al. (1991) (Appendix A in the original work), adapted to our value of $N_{H_2}/\ I_{CO}$:

$$M_{H_2} = \frac{2}{3}(1.18 \times 10^4) Flux \times D^2 \tag{3.2}$$

where the flux is expressed in Jy km $s^{-1}$ and D is the distance to the source in Mpc. The factor $\frac{2}{3}$ is introduced to correct the different $N_{H_2}/I_{CO}$ ratio we assume, which is X=$N_{H_2}/\ I_{CO} = 2\times10^{20}$cm$^{-2}$ (K km s$^{-1}$)$^{-1}$ (e.g. Dickman et al. 1986).

The $H_2$ masses obtained with OVRO for all the galaxies are listed in Table 3.5, together with values derived from the 30m observations (with no aperture correction, see Chap. 2.2.1.3). We also list the integrated flux, together with the velocity window and the area the emission was integrated within. The area is expressed in terms of the interferometer synthesized beam areas detailed above.

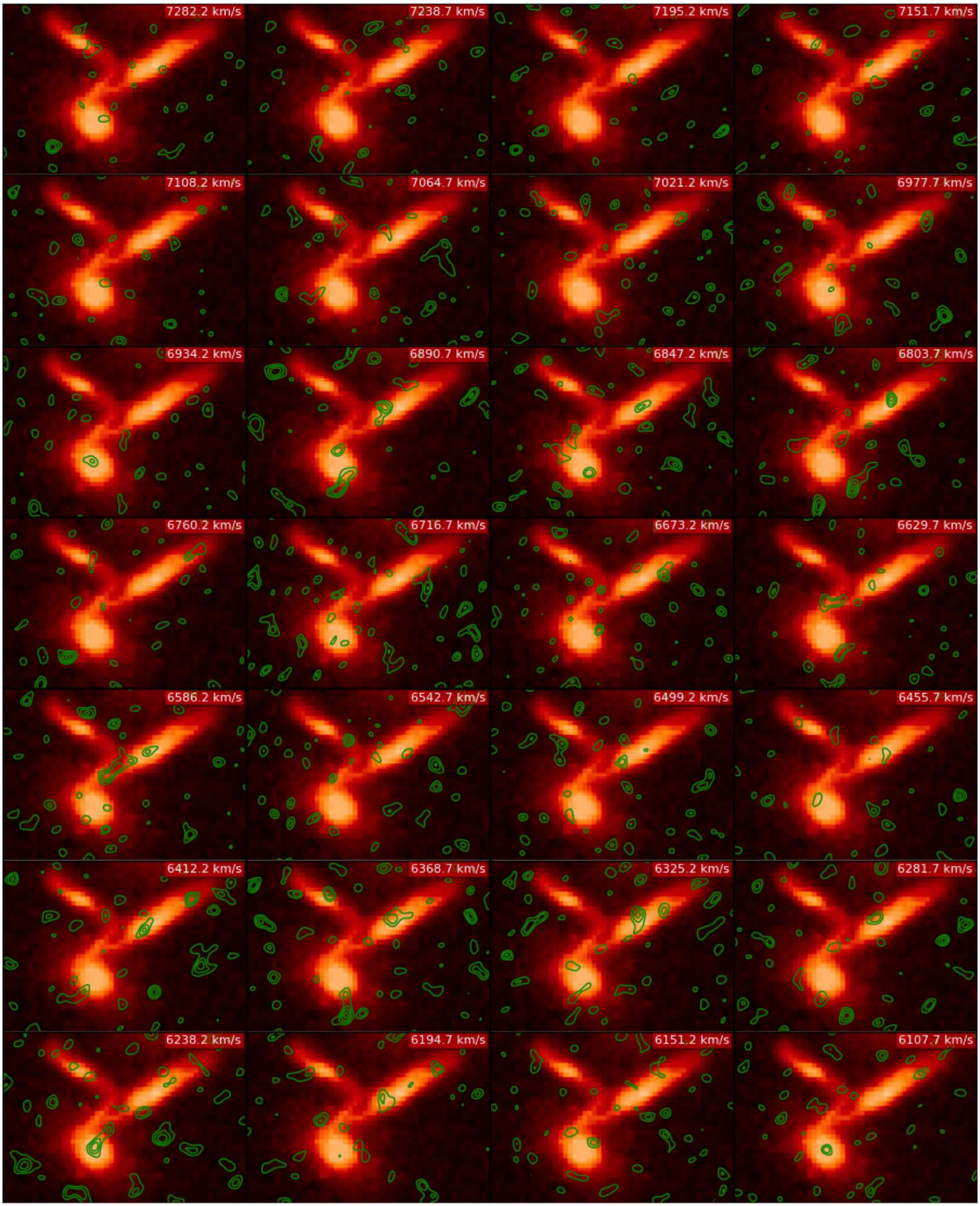


*Figure 3.10: Channel maps of the CO(1-0) emission of 40c (40b&e are also shown) over the B-band image. Emission is present from 6629 to 6194 km $s^{-1}$. The contour levels are at 2, 3 and 4$\sigma$.*

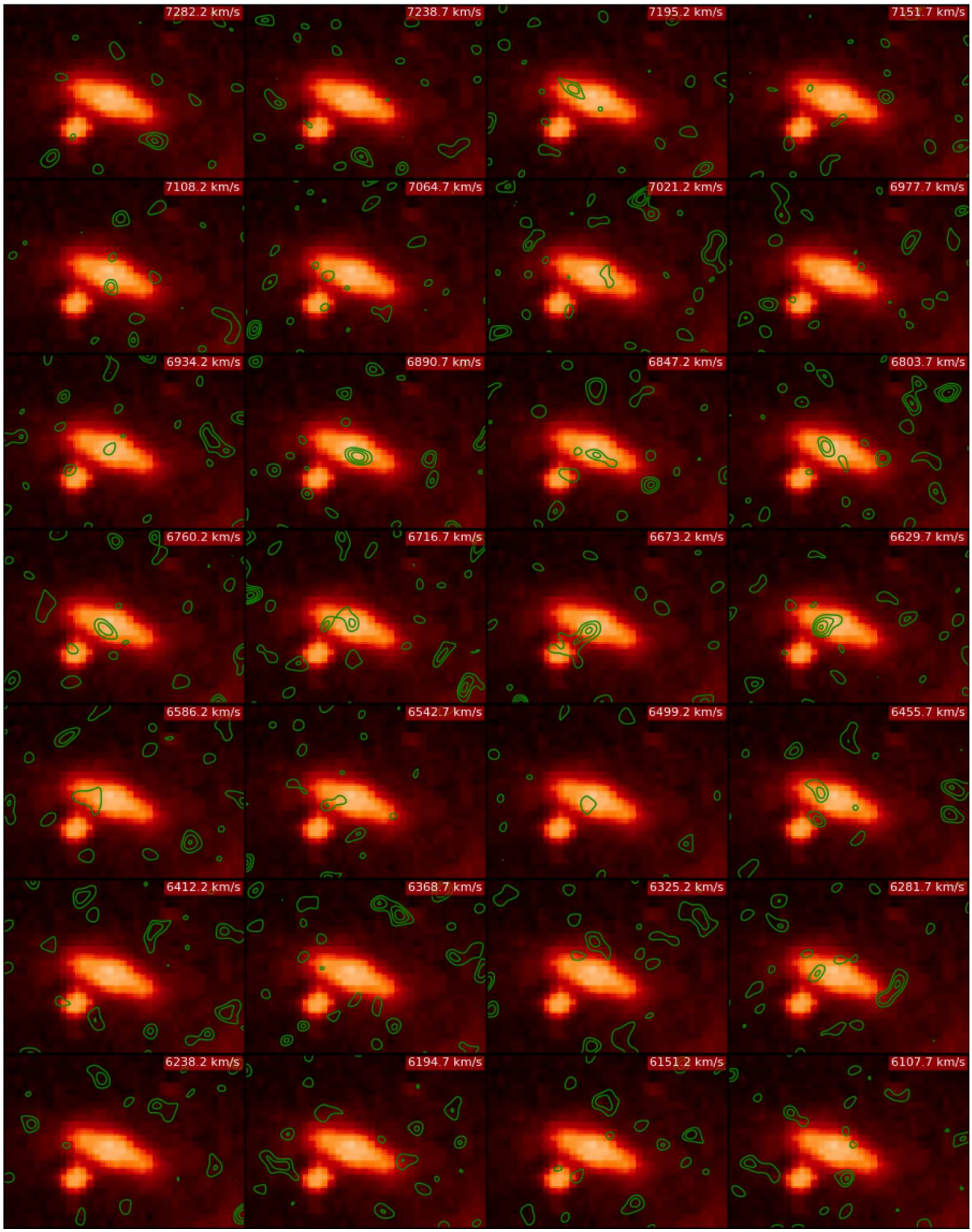


*Figure 3.11: Channel maps of the CO(1-0) emission of HCG40D over the B-band image. Emission is present from 6934 to 6629 km $s^{-1}$. The contour levels are at 2, 3 and 4$\sigma$.*

*Table 3.5: $H_2$ masses from the OVRO observations.*

| Galaxy | Flux (Jy km $s^{-1}$) | Δv (km $s^{-1}$) | Area (beams) | $log(M_{H_2})$ OVRO ($M_\odot$) | $\log(M_{H_2})30m_{obs}$ ($M_\odot$) |
|---|---|---|---|---|---|
| 40a | <20.97 | 300* | 10.53 | <9.06 | <8.69 |
| 40b | <10.32 | 110 | 6.96 | <8.75 | 8.47±0.06 |
| 40c | 39.84±6.33 | 560 | 4.71 | 9.34±0.07 | 9.56±0.03 |
| 40d | 29.60±4.53 | 390 | 3.46 | 9.21±0.06 | 9.28±0.04 |
| 40e | <22.01 | 480** | 7.26 | <9.08 | 8.78±0.11 |
| 79a | <25.55 | 300* | 26.51 | <8.81 | <8.47 |
| 79b | <21.93 | 320 | 18.29 | <8.75 | 8.09±0.07 |
| 79c | <6.11 | 105 | 4.33 | <8.20 | 7.75±0.13 |
| 79d | <16.63 | 300* | 11.22 | <8.63 | <8.43 |

Notes: (*) Galaxies not detected neither in OVRO, nor in the 30m. (**) The table in Leon et al. (1998) shows a mistake in the value of the HCG40e detection window (Leon, private communication). Thus, we have calculated Δv directly from the spectrum shown in their paper.

One possible problem we can find when studying interferometric observations comes from the fact that an interferometer is a spatial filter, so part of the emission from a galaxy can be lost. In our case, we can see that the $H_2$ masses detected with OVRO and the ones observed with the 30m are quite similar. Thus, almost all the $H_2$ in 40c and 40d has been detected with OVRO, which allows us to study the distribution of the main part of the molecular gas present in these galaxies.

In Fig. 3.12 we display the position-velocity diagrams of 40c and 40d. For 40d, which diagram is traced along a position angle of 59º, we can see the emission features from -4″ to 6″ (which corresponds to a spatial extension of 4.8 kpc) , in the velocity interval shown in the spectrum in Fig. 3.8. The 0 moment map shows that the CO is placed in the inner part of the galaxy, with a distribution concentric to the optical isophotes of the galaxy. All the emission detected with the 30m has been detected also with OVRO (the $H_2$ mass measured with both telescopes match within the error bars), which is an indicator of the high compactness of the emission.

For 40c, we can see the emission between -4″ and 5″ (corresponding to 4.4 kpc) in the position-velocity diagram, traced along a position angle of 147º. In the 0 moment map we can see that the emission in this galaxy presents clumpy features, with two lobes in the inner part of the galaxy. A higher sensitivity would be needed to discern whether the emission is really clumpy or this features in the map are only the peaks in a smooth emission distribution. From the comparison between the 0 moment map and the optical image displayed in Fig. 3.2, we can see that the CO emission comes from the prominent dustlane along the galaxy disk.

A comparison between the $H_2$ masses achieved from OVRO and the 30m leads to the conclusions expected from the different sensitivities achieved with the different telescopes:

- In the case of the detected galaxies (40c and 40d), the $H_2$ mass from the OVRO observations roughly agrees with the one from the 30m. In the case of 40d, the masses match within the error bars. In the case of 40c, the difference between both, even being low, could reflect the presence of diffuse emission from the disk of the galaxy.

- In the cases of galaxies detected with the 30m with no detection in OVRO, the value of the upper limit given by the interferometer is in agreement with the value detected of the 30m. In the case of 79b and 79c, a extended distribution of the molecular gas due

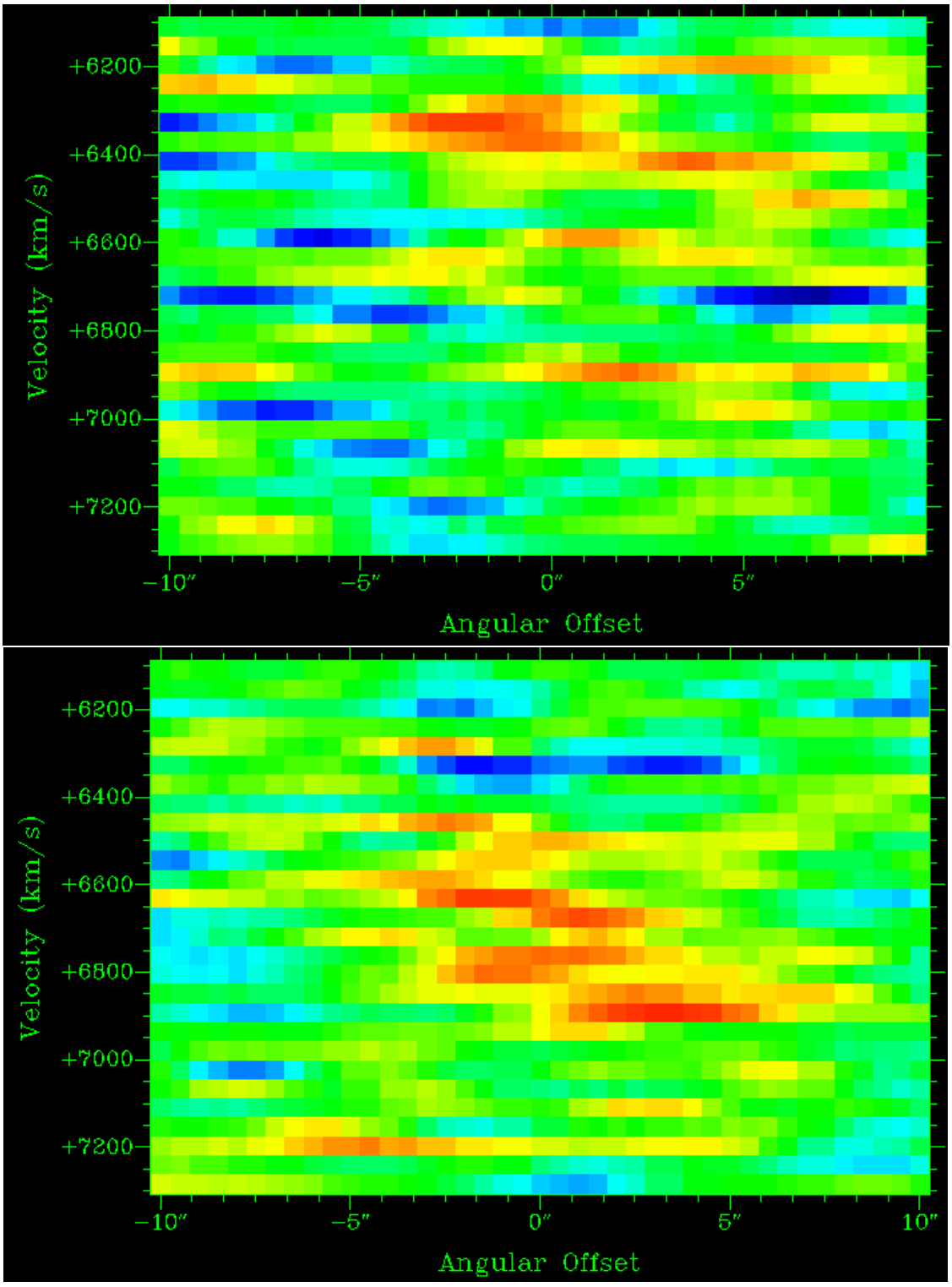


*Figure 3.12: Position-velocity diagrams of the CO(1-0) emission for 40c (top) and 40d (bottom).*

to interactions between the galaxies could explain why both galaxies are detected in the 30m but not in OVRO.

- For the galaxies with no detection neither with OVRO nor with the 30m, the upper limit from OVRO is always larger than the one from the 30m, since the sensitivity of the 30m telescope is higher than the one in the OVRO data.

## 3.3 Spitzer Infrared data of the groups

For HCG40 and HCG79 we have downloaded IR archive data from the Spitzer Space Telescope[4]. These data have a better sensitivity and higher resolution than the IRAS data shown in Chap. 2, which allows us to make a more accurate study of the SF processes within the groups and the IR colors of their galaxies.

### 3.3.1 Observations

We downloaded the emission maps at 3.6, 4.5, 5.8, 8 and 24 $\mu$m. The 24 $\mu$m data were obtained with the Multiband Imaging Photometer for Spitzer (MIPS). Its 24 $\mu$m camera has a field of view of 5.4 $\times$ 5.4 arcminutes and a resolution of 6 arcsec, with a sensitivity of 110 $\mu$Jy at the 5$\sigma$ level (measured with low background after a 500 seconds exposure).

The 3.6, 4.5, 5.8, and 8 $\mu$m data were achieved by the InfraRed Array Camera (IRAC), another Spitzer instrument, with a field of view of 5.2 $\times$ 5.2 arcminutes and a pixel size of 1.2 arcsec. The noise levels for the 4 bands are, respectively, 0.40, 0.84, 5.5 and 6.9 $\mu$Jy in conditions of low background after 200 seconds of exposure.

We downloaded post-Basic Calibrated Data, which are the result of combining all the individual calibration frames from an observation request. To download the data from the archive, we used the Leopard[5] software, part of the *Spitzer Pride* package.

### 3.3.2 Aperture photometry

We analyzed the 24 $\mu$m maps, whose emission is a good tracer of the SFR (see, e.g. Calzetti et al. 2010)). Since the downloaded data were already calibrated, we only needed to subtract the background emission from the images. This process was done by measuring the emission of 10 background areas on the image and subtracting the average emission from the image with a python routine. This background substraction has also been applied to the 8 $\mu$m images, since we have used it to determine the SF regions used in the analysis of the OVRO data (see Sec. 3.2.2). Once we completed this process, we measured the 24$\mu$m flux of each galaxy using FitsView[6] defining two different regions:

1. An elliptical region in which the total emission from the galaxy was comprised. We used different sizes and ellipticities depending on the galactic shape, to cover the full emission corresponding to each galaxy. The values of the apertures are listed in Tab. 3.6.

2. A circular region with the same diameter as the FWHM of the 30m beam at the CO(1-0) emission frequency (22 arcsec) centered on the coordinates where the 30m was pointed, to measure the emission in the same area where the CO emission was observed. In the

[4]The Spitzer Space Telescope is operated by the Jet Propulsion Laboratory, California Institute of Technology under a contract with NASA

[5]http://ssc.spitzer.caltech.edu/warmmission/propkit/spot/

[6]http://www.nrao.edu/software/fitsview/

*Table 3.6: Apertures used to measure the emission from the 24 μm images*

| Galaxy | Circle Radius (arcsec) | Ellipse Major semi-axis (arcsec) | Ellipse Minor semi-axis (arcsec) | Ellipse Position angle (deg) |
|---|---|---|---|---|
| 40a | 11 | 20.7 | 20.6 | 82 |
| 40b | 11 | 7.6 | 8.0 | -14 |
| 40c | 11 | 31.8 | 16.9 | -28 |
| 40d | 11 | 24.7 | 24.3 | -48 |
| 40e | 11 | 26.5 | 7.1 | 52 |
| 79a | 11 | 14.6 | 15.7 | 3 |
| 79b | 7 | 11.1 | 24.0 | 1 |
| 79c | 11 | 11.5 | 16.4 | -31 |
| 79d | 11 | 23.4 | 13.6 | 15 |

case of 79b, we assumed a diameter of 14 arcsec to avoid measuring emission from the background galaxy 79e, not physically related to the group and with a much higher velocity. In the case of the CO observations, its larger redshift prevented it from influencing the 79b spectrum, but in the case of the Spitzer images the emission from 79e can affect our measurement of 79b (see Fig. 3.14).

The fluxes calculated from the circular regions with the 30m beam size were aperture corrected following the guidelines given in the Spitzer MIPS Handbook [7]. The correction factor in the case of 79b (for which we have considered a circular region with a diameter of 14) is 1.61. For the other galaxies we calculated the factor for a circular aperture of 22 arcsec, using a polynomial fit of order 3 to the values for different apertures available in the Spitzer webpage, finding a value of 1.22 for the correction factor. In the case of the elliptical regions we have derived the correction factor with an interpolation similar to the one indicated above, but instead of the diameter of the circular region, we used the values of the geometric mean of the major and minor axis of the ellipses. The values for the correction are ∼1.1 for all the galaxies but 40b. In the case of 40b, due to the small size of the ellipse, the value for the correction factor is 1.55.

The MIPS 24$\mu$m images for HCG40 and HCG79 are displayed in Figs. 3.13 and 3.14, with the apertures listed in Table 3.6 overlayed. We also display the IRAC images at 3.6, 4.5, 5.8 and 8$\mu$m. The 8 and 24 $\mu$m images are background-subtracted.

In Tab. 3.7 we summarize the values of the 24$\mu$m fluxes calculated within the circular and elliptical apertures, together with the values derived by Bitsakis et al. (2010) (hereafter BI10). Their fluxes at 3.6, 4.5, 5.8 and 8.0 $\mu$m are also shown. Finally, we include the 60 and 100 $\mu$m fluxes from IRAS taken from Verdes-Montenegro et al. (1998). The fluxes from Spitzer calculated within the 30m beam area are aperture corrected. The 24 $\mu$m fluxes used in the analysis on this chapter will be the ones obtained from the elliptical apertures, since these are the ones which better cover the emission regions.

Comparing our fluxes to those of BI10 we find that the differences are not significant when we take into account the elliptical-regions fluxes except for 40a, 40b and 79b. These differences come from the different apertures used by BI10 and ourselves: we have adapted the shape and area of the region, trying to get all the emission from the sources.

The largest differences in the fluxes calculated from the two apertures we use are found in 40c and 79b. The latter is also one of the galaxies with discordant fluxes between BI10 measures

[7] http://ssc.spitzer.caltech.edu/mips/mipsinstrumenthandbook

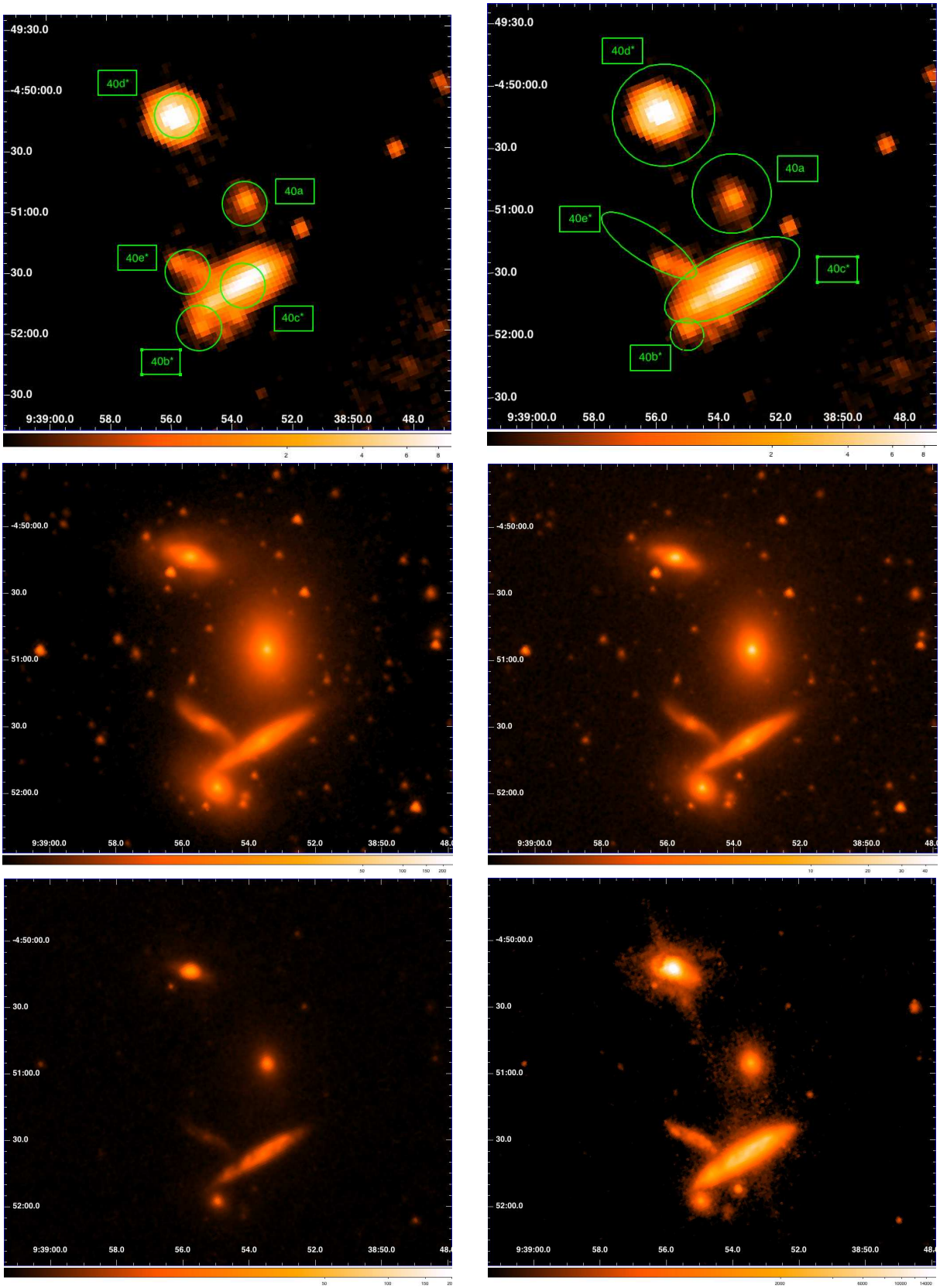


*Figure 3.13:* ***Upper****: 24µm emission maps from Spitzer for HCG40 with the circular and elliptical apertures (Tab. 3.6) displayed. The galaxies whose name is marked with an * have detected CO emission.Upper left: The aperture corresponds to the FWHM of the 30m beam. Upper right: Area considered to get the full emission from the galaxies.* ***Center****: 3.6 (Left) and 4.5 (Right) µm IRAC images from Spitzer.* ***Lower****: 5.8 (Left) and 8.0 (Right) µm IRAC images from Spitzer.*

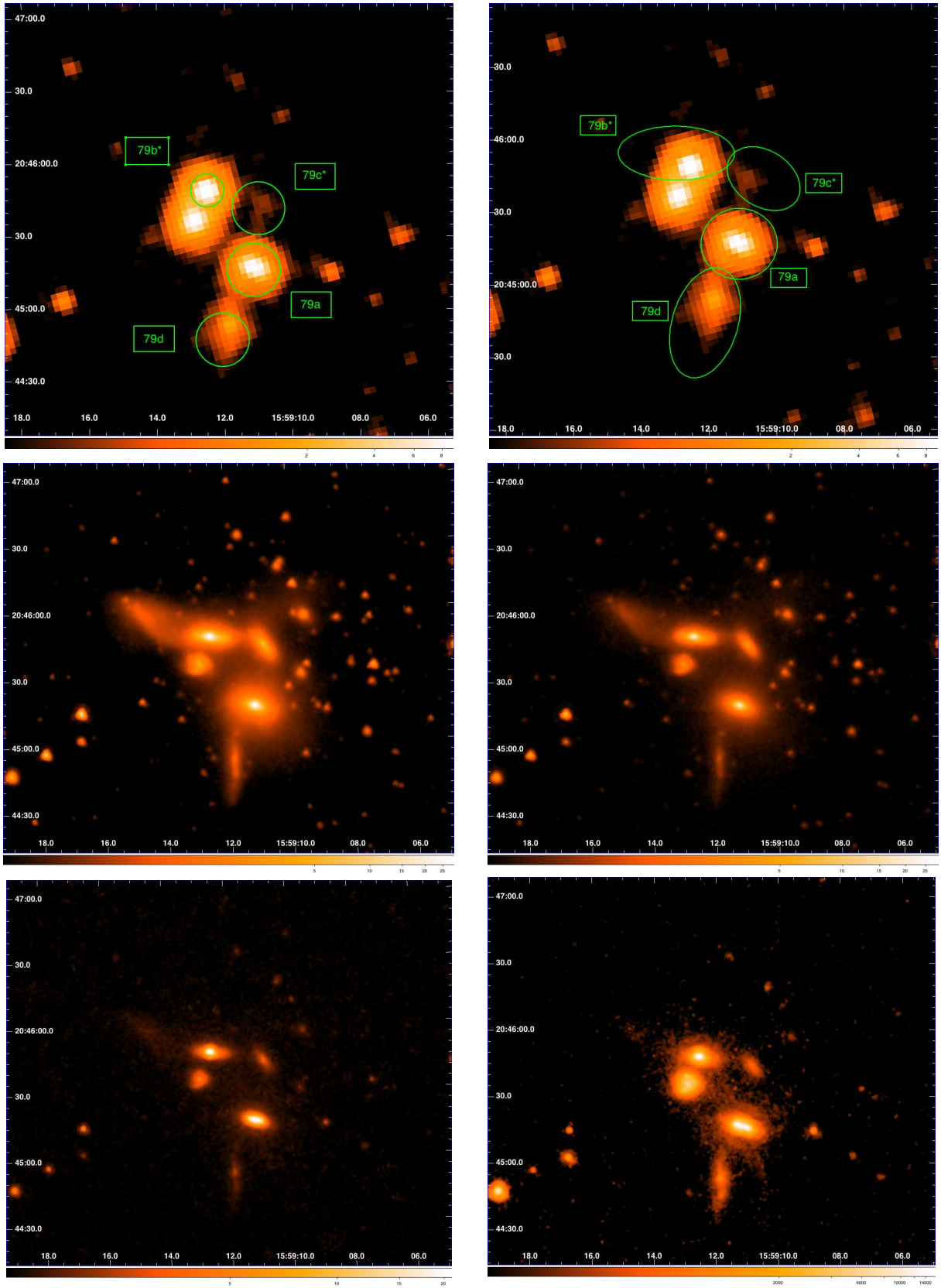


*Figure 3.14:* ***Upper****: 24µm emission maps from Spitzer for HCG79 with the circular and elliptical apertures (Tab. 3.6) displayed. The galaxies whose name is marked with an * have detected CO emission.Upper left: The aperture corresponds to the FWHM of the 30m beam. Upper right: Area considered to get the full emission from the galaxies.* ***Center****: 3.6 (Left) and 4.5 (Right) µm IRAC images from Spitzer.* ***Lower****: 5.8 (Left) and 8.0 (Right) µm IRAC images from Spitzer.*

*Table 3.7: IR fluxes of the galaxies in HCG40 and HCG79.*

| | Spitzer (ours) | | Spitzer (BI10) | | | | | IRAS | |
|---|---|---|---|---|---|---|---|---|---|
| Gal. | $24\mu m_{circ}$ (mJy) | $24\mu m_{ellip}$ (mJy) | $24\mu$m (mJy) | $3.6\mu$m (mJy) | $4.5\mu$m (mJy) | $5.8\mu$m (mJy) | $8.0\mu$m (mJy) | $60\mu$m (mJy) | $100\mu$m (mJy) |
| 40a | 4.9 | 6.8 | 4.0 | 45.4 | 28.0 | 20.2 | 15.3 | <99 | <300 |
| 40b | 6.3 | 6.7 | 3.0 | 18.7 | 12.2 | 8.9 | 8.8 | <84 | <255 |
| 40c | 52.2 | 83.8 | 73.4 | 29.4 | 19.7 | 34.7 | 83.5 | 850 | 2000 |
| 40d | 93.8 | 100.5 | 88.1 | 21.3 | 14.3 | 22.7 | 66.9 | 1030 | 2300 |
| 40e | 6.0 | 6.9 | 5.6 | 6.4 | 4.1 | 4.0 | 5.9 | <99 | <240 |
| 79a | 24.4 | 24.3 | 23.3 | 23.7 | 15.2 | 18.8 | 30.9 | 1280 | 2820 |
| 79b | 34.5 | 26.3 | 33.7 | 17.6 | 14.6 | 15.8 | 12.2 | <130 | <453 |
| 79c | 1.5 | 1.76 | 1.2 | 10.2 | 5.7 | 4.0 | 2.0 | <105 | <402 |
| 79d | 4.5 | 6.3 | 5.2 | 2.2 | 1.2 | 1.5 | 3.5 | <93 | <399 |

$24\mu m_{circ}$ are the fluxes in an area equal to the 30m beam at 115 GHz; $24\mu m_{ellip}$ are the fluxes assuming an elliptical region covering the full area of the galaxy.

and our elliptical-based ones. If we take a look on the elliptical region selected to measure the emission, we can see how its shape and orientation is affected by the presence of 79e. The intense emission of the background galaxy overlaps some of the emission from the 79b disk, which can not be measured without measuring emission from the neighbor. However, if we take a smaller region containing only the center of 79b, as the one chosen by BI10 (12.2″) or the one we have set for the circular shaped aperture, the aperture correction extrapolates the inner flux to take into account the emission outside this region and, thus, the corrected flux is a good approximation to the total luminosity of the galaxy, including the disk and halo contribution excluded in the elliptical region.

### 3.3.3 Star Formation Rate and Star Formation Efficiency

The Star Formation Rate (SFR), a measure of the stellar mass formed in a galaxy per unit of time, can be calculated from different wavelengths, such as the UV, $H_\alpha$, $24\mu$m or FIR fluxes. We chose to calculate the SFR of the galaxies in HCG40 and HCG79 from the Spitzer high resolution $24\mu$m fluxes. 24 $\mu$m emission is a good SFR tracer (e.g. Calzetti et al. 2007)) with the advantages of not being affected by extinction or dust attenuation. The SFRs obtained from $24\mu$m fluxes can be also compared with the global SFR calculated from IRAS $L_{\rm FIR}$. SFRs from both luminosities were calculated as follows:

For Spitzer, we need first to calculate the luminosity at $24\mu$m. Using the equivalence

$$1\mathrm{Jy} = 10^{-19}\mathrm{erg\,m^{-2}Hz^{-1}s^{-1}} \tag{3.3}$$

we can express the luminosity in $erg s^{-1}$ as

$$L_{24\mu m} = Flux\frac{4\pi D^2 \nu}{10^{19}} \tag{3.4}$$

where D is the distance in meters and $\nu$ is the frequency of the observed emission in Hz (in our case, $\nu = 12.5\times10^{12}$ Hz). To express $L_{24\mu}$m in terms of $L_\odot$ we have used a value of $L_\odot = 3.9 \times 10^{33}$ erg s$^{-1}$.

*Table 3.8: Summary of $L_{24\mu}$ and SFR.*

| Gal. | $\log(L_{24\mu m})$ Ellip. ($L_\odot$) | SFR $24\mu m_{Ellip}$ ($M_\odot$/yr) | SFR IRAS ($M_\odot$/yr) |
|---|---|---|---|
| 40a | 8.32 | 0.45 | <0.53 |
| 40b | 8.31 | 0.43 | <0.45 |
| 40c | 9.41 | 3.81 | 4.03 |
| 40d | 9.49 | 4.44 | 4.73 |
| 40e | 8.33 | 0.45 | <0.47 |
| 79a | 8.50 | 0.65 | 2.79 |
| 79b | 8.53 | 0.68 | <0.36 |
| 79c | 7.37 | 0.07 | <0.31 |
| 79d | 7.91 | 0.21 | <0.29 |

We have used the Zhu et al. (2008) formula to calculate the SFR from $L_{24\mu}$m. To calibrate the SFR(24$\mu$m), they used the extinction corrected UV and $H_\alpha$ luminosities together with the FIR emission of a sample of galaxies in the Spitzer SWIRE (SIRTF Wide-Area Infrared Extragalactic Survey, Lonsdale et al. 2003) fields. From the different SFR(24$\mu$m) formulae in the literature, this is the one which best covers our luminosity range. We will use the non-linear reformulation of the formula of Zhu et al. (2008), that is presented in Calzetti et al. (2010, eq. 10 in their work):

$$SFR(\mathrm{yr}^{-1}) = 8.10 \times 10^{-37} (\mathrm{L}_{24\mu}(\mathrm{erg\ s}^{-1}))^{0.848} \tag{3.5}$$

since the linear SFR(24$\mu$m) calibration has been found to underestimate the true SFR in the range of luminosities we are working on (Calzetti et al. 2010). Eq. 3.5 considers a Kroupa (Kroupa 2001) IMF, while we are uysing, as detailed in Chap. 2 a Salpeter IMF. Thus, we have to apply a conversion factor of 1.59 to convert between the SFRs with different IMFs (Leroy et al. 2008), so the formula we will finally use is:

$$SFR(\mathrm{yr}^{-1}) = 1.29 \times 10^{-36} (\mathrm{L}_{24\mu}(\mathrm{erg\ s}^{-1}))^{0.848} \tag{3.6}$$

The range of applicability of the calibration by Zhu et al. (2008) is the one which extends to the lowest values of the luminosity ($\log(L_{24\mu}\mathrm{m}) \approx 8$ in units of $L_\odot$), which is needed for our sample, containing low-luminosity galaxies, with the lowest values (for 79c and 79d) even below this range.

The values of SFR, as well as the 24$\mu$m luminosities from which they are derived are shown in Tab.3.8. Together with them, we list also the SFR calculated from IRAS, taken from Chap. 2.

The SFR of HCG40 calculated from Spitzer agree reasonably with the one obtained from IRAS. In the case of HCG79 the results do not match, with the SFR of 79a showing a significant difference between the values obtained from IRAS and Spitzer. The other three galaxies in the group show upper limits in the IRAS SFR, which are larger than the SFR obtained from Spitzer. Most likely the poor resolution of IRAS is the reason for this discrepancy.

Complementarily to the study of the SFR based on the $L_{24\mu}$m, we have downloaded the far ultra-violet (FUV) fluxes corresponding to our galaxies from the Galaxy Evolution Explorer (GALEX) satellite archive[8]. With these fluxes, available for all the galaxies in HCG40 and HCG79

[8]http://galex.stsci.edu/GR6/

*Table 3.9: Values for $M_{\rm star}$, $M_{\rm H_2}$, sSFR and SFE for different measurements.*

| Gal. | log($M_{\rm star}$) ($M_\odot$) | log(sSFR) ($\rm yr^{-1}$) | log($M_{\rm H_2}$) ($M_\odot$) | log(SFE) ($yr^{-1}$) |
|---|---|---|---|---|
| 40a | 11.51 | -11.86 | <8.97 | >-9.31 |
| 40b | 11.09 | -11.45 | 8.70 | -9.05 |
| 40c | 11.25 | -10.67 | 9.84 | -9.26 |
| 40d | 11.03 | -10.38 | 9.44 | -8.79 |
| 40e | 10.43 | -10.78 | 8.88 | -9.22 |
| 79a | 10.76 | -10.93 | <9.06 | >-9.25 |
| 79b | 10.74 | -10.91 | 8.56 | -8.72 |
| 79c | 10.07 | -11.22 | 8.13 | -9.28 |
| 79d | 9.62 | -10.30 | <8.62 | >-9.31 |

with the exception of 79a, we have calculated the SFR using the formula in Bigiel et al. (2008). which uses a linear combination of the 24$\mu$ and FUV luminosities. The FUV contribution in the SFR for our galaxies is more than a factor 10 lower than the 24$\mu$ one, so we have neglected it. The only exception is 79d, for which, as a result of its lower dust content, we found the FUV contribution to be of the same order of magnitude as the infrared one. Nevertheless, the combined (FUV+24$\mu$) SFR has the same value than the one calculated using only the 24$\mu$ luminosity, so we can consider the SFR based on IR measurements without underestimating its value.

We calculated the sSFR, defined as the ratio between the SFR, calculated from the $L_{24\mu}$m and the stellar mass. The values of the stellar mass and the sSFR are listed in Tab. 3.9. There are three galaxies, 40c, 40d and 79d with a high sSFR. We also calculated the SFE, also listed in Tab. 3.9, using the SFR($L_{24\mu}$m) and the $M_{\rm H_2}$ extrapolated from the 30m observations. The SFE lies in a narrow range, even for the galaxies with a high sSFR. We conclude that we can use the SFR base on 24 $\mu$m, as a good measure of the total SFR, and that an understimate due to unenshrouded SF is not a problem.

The average SFE for HCG40 and HCG79 calculated from the Spitzer data is -9.08±0.09. This value is not significantly different from that calculated for the full sample calculated based on IRAS data in Chap. 2, nor from the one from the AMIGA sample of isolated galaxies, all of them shown the Tab. 2.9.

In Fig. 3.15 we have plotted, with black squares, the SFR of our whole HCG sample calculated from their IRAS 60 and 100 $\mu$m fluxes as a function of their $M_{\rm H_2}$, taken from Chap. 2, together with the SFR calculated from Spitzer 24 $\mu$m fluxes for HCG40 (red circles) and HCG79 (green triangles). We can see that the behavior shown by HCG40 and HCG79 matches with that shown by our full HCGs sample, with the results from Spitzer showing the same trend as the ones from IRAS. Note that the trend between $M_{\rm H_2}$ and the SFR measured with Spitzer goes down to very low values of SFR, which could not be reached with the IRAS data due to its lower resolution and sensitivity.

### 3.3.4 Spitzer colors

Using the Spitzer IRAC fluxes at 3.6, 4.5, 5.8 and 8.0 $\mu$m detailed in Tab. 3.7 we have plotted the $f_8/f_{4.5}$ ratio versus the $f_{5.8}/f_{3.6}$ ratio in a color-color diagram (Fig. 3.16). The position of the galaxies in this diagram tells us whether the SED of a source is increasing or decreasing with wavelength. Galaxies with emission dominated by an old stellar population are expected to be

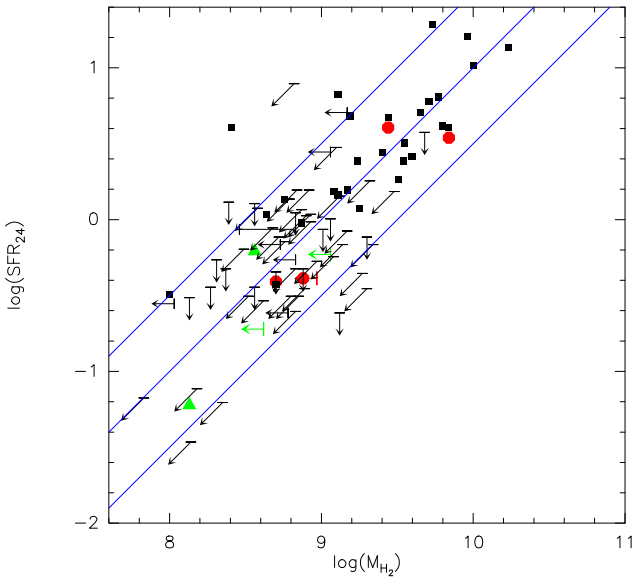


*Figure 3.15: $log_{10}(SFR)$ vs $log_{10}(M_{H_2})$. Colour code: Black squares: Full HCG sample with $SFR_{FIR}$ calculated from IRAS 60 and 100 $\mu$m fluxes. Red circles: HCG40 with $SFR_{24\mu}$m. Green triangles: HCG70 with $SFR_{24\mu}$m. The lines plotted correspond to log(SFE) = -8.5, -9, and -9.5 $yr^{-1}$*

.

located on the lower left quadrant, while galaxies with active star formation are expected to be located on the top right portion of the diagram. The area within the solid blue lines in Fig. 3.16 is where the AGNs are expected to be, according to Lacy et al. (2004).

In Fig. 3.16 we see the galaxies with low sSFR in the bottom left part of the diagram. There are two galaxies lying in the AGN area: 79a and 79b. Durbala et al. (2008) classified 79a and 79b as AGN, while Martínez (2008) classify them as transition objects, as shown in Tab. 3.1. Thus, the nuclear activity diagnostics match with the IRAC colors one. 40e, classified as AGN by Martínez, lies on the border of the AGN area. 40c and 40d, classified as transition objects by Martínez, lie out of this area.

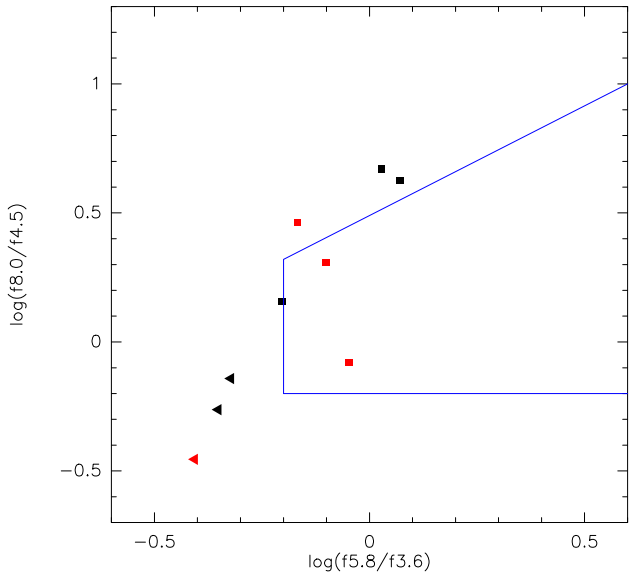


*Figure 3.16: IRAC color-color diagram for the galaxies in HCG40 and HCG79. The area within the blue lines indicates the AGN color selection criteria from Lacy et al. (2004). Colour code: Black: HCG40. Red: HCG79. The triangles indicate the galaxies with log(sSFR) < -10.5, while the squares indicates the galaxies with log(sSFR) > -10.5*

## 3.4 HI data

In Figs. 3.17 and 3.18 the 0 moment maps of the HI emission of HCG40 and HCG79 are shown, with data coming from the Very Large Array (VLA) (VM01 for the HCG79 map, Verdes-Montenegro et al (private communication) for HCG40).

HCG40 was observed using VLA CD and D configuration, with a synthesized beam of 46.9×36.0 arcsec. In the case of HCG79, observations were carried out in C and D configuration, with a resulting synthesized beam of 30.8×18.2 arcsec.

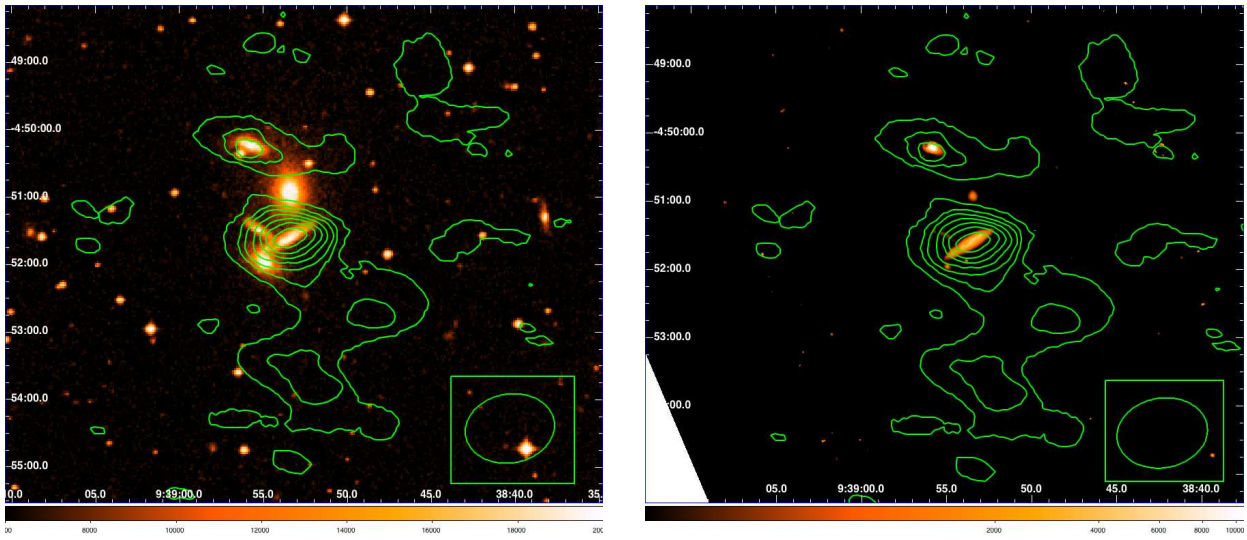


*Figure 3.17: Overlays of the HI contours of HCG40. The contour levels are set at 40, 160, 280, 400, 520, 640, 760 and 880 mJy km $s^{-1}$ $beam^{-1}$. Left: HI contours over B band image. Right: HI contours over 8$\mu$m map. The beam size is 46.9×36.0 arcsec.*

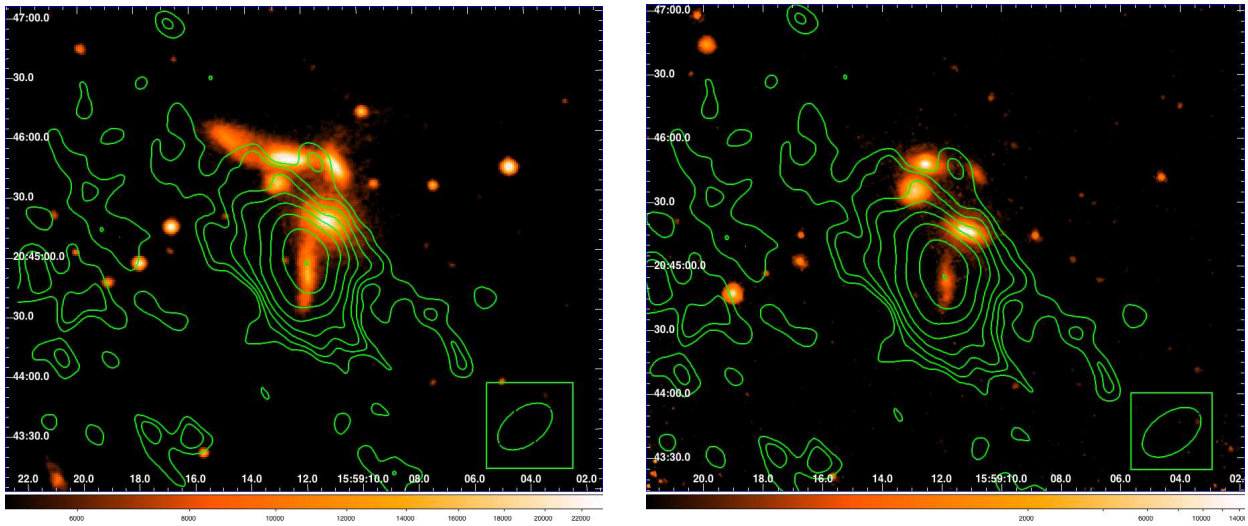


*Figure 3.18: Overlays of the HI contours of HCG79. The contour levels are set at 70, 100, 140, 200, 280, 400, 580 and 821 mJy km $s^{-1}$ $beam^{-1}$. Left: HI contours over B band image. Right: HI contours over 8$\mu$m map. The beam size is 30.8×18.2 arcsec.*

In HCG40 we see that the atomic gas is mainly concentrated in the disks of 40d and 40d. There are also faint tidal features at the S and SW of 40c. The HI content in 40d seems to be affected by the environment, with a tail extending towards the W. A certain correlation between

Table 3.10: Summary of SFE, sSFR and deficiencies in gas and $L_{FIR}$.

| Galaxy | Hubble Type | $\log(\mathrm{SFE})_{\mathrm{total}}$ ($yr^{-1}$) | $\log(\mathrm{sSFR})$ ($\mathrm{yr}^{-1}$) | $\mathrm{Def}(M_{\mathrm{H_2}})$ | $\mathrm{Def}(L_{\mathrm{FIR}})$ | $Def(M_{\mathrm{HI}})_{\mathrm{VM01}}$ |
|---|---|---|---|---|---|---|
| 40a | S0 | >-9.31 | -11.86 | > 0.47 | >0.85 | > 1.47 |
| 40b | S0 | -9.05 | -11.45 | 0.03 | > 0.25 | >1.15 |
| 40c | Sb | -9.26 | -10.67 | -1.10 | -0.69 | 0.44 |
| 40d | S0a | -8.79 | -10.38 | -0.66 | -0.72 | 0.45 |
| 40e | Sbc | -9.22 | -10.78 | -1.26 | >-0.82 | >0.87 |
| 79a | E/S0 | >-9.25 | -10.93 | >-0.72 | -0.90 | >1.48 |
| 79b | S0 | -8.72 | -10.91 | 0.01 | > 0.20 | >1.58 |
| 79c | S0 | -9.28 | -11.22 | -0.06 | >-0.20 | >1.36 |
| 79d | Sd | >-9.31 | -10.30 | >-0.66 | >-0.29 | 0.27 |

$\mathrm{SFE}_{total}$ and sSFR are both calculated from the SFR measured from elliptical apertures. $SFE_{\mathrm{total}}$ uses the extrapolated $M_{H_2}$. Deficiencies are taken from Chapter 2.

the HI and $H_2$ masses can be seen, since the two galaxies detected in HI are the ones with the highest $H_2$ mass and, as shown in Sec. 3.2.1, the only two detected with OVRO.

In the case of HCG79 we see that almost all the HI is contained in the disk of 79d, the new entering galaxy. The HI distribution and dynamics within this group have already been studied by Durbala et al. (2008), who found the emission towards the east of 79d to be continuous with the emission from the disk of the galaxy. The most plausible interpretation is that this tail is a sign of the first stages of ISM stripping from 79d, and it suggests that 79d is entering the group from the NE. In this case, the HI is present in the disk of one galaxy with no detection in CO. The atomic to molecular gas ratio for 79d is high (>3.3), which agrees with the previously found values for Sd galaxies, which usually show higher values of this ratios than Sa or Sb galaxies like 40c or 40d.

## 3.5 Discussion and conclusions

Looking for a better understanding of the SF and molecular gas properties of the galaxies in HCG40 and HCG79, we compared the trends shown by the galaxies in the different wavelengths with the deficiencies on $M_{H_2}$, $L_{FIR}$ and $M_{HI}$ calculated in Chapter 2. All these magnitudes are summarized in Tab. 3.10.

### 3.5.1 Bimodality of sSFR

We have first compared our results with those of Johnson et al. (2007), whose sample covers 12 HCGs. They found their galaxies to show a gap in the distribution in the IRAC color-color diagram, between those with high sSFR, located in the top corner and the ones with low sSFR, located at the bottom. The galaxies in HCG40 and HCG79 seem to follow a similar distribution (Fig. 3.16), with the exception of 40e, which is located in the gap found by Johnson et al. (2007).

As pointed out in Chapter 2, Tzanavaris et al. (2010), using the same sample than Johnson et al. (2007), found all the early-type galaxies to have lower sSFRs, while 22 out of 24 late-type showed high sSFRs. They also found sSFR values to show a clear bimodality, with a gap between low and high sSFR: there are 19 galaxies with log(sSFR)<-10.49, while the other 22

galaxies show log(sSFR) values larger than -9.92, with only 5 of them showing values lower than -9.42. The galaxies at each side of the sSFR gap matches with the ones at each side of the IRAC color diagram gap. These trends are not shown by the SINGS sample that they used as comparison sample, whose sSFRs are continuously distributed, showing no gap. Tzanavaris et al. (2010) suggested, based on this pronounced bimodality on their sample of HCGs, that the environment of the galaxies in groups accelerate galaxy evolution, enhancing SF processes and favoring a fast transition to quiescence.

Tzanavaris et al. (2010) derived their $M_{\rm star}$ (from which sSFR is calculated) from K-band fluxes obtained from 2MASS, as we did. Nevertheless, although the values for the fluxes they show are quite close to the ones we used for the galaxies in common between both samples, their $M_{\rm star}$ show a value which is systematically lower by a factor 10 with respect to the values we derived for the same galaxies. As a result of this, their sSFRs show a value one order of magnitude larger. Thus, we cannot perform a quantitative comparison between their results and ours.

When plotting the sSFR distribution of HCG40 and HCG79, we see that our distribution does not show a clear gap (Fig. 3.19). This sSFR distribution, together with the IRAC diagram, show that the bimodality suggested by Tzanavaris et al. (2010) turns out not to be completely followed by our galaxies. On one hand, we see the sSFR gap in Tzanavaris et al. (2010) is $\sim$2 times wider than the one in our sample. On the other hand, even when most of our galaxies are located in the IRAC diagram according to the bimodal distribution, we find one galaxy not to follow this trend.

In principle, we cannot confirm the proposed bimodality, but the small size of our sample does not allow us to set an strong conclusion on this. At this point, the study of a larger sample is required to see whether the behavior shown by HCG40 and HCG79 is present in other groups out of the Johnson/Tzanavaris sample, or we have just found some of the few galaxies that do not follow the bimodal trend. The special features of HCG40 and HCG79 already detailed (specially their very high compactness), which in essence motivate the work in this chapter should be taken into account when working with a larger sample.

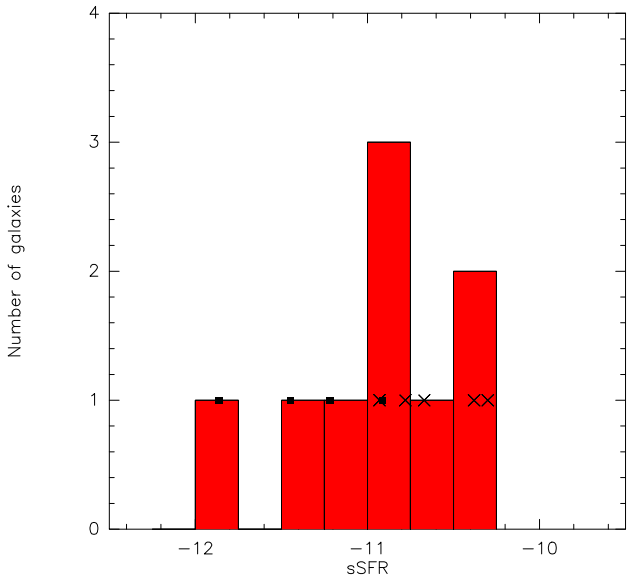


*Figure 3.19: sSFR distribution (red histogram) for HCG40 and HCG79 galaxies. The sSFR is represented with a square (cross) in the case of galaxies with a negative (positive) 8μm/4.5μm ratio*

### 3.5.2 Relation between SF, $H_2$ and HI

In contrast to the sSFR, which spans a wide range, the SFE is very similar for all our galaxies, and there is no clear relation between the value of the SFE and other parameters such as their SFR, gas deficiency or morphology. Specifically, we can not see any relation between SFE and the HI content of the galaxies. It seems that HI is not necessary for SF to take place or, at least, that SF processes have the same efficiency in absence of HI, suggesting an universal SFE independent of the HI content of the galaxies. The SF processes going on in these galaxies with low HI will finish once their molecular gas content is exhausted, since there will be not an atomic gas reservoir to replenish it. On the other hand, the HI-rich galaxies (40c, 40d, 79d) show higher values for their sSFR, which suggests HI leads to a higher sSFR. These results found here from a detailed study of HCG40 and HCG79 are in agreement with those from the statistical analysis of the 20 HCGs in Chap. 2.3.6.

If we focus on the $H_2$ content, we see that, while late-type galaxies in HCG40 and HCG79 show an excess of $H_2$, elliptical galaxies show high deficiencies and the value for the S0 galaxies is close to the average deficiency of our whole HCG sample. This seems to agree with the idea of the S0 galaxies in dense environments as the result of the loss of their spiral structure as a result of tidal stripping within the group (e.g. Moore et al. 1996).

Chapter 4

# High resolution study of HCGs with the next generation of mm/submm interferometers: ALMA

*and how many brisk lads drying in the sun at Execution Dock?*
*and all for this same hurry and hurry and hurry*

**Long John Silver** - Treasure Island

The millimeter and submillimeter wavelength range, between centimeter radio wavelengths and the infrared part of the electromagnetic spectrum, is one of the spectral windows not deeply explored yet, mostly due to the technical problems associated with the transmission of these waves in the atmosphere of the Earth. Nevertheless, as we have seen in the former chapters of this work, in this range we can find most of the information on the molecular richness of the interstellar medium.

The comparison between the single dish CO measurements shown in Chap. 2 and the interferometric ones performed with OVRO, shown in Chap. 3 is a good example of the challenge implied in mm/submm interferometric observations. The sensitivity level achieved with the 30m radiotelescope is much higher than the one we got with OVRO. At this point, it is mandatory to set some master lines on the work that should be performed in order to continue the study of the molecular gas content in HCGs, which must include high-resolution interferometric observations.

This thesis includes two main topics: the study of the molecular gas in HCGs and the preparation of observations of these type of objects with the Atacama Large Millimeter Array (ALMA). This chapter reflects this interest in two ways: first, we perform a study of the time requirements to observe HCGs with current and future interferometers, with special focus on ALMA. In addition, we present the results coming from our interest in the calibration of interferometers, and in particular our tests of the fast-switching method, a calibration technique which will be used in ALMA.

## 4.1 Observing HCGs with mm interferometers

In this chapter, we study the feasibility to observe the HCGs in our sample with different mm interferometers: the SubMillimeter Array (SMA), the Plateau de Bure interferometer (PdBi) and ALMA.

SMA, located at Mauna Kea summit (Hawaii), at 4080 meters over the sea level, is property of the Center for Astrophysics (Smithsonian Institution-Harvard University) and ASIAA (Academia Sinica-Institute for Astronomy and Astrophysics). It consists of eight 6-meters antennas that can be arranged into configurations with baselines up to 509 meters operating at frequencies from 180 to 700 GHz. We cannot observe the 115 GHz emission line with this instrument and, therefore, we have studied the feasibility of the SMA observations for the CO(2-1) emission line. At this frequency, SMA has a field of view of 50″.

The PdB interferometer, property of IRAM, is located at the Plateau de Bure, at 2550 m altitude, in the French Alps. Consisting of six 15-meters antennas with baselines ranging up to 760 meters, it can observe the millimeter range, from 80 to 267 GHz. New receivers covering higher frequencies (from 277 to 371 GHz) have started their operation during this winter observing period. Unlike SMA, it can be tuned at 115 GHz, so we can study the CO(1-0) emission line, with a field of view of 40″.

Finally, ALMA is an interferometer which is currently being built by an international consortia between the European Southern Observatory (ESO), the National Radio Astronomy Observatory (NRAO), the National Astronomical Observatory of Japan (NAOJ), the National Research Council of Canada, the Academia Sinica Institute of Astronomy & Astrophysics (ASIAA) of Taiwan and the Republic of Chile. It is placed in Llano de Chajnantor, 5000 meters high, in the desert of Atacama, Chile. It will operate in the mm and submm range, from 0.3 to 9.6 mm, which corresponds to a frequency range of 31-950 GHz, although the lower frequency bands, below 84 GHz, are part of the future development plan. For the early science observations, the 3 mm, 1.3 mm, 0.8 mm and 0.4 mm bands will be available. After several changes from the initial design, it will have at least 50 antennas, each with a diameter of 12 meters, with baselines ranging from 15 m to 18 km, and a compact sub-array (Atacama Compact Array, ACA), with four 12-meters and twelve 7-meters antennas. The field of view of the 12m antennas array at 115 GHz is 50″.

Right now, there are 9 antennas at the Array Operations Site (AOS, the place where the interferometer will operate), with which the commissioning and science verification procedures are being performed. ALMA will bring new opportunities to the astronomical community, offering a much higher sensitivity and resolution than current interferometers, in addition to the possibility of performing observations in the submm range.

### 4.1.1 The sample

In a hypothetical situation of no constraints on the available observing time, we would observe our full sample of 20 HCGs but, even in these conditions, it would be useful to classify the objects according to their scientific interest. Considering a realistic scenario, in which the pressure for observing time is usually very high, it is essential to define some observing priorities within our sample. Thus, we have defined three sets of HCGs according to their interest:

First, we would observe the groups with the highest galaxy density, looking for strong interactions between the members. The groups previously studied in Chap. 3, HCG40 and HCG79 are thus good candidates. HCG31 and HCG92 (also called "Stephan's Quintet", see Chapter 1) show a high surface brightness and strong interactions between their members (see e.g. Natale et al. 2010; Verdes-Montenegro et al. 2005a, and references therein for HCG92 and HCG 31, respectively) and, therefore, should also be prioritized.

Other interesting groups, with unusual features or with previous studies in other wavelengths are HCG 7 (Konstantopoulos et al. 2010), HCG15 (Da Rocha et al. 2008), HCG16

(de Carvalho & Coziol 1999), HCG37 (very compact, showing a variety of morphological types), HCG44 (Aguerri et al. 2006, which is also the nearest group and can be studied with a high linear resolution) and HCG100 (with a large amount of HI, which is distributed between the galaxies and a cloud on which they are embedded).

In the case of the above mentioned HCGs, and also for the other groups in our sample, we would give priority to those with available HI maps and/or Spitzer data. For the groups that fulfill these conditions, it would be interesting to start with those with signs of interaction. Along the process, we should try to keep a balance of the distribution of the groups as a function of their evolutionary stage.

### 4.1.2 HCG observations with current and future interferometers

In this section, we aim to study the observing times required to map the CO emission in HCGs using SMA, PdB and ALMA. To illustrate the difference on the sensitivities of the interferometers, we have calculated the time required to reach a rms of 10 mJy beam$^{-1}$ at 0 degrees of declination with a velocity resolution of 20 km s$^{-1}$. Using SMA, we would need 6.2 hours of on-source integration, while for PdB we would need 6.6 minutes. For ALMA, considering a sixteen 12-meters antennas array with $T_{sys} = 116$ K (which corresponds to bad observing conditions), the time required would be only 1.2 minutes. Due to this difference in the sensitivity of the instruments, we set a different strategy for each one. For SMA, the one with the lowest sensitivity, we calculated the S/N ratio expected after a full track for those HCGs with the highest fraction of detected galaxies with the single-dish. In the case of PdB, we calculated the observing time required to achieve a S/N ratio of 10 for the galaxies detected with single-dish. Finally, for ALMA, the one with the best sensitivity, we also calculated the observing time required to achieve a S/N ratio of 10 but, in this case, we have considered all the 86 galaxies in our 20 HCGs.

We considered for all the instruments an angular resolution of 3″, which corresponds to the SMA compact configuration at CO(2-1), the ALMA most compact configuration and the PdB CD configuration at CO(1-0). In all the cases, we calculated the level of sensitivity required following the same procedure:

1. Calculating the CO velocity integrated fluxes per beam from the velocity integrated intensities observed with a single-dish telescope. Depending of the single-dish telescope used in the observations, we have assumed a different factor $S/T_{mb}$ to convert from the main beam temperature to the flux scale: 4.95 Jy/K for the IRAM 30m telescope, 27 Jy/K for the SEST 15m telescope and 29 Jy/K for the NRAO 12m telescope.

2. Calculating the flux per beam, by dividing the integrated flux by the line width, $\Delta v$ of the observed emission. In the case on non-detections, we adopted $\Delta v = 150$ km s$^{-1}$.

3. Calculating the emission expected in the interferometer synthesized beam. In order to do this, we have assumed a filling factor, $f$ for the 30m CO(1-0) observations of 0.10, which corresponds to 0.026 and 0.016 in the case of the SEST 15m telescope and the NRAO 12m telescope, respectively. Thus, the area of the single-dish beam where we expect to find emission would be $f \times \mathrm{Area}_{\mathrm{single-dishbeam}}$. We also have to correct the effect of the different beam sizes, so the flux expected in the beam of the interferometer is the result of multiplying the single-dish flux by a factor $\frac{\mathrm{Area}_{\mathrm{interf.beam}}}{\mathrm{f}\times\mathrm{Area}_{\mathrm{single-dishbeam}}}$.

   We have assumed the CO(2-1) emission to cover the same area as the CO(1-0) emission. As the area covered by the 30m CO(2-1) beam is 1/4 of the area covered by the CO(1-0)

beam, we adopt a filling factor of 0.4 for the CO(2-1) flux from the 30m telescope. Thus, for the CO(2-1) observations used in the case of SMA we multiply the 30m flux by a factor $\frac{\text{Area}_{\text{interf.beam}}}{0.4\times\text{Area}_{\text{30mbeam}}}$.

Thus, the flux expected in the interferometers beam is:

$$\text{Flux}_{\text{interferometer}}(\text{Jy beam}^{-1}) = \text{I}_{\text{CO}}(\text{K kms}^{-1}) \times \frac{\text{S}}{\text{T}_{\text{mb}}} \times \frac{1}{\Delta\text{v}} \times \frac{\text{Area}_{\text{interf. beam}}}{\text{Area}_{\text{single-dish beam}}} \times \frac{1}{\text{f}} \quad (4.1)$$

#### 4.1.2.1 Observing HCGs with SMA

As noted before, SMA receivers cannot be tuned at 115 GHz, so we chose to observe the CO(2-1) emission line. In order to restrict ourselves to reasonable observing times, we considered only those galaxies previously detected in the single-dish observations. As detailed in Chap. 2, we have detected the CO(2-1) emission in 22 galaxies, which we consider for observations with the SMA. In order to increase the sample, we have taken into account also those galaxies detected at CO(1-0) and not detected at CO(2-1) (or without CO(2-1) observations, as the galaxies with data taken from the literature). To calculate the expected CO(2-1) emission from the CO(1-0) observations we have assumed a ratio of $I_{\text{CO(2-1)}}/I_{\text{CO(1-0)}} = 1$.

The groups proposed for observations are: HCG16 and HCG 88 (with all their 4 galaxies detected), HCG23 (with 3 out of 4 galaxies detected), HCG37 (4 out of 5), HCG40 (4 out of 5), HCG93 (3 out of 4) and HCG100 (3 out of 4). HCG44, which also has 3 detected galaxies out of 4, was discarded due to its large angular size, which would require several pointings to cover each galaxy.

To study the S/N achieved when observing these groups with SMA, we ran a simulation of a full track with the SMA Sensitivity Estimator [1]. We set the parameters to observe the target source during its path in the sky in a day, constraining the observations to be performed over 20 degrees of elevation. This resultes in a typical on-source integration time of around 6 hours, with a typical rms of 10 mJy beam$^{-1}$. In Table 4.1 we detail the integrated flux calculated from the single-dish intensitity (Integrated Flux)$_{\text{SD}}$, the line width of the emission detected with the single-dish ($\Delta$V), the flux expected in the synthesized beam of SMA (Flux$_{\text{interf}}$) and the S/N ratio achieved considering the interferometer to be pointed on the galaxy.

From the analysis of the results in 4.1, we see that only HCG16 could be observed with SMA with a good S/N ratio, with 3 out of the 4 galaxies showing ratios higher than 20. For the other groups, several tracks would be required to detect at least one galaxy with a good S/N ratio.

#### 4.1.2.2 Observing HCGs with PdB

For PdB we performed a different analysis: we calculated the observing time required to map with a S/N = 10 all the galaxies detected in the single-dish observations. We chose this high S/N in order to detect not only the strong emission at the center of the galaxies, but also a fainter, more extended component. The S/N ratio has been calculated as explained in Sec. 4.1.2 and quantified in Eq. 4.1. From the expected flux in the interferometer beam, we have set the required rms as $\frac{1}{10}$ of the flux. The on-source integration time required to achieve this rms has been calculated using the formula in the IRAM Newsletter 72

[1] http://sma1.sma.hawaii.edu/beamcalc.html

*Table 4.1: S/N ratios achieved for different galaxies after a full SMA track*

| Group | Galaxy | Integrated $Flux_{SD}$ (Jy km $s^{-1}$) | $\Delta V$ (km $s^{-1}$) | $Flux_{interf}$ (mJy) | S/N ratio |
|---|---|---|---|---|---|
| HCG16 | 16a | 212.2 | 150 | 304.1 | 31.2 |
| | 16b | 62.1 | 560 | 24.0 | 2.5 |
| | 16c | 248.4 | 270 | 199.2 | 20.4 |
| | 16d | 163.2 | 150 | 233.9 | 24.0 |
| HCG23 | 23a | 4.5 | 360 | 2.7 | 0.3 |
| | 23b | 48.0 | 318 | 32.5 | 3.3 |
| | 23c | ND | | | |
| | 23d | 10.6 | 83 | 27.6 | 2.8 |
| HCG23 | 37a | 1.9 | 185 | 1.96 | 0.2 |
| | 37b | 42.8 | 552 | 14.9 | 1.8 |
| | 37c | 2.8 | 240 | 2.2 | 0.3 |
| | 37d | 2.5 | 200 | 2.4 | 0.3 |
| | 37e | ND | | | |
| HCG40 | 40a | ND | | | |
| | 40b | 4.8 | 130 | 7.6 | 0.8 |
| | 40c | 48.0 | 233 | 42.9 | 4.6 |
| | 40d | 25.2 | 295 | 17.8 | 1.9 |
| | 40e | 8.0 | 480 | 3.5 | 0.4 |
| HCG88 | 88a | 26.8 | 575 | 9.8 | 1.0 |
| | 88b | 15.4 | 505 | 6.4 | 0.7 |
| | 88c | 23.7 | 150 | 33.0 | 3.5 |
| | 88d | 3.9 | 190 | 4.3 | 0.5 |
| HCG93 | 93a | 14.9 | 295 | 9.8 | 1.1 |
| | 93b | 64.9 | 270 | 46.3 | 5.4 |
| | 93c | 18.6 | 465 | 7.7 | 0.9 |
| | 93d | ND | | | |
| HCG100 | 100a | 16.6 | 275 | 11.7 | 1.3 |
| | 100b | 7.9 | 180 | 8.5 | 1.0 |
| | 100c | 7.0 | 190 | 7.1 | 0.8 |
| | 100d | ND | | | |

ND: Galaxies non-detected in the single-dish observations

(http://iram.fr/IRAMFR/ARN/feb09/feb09.html). As explained in that document, the total observing time, including the different calibrations, is usually 1.6 times larger.

The integration times required to achieve a S/N = 10 for PdB are detailed in Table. 4.2. Together with it, we display the fluxes observed with the 30m and the expected flux in the interferometer beam, calculated from Eq. 4.1.

*Table 4.2: Integration times required to achieve a S/N = 10 for PdB and ALMA*

| Galaxy | (Integrated Flux)$_{SD}$ (Jy km $s^{-1}$) | $\Delta$V (km $s^{-1}$) | Flux$_{interf}$ (mJy beam$^{-1}$) | t$_{Pdb}$ (min) | t$_{ALMA}$ |
|---|---|---|---|---|---|
| 7a | 194.40 | 500 | 72.8 | 13.0 | 2.2 |
| 7b | 7.25* | 150 | 9.0 | | 147 |
| 7c | 40.60 | 183 | 41.3 | 40.5 | 7.0 |
| 7d | 15.12* | 150 | 18.9 | | 33.3 |
| 10a | 13.46 | 339 | 7.4 | 1265 | 292 |
| 10b | <26.10 | 150 | 32.4 | | >15.2 |
| 10c | 35.34 | 359 | 18.3 | 206 | 47.7 |
| 10d | < 6.67 | 150 | 8.3 | | > 232 |
| 15a | 2.08* | 150 | 2.6 | | 1757 |
| 15b | 3.71* | 150 | 4.6 | | 565 |
| 15c | 2.57* | 150 | 3.2 | | 1167 |
| 15d | 3.07 | 160 | 3.6 | 5422 | 922 |
| 15e | < 2.23 | 150 | 2.8 | | >1642 |
| 15f | < 2.13 | 150 | 2.6 | | >1642 |
| 16a | 212.16 | 150 | 263.0 | 0.96 | 0.17 |
| 16b | 62.10 | 560 | 20.8 | 160 | 26.8 m |
| 16c | 248.40 | 270 | 172.2 | 2.3 | 0.38 |
| 16d | 163.15 | 150 | 202.3 | 1.68 | 0.28 |
| 23a | 4.45 | 360 | 2.3 | 13026 | 2203 |
| 23b | 48.01 | 318 | 28.1 | 87.4 | 14.7 |
| 23c | < 2.13 | 150 | 2.6 | | >1714 |
| 23d | 10.64 | 83 | 23.8 | 121.3 | 20.5 |
| 25a | 12.67 | 193 | 12.2 | 463 | 79.8 |
| 25b | 12.92 | 510 | 4.7 | 3109 | 536 |
| 25d | < 1.53 | 150 | 1.9 | | >3283 |
| 25f | < 0.89 | 150 | 1.1 | | >9792 |
| 30a | 20.30* | 150 | 25.2 | | 18.5 |
| 30b | <12.47 | 150 | 15.5 | | 49.0 |
| 30c | < 2.32 | 150 | 2.9 | | >1400 |
| 30d | < 0.87 | 150 | 1.1 | | >9734 |
| 31a | < 3.77 | 150 | 4.7 | | >533 |
| 31b | < 5.80 | 150 | 7.2 | | >227 |
| 31c | 7.57 | 148 | 9.5 | 761 | 130 |
| 31g | < 2.32 | 150 | 2.9 | | >1400 |
| 37a | 1.88 | 185 | 1.9 | 19297 | 4075 |
| 37b | 42.82 | 552 | 14.4 | 331 | 70.8 |
| 37c | 2.77 | 240 | 2.1 | 14954 | 3038 |
| 37d | 2.47 | 200 | 2.3 | 13026 | 2779 |

*Table 4.2: Integration times required to achieve a S/N = 10 for PdB and ALMA (continued)*

| Galaxy | Integrated $Flux_{SD}$ (Jy km $s^{-1}$) | $\Delta$V (km $s^{-1}$) | $Flux_{interf}$ (mJy beam$^{-1}$) | $t_{Pdb}$ (min) | $t_{ALMA}$ (min) |
|---|---|---|---|---|---|
| 37e | < 1.14 | 150 | 1.4 | | >7502 |
| 40a | 6.53* | 150 | 8.1 | | 179 |
| 40b | 5.15 | 110 | 8.7 | 910 | 155 |
| 40c | 48.01 | 233 | 38.3 | 47.0 | 8.0 |
| 40d | 25.20 | 295 | 15.9 | 273 | 46.4 |
| 40e | 8.02 | 480 | 3.1 | 7147 | 1220 |
| 44a | 51.97 | 269 | 35.9 | 53.4 | 10.4 |
| 44b | 3.46* | 150 | 4.3 | | 726 |
| 44c | 37.77 | 165 | 42.6 | 38.0 | 7.39 |
| 44d | 11.53 | 155 | 13.8 | 360 | 70.2 |
| 58a | 145.33 | 550 | 49.1 | 28.6 | 5.1 |
| 58b | 19.65 | 625 | 5.8 | 2017 | 367 |
| 58c | 2.43* | 150 | 3.0 | | 1368 |
| 58d | 2.38* | 150 | 2.9 | | 1422 |
| 58e | 14.75 | 195 | 14.1 | 349 | 61.8 |
| 67a | 26.10* | 150 | 32.4 | | 11.12 |
| 67b | 66.70 | 234 | 53.0 | 24.5 | 4.15 |
| 67c | < 4.93 | 150 | 6.1 | | >314 |
| 68a | 2.33* | 150 | 2.9 | | 17971 |
| 68b | 20.30* | 150 | 25.2 | | 28.29 |
| 68c | 34.75 | 214 | 30.2 | 75.6 | 19.7 |
| 68d | < 6.38 | 150 | 7.9 | | >285 |
| 68e | < 3.71 | 150 | 4.6 | | >849 |
| 79a | < 6.19 | 150 | 7.7 | | >226 |
| 79b | 4.50 | 320 | 2.6 | 10068 | 1958 |
| 79c | 2.08 | 105 | 3.7 | 5088 | 971 |
| 79d | < 2.57 | 150 | 3.2 | | >1298 |
| 88a | 31.63 | 550 | 10.7 | 603 | 102 |
| 88b | 15.69 | 355 | 8.2 | 1020 | 173 |
| 88c | 58.00 | 251 | 43.0 | 37.4 | 6.33 |
| 88d | 5.25 | 330 | 3.0 | 7891 | 1300 |
| 92b | 14.50* | 150 | 18.0 | | 48.40 |
| 92c | 17.40 | 195 | 16.6 | 250 | 56.91 |
| 92d | 14.50* | 150 | 18.0 | | 48.40 |
| 92e | 2.43* | 150 | 3.0 | | 1742 |
| 93a | 8.12 | 255 | 5.9 | 1968 | 376 |
| 93b | 55.74 | 325 | 31.9 | 67.8 | 12.8 |
| 93c | 18.96 | 520 | 6.8 | 1501 | 283 |
| 93d | < 3.56 | 150 | 4.4 | | >676 |
| 97a | 6.68* | 150 | 8.3 | | 172 |
| 97b | 17.57 | 430 | 7.6 | 1194 | 204 |
| 97c | 1.14* | 150 | 1.4 | | 6019 |
| 97d | 4.50* | 150 | 5.6 | | 377 |
| 97e | < 0.69 | 150 | 0.9 | | >14573 |

*Table 4.2: Integration times required to achieve a S/N = 10 for PdB and ALMA (continued)*

| Galaxy | Integrated $\text{Flux}_{SD}$ (Jy km $s^{-1}$) | $\Delta$V (km $s^{-1}$) | $\text{Flux}_{interf}$ (mJy beam$^{-1}$) | $t_{Pdb}$ (min) | $t_{ALMA}$ (min) |
|---|---|---|---|---|---|
| 100a | 21.48 | 435 | 9.2 | 818 | 148 |
| 100b | 4.11 | 185 | 4.1 | 4045 | 746 |
| 100c | 5.05 | 185 | 5.1 | 7520 | 482 |
| 100d | $<1.63$ | 150 | 2.0 | | >3139 |

The fluxes marked with * are derived from the expected $M_{H_2}$ of the galaxy

Considering the high integration times estimated for some galaxies, the observing strategy should focus on covering groups with a high rate of detected galaxies. HCG16, selected to be observed with SMA is a good choice. In addition, other groups with a high rate of detected galaxies to be observed with PdB are HCG23, HCG40, HCG58 or HCG88. HCG44, with 3 detected galaxies, is the closest group of our full sample and their galaxies show angular diameters ranging from 2′ to 3.6′, so several pointings would be needed to map each galaxy, increasing the required observing time.

#### 4.1.2.3 Observing HCGs with ALMA

As we have done for PdB in the former section, we calculated the integration time required to observe the galaxies in our sample with ALMA. We performed our calculations using the Early Science Sensitivity Calculator for ALMA [2], which allows us to calculate the integration time required to achieve a certain rms. We ran our simulations with an array consisting of sixteen 12-meters antennas.

In the case of ALMA, we considered not only the galaxies detected with the single-dish observations, but also those not detected. ALMA provides us with a higher sensitivity and, thus, we aim for a more ambitious observing plan. To calculate the rms needed to achieve a S/N = 10 for the galaxies not detected with a single-dish telescope, we considered first the expected $I_{CO}$, derived from the $M_{H_2}$ expected from the blue luminosity of the galaxy, as detailed in Chap. 2. When the upper limit derived from the single-dish $I_{CO}$ observations was lower than the value derived from the expected $M_{H_2}$, we adopted the upper limit. The integration times required to achieve a S/N = 10 are detailed in Table. 4.2. Some interesting groups that would be discarded for PdB, as HCG79, HCG31 or HCG92 could be observed with ALMA.

If instead of the early science array consisting of 16 antennas we take into account the full array for ALMA (considering 50 antennas), the time required to achieve a 10 mJy beam$^{-1}$ sensitivity is only 6 seconds, 1 order of magnitude smaller than the Early Science 16-antennas array and 3 orders of magnitude smaller than that of SMA.

To summarize the results achieved for PdB and ALMA, we display in Tab. 4.3 the time required to map all the galaxies in each HCG of our sample, taking into account the observing time required for each galaxy listed in Table. 4.2. We have summed the time required to observe with PdB and ALMA (with the Early Science array) the galaxies detected with the single dish, taking into account that, for some groups, we can observe several galaxies in a single pointing. In the case of ALMA, we detail also the time and the pointings required to map all the galaxies in the group, including those not previously detected in the single-dish observations.

[2] http://www.eso.org/sci/facilities/alma/observing/tools/etc/

Table 4.3: Time required to map the galaxies in each HCG with PdB and ALMA

| Group | Pointings (detected) | $t_{PdB}$ (min) | $t_{ALMA}$ (detected) (min) | Pointings (all) | $t_{ALMA}$ (all) (min) |
|---|---|---|---|---|---|
| HCG7 | 2 | 53.4 | 9.2 | 4 | 189 |
| HCG10 | 2 | 1470 | 339 | 4 | >587 |
| HCG15 | 1 | 5422 | 922 | 5 | >7694 |
| HCG16 | 4 | 165 | 27.3 | 4 | 27.3 |
| HCG23 | 3 | 13235 | 2238 | 4 | >3952 |
| HCG25 | 2 | 3571 | 616 | 3 | >13155 |
| HCG30 | 0 | | | 4 | >11202 |
| HCG31 | 1 | 762 | 130 | 3 | >2161 |
| HCG37 | 4 | 47608 | 9963 | 5 | >17466 |
| HCG40 | 2 | 7422 | 1429 | 3 | 1445 |
| HCG44 | 3 | 452 | 94.8 | 4 | 821 |
| HCG58 | 3 | 2394 | 434 | 5 | 3224 |
| HCG67 | 1 | 24.5 | 4.15 | 4 | >329 |
| HCG68 | 1 | 76.4 | 19.7 | 5 | >19156 |
| HCG79 | 2 | 10067 | 1958 | 2 | >3481 |
| HCG88 | 4 | 9552 | 1581 | 4 | 1581 |
| HCG92 | 1 | 250 | 59.9 | 3 | 1895 |
| HCG93 | 3 | 3537 | 671 | 4 | >1347 |
| HCG97 | 1 | 1194 | 3.3 | 5 | >3050 |
| HG100 | 3 | 12382 | 1377 | 4 | >4516 |

## 4.2 Calibrating the interferometers: the fast-switching

### 4.2.1 The atmosphere and its influence on the observations

The atmosphere always presents different restrictions to the astronomical observations, regardless of the wavelength we are observing in. The main difference between radioastronomical observations carried out at centimeter wavelengths and those performed at higher frequencies can be seen in Fig. 4.1. At centimeter wavelengths, where we find the so-called "radio window", most of the radiation can pass through the atmosphere without absorption. In the case of mm and submm observations, there are only some frequency bands where the atmosphere allows us to perform observations. Furthermore, the opacity of these regions strongly depends on atmospherical conditions such as the water vapour content, as can be seen in Fig. 4.2.

Apart from the opacity, there are other effects produced by either the low neutral atmosphere or the ionosphere which can affect our observations. These phenomena are:

- Refractive effects produced by large-scale structures, which results in a propagation delay of the electromagnetic waves.
- Scattering phenomena produced by the turbulent structure of the medium, resulting in degradation of the angular resolution.

In the case of mm and submm wavelengths, water vapor in the troposphere plays a key role, since the refractivity of water vapor at these wavelengths is 20 times larger than in the optical

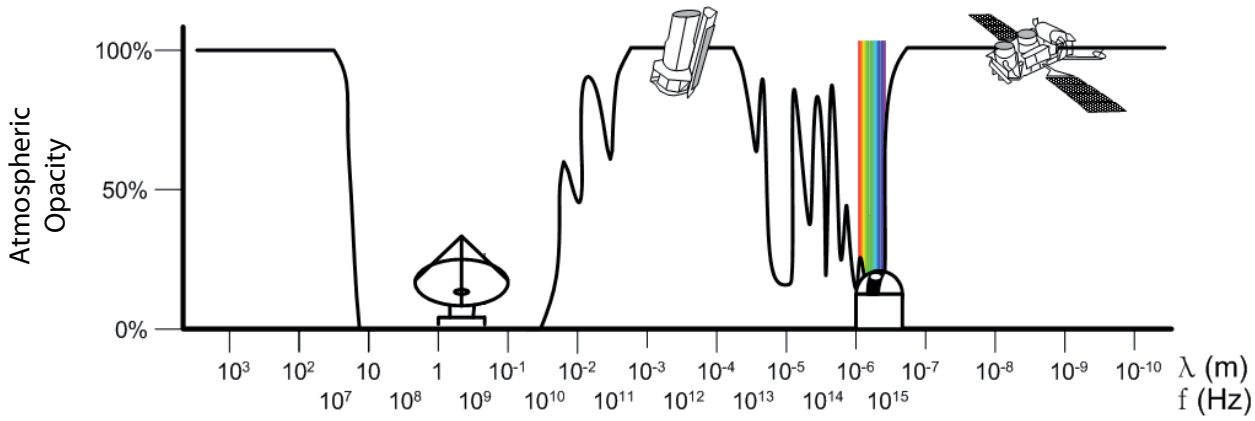


*Figure 4.1: Atmosphere opacity as a function of the wavelength. Plot under free-use license taken from http://no.wikipedia.org.*

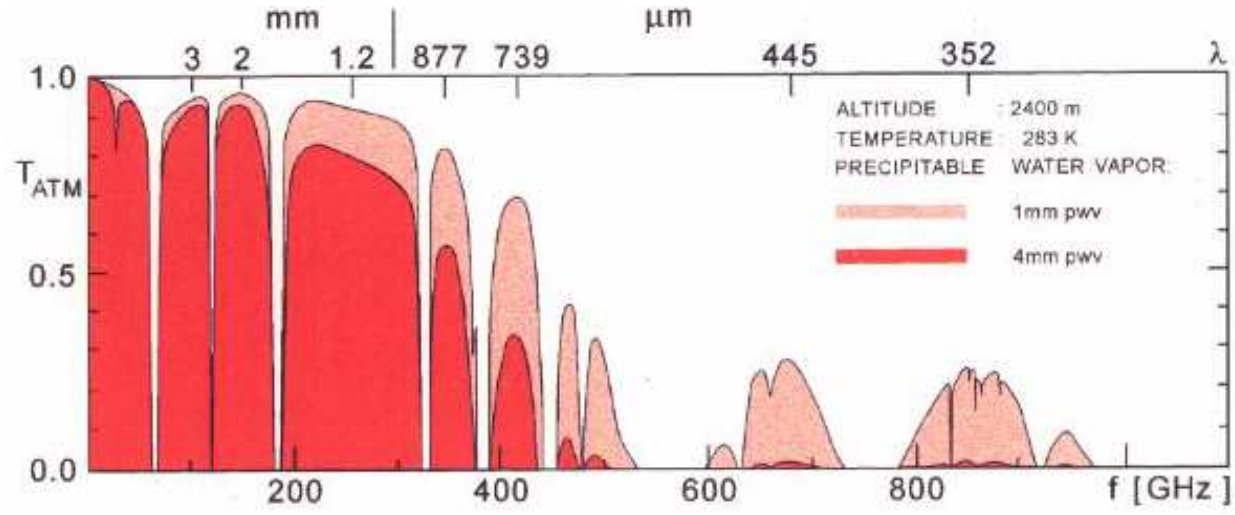


*Figure 4.2: Atmospherical transmission at mm and submm wavelengths measured at PdB site for water vapor contents of 1 and 4 mm, taken from the Submillimeter Telescope Observatory (SMTO) webpage (http://www.mpifr-bonn.mpg.de/div/hhertz/general_info.html).*

regime. Thus, radiotelescopes are placed in sites with a relative humidity index as low as possible. Fluctuations of the water vapor distribution, which are hard to measure with precision from ground-based atmospherical measurements, are the main origin of phase fluctuations of the observed visibilities of mm and submm interferometers. These turbulences limit the interferometer angular resolution, playing a role similar to the seeing effect produced by temperature changes when observing in optical frequencies. The effect of water vapor in the measurements is described by the Smith-Weintraub empirical equation

$$N = 77.6\frac{P_D}{T} + 64.8\frac{P_V}{T} + 3.776\times 10^5\frac{P_V}{T^2} \tag{4.2}$$

which gives the refractivity of humid air (N) as a function of the temperature (T) in K, the partial pressure of dry air ($P_D$) and the partial pressure of water vapor ($P_V$) (pressures are expressed in millibars). It can be seen how the time-dependent water vapor pressure generates a time-dependence on the air refractivity, producing an excess on the optical path of the wave.

The air refractivity, due to its dependence on the water vapor pressure, can be defined only locally. The variations of the optical path will generate fluctuations of the wave front, which can be characterized using a phase structure function defined as:

$$D(\phi)(d) = < [\phi(x) - \phi(x-d)]^2 > \tag{4.3}$$

where $\phi$ is the phase at the point (x) and $\phi$(x-d) the phase at (x-d). It is generally assumed that D($\phi$) depends only on the baseline length. From this parameter, we can define the rms deviation $\sigma(\phi)$ on the interferometer phase as:

$$\sigma(\phi) = (D_\phi(d))^{1/2} \tag{4.4}$$

In the current models, $\sigma(\phi)$ is considered to be a power law function of the distance between antennas, with the exponent depending on the chosen model (gaussian, lorentzian, Kolmogorov). This dependence is found only below the outer scale length of the interferometer $d_m$, defined as the distance beyond which optical path fluctuations are not longer correlated and, thus, the rms deviation becomes constant. This phenomenon allows the astronomers to perform very large baseline interferometry (VLBI) observations. If we consider an interferometer operating with baselines shorter than $d_m$, we find the measured visibility, $V_\mathrm{m}$, to be related with the real one, V, as:

$$V_m = V e^{i\phi} \tag{4.5}$$

Assuming $\phi$ as a random gaussian variable with an average value equal to zero, the expected visibility is:

$$< V_m > = V < e^{i\phi} > = V e^{\frac{-\sigma_\phi^2}{2}} \tag{4.6}$$

which makes evident that phase fluctuations caused by atmospherical turbulences results in a worse image obtained from the interferometric observations.

### 4.2.2 Gain calibration in mm and submm wavelengths

In mm and submm wavelengths, we different calibration techniques are used, including:

- Passband calibration, to calibrate the different sensitivity of the spectral channels.
- Gain calibration, to correct the temporal variations of phase and amplitude due to the atmosphere and instrumentation.
- Flux calibration, to establish an absolute flux scale.

I order to improve the gain calibration at mm/submm wavelengths different techniques can be used:

- The self-calibration technique.

- The water vapor radiometry (WVR).
- The fast-switching technique.

The self-calibration technique requires a previous model of the target brightness distribution. Complex gains corresponding to the different antennas are calculated with a minimum square fit, which minimizes the differences between the model and the observed visibilities. This process is applied in successive iterations, generating a new model once the visibilities are corrected. The main advantage of the self-calibration is that the gains are derived from a pointing on the target, not on a calibrator.The solution becomes more robust as we increase the number of baselines. On the other hand, this technique is strongly dependent on the original model chosen. A wrong model will lead to incorrect visibilities and images.

Water vapor radiometry aims to determine the excess of the optical path due to the total water vapor content in the line of sight of the antennas. This content can be determined with precision measuring the brightness temperature of a water vapor emission line, mostly those at 22 and 183 GHz, depending on the atmospherical conditions of the interferometer site. At medium heights, such as the PdB site, the 183 GHz line is saturated, so the one at 22 GHz is generally used, while the 183 GHz line is preferred in sites with a very dry atmosphere. This is the case of Chajnantor, the ALMA site.

An inconvenience when using water vapor radiometry is that the dependence of the path excess on the water vapor measurement, which depends on atmospherical models, is approximated. The behavior of the atmosphere can not be modeled with precision and thus the water vapor radiometry can correct with full precision only the effects of phase fluctuations at a timescale of seconds and under specific weather conditions. When facing larger timescales, a more general technique, complementary to the water vapor radiometry, is required to correct phase fluctuations. This is the aim of the fast-switching technique, which we develop in the next section.

### 4.2.3 The fast-switching. Technical basics.

#### 4.2.3.1 The fast-switching technique

As we have already pointed out, the problem we want to study is the effect of the rapid variations of the water vapor content in the troposphere, more specifically, the water vapor contained in the line of sight of the antennas. The local concentration of water vapor changes rapidly in a random and turbulent way with time, in such a way that the changes it generates on the received signal also vary rapidly with time.

Fast-switching basically consists on reducing the time between successive pointings on the calibrator, aiming for a more accurate monitoring of the phase distortions introduced by the atmosphere. At the VLA, observing at centimeter wavelengths, this technique has been satisfactorily applied, with angular separations between the source and the calibrator between 5 and 10 degrees. In the centimeter observations, the ionosphere is the main origin of phase variations, with a contribution to the phase lag that scales with the square of the wavelength. Thus, the minimum wavelength for which the ionosphere is the main responsible of phase variations is usually set at 3.6 or 1.3 cm. For shorter wavelengths, the troposphere plays a more important role.

Since we are interested in mm and submm wavelengths, our work will be focused on the troposphere and, more precisely, on the part of the phase distortion in the troposphere associated to the effects of the wet air.

The solution proposed to reduce the effects of the wet atmospherical component variability in the astronomical image is based on choosing a point-like source that is powerful in mm or submm (typically a quasar) and near to the target we want to study. By performing rapid pointing changes to the quasar we can get real time information about the variation of water vapor in the line of sight of the target. The behavior of the atmosphere strongly depends on the line of sight selected and, thus, we need a calibrator with a short angular distance to the target. The more we know about the changes in the wave front produced by water vapor in the troposphere, the better we can determine the delay generated by them and, in consequence, the better we can correct the phase and the time delay between the interferometer antennas.

The development of fast-switching is significant in the context of ALMA since it is expected to be, together with WVR, one of the gain calibration techniques to be used.

#### 4.2.3.2 Fast-switching in the SubMillimeter Array

The work we present consists of testing the fast-switching technique in the SMA in collaboration with members of the Academia Sinica-Institute for Astronomy and Astrophysics of Taiwan. The SMA antennas were originally designed to allow rapid pointing changes to allow the application of such a technique. As displayed in Fig. 4.3, the SMA observing bands match quite well with those of ALMA. Therefore, the tests performed at the SMA have a direct application for ALMA. Furthermore, SMA allows us to perform observations in the submm range, which cannot be reached with other current interferometers such as PdB or CARMA.

### 4.2.4 Observations and data reduction

We present here observations of different sets of 3 quasars located at short angular distances. The observations were carried out under different atmospherical conditions to test how the technique works each case. The observations, carried out during september 2, 4, 5 and 6th, 2004, were performed at 230 and 345 GHz, to test the technique at different frequencies. The different parameters of the observations are shown in Tab. 4.4, which includes:

- Column 1: Dataset designation.
- Column 2: Date of the observations (dd/mm/yy).
- Column 3: Antennas used in the observations.
- Column 4: $\tau$, zenithal opacity at 225 GHz, observed with the Caltech Submillimeter Observatory (CSO) antenna, also placed at Mauna Kea.
- Column 5: Observing frequency.
- Column 6: Set of quasars observed.

The aim of these tests was to determine which calibration time provides the best image, i.e., with the highest S/N ratio. Thus, we have calibrated the data using different time lapses between consecutive pointings to the calibrator, from the usually adopted of 20 or 30 minutes in cm experiments down to 1 or 2 minutes.

The observations were performed at a single frequency for the set of 3 quasars, which changed depending on the observation date (Tab. 4.4). For each quasar, 4 integrations of 5

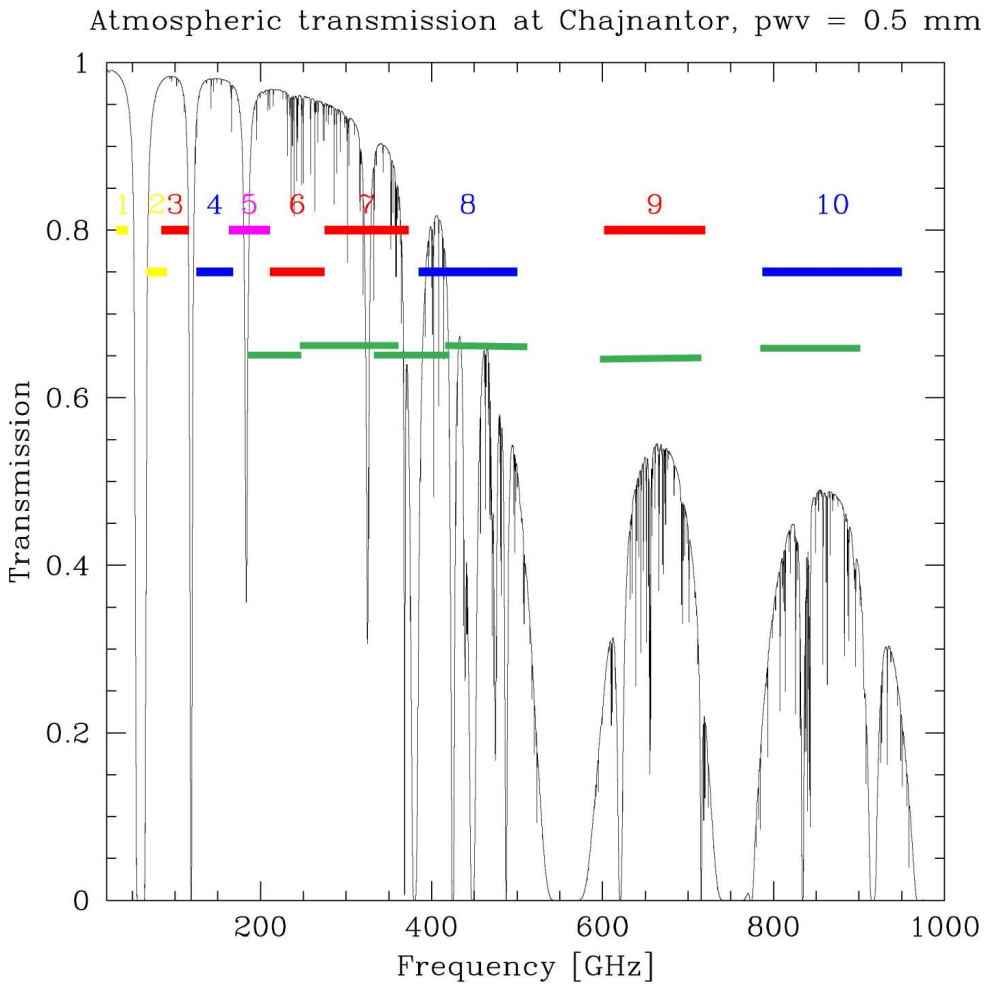


*Figure 4.3: ALMA observing bands overlayed on atmospherical transmission at Chajnantor. In green, SMA observing bands. Image taken from the ALMA webpage (http://www.eso.org/sci/facilities/alma/observing/specifications)*

seconds were performed, giving a total integration time of 20 seconds per pointing. Then, the interferometer was pointed to the next quasar and the sequence was repeated. Finally, an identical observation was performed on the third quasar and then the full sequence was started again. At the end of the observing track, the total integration time was approximately one hour per source. If we consider an angular separation of 10 degrees between the quasars, the time required to switch from one source to another was approximately 5 seconds.

#### 4.2.4.1 Data calibration and reduction

From the set of quasars observed at each frequency we chose the most luminous one as the gain calibrator. Taking into account all the integrations in this source, we calibrated the other two sources in phase and amplitude. As a result, we obtained a calibration with a time interval between consecutive pointings to the calibrator (hereafter *calibration cycle*) of approximately 1min 40sec. This calibration cycle slightly changed depending on the dataset, since the time needed to switch from one source to another depends on the angular separation between the quasars.

After this first calibration, we flagged every other pointing to the calibrator to discard it for the calibration. In this way, we duplicated the calibration cycle interval, from 1min 40 sec to

Table 4.4: Technical data of the SMA observations

| Dataset | Date | Antennas | $\tau$ | Frequency (GHz) | Sources |
|---|---|---|---|---|---|
| 040902-104551 | 2/9/04 | 1,2,3,4,7,8 | 0.08-0.10 | 230 and 345 | 3c454.3, 2145+067, 2230+114 |
| 040902-044603 | 2/9/04 | 1,2,3,4,7,8 | 0.13 | 345 | 1921-293, 1908-201, nrao530 |
| 040904-195452 | 4/9/04 | 1,2,3,4,5,6,7,8 | 0.1 | 230 | 3c279, 1334-127, 1244-255 |
| 040905-215041 | 5/9/04 | 1,2,3,4,5,6,7,8 | 0.1-0.14 | 230 | 3c279, 1334-127, 1244-255 |
| 040906-013535 | 6/9/04 | 1,2,3,4,5,6,7,8 | 0.17 | 230 | 3C279, 1334-127, 1921-293 |

Table 4.5: Times of calibration for the different calibration schemes

| Calibration number | Pointings to the calibrator taking into account | Calibration cycle interval |
|---|---|---|
| 1 | All | 1min 43sec |
| 2 | 1 out of 2 | 3min 26sec |
| 3 | 1 out of 3 | 5min 10sec |
| 4 | 1 out of 5 | 8min 36sec |
| 5 | 1 out of 6 | 10min 20sec |
| 6 | 1 out of 7 | 12min 3sec |
| 7 | 1 out of 10 | 17min 12sec |
| 8 | 1 out of 12 | 20min 40sec |

3min 20sec. A similar procedure was applied for the third calibration, taking into account only 1 in 3 pointings to the calibrator. This process was iterated in the way shown in Tab. 4.5. We also include the calibration cycles of the dataset 040902-104551, which are quite similar in all the datasets.

A standard phase and amplitude calibration was performed using the MIR/IDL[3] data reduction package for SMA. After that, we performed the imaging process with Miriad, following a standard 3-steps scheme as the one used in the OVRO images detailed in Chap. 3, consisting in generating the dirty image from the UV visibilities with the INVERT task, producing the clean components map with the CLEAN task and, finally, using the RESTOR task to generate the clean map where the intensity of the source and the rms was measured in such a clean map, and we obtained a measurement of the signal-to-noise (S/N) ratio. This process was performed for each calibration scheme, getting a different value of the S/N ratio for each source and calibration cycle.

The description of the results for each dataset we present here includes:

- The elevation and flux of the three quasars observed. Since quasars are variable sources, we adopted flux measurements from previous observations performed in a date close to our observations.

- The continuum visibilities (phase and amplitude) for different baselines and as a function of time. We show the visibilities before the calibration and the ones corresponding to different calibration cycles.

[3]http://cfa-www.harvard.edu/~cqi/mircook.html, MIR is a software package to reduce data taken with the Smithsonian Submillimeter Array (SMA). The MIR package was originally developed by Nick Scoville at Caltech.

*Table 4.6: Flux and elevation of the quasars observed in the dataset 040902-104551*

| Source | Elevation (deg) | Flux density (Jy/beam) |
|---|---|---|
| 2230+114 (calibrator) | 70 | 7.37± 0.39 |
| 3c454.3 | 50-75 | 3.44± 0.18 |
| 2145+067 | 30-50 | 3.81± 0.20 |

- A plot with the S/N ratio of the two targets as a function of the calibration cycle.

#### 4.2.4.2 Dataset 040902-104551

The observations were performed at 345 GHz with an atmospherical opacity of $\tau_{225GHz} =$ 0.08 - 0.10, which can be considered good atmospherical conditions. The observed sources and their fluxes are shown in Tab. 4.6. 2230+114 was chosen as the calibrator.

To illustrate the behavior of the data trhough the different calibrations, we display in Figs. 4.4, 4.5 and 4.6 the visibilities for three different baselines (1-2, 1-3 and 1-4) corresponding to the uncalibrated data and the data calibrated using a calibration cycle of 1min 43sec and 8min 36sec, respectively.

The calibrator shows a low phase scatter for many of the baselines, with a deviation with respect to the median value around ± 50º, but with a variation of ∼150º between peaks for some baselines. 3c454.3 shows a slightly larger scatter. 2145+067 shows a scatter that, even being low, is larger than the one shown by the other two sources. The difference can be easily seen once the data are calibrated, since phase scatter for 3c454.3 turns to be quite low, around ± 50º, while for 2145+067 is larger. This trend can be due to the low elevation of the source, which was below 40º at some points during the observations. Comparing the visibilities of the data resulting from a calibration cycle of 1min 43sec with those of 8min 36sec we see that the peak to peak variation for the data with the shortest calibration cycle is very low, while for the 8min 36sec calibration cycle shows a much higher systematic variation, close to the one shown by the uncalibrated data.

In Fig. 4.7 we display the S/N ratio of the images of the targets generated from the visibilities as a function of the calibration cycle. From a joint analysis of this plot and the visibilities of the sources we get the following results:

- 3c454.3: The flux peaks are some of the highest of all datasets. The S/N ratio is between 38 and 41. The S/N ratio decreases as we increase the calibration time, with a difference of $\Delta$(S/N) = 4 between the shortest (t $\simeq$ 1.7 min) and longest (t $\simeq$ 20min) calibration time.

- 2145+067: The maximum value of the flux is close to the one of 3c454.3, with values of S/N $\simeq$ 28. The trend shown by the data is the same as for 3c454.3, with the S/N decreasing as the calibration time increases. The flux of 3c454.3 and of this source are quite similar (S$\sim$ 3.5 Jy), so the lower value for the S/N ratio of 2145+067 can be due to the lower elevation of this source.

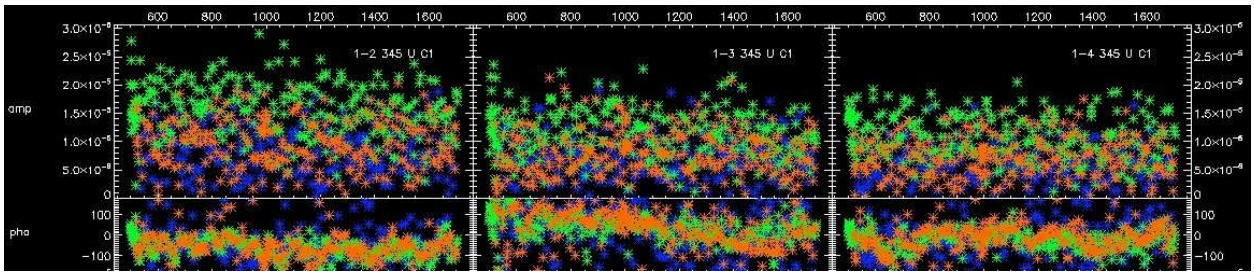


*Figure 4.4: Visibilities of the uncalibrated data in 040902-104551. Green: 2230+114, calibrator. Blue: 2145+067. Orange: 3c454.3*

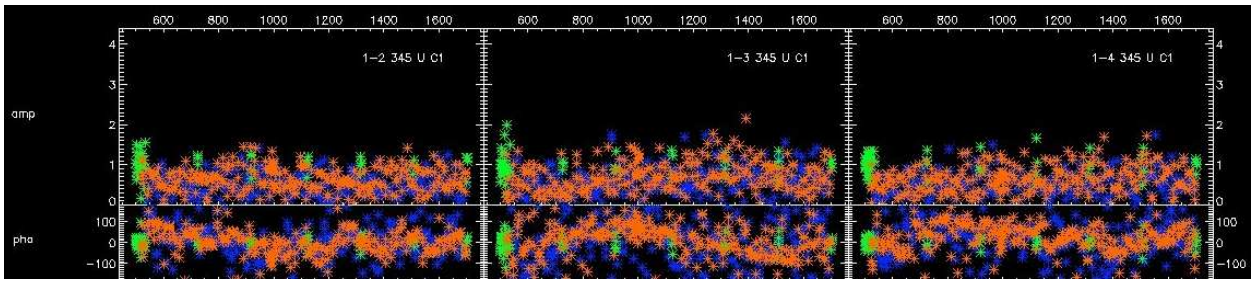


*Figure 4.5: Visibilities of the data in 040902-104551 corresponding to a calibration cycle of 8min 36sec, with the color code described in Fig. 4.4.*

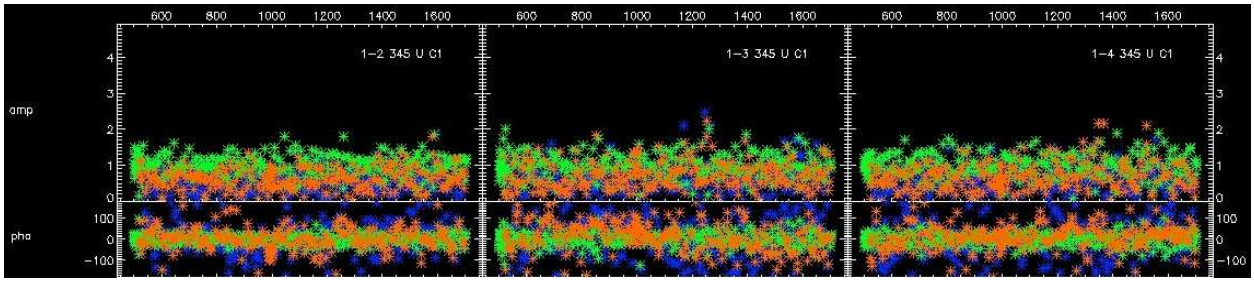


*Figure 4.6: Visibilities of the data in 040902-104551corresponding to a calibration cycle of 1min 43sec, with the color code described in Fig. 4.4.*

#### 4.2.4.3 Dataset 040902-044603

The observations of this dataset were performed at 345 GHz, with an opacity $\tau_{225GHz} = 0.13$, close to the limit recommended for this frequency. Due to the high opacity, the quality of the data is not good. The observed sources and their fluxes are shown in Tab. 4.7. 1921-293 was chosen as the calibrator.

The continuum visibilities for some baselines are shown in Appendix B, together with those of the following datasets. Due to the atmospherical conditions, the visibilities show a high phase scatter. The targets, with fluxes around 1 Jy, are too low to be observed successfully under this atmospherical conditions.

In the case of nrao530, the phase scatter decrease slightly after the calibration from an original scatter of $\sim 150^o$ to $\sim 100^o$. For 1908-201, the scatter seems to be quite similar to that of nrao530, but there are baselines with no significant differences between uncalibrated and calibrated data (see the plots in B.2).

From the analysis of the calibrated images and the study of the S/N vs calibration plot in Fig. 4.8 we reach the following conclusions:

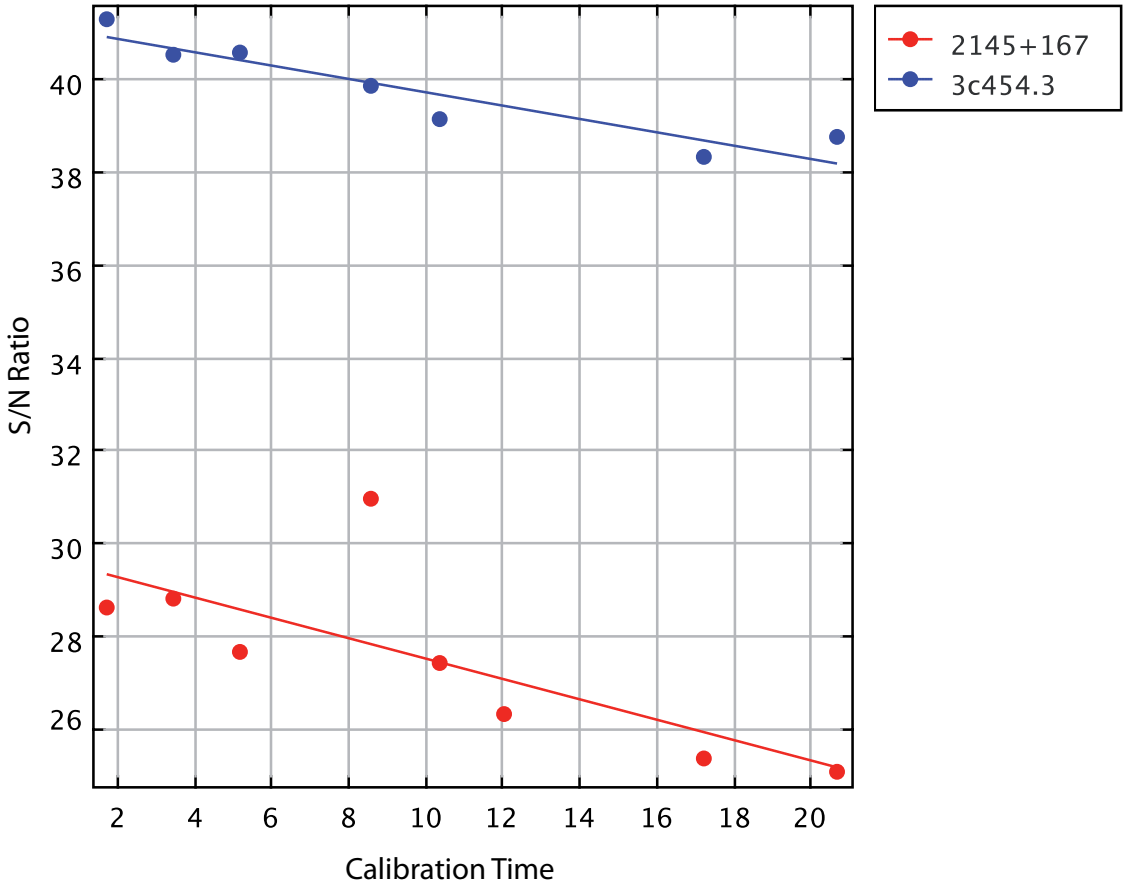


*Figure 4.7: S/N as a function of the calibration cycle interval (in minutes) for the dataset 040902-104551*

- 1908-201: The intensity peak can be seen in the clean image, but there are peaks of noise spread over the image. The S/N ratio has a value around 12 for all the calibration cycles. In Fig. 4.8 we can see two points showing unusually high values of the S/N ratio. The lower values corresponding to other calibration times are probably due to the noise peaks out of the center of the image. The linear fit is almost constant with the calibration time.

- nrao530: The S/N ratio is almost constant for the different calibration times (S/N $\sim$ 7). A visual inspection of the images reveals that the maximum of the emission, from which the S/N ratio is calculated, is not coming from the source, but from noise peaks. The lower flux density of the source with respect to the previous dataset, together with the low elevation (20$^o$) of part of the observations are probably the cause of this behavior.

*Table 4.7: Flux and elevation of the quasars observed in the dataset 040902-044603*

| Source | Elevation (deg) | Flux density (Jy/beam) |
|---|---|---|
| 1921-293 (calibrator) | 30-40 | 5.57± 0.36 |
| 1908-201 | 35-50 | 1.72±0.11 |
| nrao530 | 20-60 | 1.49±0.14 |

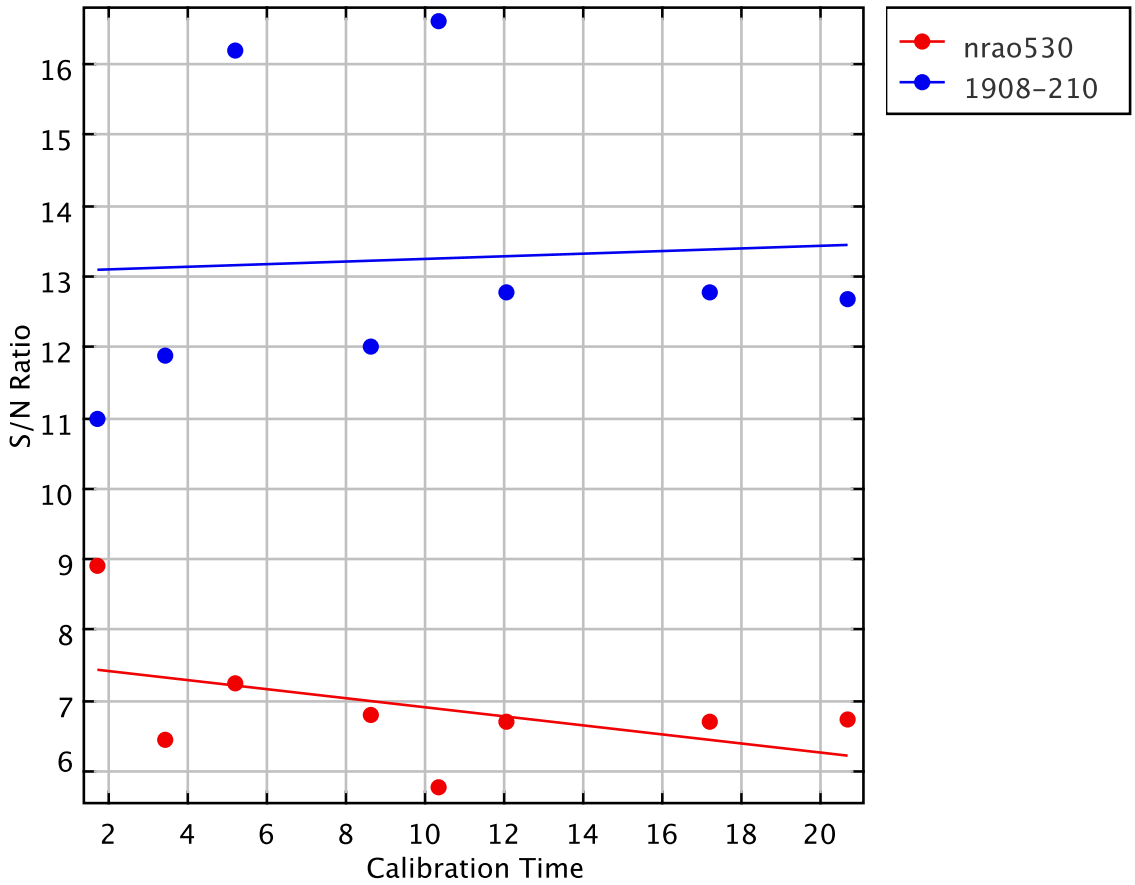


*Figure 4.8: S/N as a function of the calibration cycle interval (in minutes) for the dataset 040902-044603*

The main conclusion for this dataset is that we cannot perform a satisfactory correction of the phase variations due to the combination of adverse atmospherical conditions and a faint source.

#### 4.2.4.4 Dataset 040904-195454

The observations were carried out at 230 GHz with an opacity $\sim 0.1$.

The observed sources and their fluxes are shown in Tab. 4.8. 3c279 was chosen as the calibrator.

The atmospheric conditions were good, and a visual inspection of the visibility plots also shows the good quality of the data. The calibrator has a low phase scatter, below $50^o$ once the calibration was performed, though for some baselines (1-3, for example) there are peak to peak variations larger than $200^o$ with rapid variations of less than 1 minute. This low phase scatter is a consequence of the good atmospherical conditions and the high flux density of the source.

For all the sources, the calibrations reduce the phase scatter with respect to the uncalibrated data. In the case of 1334-127, the phase scatter is also low, being reduced once the data are calibrated from the original $100^o$ to $50^o$. This behavior is also shown by 1244-127, but with a larger

*Table 4.8: Flux and elevation of the quasars observed in the dataset 040904-195454*

| Source | Elevation (deg) | Flux density (Jy/beam) |
|---|---|---|
| 3c279 (calibrator) | 45-65 | 7.33± 0.42 |
| 1334-127 | 30-50 | 4.24±0.24 |
| 1244-255 | 30-45 | 0.69±0.06 |

scatter, due to the lower intensity of the source, which is a factor 6 and 10 lower, respectively, than the other two quasars.

The phase stability of the two targets is not correlated with the calibrator, probably due to their low elevation, which results in an increase of the optical path trhough the atmosphere. For the shortest baselines, the phase plot shows a flat profile. In the case of longer baselines, the calibrations slightly improve the peak to peak dispersion in the phase plot, specially for 1334-127.

From the analysis of the resulting images and the plot of the S/N ratio vs calibration time shown in Fig. 4.9 we can extract the following conclusions:

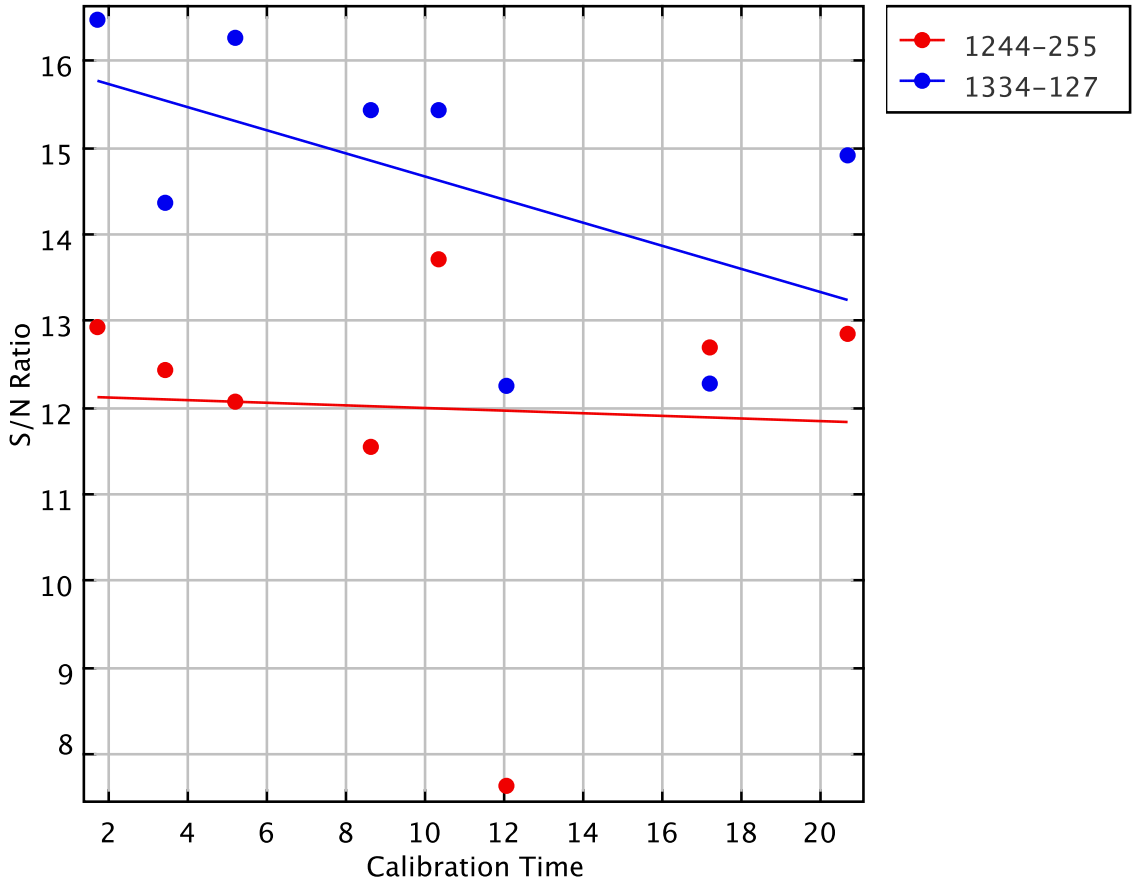


*Figure 4.9: S/N as a function of the calibration cycle interval (in minutes) for the dataset 040904-195454*

*Table 4.9: Flux and elevation of the quasars observed in the dataset 040905-215041*

| Source | Elevation (deg) | Flux density (Jy/beam) |
|---|---|---|
| 3c279 (calibrator) | 45-65 | 7.33± 0.42 |
| 1334-127 | 35-55 | 4.24±0.24 |
| 1244-255 | 35-45 | 0.69±0.06 |

- 1244-255: The maximum intensity peaks and the S/N ratios of this source are quite high, with a value of ∼12. The rms does not change very much as we increase the calibration time. As a consequence, the linear fit of S/N vs calibration cycle interval is almost flat. One of the points, corresponding to a calibration time of 12min 3sec, shows an artificial high dispersion in both this source and the other target.

- 1334-127: The S/N ratios have a value around 15, and therefore in the images the source is clearly seen with a a low level of noise. The S/N ratio decreases as the calibration time increases, as can be seen in the S/N vs calibration time plot.

The trend in the case of 1334-127 is that the S/N ratio decreases as we increase the calibration time, while for the 1244-255 there is no significant trend. The main difference with respect to 040902-104551 is that the phase scatter is high for many baselines, probably due to the higher elevation of the calibrator with respect to the other two sources.

#### 4.2.4.5 Dataset 040905-215041

The observations of this dataset were carried out at 230 GHz, with an opacity between 0.10 and 0.14. 3c279 was the calibrator.

The continuum visibility plots show that, even with similar opacities and observing the same sources, the phase stability of this dataset is clearly worse than for the previous one (dataset 040904-195454). The calibrator shows an high scatter in the visibility plot that is not shown by the other two sources. Even the first calibration, with a calibration cycle of 1.7 min, shows a very faint emission, below the noise level in most cases. As described below, the quality of the data was very poor, so the S/N vs calibration plot is quite uncertain and is not presented.

From the images generated and the analysis of the numerical results extracted from them, we come to the following conclusions:

- 1244-255: The S/N ratios are quite low, with values below 8 and one of them (the one corresponding to a calibration time of 17min) below 5. Thus, it is hard to recognize the source in the image. The rms is not too high ($\sim 7 \times 10^{-4}$ Jy beam$^{-1}$, once the flux of the calibrator is normalized), but the values for the peak are quite low and the S/N ratio shows a high dispersion and no trend with respect to the calibration cycle.

- 1334-127: The values of the peak found in the images of this source are higher than the ones for the other target. Nevertheless, the noise is also higher and, thus, the S/N ratio have low values, being below 5 for some calibrations. The maximum in the images appears with an offset from the center, so it could be a noise peak, instead of the target emission. Assuming we are measuring the maxima in the peaks corresponding to the source, the S/N ratios do not show any clear trend with the calibration time, and it is difficult to extract a strong conclusion due to to the high dispersion of the data.

*Table 4.10: Flux and elevation of the quasars observed in the dataset 040905-135353*

| Source | Elevation (deg) | Flux density (Jy/beam) |
|---|---|---|
| 3c279 (calibrator) | 38-46 | 7.33± 0.42 |
| 1334-127 | 32-42 | 4.24±0.24 |
| 1244-255 | 20-30 | 0.69±0.06 |

Even observing the same sources as in the former dataset and with similar values of the opacity, the fast-switching does not modify the results due to the poor phase stability they show, with fluctuations of at least a few seconds. A central strong peak corresponding to the target can not be detected, even in the case of the strongest source.

#### 4.2.4.6 Dataset 040906-135353

The observations of this dataset were carried out at 230 GHz, with an opacity of 0.17. 3c279 was the calibrator.

Looking at the visibility plots, we see that the phase scatter of the calibrator is quite low, reaching values below 50º and showing an almost flat profile. 1334-127 also shows low phase scatter, with values around 50º once calibrated. The case of 1244-255 is totally opposed: the phase scatter is high even before the calibration, with values near 180º and showing no clear trend. This high phase scatter, together with the fact 1244-255 is a faint source has led us to exclude it from the S/N plot (Fig. 4.10).

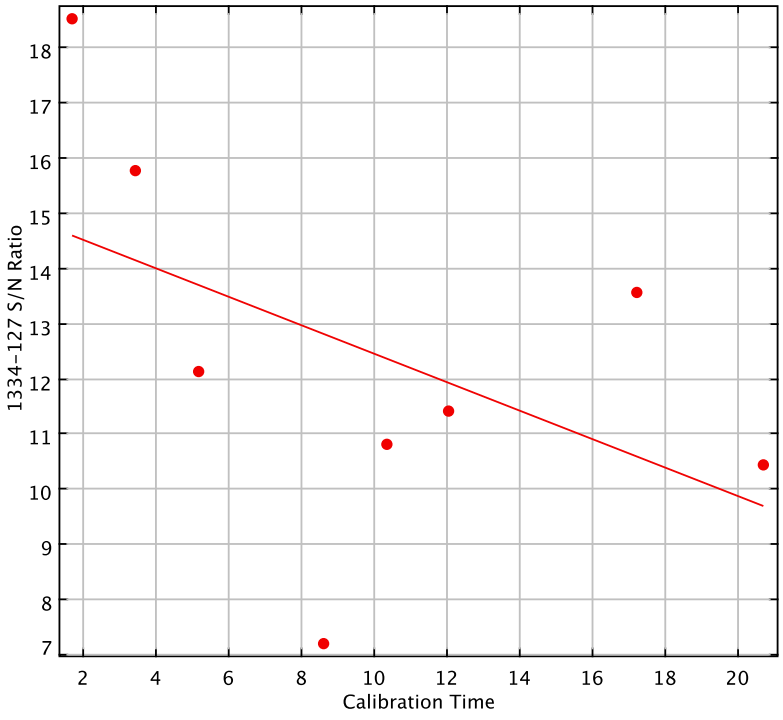


*Figure 4.10: S/N as a function of the calibration cycle interval (in minutes) for the dataset 040905-135353*

After the analysis of the images and their parameters we reach the following conclusions:

- 1244-255: The quality of the images is poor. The peaks, which are very faint are not placed in the center of the image. Relative to the peak, the noise shows high values, around $\frac{1}{4}$ of the peak value. As a consequence, the S/N ratio is below 5 for half the calibrations, showing no visible trend with the calibration time.
- 1334-127: The intensity peaks of the different calibrations show high values, while the rms has values lower than the ones in the other targets. Thus, S/N ratio is above 6 for all the calibrations. In the S/N plot, we can see that the S/N ratio seems to decrease as we increase the calibration cycle interval.

The behavior of the results of this dataset is quite similar to the dataset 040904-195454, with the same sources and elevation and similar atmospherical conditions. A slight improvement of the S/N ratio of the strongest source is found as we decrease the calibration time. The other target appears to be too faint. For some baselines, the phase of the calibrator shows no correlation with the one of the target.

### 4.2.5 Conclusions and future work

From the analysis of the results in Sec. 4.2.4 we can extract three main conclusions:

1. There is no connection between opacity and phase stability.

   The timescale of the phase fluctuations is between some tens of seconds and a few minutes. Even the same sources with similar elevation can lead to different results in different days. For some cases, phase stability is good for all the baselines, while for other cases, the longer baselines show a clear instability. A possible explanation for this phenomenon is a difference on the content of water vapor along the line of sight of the different antennas.

   For our observations, we did not have opacity measurements that were fast enough to discuss whether there is a relation between the time variation of the opacity ($\Delta\tau$) and the seeing.

2. The calibrator must be at the smallest possible angular distance from the target, in order to minimize the difference in the water vapor content that the signal coming from the calibrator and the target has to cross. In case of large angular distances, the phase calibration scheme obtained from the calibrator is not valid for the target.

   A lower elevation of the calibrator or the target implies a larger air mass to be crossed by the signal, being exposed to larger distortions by the atmosphere.

3. For bright sources with good atmospherical conditions (i.e. with phase fluctuations with a timescale of a few minutes), the S/N ratio decreases as we increase the calibration time (datasets 040902-104551, 040906-013535), finding a S/N ratio decrease of $\Delta(\mathrm{S/N}) \sim 4$ when changing the calibration time from 2 to 20 minutes in observations running for 3 hours. Our results are consistent with the ones in Vir Lal et al. (2007):

   - In very good atmospherical conditions, the improvement of the S/N ratio when we decrease the calibration time is not significant.
   - In bad atmospherical conditions, fast-switching does not improve the results.

- For medium atmospherical conditions fast-switching clearly helps to improve the quality of the resulting images, where *medium* stands for not very good nor very bad conditions.

With these conclusions, it is expected that fast-switching can improve the quality of the data from ALMA. Nevertheless, as part of the future work, a deep quantitative comparison between Mauna Kea and Chajnantor atmospherical conditions would be needed. New fast-switching tests at the SMA, trying to cover the widest range of atmospherical conditions possible would also be useful.

Finally, the implementation of fast-switching in ALMA will present three main differences with the work we have developed at SMA:

- Sensitivity. SMA consists on eight 6-meters antennas, while ALMA, once finished, will have fifty 12-meters antennas, with a dramatical increase of sensitivity, that will allow the observers to use quasars fainter than the ones we have used as calibrators. Actually, the main restriction of our tests was the need of a strong quasar near to the problem sources. This problem will be minimized in ALMA, so fast-switching could be applied for any source.

- Baseline lengths. This will be the major challenge for the fast-switching implementation in ALMA. The longest SMA baseline used in our tests is shorter than 200 meters. In ALMA, baselines up to 10 km will be reached. As pointed out in 4.2.1, the phase rms increases as we increase the baseline length. Thus, the longest baselines will have a large phase fluctuation even under good atmospherical conditions. In this cases, fast-switching can play a key role.

- Atmospherical conditions. The conditions at Llano de Chajnantor, the ALMA site, are better for mm and submm observations than the ones at Mauna Kea, where SMA is installed. The lower water vapor content in Chajnantor will reduce the phase fluctuations generated by the atmosphere. Thus, the combination of longer baselines with better atmospherical conditions allows the main part of the observing time to be expected with optimal atmospherical conditions for the application of fast-switching.

# Chapter 5
# Conclusions and future work

*Hör auf zu beben!*
*Bereite dich zu leben!*

**Gustav Mahler** - Auferstehung

In this work, we have tried to shed light on the relation between the $M_{H_2}$ and SFR in HCGs, and see whether there is a relation of these magnitudes with the HI content of the galaxies and the HI content and evolutionary stage of the group. In order to do so, we have analyzed CO data coming from single-dish and interferometric measurements together with SFR, calculated from IR data, and HI maps. In parallel, we have tested a calibration technique with possible application in ALMA.

We have performed the first analysis of the $M_{H_2}$ and SFR in a sample of 86 galaxies in 20 HCGs with HI data available for all the groups and for ∼75% of the galaxies, and compared our results with those of the AMIGA sample of isolated galaxies. The $L_{FIR}$ in HCG galaxies shows no deficiency, while there is a slight $M_{H_2}$ enhancement in the spiral galaxies. The HI deficiency of the galaxies shows values much larger than the ones for $M_{H_2}$ and $L_{FIR}$. The $M_{H_2}$ and $L_{FIR}$ deficiencies, which are strongly correlated, are not related to the HI content of the group, but there is a trend of these deficiencies to increase as the galaxies are more HI deficient. The $M_{H_2}$ deficiency seems to increase as the group evolves, but there is no relation between the $L_{FIR}$ deficiency and the evolutionary stage of the group. The environment in HCGs do not enhance, nor inhibit, the SFE, that show no relation with the deficiency in$M_{HI}$ nor in $M_{H_2}$. We have found a trend in the sSFR tends to increase with decreasing deficiency in $M_{HI}$ and with decreasing deficiency in $M_{H_2}$.

The comparison of the $M_{H_2}$ obtained from the single-dish observations and from the high-resolution OVRO observations of HCG40 and HCG79 showed that 40d has a highly compact distribution of its molecular gas, while for 40c, where CO emission was mainly found in the dustlane of the galaxy disk, the results argue for a more extended distribution. The two galaxies previously detected in HCG79 have not been detected with OVRO, which suggest an extended distribution of the molecular gas possibly due to the interactions between galaxies. The sSFR calculated from the Spitzer data for these 2 HCGs, as well as the sSFR, calculated from IRAS data for the entire sample, was found to show a continuous distribution, in opposition to previous claims of a bimodal distribution of the sSFR in HCGs.

Finally, we have performed a study of the fast-switching gain calibration technique, using data from tests performed at SMA, finding that this technique can improve the quality of the data coming from interferometric observations under certain atmospherical conditions.

Based on the analysis we have performed, the study of $M_{H_2}$ in HCGs in the future could be continued in the following lines of work:

- The most important progress can be achieved by high-resolution studies of the molecular gas distribution in the groups with high-sensitivity instruments like Plateau de Bure or, most importantly, ALMA. As has been shown in Chapter 3, the full ALMA array will enable us to observe almost all HCGs in our sample within a few hours. The high resolution and sensitivity will show how the molecular gas is distributed within the galaxies in HCGs and reveal whether there are any differences with respect to the distribution in isolated galaxies. Most likely, extragalactic CO emission, associated with the extragalactic atomic hydrogen, will be detected. Futhermore, the higher sensitivity and spatial resolution will allow studies of the kinematical properties of the molecular gas.

- Data from the Spitzer, in particular the emission at 24$\mu$m, can be used as a high-resolution and sensitive tracer for the SFR. In the Spitzer archive, there is data for the emission at 24 $\mu$m available for a total of 10 HGCs (including HCG40 and HCG79) of our sample. Thus, although the study presented in this thesis has not been possible based on Spitzer data alone, the data can be used to check the consistency of the IRAS data. Also the IR data from Herschel, available in the future, are useful SF indicators (e.g. Verley et al. 2010). These data, when combined with future interferometric CO data, allow to perform a more detailed comparison of the molecular gas and SF distribution.

- We have based our analysis of the deficiency on the blue luminosity, from which the expected values for $M_{H_2}$, $M_{HI}$ and $L_{FIR}$ were calculated. A complementary study should carry out the same analysis based on the stellar mass as a quantity expected to be very little affected by the environment.

- In addition to the statistical analysis presented in this work, more detailed studies of individual groups and galaxies will be useful.

# Chapter 6
# Conclusiones y trabajo futuro

**En cumplimiento de la normativa de la Universidad de Granada relativa al depósito de tesis en inglés, se presenta a continuación la traducción al castellano del capítulo de conclusiones de la tesis**

En el presente trabajo hemos intentado arrojar luz sobre la relación entre $M_{H_2}$ y la SFR in HCGs, viendo si existe una relación de dichas magnitudes con el contenido en HI de las galaxias, así como con el contenido de HI y la fase evolutiva del grupo en que se encuentran. Para llevarlo a cabo se han analizado datos de CO procedentes de observaciones de antena única e interferométricas junto a datos de SFR, calculados a partir de observaciones en IR, y mapas de HI. En paralelo, se han llevado a cabo pruebas en una técnica de calibración de posible aplicación en ALMA.

Hemos llevado a cabo el primer análisis de $M_{H_2}$ y SFR para una muestra de 86 galaxias en 20 HCGs con datos de HI disponibles para todos los grupos y para el 75% de las galaxias, y hemos comparado nuestros resultados con los de la muestra AMIGA de galaxias aisladas. Las galaxias de los HCGs no muestran deficiencia en $L_{FIR}$, mientras que hay un ligero realce en $M_{H_2}$. La deficiencia en HI de las galaxias muestra valores mucho más altos que las deficiencias en $M_{H_2}$ y $L_{FIR}$. Las deficiencias en $M_{H_2}$ y $L_{FIR}$ presentan una fuerte correlación y no están relacionadas con la deficiencia en HI del grupo, aunque se aprecia una tendencia de estas deficiencias a incrementarse a medida que las galaxias presentan mayor deficiencia en HI. La deficiencia en $M_{H_2}$ parece aumentar a medida que el grupo evoluciona, mientras que dicho comportamiento no se aprecia para $L_{FIR}$. El entorno de los grupos no inhibe ni realza la SFE, que no muestra relación con la deficiencia en $M_{HI}$ ni en $M_{H_2}$. La sSFR tiende a aumentar a medida que als deficiencias en $M_{HI}$ y en $M_{H_2}$ disminuyen.

La comparación de la $M_{H_2}$ obtenida a partir de observaciones de antena única y a partir de las observaciones de OVRO de alta resolución para HCG40 y HCG79 muestran que 40d presenta una distribución de molecular gas altamente compacta, mientras que 40c, donde la emisión de CO se encuentra principlamente en el dustlane del disco de la galaxia, muestra una distribución más extendida. Las dos galaxias previamente detectadas en HCG79 no se han detectado con OVRO, lo cual sugiere una distribución extendida del gas molecular, probablemente debida a las interacciones entre galaxias. La sSFR calculada a partir de los datos de Spitzer, así como la calculada a partir de datos de IRAS para la muestra completa, muestra una distribución continua, contradiciendo estudios anteriores que presentaban una distribución bimodal para la sSFR en HCGs.

Finalmente, se ha llevado a cabo un estudio de la técnica fast-switching de calibración en ganancia utilizando datos procedentes de pruebas llevadas a cabo en SMA, hallándose que esta

téncica mejora la calidad de los datos procedentes de observaciones interferométricas bajo determinadas condiciones atmosféricas.

Basados en el análisis que hemos llevado a cabo, el estudio del $M_{H_2}$ en HCGs en el futuro debería seguir las siguientes líneas de trabajo:

- El mayor progreso se puede llevar a cabo mediante estudios de alta resolución de la distribución de gas molecular con instrumentos de alta sensibilidad como Plateau de Bure o, con mayor importancia, ALMA. Como se muestra en el Capítulo 3, el array completo de ALMA puede observa casi todos los HCGs de nuestra muestra en unas pocas horas. Su alta resolución y sensibilidad permitirá mostrar cómo se distribuye el gas molecular en las galaxias en HCGs y revelar si existen diferencias con la distribución en galaxias aisladas. Probablemente, emisión de CO extragaláctica, asociada con el hidrógeno atómico extragaláctico, será detectada. Además, su mayor sensibilidad y resolución espacial permitirá estudios de las propiedades cinéticas del gas molecular.

- Los datos de Spitzer, en particular la emisión a 24$\mu$m, pueden ser usados como un trazador de alta resolución y sensibilidad para la SFR. En el archivo de Spitzer hay datos de la emisión a 24$\mu$m disponibles para un total de 10 HCGs (incluyendo HCG40 y HCG79) de nuestra muestra. Así, aunque el estudio que se presenta en esta tesis no se ha podido llevar a cabo basado tan solo en datos de Spitzer, los datos se pueden utilizar para comprobar la consistencia de los datos de IRAS. También los datos de Herschel, disponibles en un futuro, son útiles indicadores de la SF (ver, p.e. Verley et al. 2010).. Estos datos, combinados con futuras observaciones interferométricas de CO, permitirán una comparación más detallada de la distribución de gas molecular y SF.

- Nuestro análisis de la deficiencia de $M_{H_2}$, $M_{HI}$ and $L_{FIR}$ se ha basado en sus valores esperados en función de su luminosidad azul. Se debería llevar a cabo un estudio complementario del mismo análisis basado en la masa estelar, magnitud que se espera que esté poco afectada por el entorno.

- Junto al estudio estadístico que se presenta en este trabajo, estudios más detallados de los grupos y galaxias individualmente serían también de gran utilidad.

# Appendix A
# CO spectra of the galaxies observed with the 30m

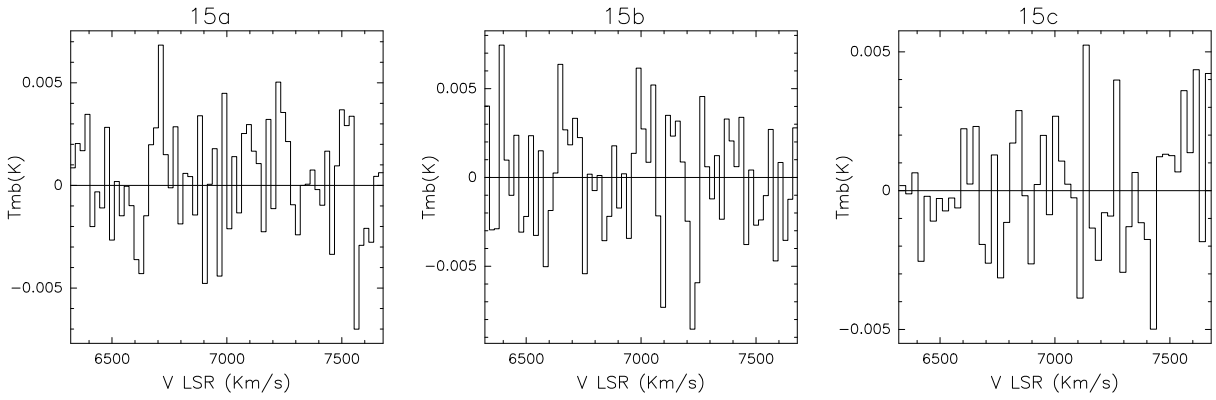


*Figure A.1: CO(1-0) spectra for the HCG galaxies. The detection window is shown with a red horizontal line. Main beam temperature (Tmb, in K) is displayed in the Y axis, and the velocity with respect to LSR in km $s^{-1}$ is displayed in X axis. Velocity resolution is smoothed to 21 or 27 km $s^{-1}$. The velocity of the galaxy, converted to the radio definition, is marked with an arrow.*

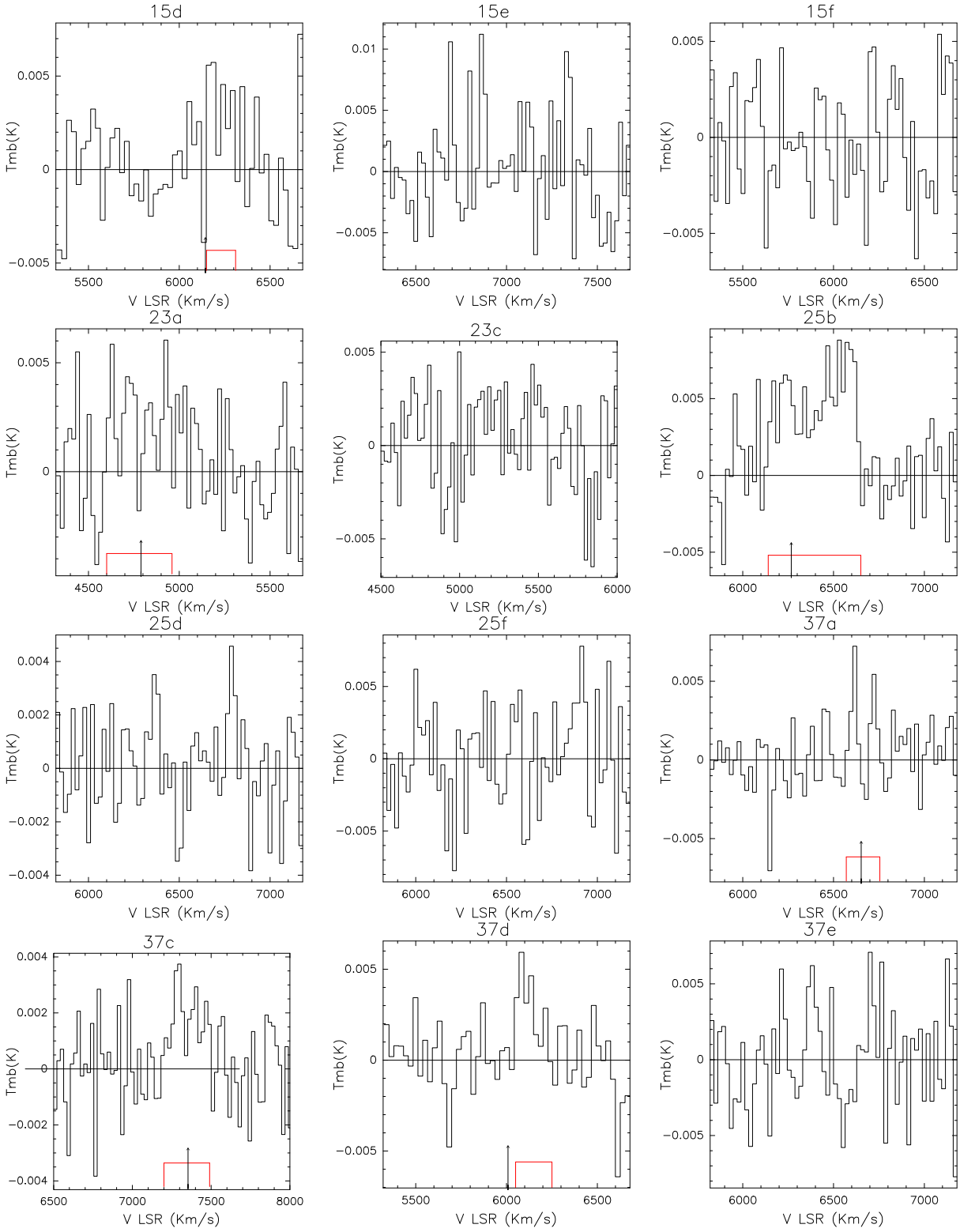


*Figure A.1: (Continued)*

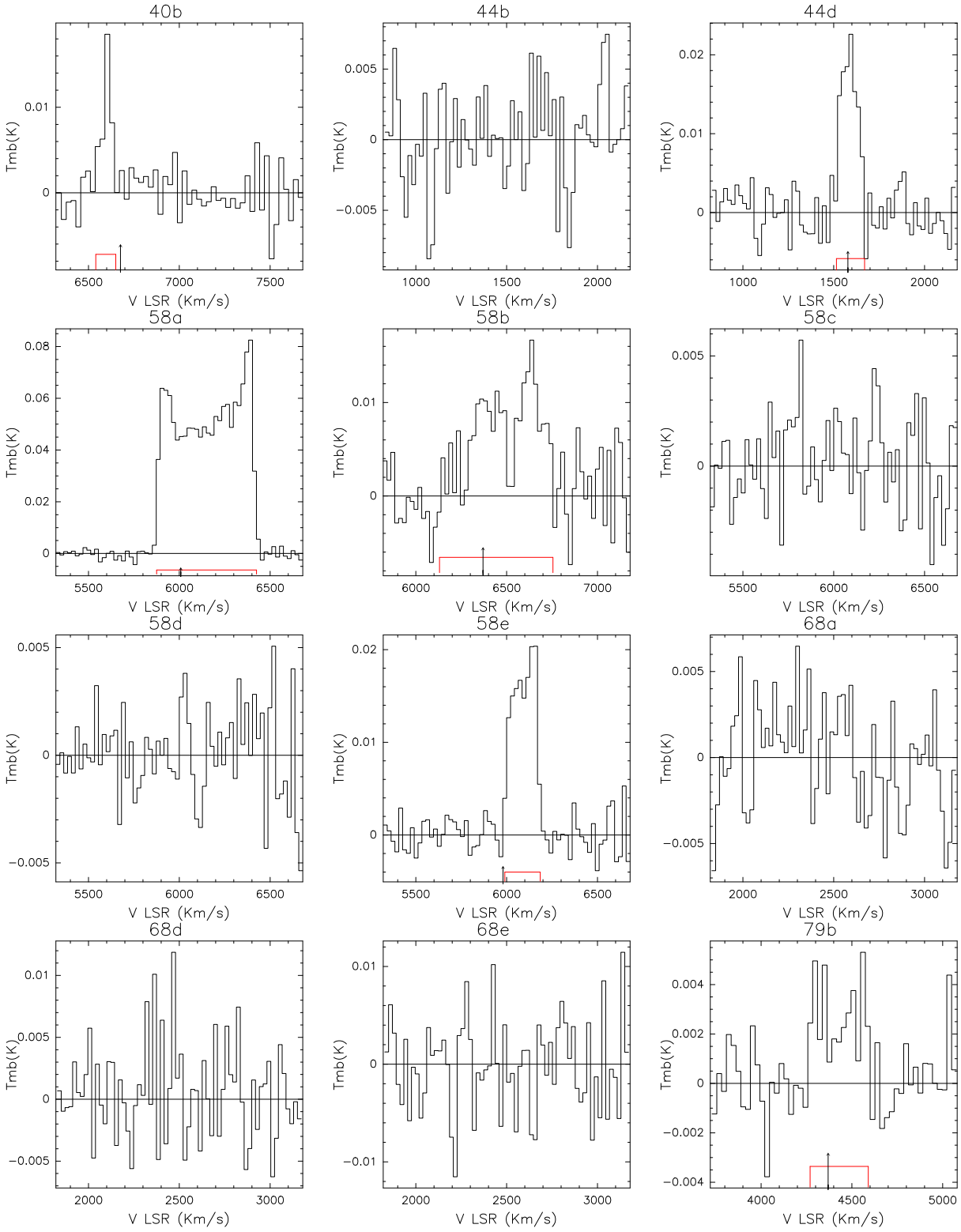


*Figure A.1: (Continued)*

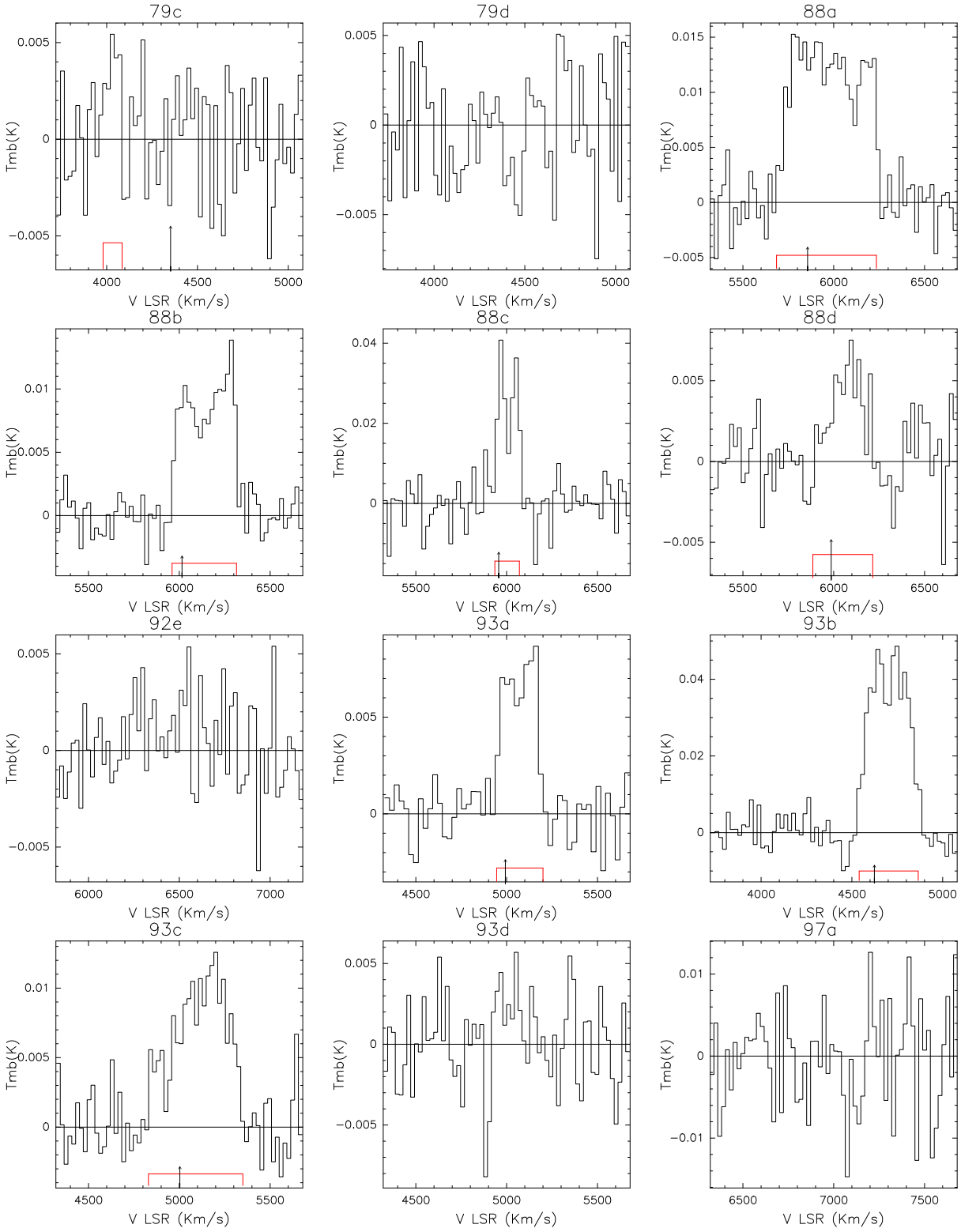


*Figure A.1: (Continued)*

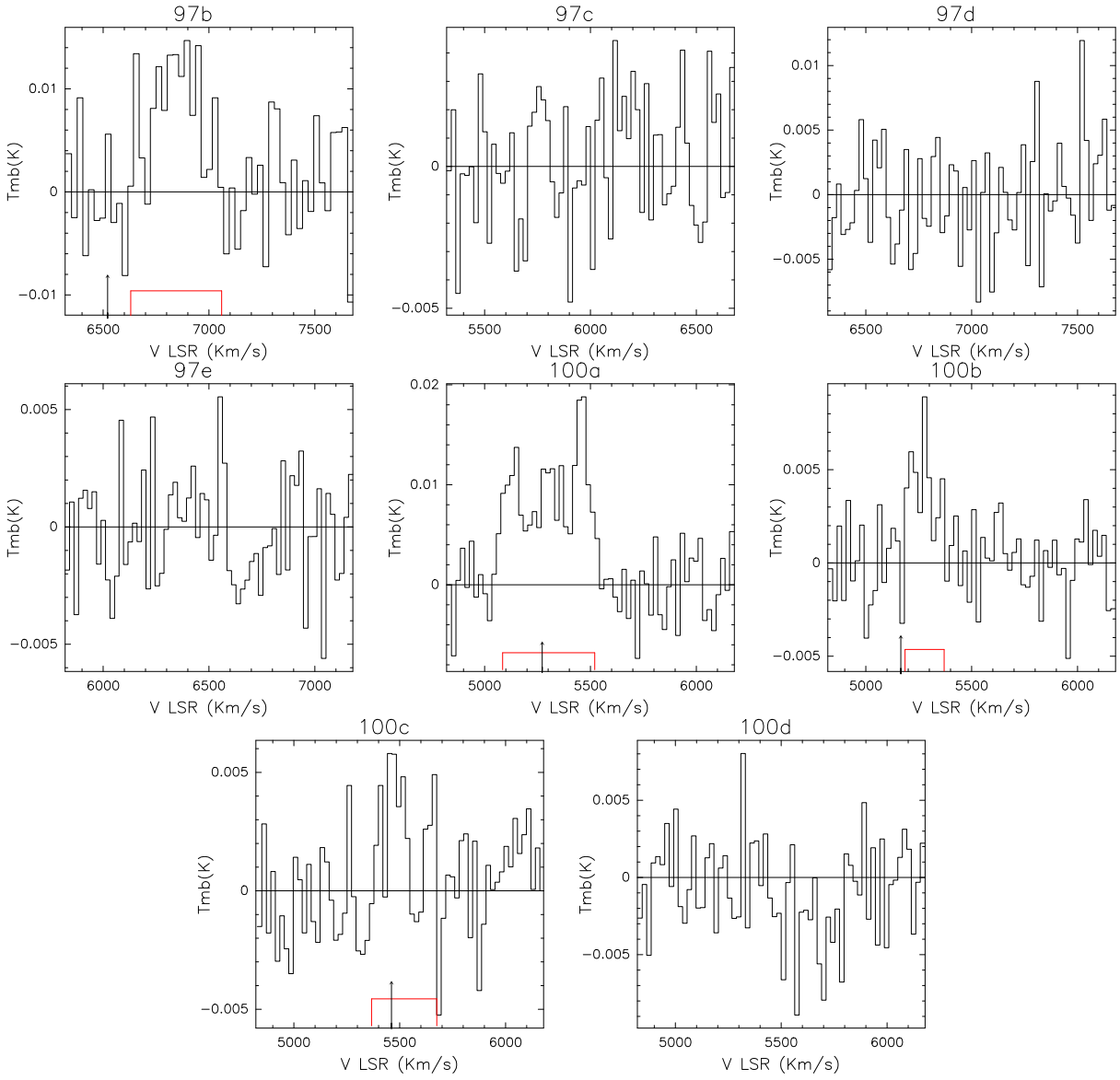


*Figure A.1: (Continued)*

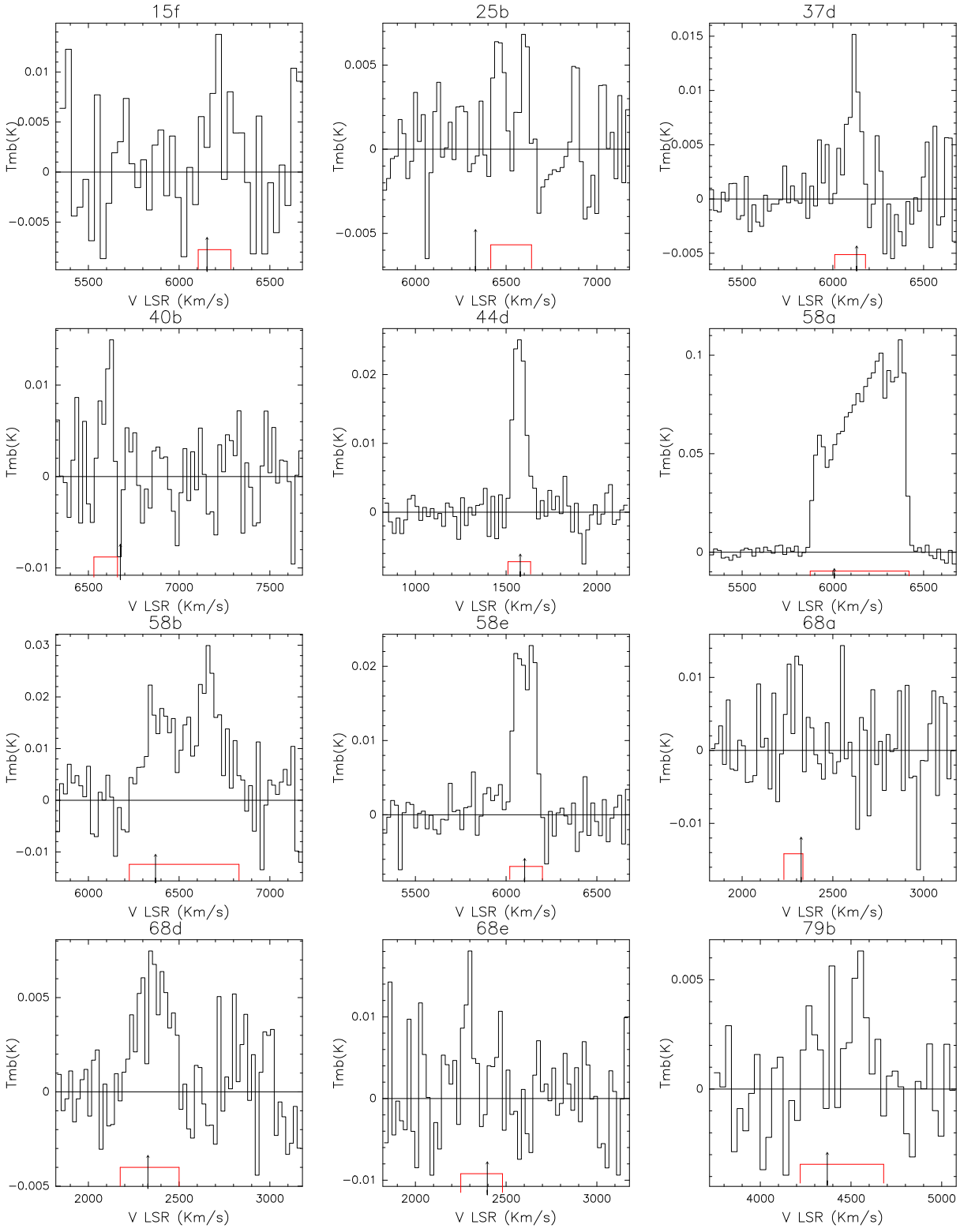


*Figure A.2: CO(2-1) spectra for the HCG galaxies detected in this wavelength. The detection window is shown with a red horizontal line. Main beam temperature (Tmb, in K) is displayed in the Y axis, and the velocity with respect to LSR in km $s^{-1}$ is displayed in X axis. Velocity resolution is smoothed to 21 or 27 km $s^{-1}$. The optical velocity of the galaxy, converted to the radio definition, is marked with an arrow.*

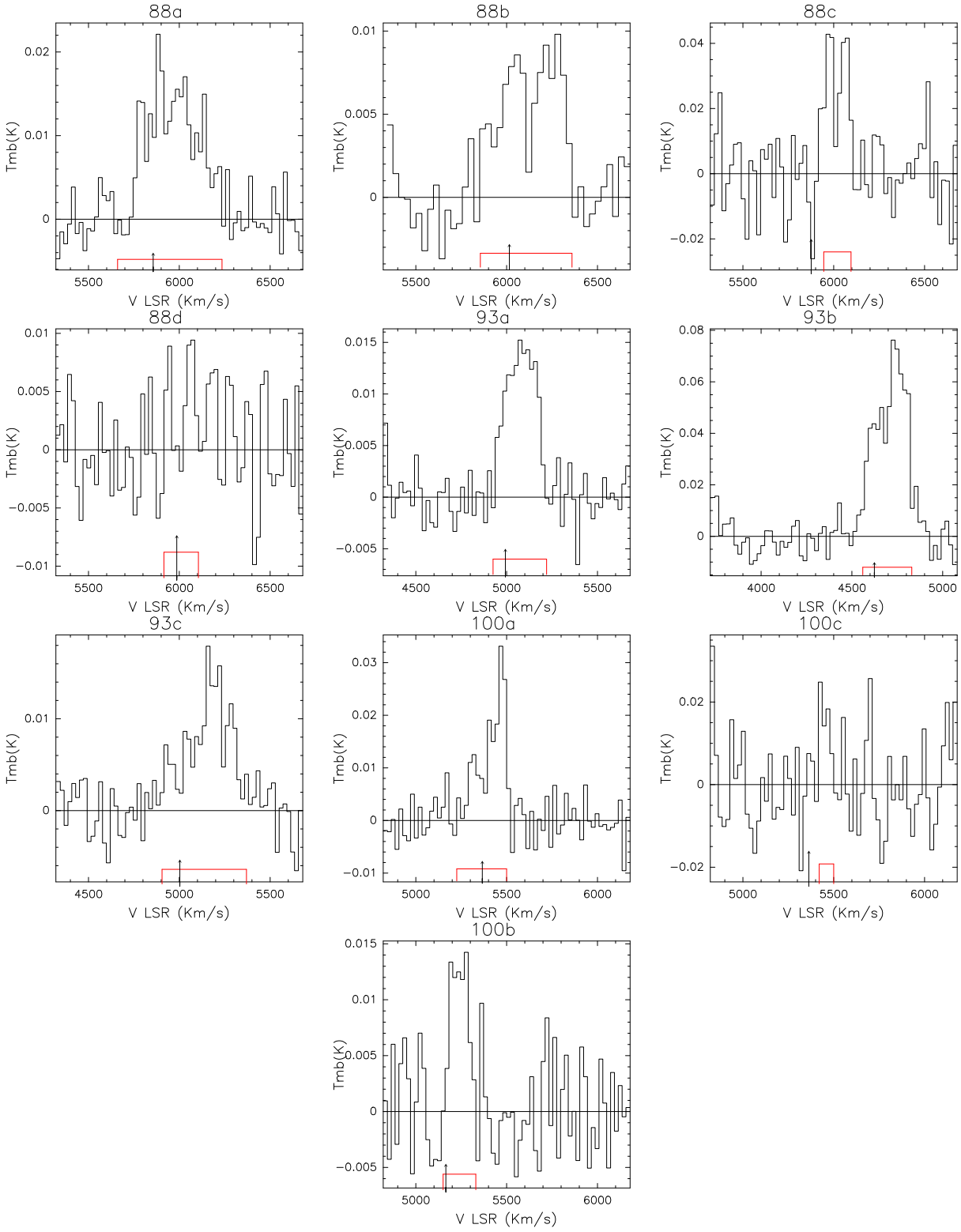


*Figure A.2: (Continued)*

# Appendix B
# Visibility plots of the fast-switching tests

In this appendix we present the visibility plots of the savesets described in Chap. 4

## B.1 Saveset 040902-104551

For this saveset, we present the plots corresponding to the uncalibrated data, the calibration corresponding to a calibration time of 1 min 43 sec and the one corresponding to 8 min 36 sec for 9 different baselines, in order to show an example of the data given by the interferometer not only for 3 baselines, as shown for the other savesets. The color code of the sources is as follows:

- Green: 2230+114, primary calibrator
- Blue: 2145+067
- Orange: 3c454.3

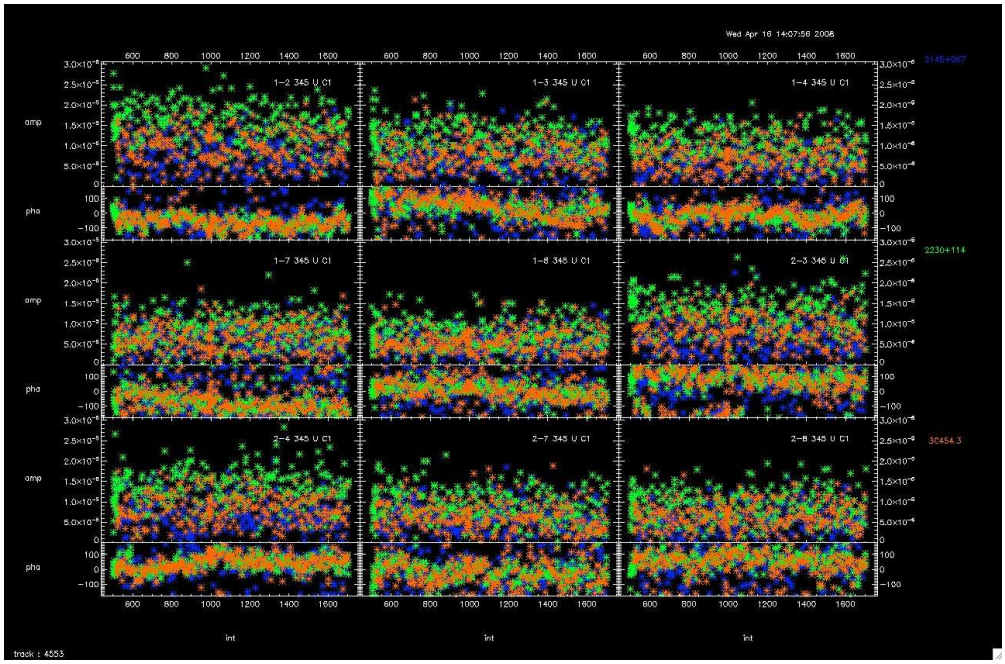


*Figure B.1: Visibilities of the uncalibrated data*

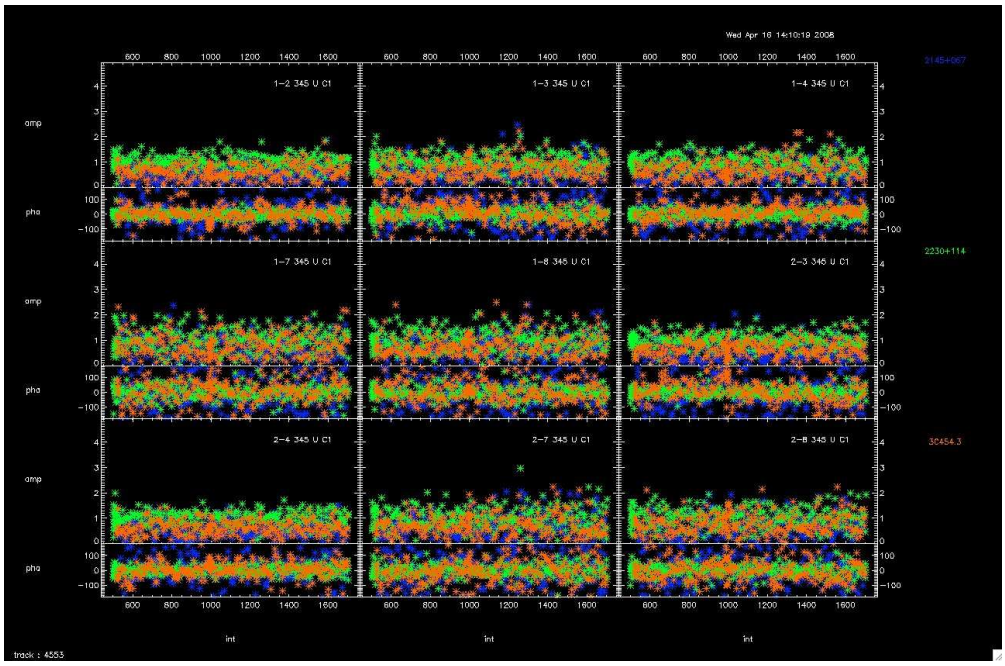


*Figure B.2: Visibilities corresponding to a calibration time of 1min 43sec*

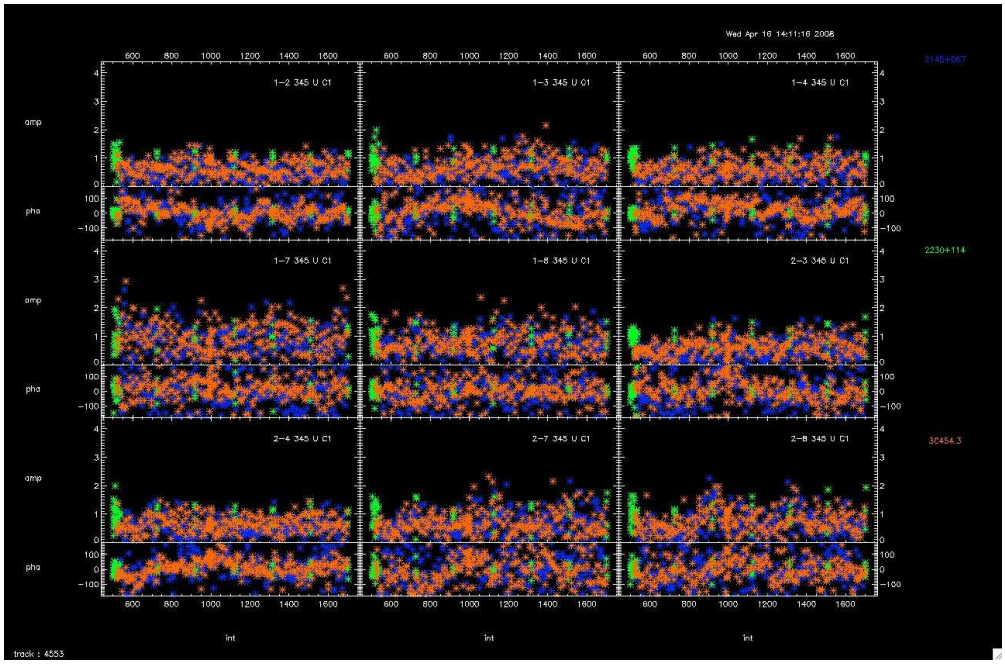


*Figure B.3: Visibilities corresponding to a calibration time of 8min 36sec*

## B.2 040902-044603

For this saveset, as well as for the next ones, we present the data corresponding to 3 baselines of the interferometer (1-2, 1-3 y 1-4). The color code for the visibilities of this dataset is:

- Green: 1921-293, primary calibrator
- Blue: 1908-201
- Orange: nrao530

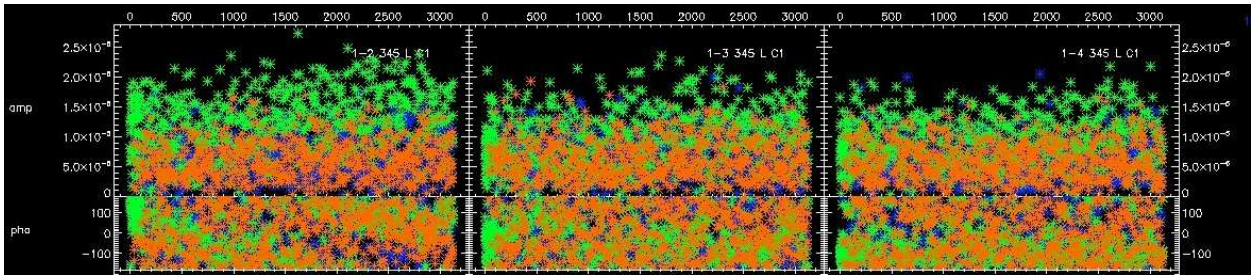


*Figure B.4: Visibilities of the uncalibrated data*

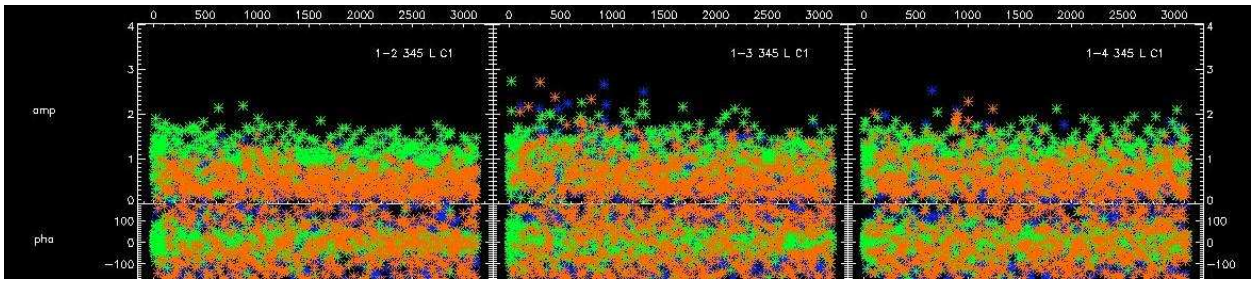


*Figure B.5: Visibilities corresponding to a calibration time of 1min 43sec*

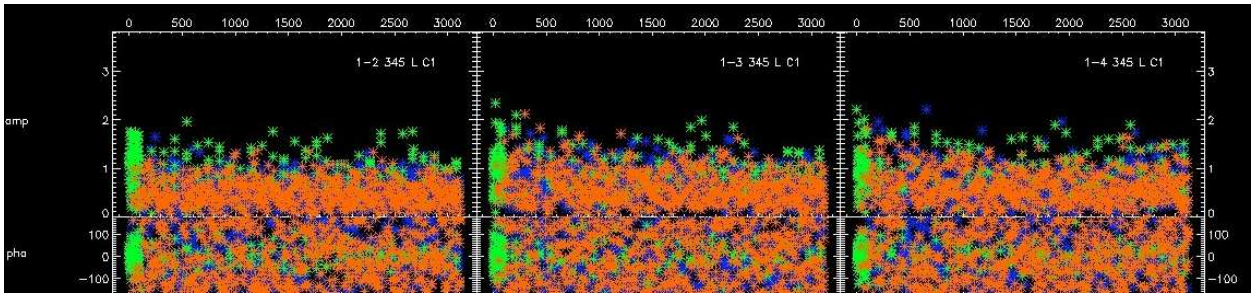


*Figure B.6: Visibilities corresponding to a calibration time of 8min 36sec*

## B.3 040904-195454

Color code:

- Orange: 3c279, primary calibrator
- Blue: 1244-255
- Green: 1334-127

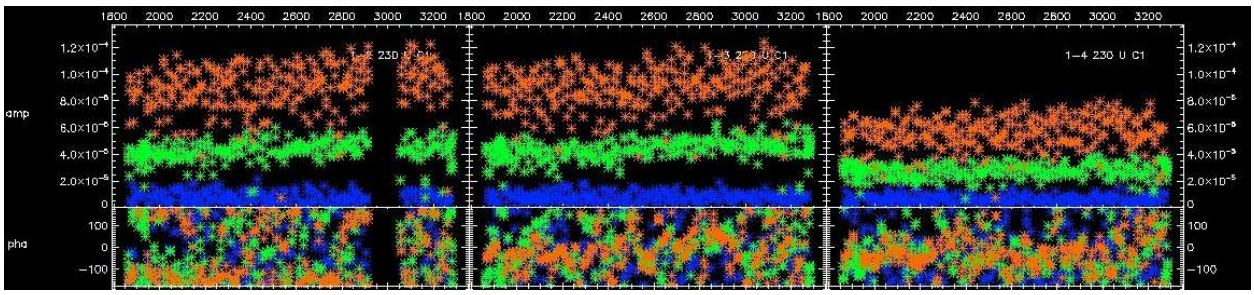


*Figure B.7: Visibilities of the uncalibrated data*

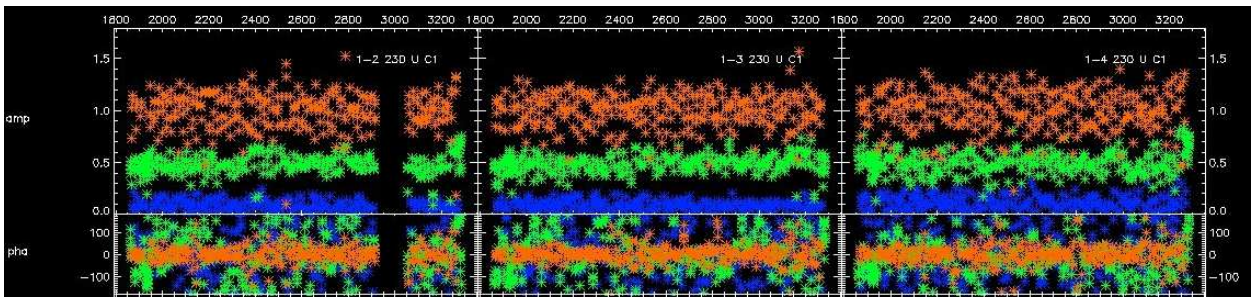


*Figure B.8: Visibilidades correspondientes a un tiempo de calibración de 1min 43sec*

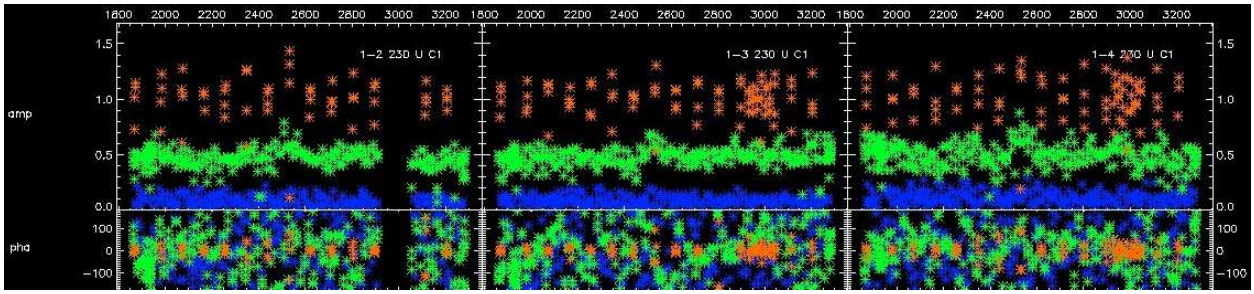


*Figure B.9: Visibilities corresponding to a calibration time of 8min 36sec*

## B.4 040905-215041

Color code:

- Orange: 3c279, primary calibrator
- Blue: 1244-255
- Green: 1334-127

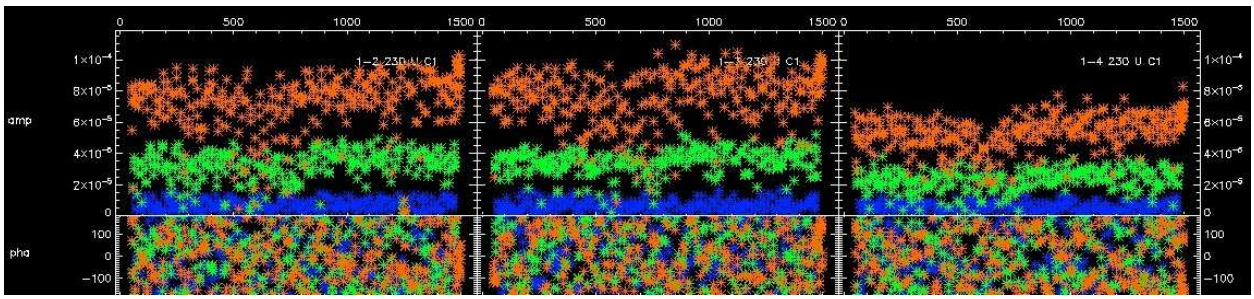


*Figure B.10: Visibilidades correspondientes a los datos sin calibrar*

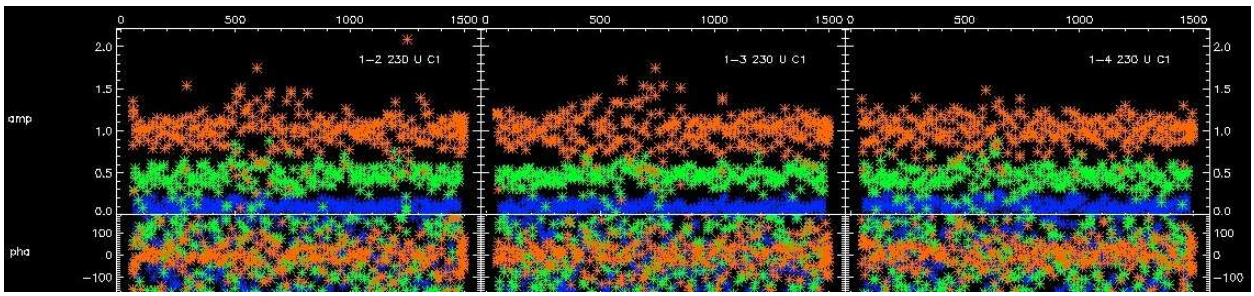


*Figure B.11: Visibilities corresponding to a calibration time of 1min 43sec*

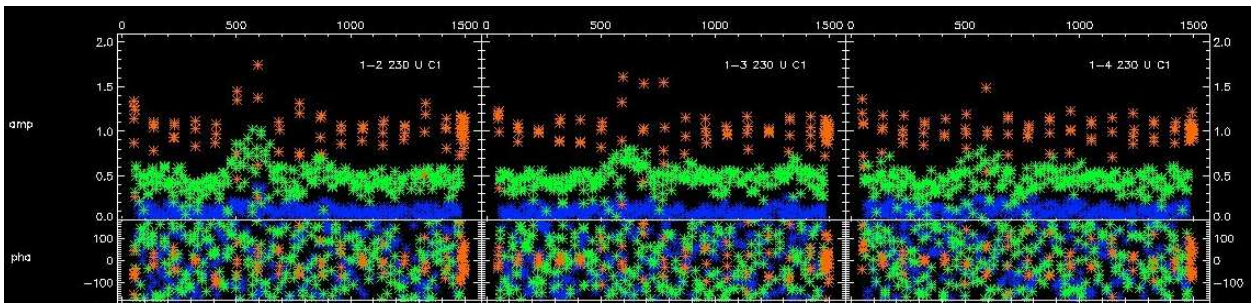


*Figure B.12: Visibilities corresponding to a calibration time of 8min 36sec*

## B.5 040906-013535

For this saveset we present the visibility plots corresponding to the baselines (1-0) and (2-1). The color code is as follows:

- Orange: 3c279, primary calibrator
- Blue: 1244-255
- Green: 1334-127

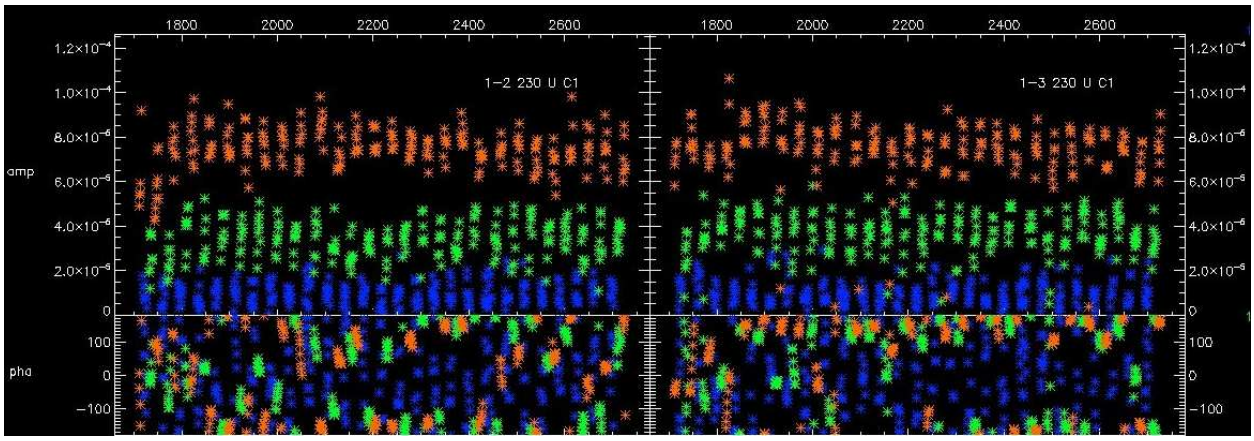


*Figure B.13: Visibilities of the uncalibrated data*

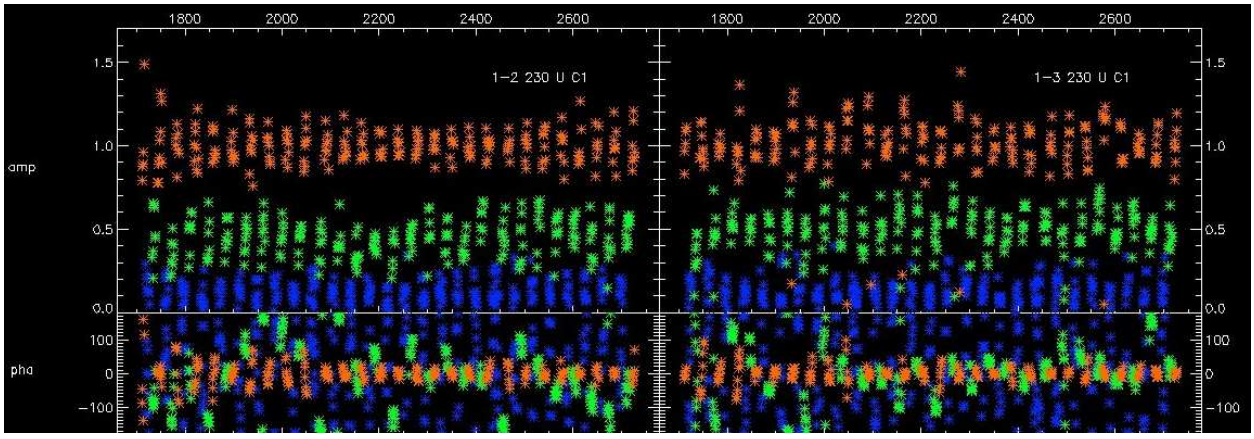


*Figure B.14: Visibilities corresponding to a calibration time of 1min 43sec*

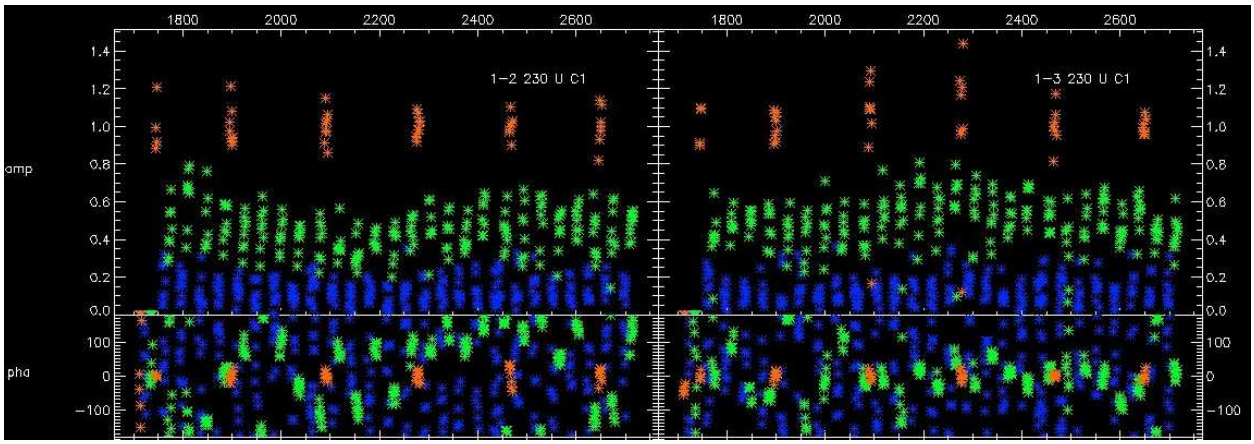


*Figure B.15: Visibilities corresponding to a calibration time of 8min 36sec*

# Bibliography


Aguerri, J. A. L., Castro-Rodríguez, N., Napolitano, N., Arnaboldi, M., & Gerhard, O. 2006, A&A, 457, 771

Amram, P., Plana, H., Mendes de Oliveira, C., Balkowski, C., & Boulesteix, J. 2003, A&A, 402, 865

Arp, H. 1966, ApJS, 14, 1

Athanassoula, E., Makino, J., & Bosma, A. 1997, MNRAS, 286, 825

Barnes, J. 1985, MNRAS, 215, 517

Barnes, J. E. 1989, Nature, 338, 123

Barnes, J. E. 1990, Nature, 344, 379

Barnes, J. E. & Hernquist, L. E. 1991, ApJ, 370, L65

Bell, E. F. 2003, ApJ, 586, 794

Bigiel, F., Leroy, A., Walter, F., et al. 2008, AJ, 136, 2846

Bigiel, F., Leroy, A. K., Walter, F., et al. 2011, ArXiv e-prints

Bitsakis, T., Charmandaris, V., Le Floc'h, E., et al. 2010, A&A, 517, A75+

Bode, P. W., Cohn, H. N., & Lugger, P. M. 1993, ApJ, 416, 17

Borthakur, S., Yun, M. S., & Verdes-Montenegro, L. 2010, ApJ, 710, 385

Boselli, A., Mendes de Oliveira, C., Balkowski, C., Cayatte, V., & Casoli, F. 1996, A&A, 314, 738

Braine, J., Combes, F., Casoli, F., et al. 1993, A&AS, 97, 887

Calzetti, D., Kennicutt, R. C., Engelbracht, C. W., et al. 2007, ApJ, 666, 870

Calzetti, D., Wu, S., Hong, S., et al. 2010, ApJ, 714, 1256

Casasola, V., Bettoni, D., & Galletta, G. 2004, A&A, 422, 941

Cole, S., Norberg, P., Baugh, C. M., et al. 2001, MNRAS, 326, 255

Coziol, R., Brinks, E., & Bravo-Alfaro, H. 2004, AJ, 128, 68

Da Rocha, C., Ziegler, B. L., & Mendes de Oliveira, C. 2008, MNRAS, 388, 1433

de Carvalho, R. R. & Coziol, R. 1999, AJ, 117, 1657

de Vaucouleurs, G., de Vaucouleurs, A., Corwin, Jr., H. G., et al. 1991, Third Reference Catalogue of Bright Galaxies, ed. Roman, N. G., de Vaucouleurs, G., de Vaucouleurs, A., Corwin, H. G., Jr., Buta, R. J., Paturel, G., & Fouqué, P.

Di Matteo, P., Combes, F., Melchior, A., & Semelin, B. 2007, A&A, 468, 61

Diaferio, A., Geller, M. J., & Ramella, M. 1994, AJ, 107, 868

Diaferio, A., Geller, M. J., & Ramella, M. 1995, AJ, 109, 2293

Dickman, R. L., Snell, R. L., & Schloerb, F. P. 1986, ApJ, 309, 326

Dressler, A. 1980, ApJ, 236, 351

Dressler, A., Oemler, Jr., A., Couch, W. J., et al. 1997, ApJ, 490, 577

Durbala, A., del Olmo, A., Yun, M. S., et al. 2008, AJ, 135, 130

Feigelson, E. D. & Nelson, P. I. 1985, ApJ, 293, 192

Freeland, E., Stilp, A., & Wilcots, E. 2009, AJ, 138, 295

Gallagher, S. C., Johnson, K. E., Hornschemeier, A. E., Charlton, J. C., & Hibbard, J. E. 2008, ApJ, 673, 730

Gao, Y. & Solomon, P. M. 2004, ApJ, 606, 271

Gil de Paz, A., Boissier, S., Madore, B. F., et al. 2007, ApJS, 173, 185

Governato, F., Tozzi, P., & Cavaliere, A. 1996, ApJ, 458, 18

Hashimoto, Y., Oemler, Jr., A., Lin, H., & Tucker, D. L. 1998, ApJ, 499, 589

Haynes, M. P. & Giovanelli, R. 1984, AJ, 89, 758

Helou, G., Khan, I. R., Malek, L., & Boehmer, L. 1988, ApJS, 68, 151

Hernquist, L. 1989, Nature, 340, 687

Hernquist, L., Katz, N., & Weinberg, D. H. 1995, ApJ, 442, 57

Hickson, P. 1982, ApJ, 255, 382

Hickson, P., Mendes de Oliveira, C., Huchra, J. P., & Palumbo, G. G. 1992, ApJ, 399, 353

Hickson, P., Menon, T. K., Palumbo, G. G. C., & Persic, M. 1989, ApJ, 341, 679

Huchtmeier, W. K. 1997, A&A, 325, 473

Iglesias-Páramo, J. & Vílchez, J. M. 1999, ApJ, 518, 94

Jarrett, T. H., Chester, T., Cutri, R., et al. 2000, AJ, 119, 2498

Johnson, K. E., Hibbard, J. E., Gallagher, S. C., et al. 2007, AJ, 134, 1522

Karachentseva, V. E. 1973, Soobshcheniya Spetsial'noj Astrofizicheskoj Observatorii, 8, 3

Kennicutt, Jr., R. C. 1998, ARA&A, 36, 189

Kennicutt, Jr., R. C., Roettiger, K. A., Keel, W. C., van der Hulst, J. M., & Hummel, E. 1987, AJ, 93, 1011

Kewley, L. J., Groves, B., Kauffmann, G., & Heckman, T. 2006, MNRAS, 372, 961

Konstantopoulos, I. S., Gallagher, S. C., Fedotov, K., et al. 2010, ApJ, 723, 197

Kroupa, P. 2001, MNRAS, 322, 231

Lacy, M., Storrie-Lombardi, L. J., Sajina, A., et al. 2004, ApJS, 154, 166

Larson, R. B. & Tinsley, B. M. 1978, ApJ, 219, 46

Laurikainen, E. & Moles, M. 1989, ApJ, 345, 176

Lavalley, M. P., Isobe, T., & Feigelson, E. D. 1992, in Bulletin of the American Astronomical Society, Vol. 24, Bulletin of the American Astronomical Society, 839–840

Leon, S., Combes, F., & Menon, T. K. 1998, A&A, 330, 37

Leroy, A. K., Walter, F., Bigiel, F., et al. 2009, AJ, 137, 4670

Leroy, A. K., Walter, F., Brinks, E., et al. 2008, AJ, 136, 2782

Lisenfeld, U., Verdes-Montenegro, L., Sulentic, J., et al. 2007, A&A, 462, 507

Lonsdale, C. J., Smith, H. E., Rowan-Robinson, M., et al. 2003, PASP, 115, 897

Mamon, G. 1990, in , 609

Mamon, G. A. 1986, ApJ, 307, 426

Mamon, G. A. 1987, ApJ, 321, 622

Martínez, M. 2008, PhD thesis, Universidad de Granada (Spain)

Mazzarella, J. M., Bothun, G. D., & Boroson, T. A. 1991, AJ, 101, 2034

Mendes de Oliveira, C. & Hickson, P. 1994, ApJ, 427, 684

Mendes de Oliveira, C., Plana, H., Amram, P., Bolte, M., & Boulesteix, J. 1998, ApJ, 507, 691

Merluzzi, P., Shaker, A. A., & Longo, G. 2000, in Astronomical Society of the Pacific Conference Series, Vol. 209, IAU Colloq. 174: Small Galaxy Groups, ed. M. J. Valtonen & C. Flynn, 205–+

Mihos, J. C., Richstone, D. O., & Bothun, G. D. 1991, in Bulletin of the American Astronomical Society, Vol. 23, Bulletin of the American Astronomical Society, 1401–+

Moles, M., del Olmo, A., Perea, J., et al. 1994, A&A, 285, 404

Moore, B., Katz, N., Lake, G., Dressler, A., & Oemler, A. 1996, Nature, 379, 613

Natale, G., Tuffs, R. J., Xu, C. K., et al. 2010, ApJ, 725, 955

Negroponte, J. & White, S. D. M. 1983, MNRAS, 205, 1009

Nishiyama, K., Nakai, N., & Kuno, N. 2001, PASJ, 53, 757

Ostriker, J. P., Lubin, L. M., & Hernquist, L. 1995, ApJ, 444, L61

Perea, J., del Olmo, A., Verdes-Montenegro, L., & Yun, M. S. 1997, ApJ, 490, 166

Perea, J., del Olmo, A., Verdes-Montenegro, L., et al. 2000, in Astronomical Society of the Pacific Conference Series, Vol. 209, IAU Colloq. 174: Small Galaxy Groups, ed. M. J. Valtonen & C. Flynn, 377–+

Pietsch, W., Trinchieri, G., Arp, H., & Sulentic, J. W. 1997, A&A, 322, 89

Plana, H., Amram, P., Mendes de Oliveira, C., Balkowski, C., & Boulesteix, J. 2003, AJ, 125, 1736

Ramella, M., Diaferio, A., Geller, M. J., & Huchra, J. P. 1994, AJ, 107, 1623

Rasmussen, J., Ponman, T. J., Verdes-Montenegro, L., Yun, M. S., & Borthakur, S. 2008, MNRAS, 388, 1245

Regan, M. W., Thornley, M. D., Helfer, T. T., et al. 2001, ApJ, 561, 218

Ribeiro, A. L. B., de Carvalho, R. R., Capelato, H. V., & Zepf, S. E. 1998, ApJ, 497, 72

Rood, H. J. & Struble, M. F. 1994, PASP, 106, 413

Rood, H. J. & Williams, B. A. 1989, ApJ, 339, 772

Rose, J. A. 1977, ApJ, 211, 311

Rubin, V. C., Hunter, D. A., & Ford, Jr., W. K. 1990, ApJ, 365, 86

Ryle, M. & Hewish, A. 1960, MNRAS, 120, 220

Salpeter, E. E. 1955, ApJ, 121, 161

Sanders, D. B., Scoville, N. Z., & Soifer, B. T. 1991, ApJ, 370, 158

Scoville, N. Z., Carlstrom, J. E., Chandler, C. J., et al. 1993, PASP, 105, 1482

Shakhbazyan, R. K. 1973, Astrophysics, 9, 296

Stephan, M. 1877, MNRAS, 37, 334

Sulentic, J. W. 1983, ApJ, 270, 417

Sulentic, J. W. 1987, ApJ, 322, 605

Sulentic, J. W. 1997, ApJ, 482, 640

Sulentic, J. W. 2000, in Astronomical Society of the Pacific Conference Series, Vol. 209, IAU Colloq. 174: Small Galaxy Groups, ed. M. J. Valtonen & C. Flynn, 226–+

Sulentic, J. W. & de Mello Rabaca, D. F. 1993, ApJ, 410, 520

Sulentic, J. W., Rosado, M., Dultzin-Hacyan, D., et al. 2001, AJ, 122, 2993

Toomre, A. & Toomre, J. 1972, ApJ, 178, 623

Tovmassian, H. M. 2001, PASP, 113, 543

Tovmassian, H. M. & Chavushyan, V. H. 2000, AJ, 119, 1687

Tzanavaris, P., Hornschemeier, A. E., Gallagher, S. C., et al. 2010, ApJ, 716, 556

Vennik, J., Richter, G. M., & Longo, G. 1993, Astronomische Nachrichten, 314, 393

Verdes-Montenegro, L., del Olmo, A., Perea, J., et al. 1997, A&A, 321, 409

Verdes-Montenegro, L., Del Olmo, A., Yun, M. S., & Perea, J. 2005a, A&A, 430, 443

Verdes-Montenegro, L., Sulentic, J., Lisenfeld, U., et al. 2005b, A&A, 436, 443

Verdes-Montenegro, L., Yun, M. S., Borthakur, S., et al. 2007, in Groups of Galaxies in the Nearby Universe, ed. I. Saviane, V. D. Ivanov, & J. Borissova, 349–+

Verdes-Montenegro, L., Yun, M. S., Perea, J., del Olmo, A., & Ho, P. T. P. 1998, ApJ, 497, 89

Verdes-Montenegro, L., Yun, M. S., Williams, B. A., et al. 2001, A&A, 377, 812

Verley, S., Relaño, M., Kramer, C., et al. 2010, A&A, 518, L68+

Véron-Cetty, M. & Véron, P. 2010, A&A, 518, A10+

Vir Lal, D., Matsushita, S., & Lim, J. 2007, ArXiv e-prints, 706

Walter, F., Brinks, E., de Blok, W. J. G., et al. 2008, AJ, 136, 2563

West, M. J. 1989, ApJ, 344, 535

Williams, B. A. & Rood, H. J. 1987, ApJS, 63, 265

Wilman, D. J., Balogh, M. L., Bower, R. G., et al. 2005, MNRAS, 358, 88

Woods, D. F., Geller, M. J., & Barton, E. J. 2006, AJ, 132, 197

Young, J. S. & Scoville, N. Z. 1991, ARA&A, 29, 581

Zepf, S. E. & Whitmore, B. C. 1993, ApJ, 418, 72

Zepf, S. E., Whitmore, B. C., & Levison, H. F. 1991, ApJ, 383, 524

Zhu, Y., Wu, H., Cao, C., & Li, H. 2008, ApJ, 686, 155

Zwicky, F. 1959, Handbuch der Physik, 53, 373